Above 10 cm^{-1} (i.e., in the far infrared), $\epsilon'(\bar{\nu}) \doteqdot \epsilon_\infty$ and $\epsilon''(\bar{\nu})$ is small [although $\alpha(\bar{\nu})$ is large]. Using these approximations, both these equations reduce to

$$C_{\mathbf{u}}(t) = \frac{3kT}{4\pi^3 N_u^2}\left[\frac{9n}{(n^2+2)^2}\right]\int_0^\infty \frac{\alpha(\bar{\nu})}{\bar{\nu}^2}\cos(2\pi\bar{\nu}ct)\,d\bar{\nu} \tag{II.25}$$

where the square brackets enclose a nondispersive correction. Numerically, therefore, $C_{\mathbf{u}}(t)$ is independent of any severe internal field correction above 10 cm^{-1}. Therefore, the shift in $\bar{\nu}_{max}$ in Fig. 20, and the features of Fig. 1, may be ascribed to the molecular dynamics. $C_{\mathbf{u}}(t)$ is a real, even function of time, so that it can be expanded as a Taylor series:

$$\langle \mathbf{u}(t)\cdot\mathbf{u}(0)\rangle = \langle u^2(0)\rangle - \frac{t^2}{2!}\langle \dot{u}^2(0)\rangle + \frac{t^4}{4!}\langle \ddot{u}^2(0)\rangle - \cdots \tag{II.26}$$

with $\langle u^2(0)\rangle = 1$ by definition. For a linear molecule

$$-\ddot{C}_{\mathbf{u}}(0) = \langle \dot{u}^2(0)\rangle = 2\frac{kT}{I}$$

where I is the moment of inertia, since for rotational kinetic energy $\frac{1}{2}I\omega^2$ becomes on average kT. The mean-square acceleration $\langle \ddot{u}^2(0)\rangle$ is the sum of a radial part (centripetal acceleration, owing to the fact that the vector $\mathbf{u}$ is of a fixed length), independent of interactions and having the value $8k^2T^2/I^2$; and a tangential part $\langle O(V)^2\rangle/I^2$ produced by the mean-square torque $\langle O(V)^2\rangle$ that the environment produces in the molecule. Therefore, (II.26) becomes

$$C_{\mathbf{u}}(t) = 1 - \frac{kT}{I}t^2 + \left[\frac{k^2T^2}{3I^2} + \frac{\langle O(V)^2\rangle}{24I^2}\right]t^4 - \cdots$$

Gordon[34] has calculated the first two odd moments, which appear in quantum mechanical treatments of $C_{\mathbf{u}}(t)$, as well as some quantum corrections to the even moments. Classically, we have

$$\ddot{C}_{\mathbf{u}}(t) = \frac{3kTVnc}{4\pi N^2\mu}\int_{-\infty}^{\infty}\exp(i\omega t)\alpha(\omega)\,d\omega \tag{II.27}$$

Taking (II.27) at $t=0$ produces a relation for the integrand absorption intensity per molecule for all rotational-type zero-THz absorptions:

$$\int_0^\infty \frac{V}{N}\alpha(\omega)\,d\omega = \frac{4\pi^2\mu^2}{3Inc} \tag{II.28}$$

which is Gordon's sum rule, derived classically by Brot.[52]

B. A Continued-Fraction Expansion of $C_{\mathbf{u}}(t)$

Under certain conditions we may write (I.6) with $\mathbf{A}=[\mathbf{u}]$. Therefore we have, with these restrictions,

$$\dot{\mathbf{u}}(t) = -\int_0^t K_0(t-\tau)\mathbf{u}(\tau)\,d\tau + \mathbf{f}(t)$$

where

$$K_0(t) = \langle \mathbf{f}(t)\cdot\mathbf{f}(0)\rangle / \langle \mathbf{u}(0)\cdot\mathbf{u}(0)\rangle \tag{II.29}$$

Here $\mathbf{f}(t)$ is a stochastic quantity whose correlation function defines the memory $K_0(t)$. This relation is referred to often as the second fluctuation–dissipation theorem derived initially by Kubo.[65] Equation (II.29) may be solved to give

$$\dot{C}_{\mathbf{u}}(t) = -\int_0^t K_0(t-\tau)C_{\mathbf{u}}(\tau)\,d\tau \tag{II.30}$$

which may be expanded in the Mori continued-fraction form

$$\tilde{C}_{\mathbf{u}}(s) = \frac{C_{\mathbf{u}}(0)}{s+\tilde{K}_0(s)} = \frac{C_{\mathbf{u}}(0)}{s+\dfrac{K_0(0)}{s+\tilde{K}_1(s)}} = \cdots \tag{II.31}$$

in the space (s) of Laplace transforms. Now if

$$C_{\mathbf{u}}(t) = \sum_{n=0}^{\infty} a_n \frac{t^{2n}}{(2n)!}$$

as is required by time-reversal symmetry for the classical autocorrelation function of $\mathbf{u}$, it follows that

$$\begin{aligned} K_0(t) &= \sum_{n=0}^{\infty} {}^0k_n t^{2n}/(2n)! \\ K_1(t) &= \sum_{n=0}^{\infty} {}^1k_n t^{2n}/(2n)! \\ K_2(t) &= \sum_{n=0}^{\infty} {}^2k_n t^{2n}/(2n)! \end{aligned} \tag{II.32}$$

Therefore, solving for ${}^0k_n$ in terms of a_N gives for $N \geq 1$:

$${}^0k_N = -a_{N+1} - \sum_{n=1}^{N} {}^0k_{N-n}a_n \tag{II.33}$$

so that the coefficients ${}^0k_N$ are known in terms of a_N and their precursors. The coefficients a_N themselves are given in terms of experimental spectral moments $(1/N_0)\int_0^\infty \omega^n \alpha(\omega) d\omega$, with N_0 as the molecular number density. Ideally, therefore, measurement of the experimental spectral moments is enough to define the memory functions $K_0(0), \ldots, K_N(0)$. In reality, of course, we are limited by experimental uncertainty in the high-frequency side of the absorption band for $n > 1$, so that to obtain a tractable expression for $C_u(t)$ we must minimize the number of parameters $K_0(0), \ldots, K_N(0)$ by truncating the continued fraction at a level N where the decay of $K_N(t)$ is so sharp as to be virtually a delta function compared with that of $C_u(t)$ itself. The value of N at which this is so is not known a priori, and must therefore be arrived at by physical intuition similar to that used in deriving (I.30). We aim therefore at a compromise—avoiding too early an approximant (some of the models in Table I) and also avoiding adjustable parameters, which obscure the true quality of the fit between theory and experiment. If we can, in this way, devise a method for evaluating $K_0(0), \ldots, K_N(0)$ from the experimental zero-THz bandshape, then effectively this is providing us with information on the mean intermolecular potential energy in terms of the mean-square torque [related to $K_1(0)$ via (II.26)], the mean of the torque derivative squared [via $K_2(0)$], and so on. In the next section we discuss the recent attempts at this problem and thereafter the results in the gaslike environment. The relation of extended diffusion modes such as the m and J of Gordon to the continued fraction is explained.

1. *Approximants of the Continued Fraction for $\tilde{C}_u(s)$*

Since molecular interaction is the essential element in the characteristic shift to high frequencies of $\tilde{\nu}_{max}$ (in Fig. 1, for example) and since the intermolecular potential is basic in this context, a truncation of (II.131) is unrealistic unless the final expression for $C_u(t)$ involves at least the equilibrium averages $K_0(0)$ and $K_1(0)$. This minimum requirement is fulfilled by the assumption that $K_2(t)$ decays as a delta function at the origin, $t=0$. This implies that

$$K_1(t) = K_1(0)\exp(-\gamma t) \tag{II.34}$$

where γ is a characteristic decay frequency to be determined. Now $\tilde{C}_u(s)$ has the same form as (I.30):

$$\tilde{C}_u(s) = \frac{s^2 + \gamma s + K_1(0)}{s^3 + \gamma s^2 + (K_0(0) + K_1(0))s + \gamma K_0(0)} \tag{II.35}$$

and $C_u(t)$ is recoverable analytically. This is essentially also the form used by Kivelson and Madden in relating $C_u(t)$ to $C_M(t)$, and was first considered by Barojas, Levesque, and Quentrec[42] to explore some molecular dynamics simulations of nitrogen using the atom–atom potential of Section III. Recently, the same approximant has been considered carefully by Drawid and Halley[44] in order to calculate a time-dependent spin–spin correlation function for the classical Heisenberg model of ferromagnetism. Using the relationships devised by these authors, it may be deduced that (II.35) may also be derived from

$$K_0(t) = K_0(0)\exp\left(-K_1(0)t^2/2\right) \tag{II.36}$$

when it seems clear that

$$\gamma = \left(\frac{\pi}{2} K_1(0)\right)^{1/2} \tag{II.37}$$

Equations (II.36) and (II.37) ensure that $K_0(t)$ have the correct first two terms in Taylor's series expansion (II.32). The "mean-square-torque" term $K_1(0)$ in (II.35) may be fixed by differentiating the model absorption coefficient [essentially the Fourier–Laplace transform of (II.35)] with respect to ω, whereupon $K_1(0)$ can be obtained from the measured peak frequency $\tilde{\nu}_{max}$. Since $K_0(0)$ is the mean-square angular velocity, (II.35) may be used for reproducing experimental data without recourse to least-mean-squares iteration. Alternatively, it is sometimes convenient to iterate on γ and $K_1(0)$ so that (II.37) may be tested out empirically.

It is possible also to take the next approximant represented by

$$K_2(t) = K_2(0)\exp\left[-(\pi/2K_1(0))^{1/2} t\right] \tag{II.38}$$

and to estimate both $K_1(0)$ and $K_2(0)$ without recourse to least-mean-squares iteration by differentiating both $\epsilon''(\omega)$ and $\alpha(\omega)$ with respect to ω. Since $\epsilon''(\omega)$ peaks at a much lower frequency than $\alpha(\omega)$, this leads to two simultaneous equations for $K_1(0)$ and $K_2(0)$.

The absorption coefficient may be recovered from $\tilde{C}_u(s)$ using equations such as (II.23) to (II.25). The autocorrelation function is a sum of three complex exponentials, which, when the denominator discriminant in (II.35) is negative, becomes

$$C_u(t) = \left(\frac{\cos\beta t}{1+\Gamma} + \frac{1}{\beta}\left(\frac{\alpha_1 + \Gamma\alpha_2}{1+\Gamma}\right)\sin\beta t\right)\exp(-\alpha_1 t) + \frac{\Gamma}{1+\Gamma}\exp(-\alpha_2 t) \tag{II.39}$$

where

$$\Gamma = \frac{-2\alpha_1(\alpha_1^2+\beta^2)}{\alpha_2(3\alpha_1^2-\beta^2-\alpha_2^2)}$$

with

$$\alpha_2 = -\frac{1}{2}(s_1+s_2)+\frac{\gamma}{3} \qquad \alpha_1 = \frac{1}{2}(s_1+s_2)+\frac{\gamma}{3} \qquad \beta = \frac{\sqrt{3}}{2}(s_1-s_2)$$

The parameters s_1 and s_2 are defined by

$$s_1 = \left[-\frac{B}{2}+\left(\frac{A^3}{27}+\frac{B^2}{4}\right)^{1/2}\right]^{1/3}$$

$$s_2 = \left[-\frac{B}{2}-\left(\frac{A^3}{27}+\frac{B^2}{4}\right)^{1/2}\right]^{1/3}$$

where

$$A = K_0(0)+K_1(0)-\frac{\gamma^2}{3} \qquad B = \frac{\gamma}{3}\left(\frac{2\gamma^2}{9}+2K_0(0)-K_1(0)\right)$$

The Taylor series of (II.39) is even to the fourth power of time, but has a term in t^5, and all odd terms thereafter are also nonzero. The form of (II.39) although cumbersome is useful since it is derivable from (I.30) *and* also (II.53). It represents the autocorrelation functions $C_u(t)$ and $C_\theta(t)$ therefore for at least four seemingly unrelated models of the fluid state.

2. *Molecular Orientations in the Compressed Gas*

With only the mean-square torque properly defined [through $K_1(0)$] it is interesting to evaluate the usefulness of (II.35) in a compressed gas of dipolar molecules before proceeding to the liquid state as embodied in, for example, pure benzonitrile at ambient temperature. In so doing we may observe, by compressing the gas into the liquid, how changes of bandshape and intensity result from the additional constraints which may be imposed on rototranslational freedom on going from one phase to the next.

We have chosen for experimental convenience the symmetric top CH_3Cl and the asymmetric top CH_2CF_2. In the limit of free rotation, the *infinite* continued fraction reduces to the classical Kummer function for $C_u(t)$, but the approximant embodied in (II.35) does not, as shown in Fig. 28 with

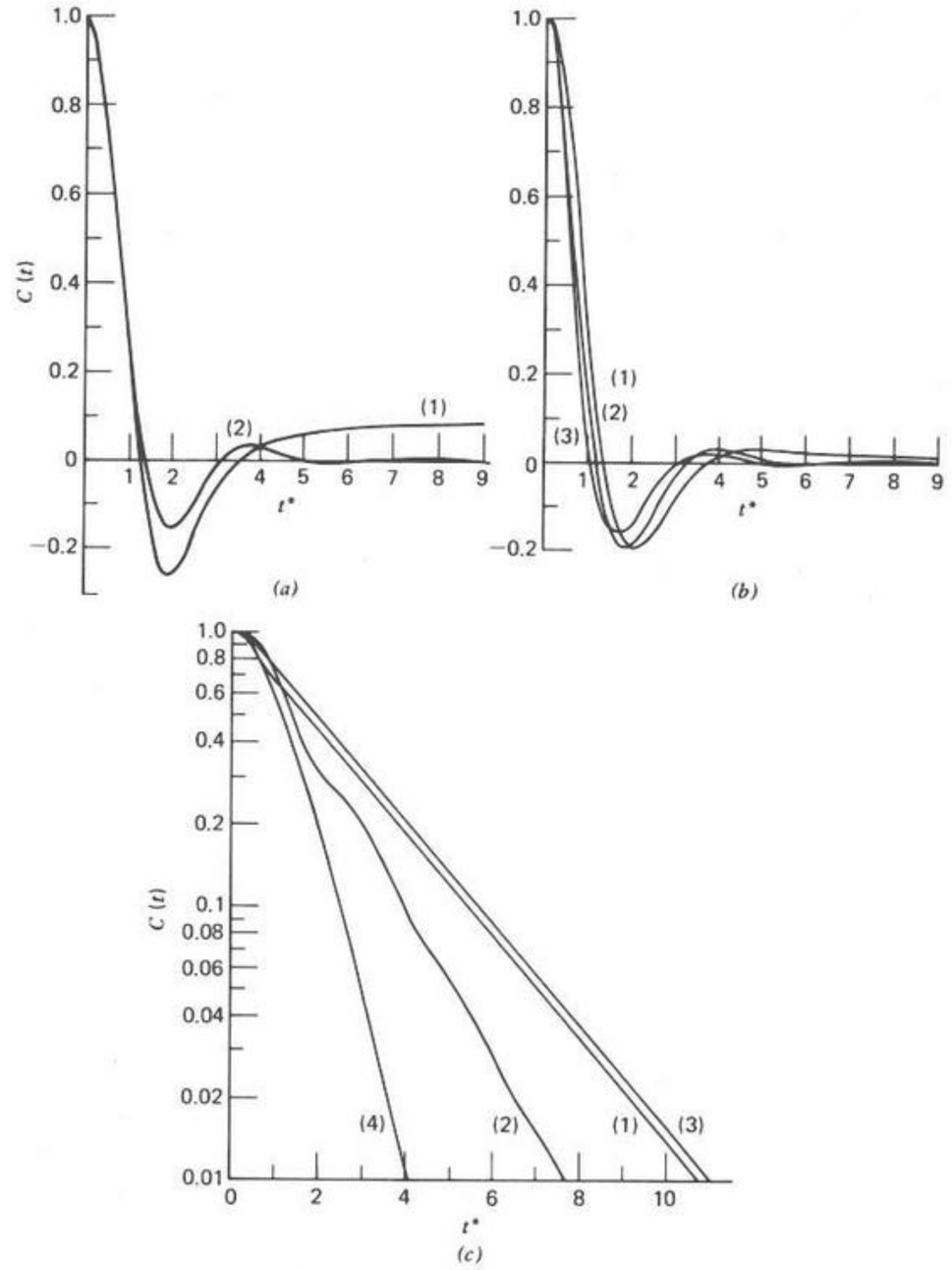

Fig. 28. (*a*) $t^* = (kT/I_B)^{1/2}t$. (1) True free-rotor orientational autocorrelation function for CH_3Cl at 296°K; (2) best fit of three variable theory to the free-rotor $J \rightarrow J+1$ contour. (*b*) (1) $C_u(t)$ for CH_3Cl(g) at 5.8 bars, 296°K; (2) J-diffusion model with $\tau^* = (kT/I_B)^{1/2}\tau = 4.0$ as the reduced time between collisions; (3) $C_u(t)$ for CH_3Cl+ethane(*g*) at 33.5 bars, 296°K. (*c*) (1) $C_u(t)$ for CH_3Cl (liquid), at 296°K; (2) $C_u(t)$ for CH_3Cl+ethane(*l*) at 296°K; (3) J-diffusion model with $\tau^* = 0.2$; (4) J-diffusion model with $\tau^* = 0.5$. [Reproduced by permission from *J. Chem. Soc. Faraday Trans. 2*, **72**, 1907 (1976).]

$\langle O(V)^2 \rangle = 0$ and $K_1(0) = 4kT/I_B$, where I_B is the moment of inertia about the dipole axis in CH_3Cl. In the limit of vanishing torque, therefore, (II.35) reduces to the Kummer function for classical free rotation at short times only, when the free-rotor Taylor series is approximated adequately by its first few terms.

A typical fit[66] of $\alpha(\omega)$ from (II.35) to the CH_3Cl *compressed* gas[67] is shown in Fig. 28 together with that for a gaseous mixture of CH_3Cl in ethylene (to remove dipole–dipole coupling). The torque term $K_1(0)$ in the latter is almost twice that needed to fit the free-rotor contour, as can be seen in Table IV.

The fit for pure liquid CH_3Cl (Fig. 28*c*) is good, with $K_1(0)$ considerably increased—reflecting the increase in the apparent root-mean-square torque. In a mixture with ethane in the liquid state, $K_1(0)$ needs to be surprisingly small for best fit since the observed band is surprisingly narrow, with the half-width reflected in the low value of γ needed (Table IV). Within the limitations of the early approximant used for $C_u(t)$ we may take this as a rough indication of the less severe angular constraints in the ethane environment. This is reflected in the form of $C_u(t)$ (Fig. 28*c*), which becomes exponential at long times only, in contrast to that of the pure liquid, which exhibits logarithmic decay very quickly, suggestive of small-step rotational diffusion. Below $t^* = (kT/I_B)^{1/2}t = 1$, $C_u(t)$ for liquid CH_3Cl exhibits oscillatory behavior. This shows up in the far infrared as the Poley absorption (i.e., the high-frequency extension of the microwave absorption). This short-time behavior of $C_u(t)$ reflects the torsional oscillatory, or librational, motion of **u** about an axis which is diffusing through the fluid

TABLE IV
Parameters γ and $K_1(0)$ Least Mean Squares
Fitted to Compressed Gaseous Data for CH_3Cl and CH_2CF_2[a]

System	Pressure (bars)	$\left(\frac{2kT}{I_B}\right)K_1(0)$	$\left(\frac{2kT}{I_B}\right)^{1/2}\gamma$	$10^{40}I_B$(g·cm²)
CH_3Cl	5.8	3.61	3.74	63.12
CH_3Cl/ethane	39.3	4.21	3.74	63.12
CH_3Cl/ethane(*l*)	—	4.00	1.90	63.12
CH_3Cl(*l*)	—	14.39	4.29	63.12
CF_2CH_2	35.2	3.67	3.86	80.45
CF_2CH_2(*l*)	—	6.15	3.91	80.45
CH_3Cl ($J \to J+1$ contour)	—	2.51	2.54	63.12

[a]Reproduced by permission from *J. Chem. Soc. Faraday Trans.* 2, **72**, 1907 (1976).

(i.e., performing itinerant oscillation–libration). As Fig. 28*c* shows, the *J*-diffusion model for the symmetric top is incapable of reproducing this oscillating form for $C_u(t)$ since essentially the concept of libration is as ill-defined in this theory as is the mean-square torque. It is too early an approximant of the continued fraction.

In the asymmetric rotor CH_2CF_2 (Fig. 28), the essential difference between the compressed gas and liquid is seen more clearly in terms of $C_u(t)$. This is damped in the liquid and never becomes negative, as in the compressed gas.

If, then, we are prepared to regard γ and $K_1(0)$ for convenience as variable and to accept the limitations inherent in (II.35), the truncation procedure outlined in Section II.B.1 may be used to elucidate the compressed gas molecular dynamics, and comparison with the liquid may be made quantitatively. The stricter approach is to evaluate γ and $K_1(0)$ with no least-mean-squares fitting. This would soon bring out the deficiencies of (II.35), as is seen in the case of CH_2Cl_2 in Fig. 28. In fact, Table IV shows clearly that (II.137) is generally not obeyed, so that least-mean-squares fitting tends to mask the theoretical difficiencies in favor of empiricism.

3. *Gaslike Behavior in the Liquid State: Water Free of Hydrogen Bonding*[68]

This is discernible in systems such as hydrogen halide/SF_6 mixtures, and ammonia dissolved in the same liquid solvent: for here the broadened remnants of the $J \to J+1$ rotational contour clearly appear. These systems will be considered presently, but the motions of free, unbound water molecules in organic solvents are equally extraordinary, since $C_u(t)$ is very markedly nonexponential, with correlation times typically ca. 0.1 psec. The loss curves $\epsilon''(\omega)$ are asymmetric and peak at frequencies almost in the mid infrared, in great contrast to the "ordinary" behavior exhibited in the microwave region by the pure liquid. In producing these curves the empirical approach with (II.35) has proven useful since it is found possible, by varying γ and $K_1(0)$, to reproduce closely the far-infrared absorption data of Pardoe and Gebbie[69] for *very dilute* solutions of water in cyclohexane, carbon tetrachloride, and benzene. The results are illustrated in Fig. 29 along with $C_u(t)$, calculated therefrom. Table V shows the refined γ and $K_1(0)$ values.

The motion of the water molecules is gaslike in the sense that $C_u(t)$ is gaslike, displaying a negative region in cyclohexane, for example, at ~0.11 psec. Therefore, there is a probability that a majority of molecules will have swung through greater than $\pi/2$ of the solid angle at times greater than 0.11 psec. The overall correlation time is 0.10 ps, much shorter than

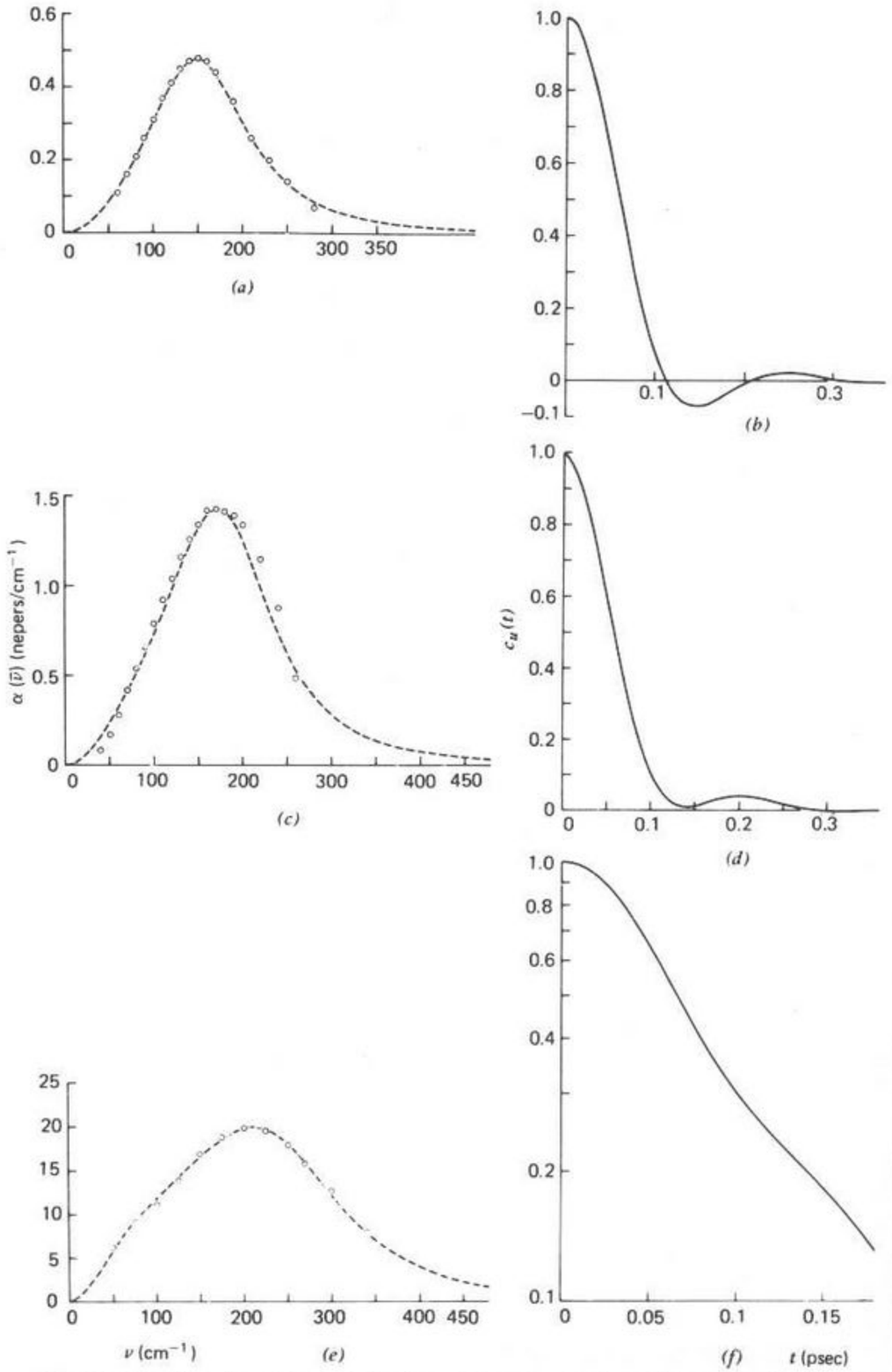

Fig. 29. (*a*) Absorption of a 0.011% w/w solution of water in cyclohexane at 296°K, corrected for solvent; (----), Mori theory best fit. (*b*) $C_u(t)$ for the absorption of Fig. 29*a*. (*c*) Absorption of a 0.01% w/w solution of water in CCl_4 at 300°K, corrected for solvent; (----), Mori theory best fit. (*d*) $C_u(t)$ for H_2O+CCl_4. (*e*) Absorption of a 0.06% w/w solution of water in benzene at 300°K, corrected for solvent; (----), Mori theory best fit. (*f*) $C_u(t)$ for H_2O + benzene. [Reproduced by permission from *J. Chem. Soc. Faraday Trans. 2*, **72**, 2143 (1976).]

TABLE V
Parameters γ and $K_1(0)$ for Solutions of Water[a]

Solution	T	$(2kT/I_B)^{-1}K_0(0)$	$(2kT/I_B)^{-1}K_1(0)$	$\left(\frac{2kT}{I_B}\right)^{-1/2}\gamma$
H_2O + cyclohexane (0.011% w/w)	296	1.11	3.00	2.58
H_2O+CCl_4 (0.01% w/w)	300	1.18	3.39	2.37
H_2O + benzene (0.06% w/w)	300	1.16	6.19	2.82

[a]Reproduced by permission from *J. Chem. Soc. Faraday Trans.* 2, **72** (1976).

the Debye relaxation time in pure liquid water [the inverse of $\omega_{max}(\epsilon'')$], the epitome of hydrogen bonding.[70] The loss curve in cyclohexane is *asymmetric on the log scale* and peaks at 140 cm^{-1}. The oscillations in $C_u(t)$ are damped in benzene but not completely so (Fig. 29*f*).

At this stage it is convenient to describe the quantized rotation observable in hydrogen halides such as HBr in liquid SF_6 in terms of the extended diffusion models of gaslike molecular dynamics developed over the last 15 years in numerous articles and reviews.[53] They are, of course, discretely classical in the sense that the $J\rightarrow J+1$ lines are broadened by classical statistical mechanics. Lindenberg and Cukier have generalized the concepts involved to an extent where direct comparison with the continued fraction is possible for higher-order approximants than those used in the well-known *m*- and *J*-diffusion models.[45]

With reference to Table I, the latter is an approximant defined by the relation

$$K_0(t)=K_{FR}(t)\exp(-|t|/\tau) \tag{II.40}$$

where $K(t)$ is the overall memory function and $K_{FR}(t)$ that associated with an ensemble of free rotors. τ is the mean time between elastic collisions which randomize the molecular angular momentum (**J**) in magnitude and direction. The correlation function associated with (II.40) is then the Laplace transform of

$$\tilde{C}_u(s)=\frac{\tilde{C}_{FR}(s+1/\tau)}{1-\tau^{-1}\tilde{C}_{FR}(s+1/\tau)}$$

$$=\sum_{n=0}^{\infty}\frac{1}{\tau^n}\tilde{C}_{FR}^{n+1}(s+1/\tau) \tag{II.41}$$

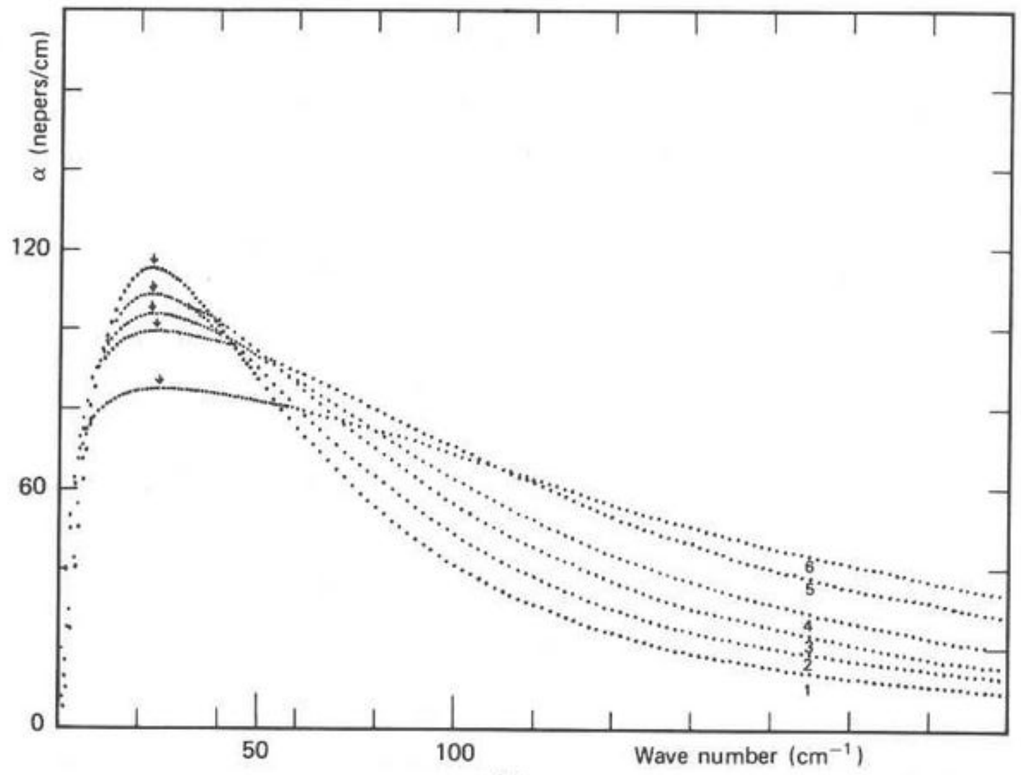

(a)

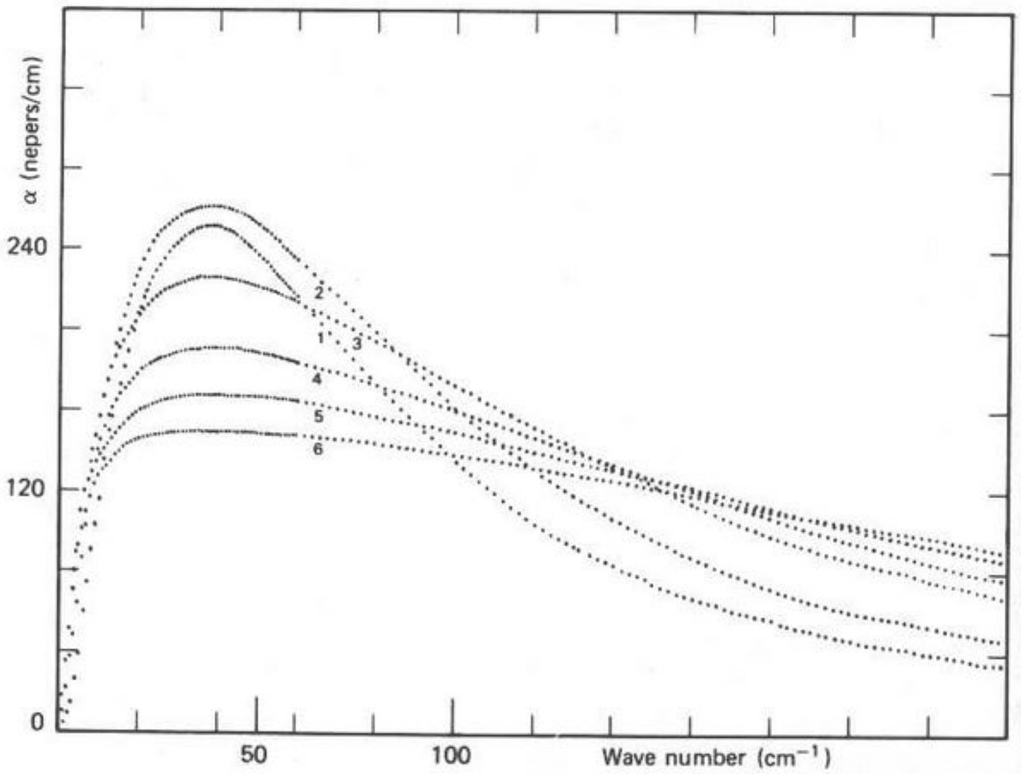

Fig. 30. Type of variation with temperature of the symmetric-top Langevin equation for (*a*) CHF_3 with (1)–(6) decreasing τ; (*b*) CH_3F with (1)–(6) decreasing τ. [Reproduced by permission from *J. Chim. Phys.*, **75**, 527 (1978).]

which is identical with the form devised by Gordon for linear molecules. It has a Taylor expansion with a term proportional to t^3, since the concept of elastic collisions implies that the torque is singular at each collision and therefore has no definable mean. The spectral consequences are illustrated in Fig. 30 for the methyl halides considered by Gerschel.[3] Experimentally, $\bar{\nu}_{max}$ moves to higher frequencies, but theoretically it remains at the frequency ω_J corresponding to the root-mean-square angular velocity of the N-particle ensemble, the high-frequency return to transparency being far too gradual. At one stage in the derivation of $C_u(t)$ for the m diffusion model, the assumption is made that

$$K_0(t) = K_0(0)\exp(-\gamma_1 t) \tag{II.42}$$

so that again the mean-square torque is undefined. The zero-THz band can be used to evaluate this model, which is also not capable of moving $\bar{\nu}_{max}$ to higher frequencies. In view of this straightforward procedure it is surprising that the same indications have been so long in forthcoming with techniques such as Rayleigh scattering, infrared and Raman line broadening, and neutron scattering.[71]

In fact, the conspicuous experimental shift in $\bar{\nu}_{max}$ (along the gas–liquid coexistence curve of Fig. 1, for example) demands the assumption of correlated collisions. This has been the basis for some modifications to the original m and J diffusion concepts whereby it becomes possible to vary the amount of angular momentum transferred during a collision and the statistics governing the distributions of intervals in between. However, the modifications still result in the aphysical t^3 of the Taylor expansion and the models are still approximants of the degree represented by (II.40) and (II.42). Denoting by $\cos(\gamma(J))$ the average cosine of the angular momentum vector, it is found[16] that the Poley absorption is ill-matched unless collisions are assumed statistically correlated and that the angular momentum is such that $\cos[\gamma(\mathbf{J})] < 0$.

Chandler[33] has discussed the translational and rotational diffusion of rough hard spheres starting from the Liouville equation, and has found that the derivation from Poisson behavior in dense systems means that the first term in the *cumulant* expansion of the memory kernel is insufficient to describe the dynamics of the system. This happens when the rotational motion couples strongly to collective modes in the system. It may be argued that the amount of rotational energy and momentum transfer during a collision roughly corresponds, for dense systems, to the average change in these quantities during a time of the order of the interval between collisions. Correlated collisions imply an oscillatory angular momentum correlation function (see Fig. 14 to 19) which is found in Section III with molecular dynamics systems of strongly anisotropic molecules. Restricted

to binary collision operators, the Chandler formalism reduces to the original J-diffusion model represented by (II.40), where the angular momentum is randomized onto a Poisson distribution. Frenkel, Wegdam, and van der Elsken[16] have shifted $\bar{\nu}_{max}$ in $CH_3CN(l)$ in the context of this model by invoking a statistical distribution which is basically Poisson but with an additional "pseudophonon" peak adjustable for best fit, with the zero-THz data. However, the intermolecular potential is still ill-defined (in terms of hard-sphere collisions). The usefulness of molecular dynamics simulations in this context has been demonstrated by O'Dell and Berne,[43] who have collected data on rough-sphere ensembles which meet almost all the criteria dictated by Gordon for m and J diffusion. However there is an enormous disparity between prediction and observation of correlation functions from the numerical solution of the equation of motion. Part of the discrepancy seems to be in fact that collisions in the molecular frame can, in reality, randomize only two of the three components of momentum. A similar numerical simulation of the planar itinerant oscillator produces results much more in accord with the analytical analysis, and is described in Section III.

However, some modifications to the amount of momentum and energy transfer introduced by Frenkel and Wegdam[72] are useful in describing the $HBr/SF_6(l)$ spectrum and correlation functions of Figs. 4 and 37, where the $J \rightarrow J+1$ lines are preferentially broadened (those on the low-frequency side more so than the others). Using this phenomenon, Frenkel, Wegdam, and van der Elsken[16] have obtained much valuable information on the compressed-gas and liquid-phase molecular dynamics of the hydrogen halides. Some computer simulations by Frenkel[73] complement these data. In Fig. 4 we have used an approximant defined by

$$K_1(t) = \beta K_{1FR}(t) \exp(-|t|/\tau) \tag{II.43}$$

and introduced by Bliot and Constant[40] who describe the parameters β and τ as purely stochastic in origin. By using a set of $J \rightarrow J+1$ lines for the free-rotor ensemble $C_{FR}(t)$, the variation of the computed $HBr/SF_6(l)$ spectrum with β is demonstrated in Fig. 4. No preferential broadening is possible with this model,[41] but $\bar{\nu}_{max}$ is shifted by very small changes in β.

C. Continued-Fraction Expansion and the Dense Liquid State

By "dense liquid" we mean liquids such as benzonitrile or *tert*-butyl chloride which may be classed as ordinary solvents whose critical temperatures lie well above ambient. These are characterized in the far infrared by the large difference observable between the Poley frequency maximum $\bar{\nu}_{max}$ and the peak of the $J \rightarrow J+1$ set of free-rotor transitions, which is classically its root-mean-square angular velocity. In this section we will describe how the absorption in this phase may be used to discriminate between some of the currently popular models of the fluid state which have been classified in Table I as approximants of the Mori continued fraction. It is therefore logical to commence with a description of the work carried out recently on the approximant where the first memory function is a delta function at $t=0$. In this case the (I.6) reduces to the Langevin equation for rotational Brownian motion:

$$\dot{\mathbf{J}}(t) + \zeta_R \cdot \mathbf{J}(t) = \Gamma(t) \tag{II.44}$$

where $\mathbf{J}$ is the angular momentum, ζ_R is the rotational friction tensor, and $\Gamma(t)$ is a random torque which is stationary and Gaussian, having an infinitely short correlation time, so that $\langle \Gamma(t) \cdot \Gamma(0) \rangle = 2D_J \delta(t)$, where $\delta(t)$ is the delta function in time, and D_J the rotational diffusion coefficient. No correlation exists between $\mathbf{J}$ and Γ. In a coordinate frame defined by the principal axes of inertia, we have

$$I \cdot \dot{\omega} + \omega \times (I \cdot \omega) + \zeta_R \cdot (I \cdot \omega) = \Gamma(t) \tag{II.45}$$

The solution of this nonlinear stochastic differential equation is simplified by neglecting the molecular inertia. For the asymmetric top, Perrin's equations then follow, where in the absence of an internal field correction,

$$\frac{\epsilon^*(\omega) - \epsilon_\infty}{\epsilon_0 - \epsilon_\infty} = \frac{1}{\mu^2} \left[\frac{\mu_x^2 (D_y + D_z)}{i\omega + D_y + D_z} + \frac{\mu_y^2 (D_x + D_z)}{i\omega + D_x + D_z} + \frac{\mu_z^2 (D_x + D_y)}{i\omega + D_x + D_y} \right] \tag{II.46}$$

where $D_i = kT/I_i\beta_i$, and $\mu^2 = \mu_x^2 + \mu_y^2 + \mu_z^2$. Here μ_i is the component of the permanent dipole along the principal axis denoted by i, and β_i is the friction coefficient. By substituting $D = D_i$ in (II.46) the result simplifies further to the particular case of the rotational Brownian motion of the inertialess spherical top as treated by Debye. Converting $\epsilon''(\omega)$ to power absorption gives the plateau value:

$$\alpha(\omega) \rightarrow (\epsilon_0 - \epsilon_\infty)/nc\tau_0 \tag{II.47}$$

as $\omega \rightarrow \infty$, where τ_D is the Debye relaxation time, and n is defined by $\epsilon_\infty^{1/2}$. Recently, McConnell and others,[22] and Morita,[21] have independently solved (II.45) with a full consideration of inertial effects. To give an idea of the complexity of this undertaking, we present some of their final equations below and evaluate them against some of the most accurate and comprehensive zero-THz data available.

For certain geometries, such as those of the needle and sphere with embedded dipoles, the use by McConnell of Bogoliubov–Mitropolsky matrices yields the following equations, for the complex polarizability

$\alpha^*(\omega)$ [not to be confused with $\alpha(\omega)$, the power absorption coefficient]. For the sphere, for example,

$$\frac{\alpha'(\omega)}{\alpha(0)} =$$

$$1-(F(0))^{-1}\left[\frac{\omega'^2}{G'^2+\omega'^2}-\frac{2\gamma\omega'^2}{(1+G')^2+\omega'^2}\right.$$

$$+\gamma^2\left[\frac{3/2\omega'^2}{(2+G'^2)+\omega'^2}-\frac{4(1+G')\omega'^2}{\left[(1+G')^2+\omega'^2\right]^2}-\frac{2\omega'^2}{(1+G')^2+\omega'^2}\right]$$

$$-\gamma^3\left[\frac{6(1+G')^2\omega'^2-2\omega'^4}{\left[(1+G')^2+\omega'^2\right]^3}+\frac{8(1+G')\omega'^2}{\left[(1+G')^2+\omega'^2\right]^3}+\frac{2\omega'^2}{(1+G')^2+\omega'^2}\right.$$

$$\left.\left.+\frac{3(2+G')\omega'^2}{\left[(2+G')^2+\omega'^2\right]^2}+\frac{(17/9)\omega'^2}{(3+G')^2+\omega'^2}\right]+\cdots\right] \qquad \text{(II.48)}$$

$$\frac{\alpha''(\omega)}{\alpha(0)} =$$

$$(F(0))^{-1}\left[\frac{G'\omega'}{G'^2+\omega'^2}-\frac{2\gamma(1+G')\omega'}{(1+G')^2+\omega'^2}\right.$$

$$-\gamma^2\left[\frac{2\left[(1+G')^2-\omega'^2\right]\omega'}{\left[(1+G')^2+\omega'^2\right]^2}+\frac{2(1+G')\omega'}{(1+G')^2+\omega'^2}-\frac{(3+(3/2)G')\omega'}{(2+G')^2+\omega'^2}\right]$$

$$-\gamma^3\left[\frac{2\left[(1+G')^3\omega'-3(1+G')\omega'\right]^2}{\left[(1+G')^2+\omega'^2\right]^3}+\frac{4\left[(1+G')^2-\omega'^2\right]\omega'}{\left[(1+G')^2+\omega'^2\right]^2}\right.$$

$$+\frac{2(1+G')\omega'}{(1+G')^2+\omega'^2}+\frac{(3/2)\left[(2+G')^2-\omega'^2\right]\omega'}{\left[(2+G')^2+\omega'^2\right]^2}$$

$$\left.\left.+\frac{\omega'\left(\frac{17}{3}+\left(\frac{17}{9}\right)G'\right)}{(3+G')^2+\omega'^2}\right]+\cdots\right] \qquad \text{(II.49)}$$

where

$$\gamma=kT/I\beta^2 \qquad \omega'=\omega/\beta$$

$$G'=2\gamma+\gamma^2+(7/6)\gamma^3+(25/18)\gamma^4+\cdots \qquad \text{(II.50)}$$

$$(F(0))^{-1}=1+2\gamma+(9/2)\gamma^2+(125/9)\gamma^3+\cdots \qquad \text{(II.51)}$$

There are similar expressions for the needle (the dipole axis) reorienting in space. For $\omega\to\infty$ both expressions (for the sphere and needle) reduce to

$$\frac{\alpha^*(\omega)}{\alpha(0)}\to\frac{2\gamma}{\omega'^2}-\frac{2i\gamma}{\omega'^3} \qquad \text{(II.52)}$$

in agreement with the work of Sack on the same problem. McConnell and others have solved (II.45) for the asymmetric top, and Morita the corresponding Eulerian equations of motion. We shall show presently that their results are entirely consistent numerically. However, for all geometries the memoryless (II.44) cannot reproduce the zero-THz Poley absorption, but merely causes a slow high-frequency return to transparency of the plateau value [e.g., (II.47)]. Nevertheless, the powerful theoretical methods used in solving (II.44) should be extended to the general (I.6). For the asymmetric top, Morita shows that

$$\frac{\epsilon^*-\epsilon_0}{\epsilon_0-\epsilon_\infty}=1-s\sum_{i=x,y,z}\frac{m_i^2}{\mu^2}A^{(i)}(s)$$

where $s=i\omega$, and $\mu^2=M_x^2+M_y^2+M_z^2$, in which M_i is the permanent dipole moment along the principal axis denoted by i, and β_i the corresponding frictional component. $A^{(i)}(s)$ is defined as follows:

$$A^{(i)}(s)=\left[s+\frac{p_2^{(i)}\left(q_1^{(i)}+r_1^{(i)}\right)-p_1^{(i)}\left(q_2^{(i)}+r_2^{(i)}\right)}{q_1^{(i)}r_2^{(i)}-r_1^{(i)}q_2^{(i)}}\right]^{-1} \qquad \text{(II.53)}$$

where

$$p_1^{(i)}=-4kT/I_j(s+2\beta_j)(s+\beta_i+\beta_k)(s+\beta_i+\beta_j)$$

$$p_2^{(i)}=4kT/I_k(s+2\beta_k)(s+\beta_i+\beta_j)(s+\beta_i+\beta_k)$$

$$q_1^{(i)}=4(s+\beta_j)(s+2\beta_j)(s+\beta_i+\beta_j)(s+\beta_i+\beta_k)$$

$$+8kT/I_j(s+\beta_i+\beta_j)(s+\beta_i+\beta_k)+\frac{4kT}{I_i}(s+2\beta_j)(s+\beta_i+\beta_k)$$

$$+4kT/(I_iI_jI_k)\left[(I_i-I_k)^2(s+2\beta_j)(s+\beta_i+\beta_j)\right]$$

$$q_2^{(i)} = \frac{4kT}{I_i I_k}(s+2\beta_k)\left[(I_k - I_i)(s+\beta_i+\beta_j)+(I_j - I_i)(s+\beta_i+\beta_k)\right]$$

$$r_1^{(i)} = \frac{4kT}{I_1 I_2}(s+2\beta_j)\left[(I_j - I_i)(s+\beta_i+\beta_j)+(I_k - I_i)(s+\beta_i+\beta_k)\right]$$

$$r_2^{(i)} = 4(s+\beta_k)(s+2\beta_k)(s+\beta_i+\beta_j)(s+\beta_i+\beta_k)$$
$$+\frac{8kT}{I_k}(s+\beta_i+\beta_j)(s+\beta_i+\beta_k)+\frac{4kT}{I_i}(s+2\beta_k)(s+\beta_i+\beta_j)$$
$$+\frac{4kT}{I_i I_j I_k}(I_j - I_i)^2(s+2\beta_k)(s+\beta_i+\beta_k)$$

In the foregoing, $(i=x,j=y,k=z)$, $(i=y,j=z,k=x)$, and $(i=z,j=x,k=y)$ in cyclic permutation. We denote by I_x, I_y, and I_z the principal moments of inertia. This equation reduces to Perrin's equation when inertial effects are neglected. $\epsilon^*(\omega)$ is the complex permittivity. Internal field effects are neglected.

The solution of McConnell and others is, on the other hand,

$$\alpha^*(\omega) = \frac{1}{3kT}\sum_{x,y,z}\left[\frac{D_y(D_y+D_z+\beta_y)}{(D_y+D_z+i\omega)(D_y+D_z+\beta_y+i\omega)}\right.$$
$$\left.+\frac{D_z(D_y+D_z+\beta_z)}{(D_y+D_z+i\omega)(D_y+D_z+\beta_z+i\omega)}\right]\mu_x^2 \qquad \text{(II.54)}$$

Here $D_x = kT/I_x\beta_x$, and so on. The frictional couples with respect to the rotating principal axes of inertia are $I_x\beta_x\omega_x$, $I_y\beta_y\omega_y$, and $I_z\beta_z\omega_z$. Equations (II.53) and (II.54) produce virtually identical numerical results for all β_x, β_y, and β_z of interest.

For the symmetric top, where the components μ_x and μ_y are zero, the Fokker–Planck–Kramers equation for the probability density function $p(\omega_x,\omega_y,\omega_z,\theta,\phi,\psi;t)$ in angular velocity/Euler space yields the Laplace transform of the dipole autocorrelation function $C_u(t) = \langle \boldsymbol{\mu}_z(t)\cdot\boldsymbol{\mu}_z(0)\rangle$ according to Morita as

$$\tilde{C}_\mu(s) = \cfrac{\mu_z^2/3}{s+\cfrac{2kT/I_x}{s+\beta_x+\cfrac{2kT/I_x}{s+2\beta_x+\cfrac{4kT/I_x}{s+3\beta_x}}+\cfrac{(kT/I_x)(I_z/I_x)}{s+\beta_x+\beta_z+\cfrac{(2kT/I_x)(I_z/I_x)}{s+\beta_x+2\beta_z+\cfrac{2kT/I_x}{s+2\beta_z}}}}} \qquad \text{(II.55)}$$

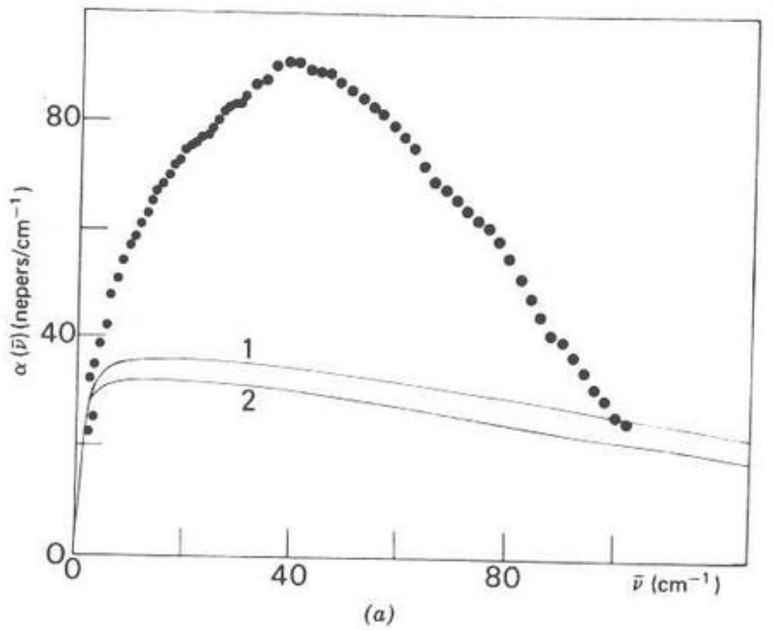

(a)

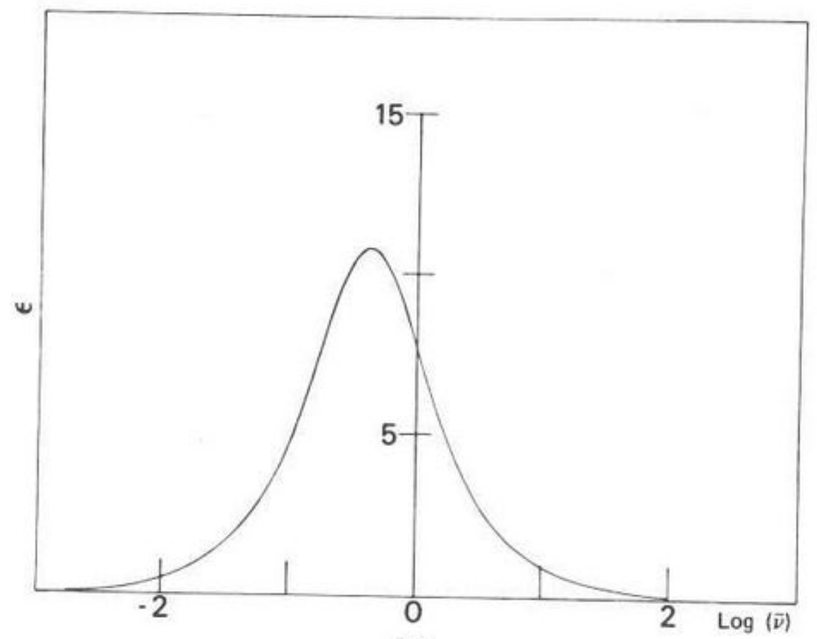

(b)

Fig. 31. (*a*) ●, Absorption of 2-chloro-2-nitropropane(*I*) at 293°K, taken with a P.O. polarizing interferometer. (—), (1) Spherical-top Langevin equation; (2) Asymmetric-top Langevin equation. (*b*) Calculated loss curve for 2-chloro-2-nitropropane, using (II.49) or (II.54). Ordinates: (*a*) α (nepers/cm), (*b*) $\epsilon''(\bar{\nu})$; abscissas: (*a*) $\bar{\nu}$ (cm^{-1}), (*b*) $\log_{10}(\bar{\nu})$ (cm^{-1}).

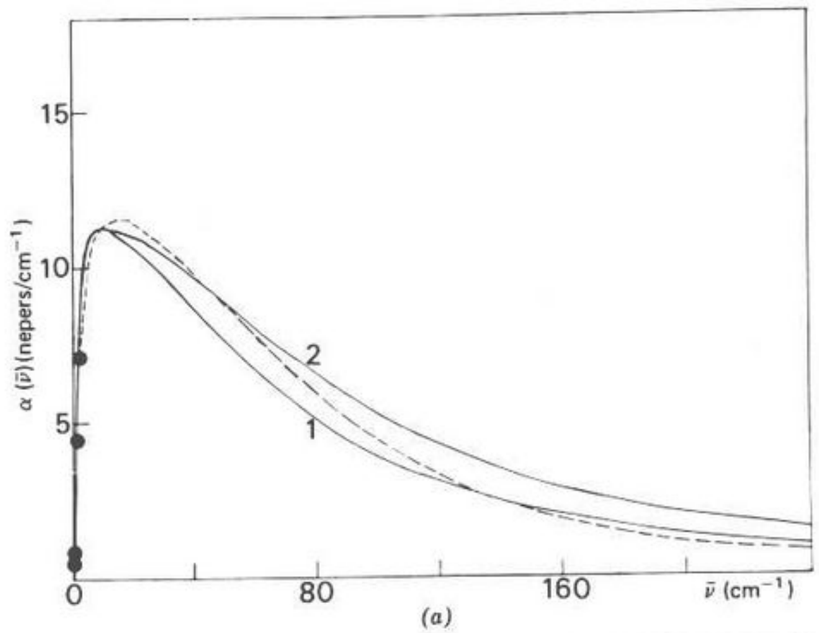

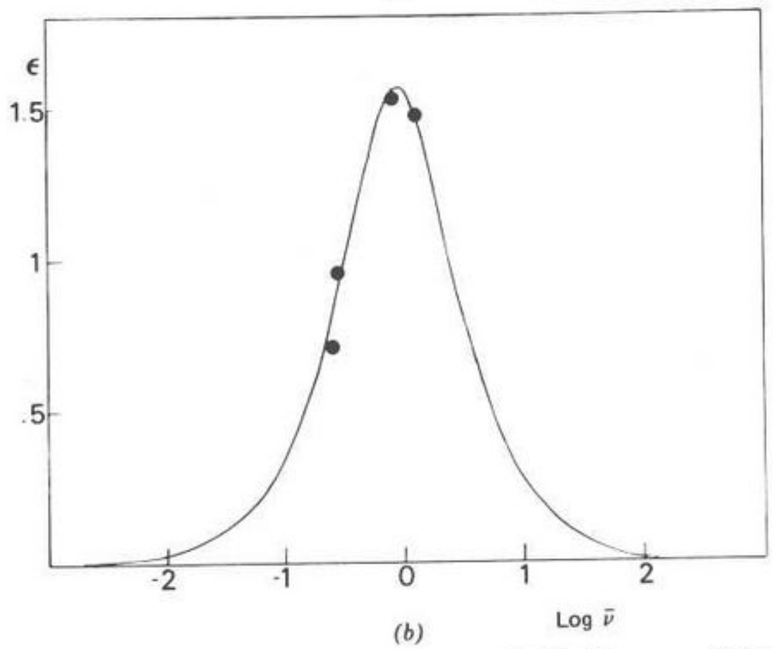

Fig. 32. Key as in Fig. 31. Liquid fluorobenzene. (----), (3) Mori theory applied to $C_*(t)$, best fit to the microwave data shown in Fig. 32b as ●.

If $\omega_i(t)$ $(i = x,y,z)$ is the angular velocity about the principal axis labelled i and I_i is the moment of inertia, then $I_i\beta_i\omega_i(t)$ is the damping torque.

Numerically (Figs. 30 to 35), (II.55) reduces, in the appropriate limits, to the sphere and needle expressions as given by McConnell [e.g., (II.48) and (II.49)]. In evaluating (II.48) to (II.55) against zero-THz data we proceed as follows with the friction parameters. The only parameter of (II.50) and

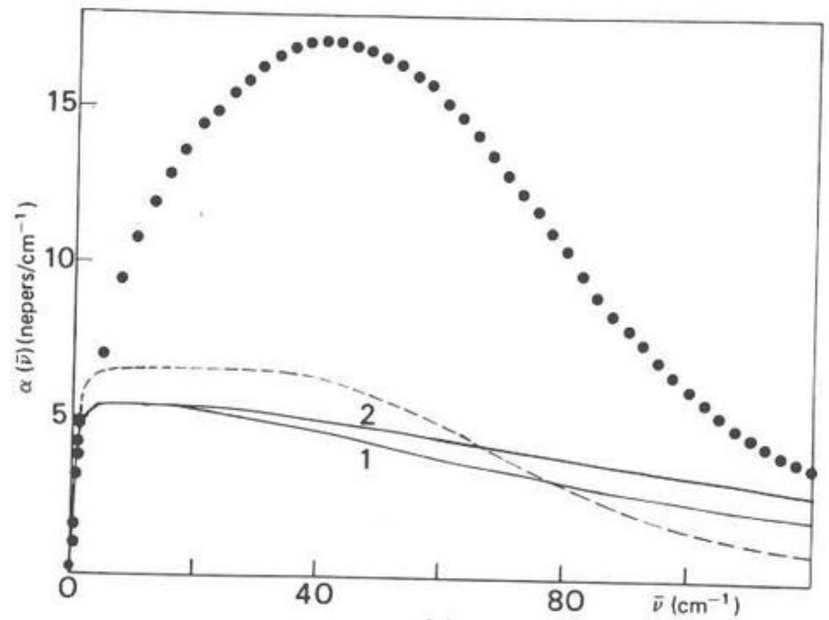

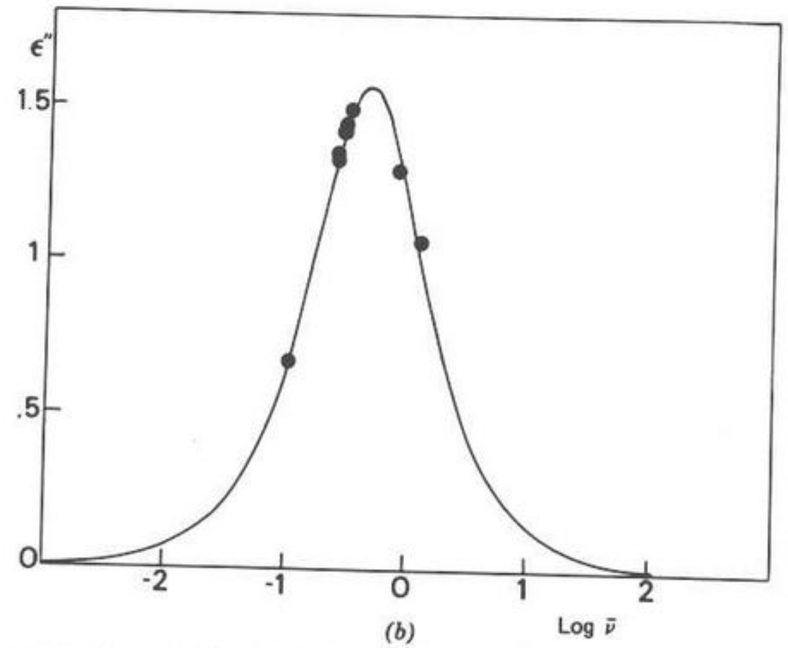

Fig. 33. Key as in Fig. 32. Chlorobenzene, iodobenzene, and nitrobenzene.

those for the needle, is β, which is directly observable from the loss peak $\epsilon''_{max}(\omega)$. When the components β_x, β_y, and β_z are all nonzero (as, e.g., in liquid 2-chloro-2-nitropropane (Fig. 31), they are estimated by shape-factor analysis. Therefore, there are no adjustable parameters for best fit. Figure 30 shows some comparisons with Gerschel's data for fluoroform at 293°K, in the liquid phases. (The internal field corrections are discussed also by

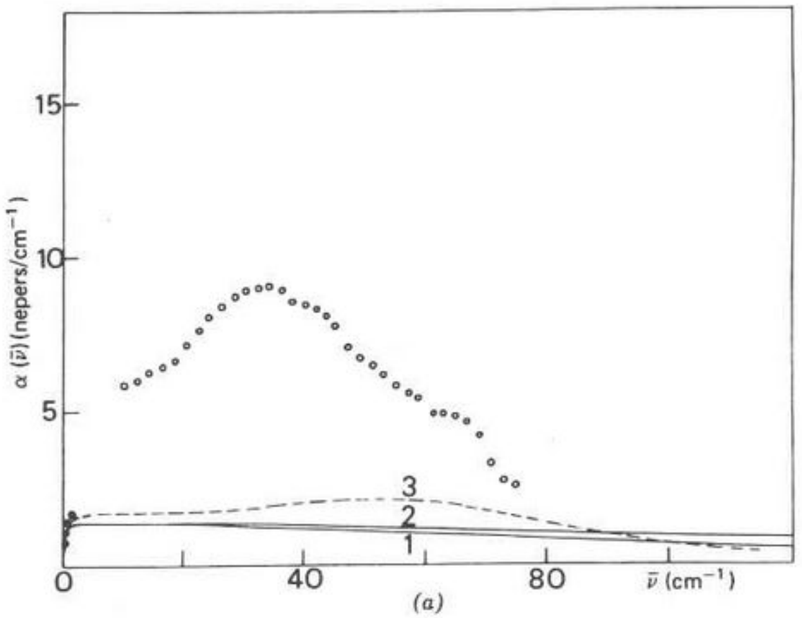

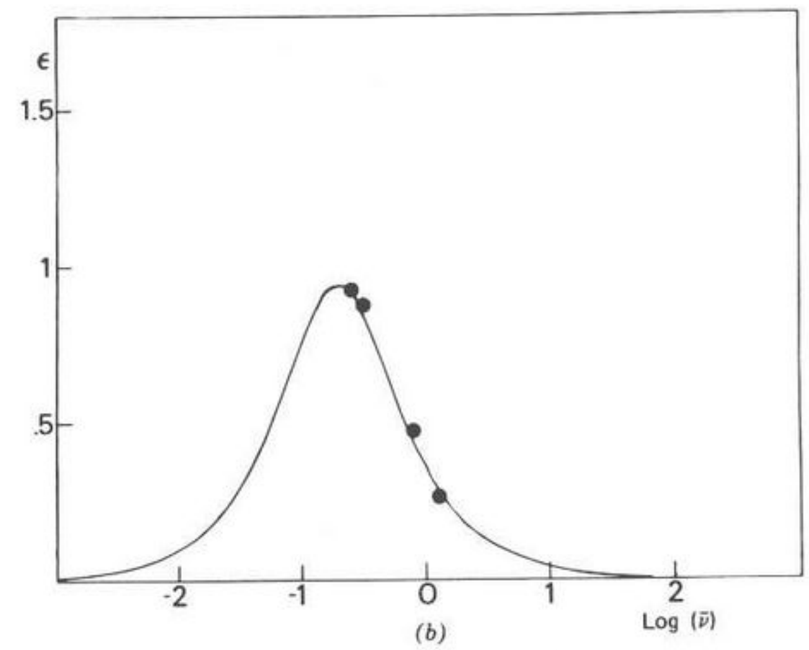

Fig. 34. Key as in Fig. 32. Iodobenzene.

Gerschel.) The needle, sphere, and symmetric-top representations yield absorption and dispersion profiles which are superimposable to a high degree of proximity, but for realistic values of the molecular parameters, β_z in (II.55) is virtually redundant (i.e., has little effect on the band contour once β_x is determined). The Poley absorption is obviously not described. Equation (II.35), on the other hand, produces a satisfactory match for both the

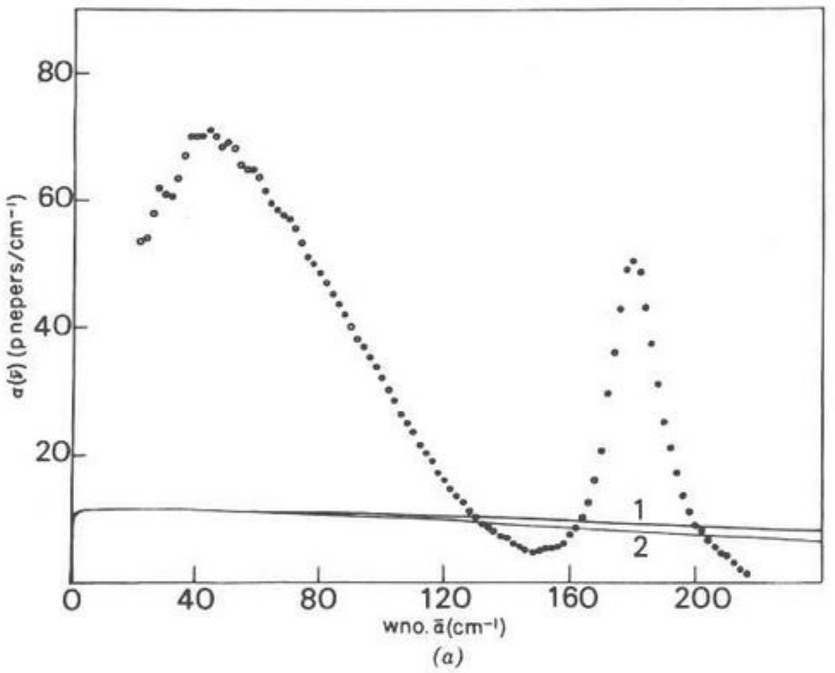

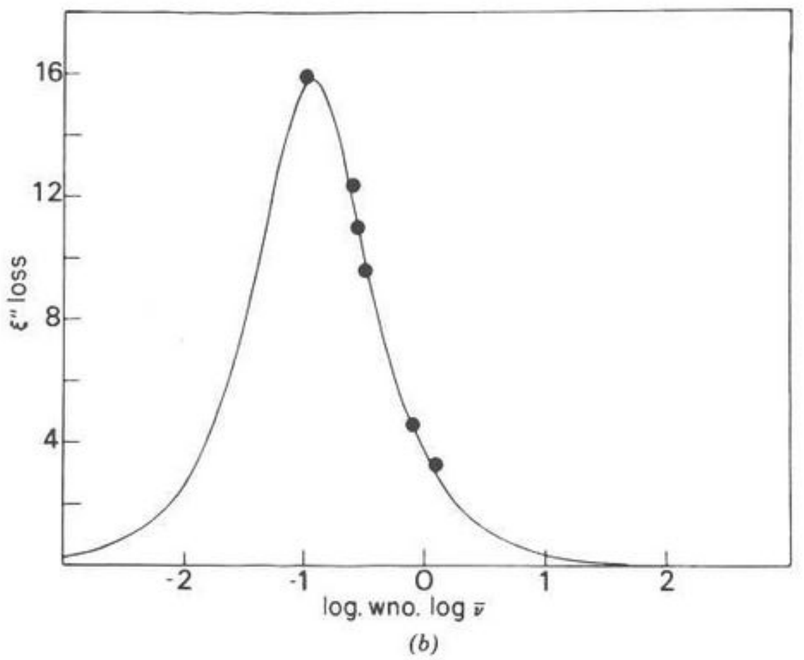

Fig. 35. Key as in Fig. 32. Nitrobenzene.

loss peaks in the zero-THz range (Fig. 44). These two loss peaks (Debye and Poley) having separated clearly in liquid MeF at 133°K offer a severe test for any approximants of (I.6), especially so when empiricism is eliminated [i.e., if γ and $K_1(0)$ are not adjusted for best fit as in Fig. 12]. An apparently good, but deceptive, agreement with the low-frequency loss (or exponential tail of $C_\mu(t)$) may be achieved easily with any one of (II.49) to (II.55), regardless of the molecule's true symmetric-top geometry. Before the development of Michelson interferometry and submillimeter spectroscopy it was common practice to use Debye's equations for any shape of molecule, regardless of the inertia tensor.

Figures 30 to 35 for the asymmetric-top halogenobenzenes demonstrate how insensitive the inertia-corrected equations are to the Poley absorption. Since the intermolecular potential is so ill defined in (II.44), the theoretical results for the sphere and asymmetric top are similar. Nevertheless, we reiterate that the theoretical methods involved are powerful enough to be extended to (I.6). Strictly speaking, of course, (II.44) was never intended by Langevin and Perrin for *molecular* dynamics, but for those of a massive

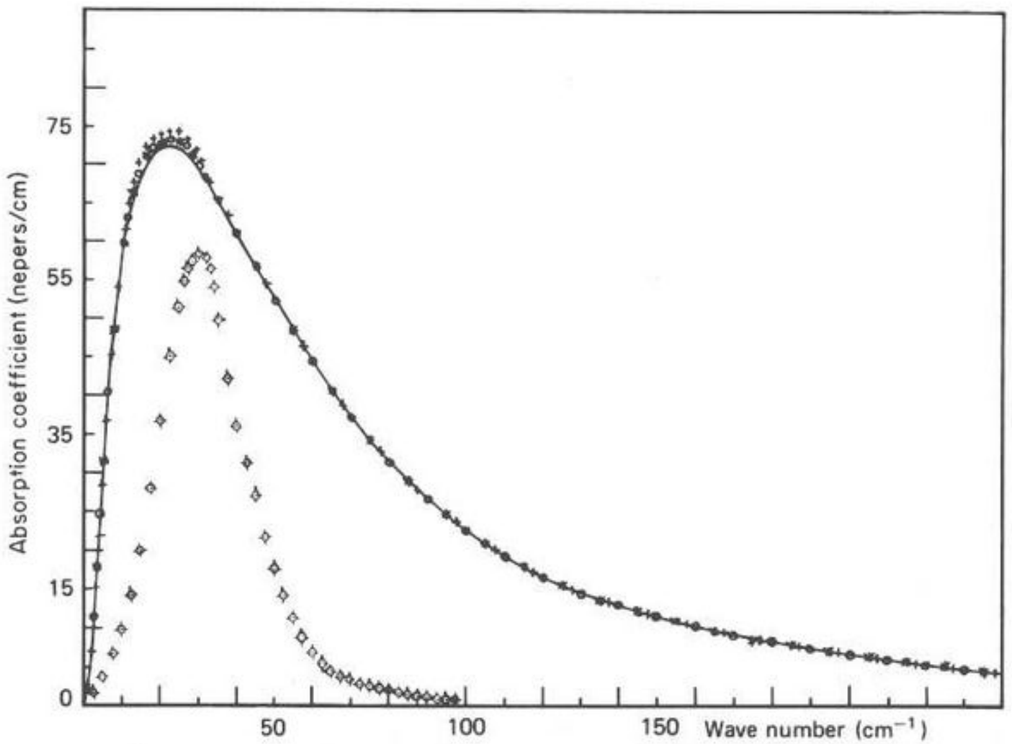

Fig. 36. ⊕ Far-infrared absorption of fluoroform (liquid) at 293°K. (—), Morita's (II.55) for the symmetric top, needle, or spherical top; (••••), McConnell's (II.48) for a needle; ○, McConnell's for a spherical top; +, Morita's model for an asymmetric top reduced to the symmetric top. [Reproduced by permission from *J. Chim. Phys.*, **75**, 526 (1978).]

particle immersed in a bath of lighter ones. Equations (II.49) to (II.55) should then be tested out against molecular dynamics simulation of this system. Finally, of course, a critique such as this detracts nothing from the immense labor involved in producing (II.49) to (II.55).

As an example of the usefulness[74] of the theoretical techniques developed by McConnell and others, we indicate briefly how they can be used to derive, using a simple kinematic principle, the correlation function $C_{\mathbf{u}}(t)$ from the approximant represented by (I.30). Consider, then, the motion of the dipole vector $\mathbf{u}(t)$ as it librates in a plane with angular velocity $\omega(t)$. Kinematics yield the relation

$$\boldsymbol{\omega}(t)=\omega(t)\mathbf{k} \tag{II.56}$$

where $\mathbf{k}$ is a unit vector and $\omega(t)=|\boldsymbol{\omega}(t)|$. Let I be the moment of inertia of the disk drawn out by the rotating dipole about the axis $\mathbf{k}$. Then

$$\mathbf{k}\cdot\mathbf{u}_0=0 \qquad \mathbf{k}\times(\mathbf{k}\times\mathbf{u}_0)=-\mathbf{u}_0$$

where $\mathbf{u}_0\equiv\mathbf{u}(0)$. Using an expansion as per McConnell and others:

$$\begin{aligned}\langle\mathbf{u}(t)\rangle=\mathbf{u}_0\Big[1&-\int\int_{0\le t_1\le t_2\le t}\langle\omega_2\omega_1\rangle\,dt_1\,dt_2\\&+\int\cdots\int_{0\le t_1\le\cdots\le t_4\le t}\langle\omega_4\omega_3\omega_2\omega_1\rangle dt_1\cdots dt_4\\&-\int\cdots\int_{0\le t_1\le\cdots\le t_6\le t}\langle\omega_6\omega_5\omega_4\omega_3\omega_2\omega_1\rangle dt_1\cdots dt_6+\cdots\Big]\end{aligned} \tag{II.57}$$

Since the ω's are Gaussian random variables, we have

$$\begin{aligned}\langle\omega_{i_1}\cdots\omega_{i_{2n+1}}\rangle&=0\\\langle\omega_{i_1}\cdots\omega_{i_{2n}}\rangle&=\sum\prod_{i_r>i_s}\langle\omega_{i_r}\omega_{i_s}\rangle\end{aligned} \tag{II.58}$$

Writing (I.6) for ω,

$$I\dot{\omega}+I\int_0^t K_0^{(\omega)}(t-\tau)\omega(\tau)\,dt=I\Theta \tag{II.59}$$

Replacing $K_0^{(\omega)}$ by the truncated continued fraction leading to (I.30) or

(II.35) implies that

$$\dot{\Theta}(t)+\int_0^t K_1^{(\omega)}(t-\tau)\Theta(\tau)\,d\tau=\Theta_1$$
$$\dot{\Theta}_1(t)+\gamma^{(\omega)}\Theta_1(t)=\dot{\Theta}_2(t) \qquad \text{(II.60)}$$

Solving (II.59) and (II.60) leads to the relation

$$\langle\omega_k\omega_l\rangle=c^2\big[A_0\exp(-\alpha_1|t_k-t_l|)+B_0\exp(-\alpha_2|t_k-t_l|)$$
$$+C_0\exp(-\alpha_3|t_k-t_k|)\big] \qquad \text{(II.61)}$$

where the discriminant (Δ_0) in the denominator cubic of (II.35) is positive. (The case $\Delta_0<0$ complicates matters by making the exponentials in (II.61) complex.) In (II.61) $\alpha_1,\ldots,\alpha_3$, C and A_0, B_0, C_0 are constants related to $\gamma^{(\omega)}$, $K_0^{(\omega)}(0)$, and $K_1^{(\omega)}(0)$. The second integral in (II.57) can be written as

$$\frac{3}{4!}\left[2\int_0^t dt_2\int_0^{t_2}\langle\omega(t_2)\omega(t_1)\rangle\,dt_1\right]^2$$

and all successive integrals, as shown by McConnell et al., follow this pattern. Accordingly,

$$\langle\mathbf{u}(t)\cdot\mathbf{u}(0)\rangle=\exp\left[-\int_0^t(t-\tau)\langle\omega(\tau)\omega(0)\rangle\,d\tau\right] \qquad \text{(II.62)}$$

A more general version of (II.61) is derivable via the probability density functions of Section I.A. This equation is useful in being the closed form for the orientational autocorrelation function of the planar itinerant librator. Using (II.61) in (II.62) and expanding in a Taylor series, there are no linear or t coefficients in $C_u(t)$ and

$$C_u(t)=\exp(-kTt^2/2I+O(t^3))$$
$$\rightarrow\exp(-kTt^2/2I) \qquad \text{(II.63)}$$

the free-rotor limit, at very short times, when $O(t^3)$ is negligibly small. At the extreme $t\rightarrow\infty$, we have

$$C_u(t)\rightarrow\exp(-t/\tau) \qquad \text{(II.64)}$$

where τ is a constant with the dimensions of time. Note, that in 3 – D (Fig. 37), the free-rotor and long time behaviours are in general more complicated. Writing (II.62) then as

$$C_u(t)=\exp(-f(t))$$

it may be shown that in three dimensions, an approximate equivalent form is

$$C_u(t)=\exp(-2f(t))$$

so that the space itinerant librator would produce a $C_u(t)$ decaying faster than that of the planar itinerant librator. To link (II.59) and (II.60) to (I.31), we have

$$\beta_2=0 \qquad K_0^{(\omega)}(0)=\gamma^2 \qquad [\text{i.e., the } \gamma \text{ of (I.31)}]$$
$$K_1^{(\omega)}(0)=(I_2/I_1)K_0^{(\omega)}(0)$$
$$\gamma^{(\omega)}=kT\tau_D/I_1 \qquad \text{(II.65)}$$

with τ_D as the inverse in the peak loss frequency produced theoretically.

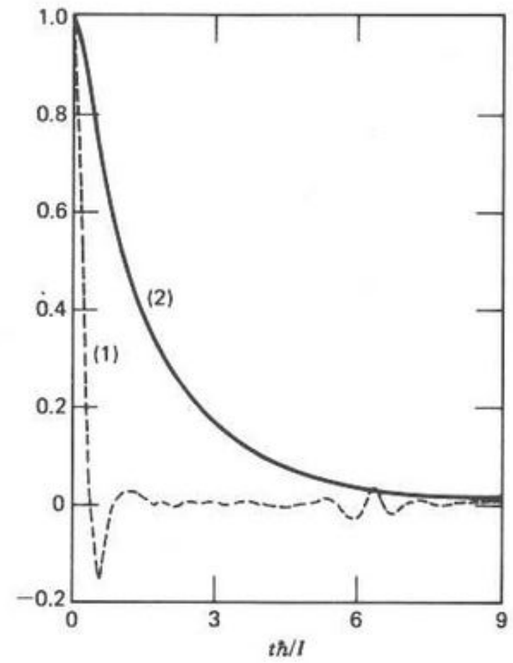

Fig. 37. (----), (1) $C_u(t)$ from the Frenkel–Wegdam curve of Fig. 4. (—), (2) Normalized angular momentum autocorrelation function. The abscissa is in time units of $t\hbar/I$. [Reproduced by permission from *Chem. Phys. Lett.*, **42**, 331 (1976).]

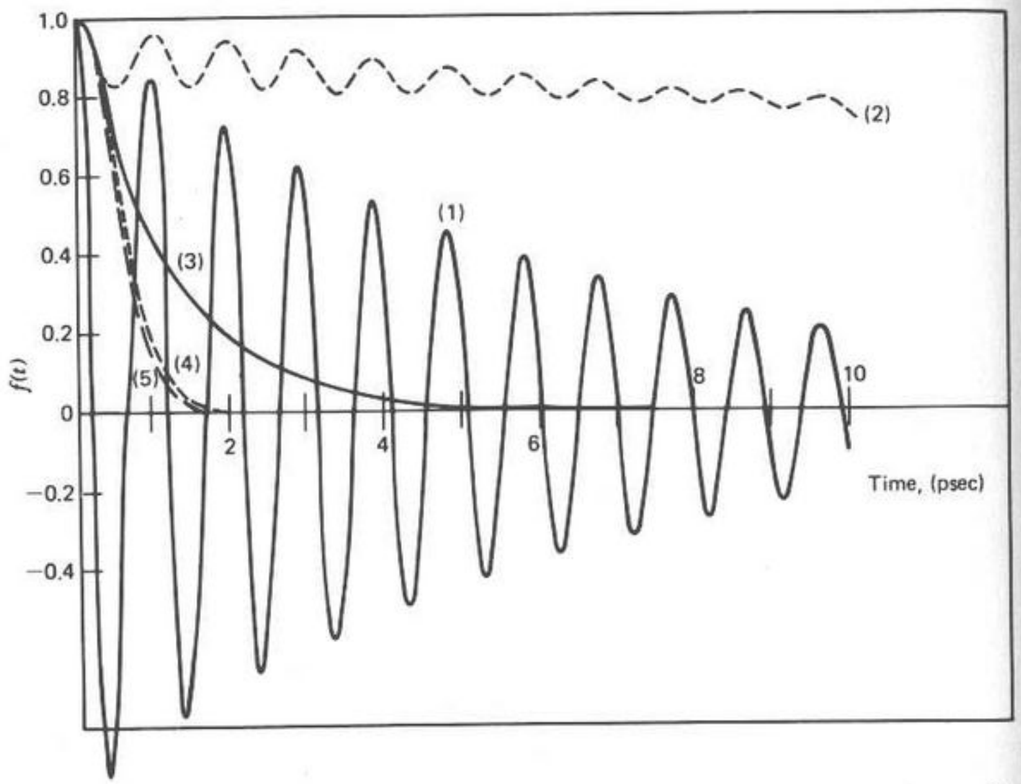

Fig. 38. Angular velocity and orientational autocorrelation functions for motion in two dimensions of the itinerant oscillator. (—) (1) Underdamped $C_{\omega\omega}(t)$; (3) overdamped $C_{\omega\omega}(t)$. (····) (2) Underdamped $C_{uu}(t)$ corresponding to (1); (4) overdamped $C_{uu}(t)$ corresponding to (3); (5) $\exp(-kTt^2/2I)$, the $C_{uu}(t)$ for free rotation of a Maxwellian ensemble of dipoles in two dimensions. For (1) to (5), $T=296°K$, and $I=10^{-38}$ gm·cm^2. [Reproduced by permission from *Mol. Phys.*, **34**, 973 (1977).]

Figure 38 illustrates some curves for the planar itinerant oscillator which should be compared with those simulated (Figs. 70a to e) in Section III.E by computer molecular dynamics with rough annuli within which are constrained disks.

1. *Evaluation of Models in Liquid CH_2Cl_2: Comparison with Other Techniques*

The reasons for and criteria employed in evaluating the foregoing models for $CH_2Cl_2(l)$ are as follows:

1. We have already made the point that the induced absorptions here are likely to be negligible. These are treated further in Section II.E.
2. The complete zero-THz band shape is available for liquid CH_2Cl_2 and in solutions thereof. The data are accurate to within a few percent.

3. At a long enough time after the initial $t=0$, the molecular interactions and motions in the densely packed N-molecule ensemble evolve such that the decay in the correlation functions $\langle A_j(t)A_j(0)\rangle$ of Section I.A is exponential [(II.64) is an example]. This is to say that after suffering many interruptions in its initial trajectory, the probability of finding a molecule with, for example, an orientation $\mathbf{u}(t)$, given an initial $\mathbf{u}(0)$, decays eventually as a Gaussian in time. [This is not so in the autocorrelation function of Fig. 37, since Frenkel and Wegdam consider there an ensemble of interacting *quantized* rotors, where $C_{\mathbf{u}}(t)$ is periodic.] Therefore, we assume in what follows that the *low-frequency* loss curve should be modeled accurately and $\alpha(\omega)$ of the THz region extrapolated therefrom. Using this method it will be shown that deviations from the experimental observations are large in the far infrared, and improvements in the modeling are generally needed.
4. The motion of CH_2Cl_2 molecules in the pure liquid have been monitored by sweep frequency, microwave klystron, and interferometric techniques (both Michelson and Martin–Pupplett). This molecule is chosen for reasons of its intense absorption, especially in the THz range. A recent review[75] has emphasized the considerable extent to which parallel studies have been carried out by incoherent, inelastic neutron scattering, and other techniques. Rotational diffusion and extended rotational diffusion $(m;J)$ have been used for the interpretation of these results.
5. CH_2Cl_2 has been used as a probe into the mesophase and glassy environments. The results of these investigations are dealt with in sections (II.D) and (II.E).
6. CH_2Cl_2 is an asymmetric top and thus endowed with interesting rotational dynamic properties. The glassy results of Section II.F show quite clearly that the shape factor (van der Waals contour) is far from that of a spherical or "pseudospherical" molecule. ($I_x=26.3\times10^{-40}$ g·cm^2; $I_y=278\times10^{-40}$ g·cm^2; $I_z=253\times10^{-40}$ g·cm^2.)
7. The evaluation of (I.31) presents no conceptual difficulty if we remember that they apply, in the dynamic interpretation, to the libration *in a plane* of the dipole vector **u** embedded in the *asymmetric top*. The terms "disk" and "annulus" are conveniences of the mathematical development.

Results and Improvements. These are summarized in Fig. 13*a*.

1. Equation (II.44) is interesting for CH_2Cl_2 since two broad peaks are produced in $\alpha(\bar{\nu})$ (Fig. 12). However, the Poley resonance is, of course, missing. In physical terms the mean intermolecular potential energy is inaccurately defined (e.g., its derivative with respect to orientation, the root-mean-square torque, is meaningless in this context). Therefore, the concept

of libration within potential wells is also meaningless. There is room for further progress by using successive approximants if the geometrical problems and their effect on the Gaussian nature of (I.6) can be overcome.

2. Equation (II.41) was fitted to the experimental data by least-mean-squares optimization of τ. The fit is poor since the model $\bar{\nu}_{max}$ remains at the value

$$\bar{\nu}_{max}=\langle\omega^2\rangle^{1/2}=\left[kT\left(\frac{1}{I_x}+\frac{1}{I_y}\right)\right]^{1/2}=21.5\ \text{cm}^{-1}$$

the root-mean-square angular velocity. Varying τ broadens the theoretical band asymmetrically. Progress in this type of model may be pursued analytically by using the idea of inelastic collisions, as has been demonstrated by computer simulations in rough spheres[61] and disks, and hydrodynamically using slip–stick interactions.[26] Satisfactory definition of a time of collision, and thus of a mean-square torque would enable the desired shift in $\langle\omega^2\rangle^{1/2}$ to take place. Obviously, zero-THz band shapes are sensitive measures of analytical realism in this respect, and will also be useful in evaluating density expressions such as those of Chandler[33] on the memory operator. These allow for the effect of multiple collisions.

3. Using (II.34) to (II.37) without recourse to fitting of any kind leads to rather too broad a band in comparison with the data (Fig. 12). Iterating on γ and $K_2(0)$ separately improves the fit, but in doing so obscures the fact that further approximants are needed before the mean intermolecular potential energy is satisfactorily described. The validity of some truncations at the level of (II.34) to (II.37) has also been investigated for the monohalogenobenzenes[59] using different versions of the memory function $K_1(t)$. A fairly realistic result is obtained only from an exponential $K_1(t)$ which gives an integrated absorption intensity A of about half that observed in the far infrared when the loss curve is matched correctly at lower frequencies. In Fig. 12 some results for a Gaussian and Lorentzian $K_1(t)$ are given which reveal the sensitivity of the Mori series to the form of truncation used. Naturally, all these forms reduce to the same type of loss curve at low frequency, and are indistinguishable without far-infrared data. The halogenobenzenes are less favorable cases than CH_2Cl_2 with which to fit data over the whole of the zero-THz range since the collision-induced component is relatively much stronger. Fitting the (II.34) to (II.37) to microwave data alone is not a satisfactory procedure because one is effectively fitting a simple exponential form with more than one phenomenological variable.

4. Using the notation of (I.31) (the itinerant librator) and the approximate geometrical relation $I_1=10I_2$ for various values of β_2, it is obvious in Fig. 12 that the resonance around $\bar{\nu}_{max}$ is too narrow theoretically. The original concept with $\beta_2=0$ would therefore produce an even sharper peak. However, iteration on I_1 and β_2 rectifies matters at the expense of physical realism in the disk–annulus sense, since for best fit $I_1<I_2$ (mathematically corresponding to the overdamped case). A parallel result was found by Damle and others[29] for the translational space itinerant oscillator where β_2 and β_1 are made time-dependent memory functions. This result is reasonable, however, in the context $\beta_2=0$ since it implies merely that $K_1^{(\omega)}(0)>K_0^{(\omega)}(0)$ (i.e., that the rate of change of torque is large). Equation (I.31) is in one sense a zeroth-order approximant of the system devised by Damle and others,[29] and perhaps successive approximants would improve matters if the problem of too many adjustable variables could be overcome. Another possibility for improvement is the inclusion of rotation translation coupling as discussed in Section I.C. Some of the adjustable variables could be evaluated separately by molecular dynamics simulations. Using $I_1=I_2$; $\beta_1=\beta_2=kT\tau_D/I_2$ in the dipole interaction representation of (I.31) produces a poor fit (Fig. 12). This suggests that a more realistic potential V is of dipole–dipole interaction is necessary. However, $K_0^{(\omega)}(0)$ and $K_1^{(\omega)}(0)$ are not wholly electrostatic in origin and an interpretation of the far-infrared absorption *solely* in these terms is obviously to be avoided.

Recently, Brier and Perry[75] have obtained time-of-flight neutron scattering data on liquid CH_2Cl_2 and have tested their results with four models of the liquid state. They have also reviewed critically the available NMR, infrared / Raman, and depolarized Rayleigh scattering work. The attempts at evaluating the anisotropy of the molecular angular motion using these techniques sometimes end in confusion and contradiction. The m- and J-diffusion models were used regarding CH_2Cl_2 as an inertial symmetric top (i.e., assuming axial symmetry of angular motion about that axis of least inertial moment). [This assumption is however contradicted by NMR results, giving $\tau_2(\text{H—H})\neq\tau_2(\text{C—H})$.] An Egelstaff-Schofield form was used for the translational correlation function in the usual decoupling approximation [e.g., (I.39)]. The conclusions drawn as to the efficacy of the model *within this approximation* are very similar to those of the zero-THz data. Changing the values of the time between collisions alters the magnitude of the inelastic peak, its position remaining virtually constant. The maximum of the predicted inelastic intensity distribution occurs at much too low an energy transfer (frequency) for both models; therefore, within the context of extended diffusion, treating CH_2Cl_2 as a spherical top (Fig. 12) or as a symmetric top (neutron scattering) makes little difference to the

final result, which is poor. It is important to realize that this does not imply that the data are insensitive to asymmetry of orientational or rototranslational motions, but rather that unrealistic and oversimplified assumptions lead to oversimplified and unrealistic results. In common with nearly all neutron-scattering studies of molecular motion, Brier and Perry work with the assumption of complete decoupling of rotation from translation. Berne and Montgomery[32] have demonstrated the severity of this restriction by showing that the analytical rototranslational neutron scattering spectrum of a rough-sphere fluid is very different from that of a smooth-sphere fluid. Molecular structure will increase the coupling. A self-consistent approach is clearly needed to this problem, which would be indicated within the framework of the (I.6). This would aim at an appreciation of the spectrum as in Section I.C.

Studies of the depolarized Rayleigh wing complement the zero-THz band. Brier and Perry have also discussed the depolarized Rayleigh, Raman, infrared and NMR data available for liquid CH_2Cl_2. Ideally, NMR and infrared/Raman band shapes provide data on single-molecule motion. The correlation times available from these techniques are confusingly disparate. An explanation is attempted based on the asymmetric-top Langevin equation, which in the light of Fig. 12, is meaningless. It is significant that only the zero-THz $[\alpha(\bar{\nu})]$ dielectric absorption shows up clearly enough the discrepancy between rotational diffusion and observation. Another feature is that interpretation in terms of jump models gives directly contradictory results. This is hardly surprising, since without far-infrared data the 180° jump and infinitesimally small jump model both fit the available loss data exactly. A similar kind of indistinguishability is present when jump models are used in the theory of incoherent neutron scattering, as demonstrated in a review by Janik (Ref. 43, p. 45).

It is clear that the available data from all sources on liquid CH_2Cl_2 have been interpreted using many different models, with each of which are associated (usually) adjustable parameters, so that an overall viewpoint is not attainable. We propose a scheme to remedy this to a modest degree.

A computer simulation, using an empirical intermolecular potential (e.g., atom–atom[61] Lennard-Jones interactions) should be carried out on CH_2Cl_2, and desired quantities such as the mean-square torque, various autocorrelation functions, and collective correlation functions extracted. These should then be compared with the values obtained from self-consistent Mori approximants used with the zero-THz and depolarized Rayleigh data, these being free from the uncertainties of vibrational relaxation, hot bands, and so on. The effect of cross-correlations may be easily estimated from the zero-THz data by dilution, and compared with those simulated. Isotropy or otherwise of angular orientations may be simulated

in detail and compared with the considerable amount of NMR data available. Rototranslational effects may be simulated and compared with the available neutron scattering data. In this way it may be possible to refine the empirical intermolecular potential by evaluation against the spectroscopic data, especially if these were available over a broad-enough range of number density and temperature. Alternatively, if the empirical potential were considered adequate, the efficacy of the continued-fraction approximation could be measured when truncated at various levels.

D. Internal Rotations: Relation with ^{13}C NMR Relaxation of the Zero-THz Absorption

We digress a little in this section to discuss the concept of *internal* libration within the framework of a nonrigid species such as *p*-dimethoxybenzene or dimethyl carbonate. This is conveniently studied[76] by means of both zero-THz data and ^{13}C NMR (T_1 and N.O.E.) relaxation. One reason is to emphasize the point that different relaxation techniques used in a cohesive study of a selected problem may be more incisive than studies undertaken separately. A second is that rotational correlation functions may apply to systems of molecules with internal freedoms, and the far infrared is a particularly suitable frequency range with which to determine the kinetics of motions such as those of the methoxy-and methyl-group internal rotations. A quantitative analysis in terms of a "chemical relaxation process" permits an estimation of both the kinetic constant $k_{cis \rightarrow trans}$ of the dielectrically "active" *cis/trans* isomerism of the *para*-dimethoxybenzene molecule, and of the jumping rate of the methyl group from any of its three equivalent positions. The methoxy torsional modes appear in the far infrared and it is also possible to assign to this frequency range the methyl torsions.

A number of low-frequency (microwave) studies has been made in the pure liquid phase or in dilute solution on compounds having one or more methoxy groups. In these previous investigations, the only practicable way of estimating qualitatively the contribution of the group rotation to the overall dielectric relaxation was by comparison within a homologous series of compounds having roughly the same molecular shape. Such analyses have been hazardous because of changes in dipole moment (magnitude or orientation in the molecular frame), internal field, microscopic viscosity, and very often in the barrier height to internal rotation itself (e.g., in the case of electron donating or withdrawing aromatic substituents). More complete and quantitative information may be extracted on the different internal motions by simultaneous measurement of the longitudinal relaxation time (T_1) and of the nuclear Overhauser enhancement factor (η), with the zero-THz electromagnetic absorption. In this section we describe such

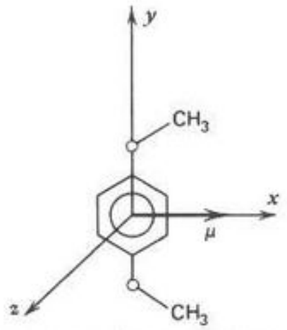

Fig. 39. *p*-Dimethoxybenzene molecule in the *cis*-position; μ represents the direction of the resultant dipole. [Reproduced by permission from *Mol. Phys.*, **30**, 974 (1975).]

a joint study of a solution of *p*-dimethoxybenzene in tetrachloroethylene (4.17_6 mol/*p*-DMB dm^3), chosen for experimental convenience. There is in the solute only one internal rotation axis, and along this, owing to the molecular symmetry, there is no component of the electric dipole (Fig. 39).

Plots of ϵ'' vs. ϵ' at 298°K, 323°K, and 348°K are shown in Fig. 40 and far-infrared absorption spectra obtained at 298°K for both the normal and the deuterated compounds in Figs. 41 and 42. The overlap between the microwave interferometric measurements (University of Nancy I) and the results obtained by Michelson free-space interferometry in the region 3 to 28

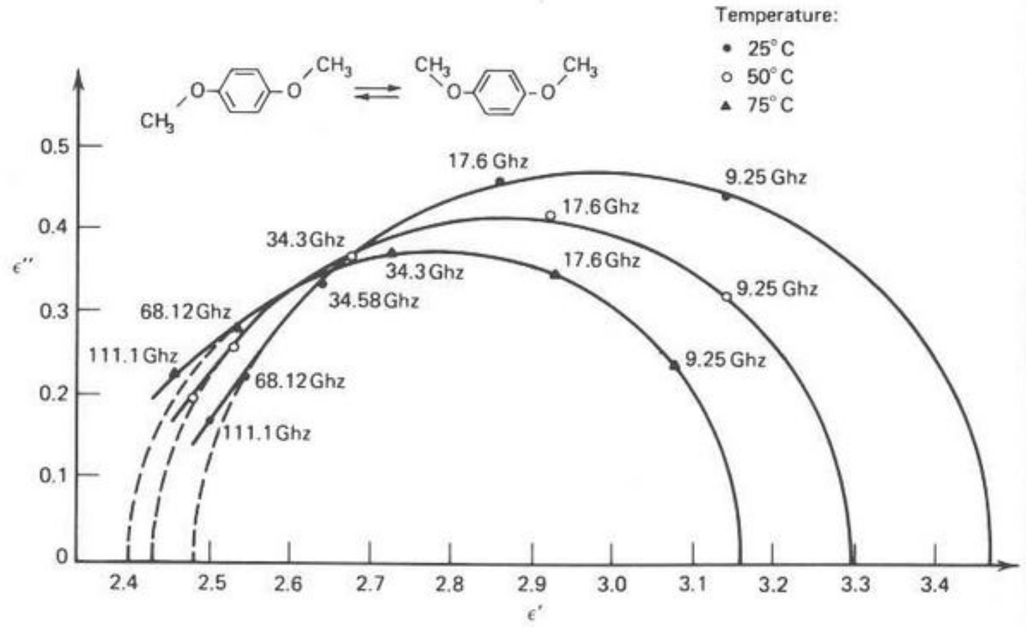

Fig. 40. Cole–Cole plots for a solution of a 4.176 mol/dm^3 *p*-dimethoxybenzene in C_2Cl_4 at 298°K, 323°K, and 348°K. The frequencies of the (ϵ'',ϵ') measurements are indicated on each plot. The dotted lines correspond to a semicircular extrapolation. [Reproduced by permission from *Mol. Phys.*, **30**, 976 (1975).]

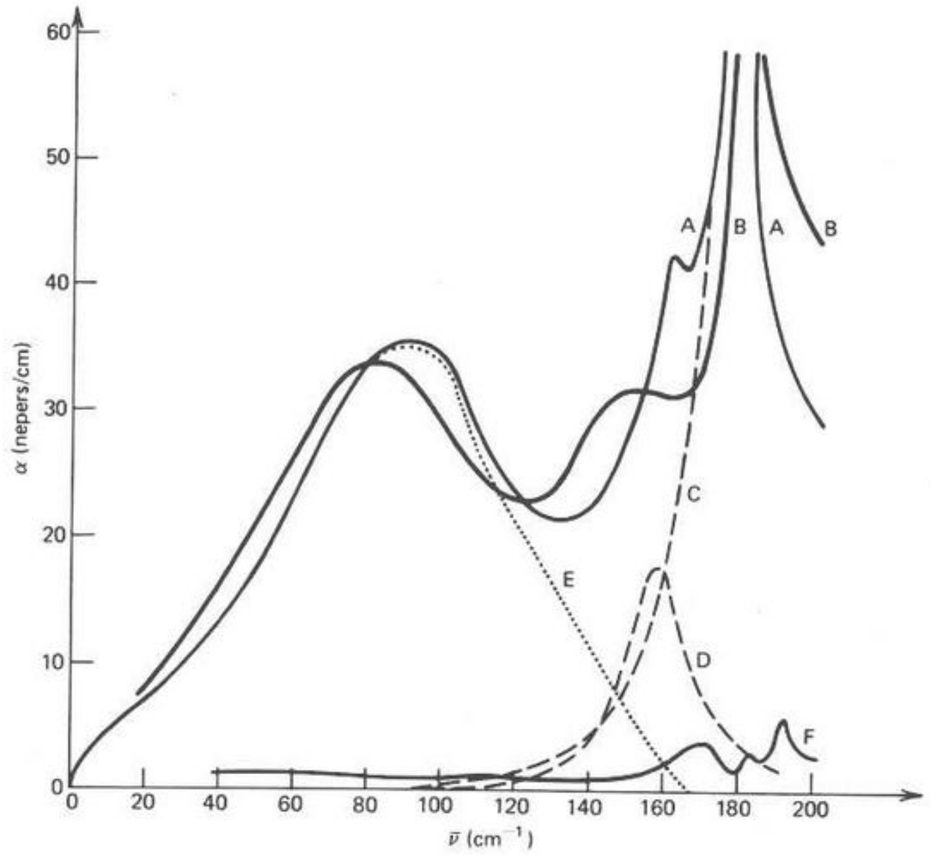

Fig. 41. (–), (*A*) Far-infrared absorption of *p*-dimethoxybenzene/C_2Cl_4 (4.176 mol/dm^3) at room temperature. (—), (*B*) Deuterated compound absorption at the same concentration. (----), (*C*), (*D*) Idealized line shapes for some of the higher-frequency absorptions. (·····), (*E*) Unresolved low-frequency band extracted from (*A*). (—), (*F*) Solvent absorption. [Reproduced by permission from *Mol. Phys.*, **30**, 977 (1975).]

cm^{-1} is satisfactory, Fig. 42. The complete zero-THz band is thus accurately defined. NMR relaxation measurements were separately made on the signal relative to the four equivalent ortho aromatic carbons, and on the line due to the methyl carbons. The solvent peak and those of the C_6D_6 reference are well separated from those of the solute.

The microwave results support the existence of only one "resultant" relaxation time accounting for the *low-frequency* part of the dielectric process. At times shorter than ca. 2 psec, however, the computed "pseudo" rotational velocity correlation function is oscillatory. These reflect both the librational motions as a whole of the *cis* conformers and the internal torsional motion of the methoxy groups, but occur at too short a time (<2 psec) to affect the exponential behavior of the vectorial dipolar correlation function (DVCF) at the time scale of the microwave measurements. The resultant value of $\mu_z = 4.5 \pm 0.4$ D calculated from the far-infrared band is

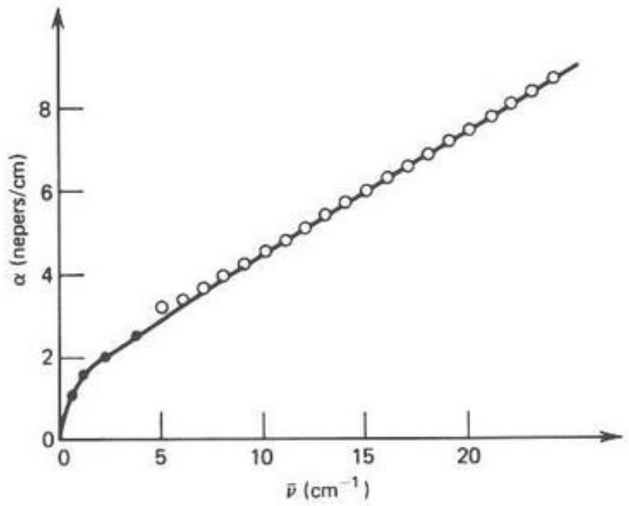

Fig. 42. Detail of the low-frequency absorption spectrum of *p-dimethoxybenzene*/C_2Cl_4 at room temperature. ●, Microwave interferometry with klystron sources; ○, Michelson interferometry with a He(*l*)-cooled Rollin detector. [Reproduced by permission from *Mol. Phys.*, **30**, 978 (1975).]

much larger than the apparent dipole moment obtained by dielectric measurements, 1.5(4) D at 298°K, and indicates that the main contribution to this band has another origin. The shift of the band center on deuteration of the methoxy groups supports quantitatively the hypothesis of torsional modes of the methoxy groups.

If, for the sake of argument, we accept the oversimplified hypothesis of isotropic molecular rotational diffusion as being adequate to reproduce the low-frequency loss data, and the aromatic ortho carbon NMR data, then the isotropic diffusion constant D_0 is related to an NMR relaxation time τ_c^{NMR} by

$$6D_0=(\tau_c^{NMR})^{-1} \tag{II.66}$$

For the symmetric-top diffusion on the other hand, τ_c^{NMR} has to be replaced by $F(D_x, D_y, D_z)$ defined for a planar molecule by

$$F(D_x,D_y,D_z)=\frac{3}{4D_r}\left[(D_x+D_s)\cos^2\phi+(D_y+D_s)\sin^2\phi - \frac{(D_y-D_x)}{D_z+D_s}\sin^2\phi\cos^2\phi\right] \tag{II.67}$$

where ϕ (in our case, 30°) defines the orientation of the internuclear vector

r_{CH} in the molecular frame, D_r and D_s being given by

$$D_r=3(D_xD_y+D_yD_z+D_zD_x)$$
$$D_s=\tfrac{1}{3}(D_x+D_y+D_z)$$

The consequences of neglecting this anisotropic character lead to a difference, however, of less than −10 to −15% in the ratio $p=3$ expected in the rotational diffusion limit between τ_c^{NMR} and the dielectric relaxation time τ_μ^{Diel} estimated after correction for the internal field.

Similarly, the methyl carbon relaxation time $\tau_{CH_3}^{NMR}$ is estimable after consideration of the problem of methyl group rotation about a fixed but arbitrary axis in the molecular frame. $\tau_{CH_3}^{NMR}$ can be related to the jumping rate $2R/3$ of the methyl group from any of its three equivalent positions by

$$\tau_{CH_3}^{NMR}=\frac{1}{2D_0}\left[1/(3+R/2D_0)\right] \tag{II.68}$$

where again the isotropic diffusion coefficient has been used for lack of knowledge of the anisotropic diffusion coefficients $D_\perp$ and $D_\parallel$.

This restriction to rotational diffusion is unsatisfactory in the light of the foregoing behavior of the model in the far infrared, but the complexity of the formulas is already beyond the data available. The use of NMR relaxation in isolation is therefore prone to vagueness of analysis, just in the way that a semicircular low-frequency Cole–Cole plot is about the least discriminating imaginable. It is not surprising therefore that the measured ratio

$$\rho_{app}=\tau_\mu^{Diel}/\tau_c^{NMR}$$

is considerably less than 3 (Table VI). This may be caused by:

1. Substantial contribution from internal methoxy group rotation to the dielectric relaxation phenomenon.
2. Breakdown of the Debye–Perrin rotational diffusion model (i.e., reorientation of the whole molecule with memory effects).
3. Strongly anisotropic rotational diffusion of the whole molecule.

The first explanation may be supported quantitatively using the model of dielectrically active "chemical relaxation processes," as previously proposed by Williams and Cook[77] and Goulon, Canet, Evans, and Davies.[76]

TABLE VI
Dielectric and NMR Relaxation Times for *p*-Dimethoxybenzene

T	298°K		323°K		348°K	
^{13}C NMR relaxation	C_{ortho}	C_{CH_3}	C_{ortho}	C_{CH_3}	C_{ortho}	C_{CH_3}
η	1.6(5)	1.7(5)	1.7(6)	1.8(0)	1.7(7)	1.8(7)
T_1/s	5.5(4)	5.1(2)	7.8	6.9(5)	10.1	9.6(5)
τ_C^{NMR}/psec	7.7(5)	2.7(3)	5.1(3)	2.0(7)	3.9(8)	1.5(5)
Dielectric relaxation	τ_μ^H	$\tau_\mu^{P.G.}$	τ_μ^H	$\tau_\mu^{P.G.}$	τ_μ^H	$\tau_\mu^{P.G.}$
τ_μ/psec	12.2	11.1	7.8(8)	7.1(9)	5.5(3)	5.0(8)
$\rho_{app} = \tau_\mu/\tau_{C(ortho)}^{NMR}$	1.8(2)	1.6(5)	1.5(3)	1.4(1)	1.3(8)	1.2(7)

[a] $\tau_\mu^H = \tau_c^{Diel}$; $\tau_\mu^{P.G.} = ((2\epsilon_0 + \epsilon_\infty)/3\epsilon_0)\tau_c^{Diel}$.

If one assumes then that the molecule takes up two planar, cis (dipolar) and trans (nondipolar) configurations, the rotation of the methoxy groups gives rise to both *cis/trans* isomerism and *cis/cis* inversion mechanisms. We can therefore summarize the internal motions using a triangular kinetic scheme (Fig. 43). The dipolar autocorrelation function is found, then, to have the following time dependence:

$$\langle \boldsymbol{\mu}(t)\cdot\boldsymbol{\mu}(0)\rangle = \tfrac{1}{2}\langle \boldsymbol{\mu}(0)\cdot\boldsymbol{\mu}(0)\rangle \times \left[\exp(-t/\tau_2) + \exp(-t/\tau_1)\right]\exp(-t/\tau_0) \quad \text{(II.69)}$$

where τ_0 characterizes the reorientational process of the whole cis conformer, considered as a rigid molecule, and τ_1 and τ_2 are given by

$$1/\tau_1 = k_{21} + 2k_{12} \equiv k_{21}\left[1 + K_{eq}\right]$$
$$1/\tau_2 = k_{21} + 2k_{22} \equiv k_{21}\left[1 + K'\right] \quad \text{(II.70)}$$

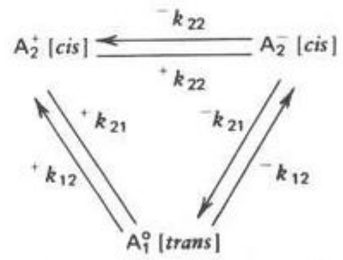

Fig. 43. Triangular kinetic scheme for *p*-dimethoxybenzene. [Reproduced by permission from *Mol. Phys.*, **30**, 984 (1975).]

According to the Curie principle stated by Prigogine and Mazur, this form of the dipolar correlation function assumes a total statistical independence between the internal (chemical) process and the external (diffusional) process. However, the analysis leading to (II.69) and (II.70) would be more convincing if associated with a model other than that of rotational diffusion, so that point 2 above ought to be considered in greater detail. Logarithmic plots of the inverse of the two correlation times of Table VI produce the apparent activation enthalpies

$$\Delta G_{NMR} = 2.2(6)\ \text{kcal/mol}$$
$$\Delta G_{Diel} = 3.3(4)\ \text{kcal/mol}$$

The difference between the two values may be an additional indication that the NMR and dielectric relaxation processes are different in nature, the former, on the basis of hypothesis 1, being insensitive to any group rotation.

A barrier height hindering the methoxy-group torsion may be evaluated from the far infrared data. The theoretical analysis of the torsion in completely asymmetric molecules remains, as usual, a very complicated problem, but it is possible, using the methods of Goulon, Canet, Evans, and Davies, to predict a band shift on deuteration from $\bar{\nu}_H = 91\cdot88\ \text{cm}^{-1}$ to $\bar{\nu}_D = 82\ \text{cm}^{-1}$. This is in excellent agreement with the experimental results, the barrier is then calculated as 5·88 kcal/mol (2058 cm^{-1}).

Therefore, there is little doubt that the methoxy-group internal rotation is fast enough to contribute significantly to the dielectric relaxation. The potential barrier hindering this motion is about 5·3 kcal/mol, estimated from the kinetic scheme of Fig. 43. This is sufficiently close to the 5·88 kcal/mol estimated above to be acceptable. Similarly, a value of 1·8±0.3 kcal/mol may be estimated for the apparent activation energy for the methyl rotation. It is also worth noting that if our results are acceptable in terms of the idea that the methyl rotation should be faster than the methoxy-group rotation of the methyl group, our evaluation of the height of the barrier hindering the methyl internal rotation might suggest an appreciable coupling of both the methyl and methoxy internal librations.

This first attempt to investigate the dynamics of internal motions by comparison of zero-THz and ^{13}C NMR relaxation data has run up against the problem of interpretation in terms other than rotational diffusion (isotropic at that). However, we have been able to deduce:

1. That internal methoxy-group rotation contributes significantly to the dielectric process.
2. Quantitative estimates of the kinetic parameters governing the internal librations and activation enthalpies.

E. Mesophases: Liquid and Plastic Crystals, Disordered Solids

The number of specialist articles and review series devoted to various researches into liquid crystal phenomena is steadily growing.[78] This section deals with the special insight these mesophases provide into the isotropic liquid state, in that the orientation correlation function $C_u(t)$ and its second derivative reflect the anisotropy of the molecular rotational characteristics brought about essentially by the molecular geometry. The alignment along the director axis (Section I) is the long-range consequence of the restricted torsional oscillation starting at the level of the nearest-neighbor cage, and reflected in the far infrared by a sharp and high-frequency Poley band (or bands) whose low-frequency loss adjunct peaks at megahertz frequencies, typically, in the aligned condition (Fig. 9). In consequence, $C_u(t)$ is virtually a pure exponential decay, whereas its second derivative, the Fourier transform of $\alpha(\omega)$, is highly oscillatory (Fig. 44). The object of this section is to demonstrate how the zero-THz profile in phases such as the nematic may be used to aid in the evaluation of the molecular dynamics. With such an objective the first far-infrared study of the nematic phase [of *p*-methoxybenzylidene-*p'* *n*-butylaniline (MBBA)] was carried out independently by Bulkin and Lok[79] and by Evans, Davies, and Larkin[80] in 1973.

The difference between the aligned nematic phase and the plastic crystalline or disordered solid mesophase also considered here is that the molecular rototranslation in the former evidently prohibits crystallization, or even solidification. This degree of dynamic freedom is propagated by the asymmetric van der Waals contours (constantly fluctuating due to intramolecular motions) of molecules such as MBBA which have liquid crystalline properties. It is possible, in consequence, to supercool the aligned nematic phase, the sample remaining a viscous fluid. The main feature of the MBBA far-infrared spectrum (taken in unaligned, aligned, isotropic solution, and solid states) is a strong and broad-band peaking at 130 cm^{-1} (Fig. 44). In the pure isotropic phase this shifts slightly to lower frequencies (123 cm^{-1}). The band seems almost to disappear in very dilute solution, and broadens considerably on heating a moderately dilute solution of MBBA in cyclooctane (Fig. 45). At the same time the peak moves to a lower frequency. Thus the absorption is markedly environment-sensitive, the near-neighbor interactions involved being strong in the pure nematic phase. It is justifiable to conclude therefore that its origin is torsional oscillation of the MBBA resultant dipole vector μ occurring at a higher frequency (given the MBBA moment of inertia effective in determining this motion) than is usual for isotropic, dipolar liquids such as the halogenobenzenes or CH_2Cl_2. On this basis Evans, Davies, and

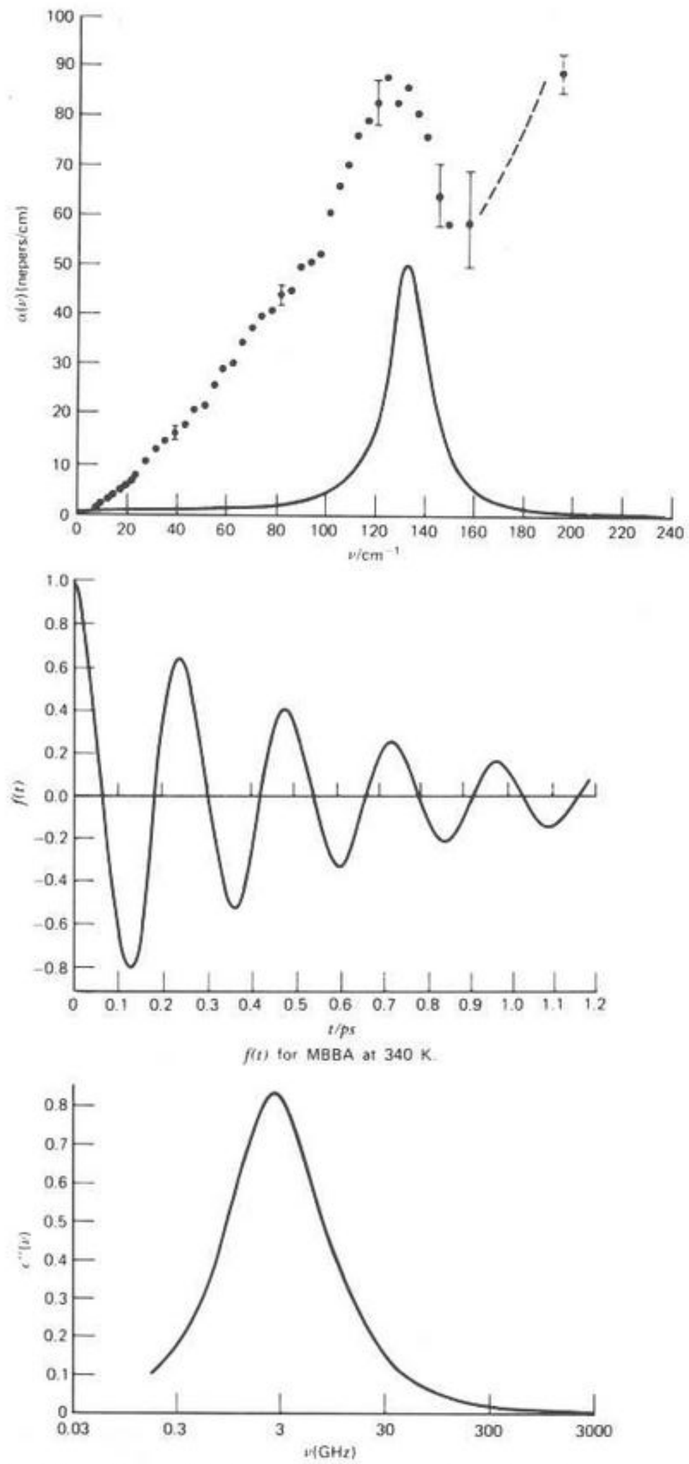

Fig. 44. (*a*) ●, Experimental absorption for *p*-methoxybenzylidene-*p'n*-butyl aniline (MBBA) in the nematic phase at 340°K. (—), Mori theory best fit. (*b*) $-\ddot{C}_u(t)$ for MBBA at 340°K. (*c*) Loss curve calculated for MBBA at 340°K. Observed $\epsilon''(\bar{\nu})=0.70$; observed critical frequency = 2.6 GHz; calculated = 2.7 GHz. [Reproduced by permission from *J. Chem. Soc. Faraday Trans. 2*, **72**, 1169 (1976).]

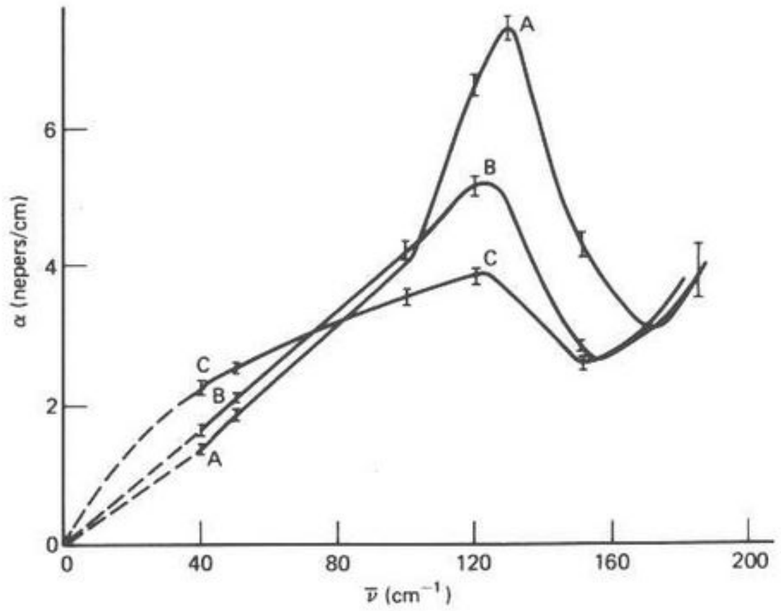

Fig. 45. (*A*) Spectrum of a 10.2% w/w solution of MBBA in cyclooctane (corrected for solvent absorption) at 297±0.5°K. (*B*) 341±1°K; (*C*) 338±1°K. [Reproduced by permission from *J. Chem. Soc. Faraday Trans. 2*, **69**, 1011 (1973).]

Larkin[80] carried out some model calculations of the MBBA absorption. The first of these involved a theory of itinerant oscillation due to Hill[81] and Wyllie,[82] and of random hopping from discrete sites due to Brot[52]—an extension of the *m* diffusion model. Both these models are early approximants and the examples of Figs. 14 to 19 compare them against direct Fourier transforms of $\alpha(\omega)$. Characteristically, the short-time behavior of approximants earlier than that of (I.30) compare badly with experiment (Fig. 19). To reproduce the observed spectrum, it was found that the potential well experienced by an MBBA molecule in the field of its neighbors needs to be considerably narrower and steeper than that of isotropic dipolar liquids. The well depth estimated for best fit agreed surprisingly well with a rough calculation using a potential of the form $V = a\exp(-br) - c/r^6$, in which the only intermolecular interactions considered were those between the benzene rings of MBBA packed in an idealized geometry.

Using (II.35) in the empirical fashion by varying γ and $K_1(0)$ gives the results of Fig. 44, where the theoretical $\alpha(\omega)$ and loss curves are in fairly satisfactory accord with experiment. The "mean-square-torque" term $K_1(0)$ takes on a high value compared with those found empirically in fluids such as CH_2Cl_2. Across the series[83] MBBA : propyne : $CBrF_3$: $CClF_3$: CHF_3, for example, the apparent mean-square torques decrease roughly in the ratio 200 : 25 : 10 : 10 : 8. This trend is the one expected on the assumption that

the greater the molecular geometrical anisotropy, the greater the mean barrier to torsional oscillation. For a high-mean-square torque the microwave and far-infrared parts of the zero-THz band must be widely separated, whereas for a low-mean-square torque (as in CHF_3, for example) the two parts are virtually fused into one.

Despite the apparently good fit obtained with γ and $K_1(0)$, it must be emphasized that any modeling such as the above of the rototranslational dynamics in MBBA must of necessity be crude and approximate because mathematical tractability demands the use of rigid, whole molecule libration, using a very simple representation of the intermolecular potential. The MBBA zero-THz profile is assuredly environment-sensitive but is best described as arising from the librations of a dipole within a flexible framework, the motions of which are determined by and in turn determine the character of the nearest-neighbor and less immediate environment. In a flexible molecular framework the previous section demonstrated the degree of extra complexity engendered even within the restricted limits of rotational diffusion—it is difficult, for example, to estimate the moment of inertia dyadic, which is time-dependent. In addition, the long-range correlations are of greater import in the mesophase, so that it is likely that collective motions are favored. The continuum theory of the mesophase as reviewed, for example, by de Gennes has to be matched by molecular theories if a cohesive picture is to be built up. Computer simulations run into the difficulties of swarm sizes being larger than the grid or cube of molecules set up initially. Finally, it has been observed that in solid MBBA the 130-cm^{-1} band splits into at least four partially resolved peaks, so that there is a possibility, as pointed out by Sciesinska, Sciesenski, Twardowski, and Janik,[84] that the torsional vibrations and other low-frequency internal modes of the MBBA molecule account for all the absorption below 170 cm^{-1}. They cite the evidence of changes in the spectra which they associate with different phases of MBBA solid and in the persistence of the absorption in solution. However, the 130-cm^{-1} band is dilution-sensitive as regards its shape and peak position, so that intermolecular sensitivity is detectable.

To extend the zero-THz monitor to phases such as the cholesteric (of cholesteryl oleate and cholesteryl oleyl carbonate, for example), it is more fruitful to look indirectly at the effect of the environment on small amounts of rigid, intensely dipolar solute molecules such as CH_2Cl_2 used as dynamical probes. (This technique is extended to glasses in the next section.) The following advantages accrue:

1. Cross-correlations terms between guest molecules (dynamic and electrostatic), not amenable to ready mathematical analysis, are minimized

in dilute solution in the cholesteric, nematic, or aligned nematic solvent.

2. The probe can be chosen to be particularly suitable for model simulation of its absorption profile (i.e., to be rigid and intensely absorbing).
3. The influence of a liquid crystalline environment on molecular motion may be measured directly against the equivalent spectra in an isotropic solvent such as CCl_4.

The far-infrared spectra of the mesophases themselves are often rich in detail but consequently very difficult to model. For example, we monitor in this section the alignment of 4-cyano-4′-*n*-heptyl biphenyl (7CB) with ac and dc electric fields of up to 7 kV/cm, and with magnetic fields, and Fig. 46 shows the appearance of extra peaks underlying the structure in the unaligned condition.[85] However, an attempt has been made[86] to use (II.35) with 7CB— for best fit to the low-frequency loss data, the THz peak corresponding to rigid end-over-end torsional oscillation is very sharp, centered at over 100 cm^{-1}, but obviously (in the light of the electric and magnetic field work) one of many possible such absorptions, all markedly environment sensitive. The effect of applying an increasing dc electric field to the nematic phase of 7CB is shown in Fig. 46. The overall intensity of the absorption decreases across the whole of the far-infrared range and the spectrum is split into peaks hitherto unresolved in the unaligned condition. An intensity decrease on application of an external field has been observed in the Raman by Schwartz and Wang.[87] In the nematic phase of two compounds, striking changes in the relative intensity of several Raman bands were observed as a function of applied electric field strength. An explanation was given in terms of the collective stabilization due to the large ensemble of molecules aligned by the field. However, the appearance of so many extra peaks in the far infrared is entirely novel. If these peaks are all intermolecular in origin, partially so, then one possible explanation of their appearance is that the increased alignment under the effect of a field accentuates the underlying lattice modes [i.e., brings out single-crystal-type behavior, but with the residual translational freedom (NMR studies) associated with the liquid crystal phase still being retained]. This kind of dynamical effect is indicated also by the fact that the overall intensity drops due to polarization of the radiation reaching the detector (i.e., the aligned nematic phase is acting as a polarizer). The question of what happens to the torsional oscillating Poley absorption in these circumstances is an interesting one. It was in an attempt to describe quantitatively this process and its low-frequency counterpart, the loss peak observed by Moutran in 7CB at 6 MHz that (II.35) was used for 7CB as described already.[86]

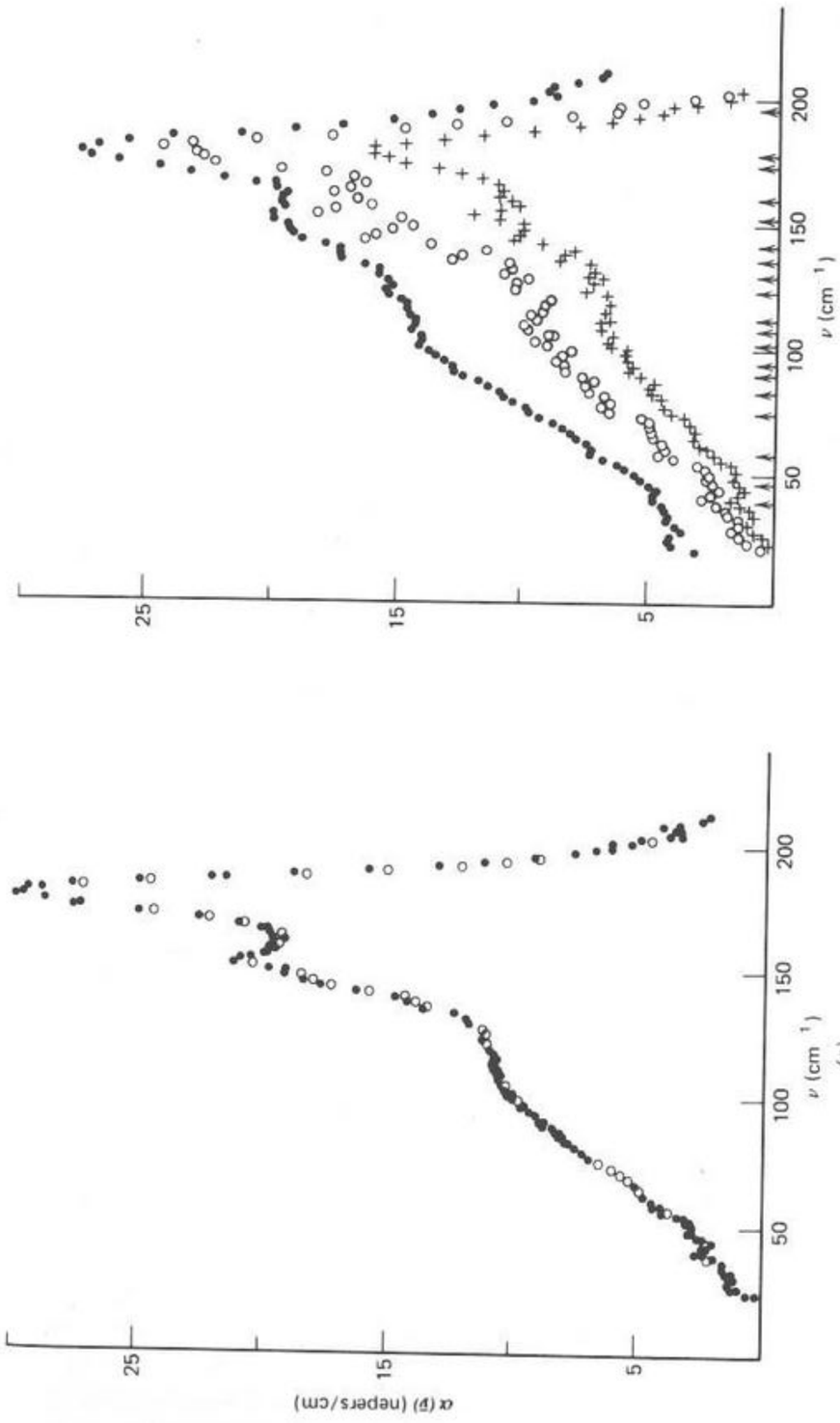

Fig. 46. (*a*) Nematic phase of 7CB at 299°K, unaligned (no applied field, no treatment of the window surfaces): ○, far-infrared absorption. (*b*) ●, Aligned nematic phase of 7CB at 299°K, applied field of 2.0 kV/cm^1; ⊙, applied field of 3.0 kV/cm^1; +, applied field of 7.1 kV/cm^1. [Reproduced by permission from *J. Chem. Soc. Chem. Commun.*, 268 (1978).]

The observation of the probe Poley absorption,[54] on the other hand, is designed to avoid for the moment the difficulties of quantitative interpretation associated with the far-infrared spectra of pure liquid crystals. We chose CH_2Cl_2 because its far-infrared absorption is intense and well defined (Fig. 20). The far-infrared broad-band absorptions in CH_2Cl_2 have been measured carefully in isotropic solutions in CCl_4, decalin, cholesteryl linoleate, cholesteryl oleyl carbonate, and 7CB in order to bring out by direct comparison unusual dynamical effects on the CH_2Cl_2 molecules themselves. Whereas the CH_2Cl_2 band maximum ($\bar{\nu}_{max}$) shifts by about 30 cm^{-1} to lower frequency on dilution in both CCl_4 and decalin, there is a smaller corresponding change when CH_2Cl_2 is dissolved in cholesteryl linoleate and cholesteryl oleyl carbonate (Fig. 47). This may be attributed to a persistence of statistical cross-correlations (time-dependent Kirkwood g-factor) which vanish gradually in isotropic solvents. The observed integrated intensity per molecule (A/N) of CH_2Cl_2 is decreased significantly compared with that in CCl_4 or decalin. However, the opposite effect is observed in the microwave region, where the CH_2Cl_2 apparent dipole moment increases on dilution in cholesteryl linoleate. Thus there is an inhibition of the intensity of the Poley process of CH_2Cl_2 when dissolved in molecules such as those which form a cholesteric phase. The integrated absorption intensity vs. molecular number density is plotted in Fig. 47 for the CH_2Cl_2 Poley band in various solvents at 298°K. These are carbon tetrachloride, decalin, cholesteryl oleyl carbonate, and 7CB. In CCl_4 and decalin, A/N is constant within the experimental uncertainty over the whole range of dilution, while it is clear that dilution in the solvents which have liquid-crystal-type phases reduces A/N considerably. This reflects an unusual constraint on angular movement (polarization) which persists when the concentrations of CH_2Cl_2 are such that no liquid crystalline properties are apparent on a macroscopic scale (e.g., when birefringence has disappeared from the 7CB solutions): this is substantiated by recent Kerr effect studies[88] where it was shown that the beginnings of liquid crystal behavior can be discerned in the "isotropic" phase long before the transition temperature into the mesophase, which is cloudy in visual appearance.

In the mesophase itself, this type of partial ordering was first observed using NMR methods of studying benzene in a nematic phase. A spectrum is obtained consisting of broad bands attributable to the solvent, superimposed on which was a series of sharp lines. Benzene acquires a preferential orientation due to solvent–solute interactions and its NMR spectrum is governed dipole–magnetic dipole interactions which are uniquely intramolecular in origin. The benzene molecules retain a translational freedom with respect to the nematic solvent which explains the sharpness of

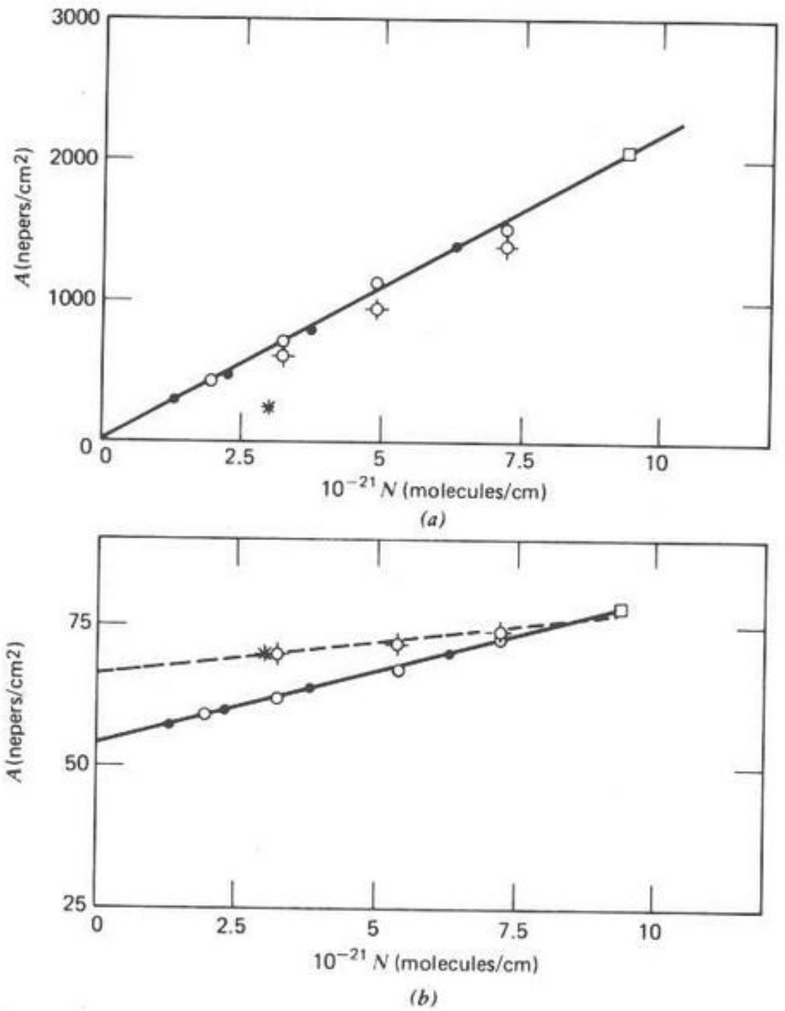

Fig. 47. (*a*) Plot of integrated absorption intensity (A) against N for all environments at 298°K: ⊙, in CCl_4; □, pure $CH_2Cl_2(l)$; ●, in decalin; ⊕, in cholesteryl oleyl carbonate (c.c.o.); •, in cholesteryl linoleate (C.L.). (—) Best straight line through the CCl_4 and decalin data. (*b*) Plot of $\bar{\nu}_{max}$ against number density in CCl_4 and decalin: (—) best straight line through the CCl_4 and decalin data; (---) best straight line through the cholesteric data; □, pure CH_2Cl_2; ⊙, CCl_4 solution; ●, decalin solution; ⊕, in cholesteryl oleyl carbonate; •, in cholesteryl linoleate. [Reproduced by permission from *J. Chem. Soc. Faraday Trans. 2*, **74**, 346 (1978).]

the NMR lines. The orientation is in the direction of the principal magnetic field. Since this discovery analogous NMR studies have shown that most molecules are preferentially oriented in a nematic phase. The effect of this on its far-infrared Poley absorption is retained in CH_2Cl_2 well into the apparently isotropic condition[54] Additional dynamical information is of course available in the zero-THz range because the band shape of the

Poley absorption contains dynamical information at short times in the orientational autocorrelation function, while NMR studies yield areas beneath a correlation function, and not the details of its analytical dependence. We illustrate this point in Fig. 48 where by roughly reproducing, using (I.30), the Fourier transform of $\alpha(\omega)$ of CH_2Cl_2 in cholesteryl oleyl carbonate, the following related functions may be produced analytically.

1. The orientational acf or dielectric decay function $\langle \cos\theta(t)\cos\theta(0)\rangle$, where θ is the angle between the dipole and the measuring field (I.30).

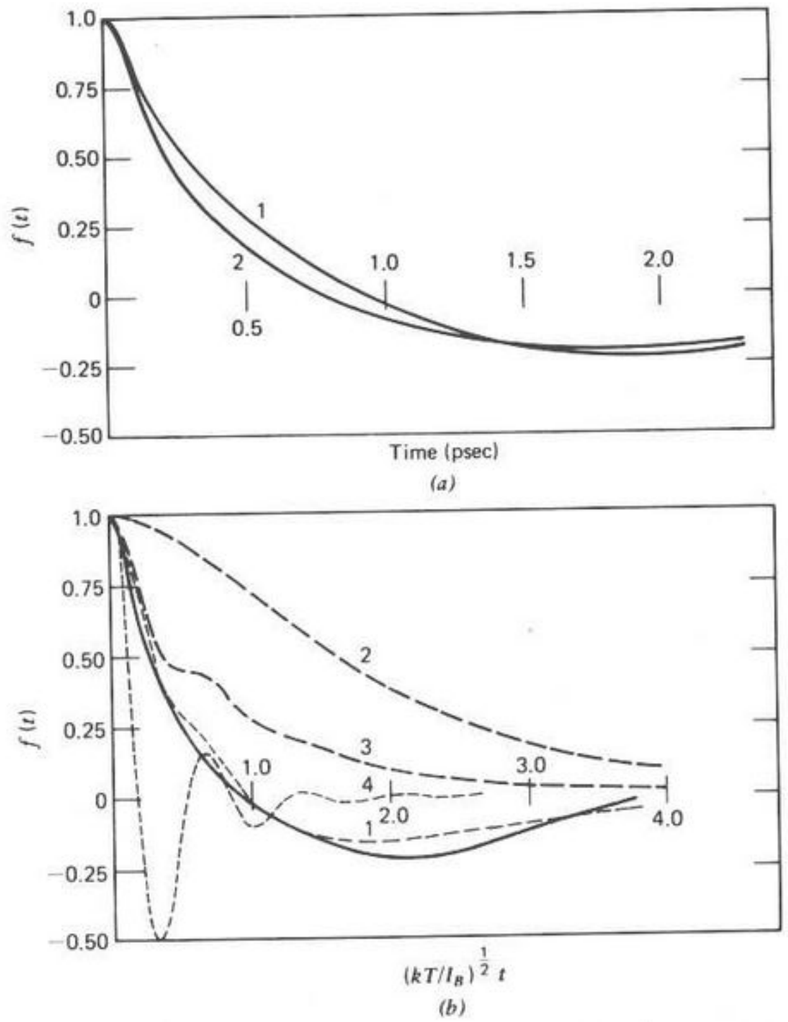

Fig. 48. (*a*) (—), (1) $\ddot{C}_u(t)$ for pure CH_2Cl_2 liquid at 296°K; (2) $\ddot{C}_u(t)$ for 1.97×10^{21} molecules CH_2Cl_2/cm^3 in CCl_4. (*b*) (—), Curve (*a*) 2; (---), (1) $-\ddot{C}_{\cos\theta}(t)$, least-mean-squares best fit to curve (*a*) 2; (2) $C_{\cos\theta}(t)$, calculated from the fitting; (3) $C_{\dot\theta}(t)$; (4) $C_{\ddot\theta}(t)$. Curves are normalized at the origin. [Reproduced by permission from *J. Chem. Soc. Faraday Trans. 2*, **74**, 350 (1978).]

2. The torque acf which mirrors the molecular librations by oscillating about the abscissa (time axis) [i.e., $\langle\ddot{\theta}(t)\ddot{\theta}(0)\rangle$].
3. The angular velocity acf the area beneath which is the NMR spin–rotation relaxation time.

1. *Plastic, Disordered, or Amorphous Solids*

We define these phases in terms of the continuing rotational freedom of individual molecules whose translation is very strongly hindered. In terms of the zero-THz profile different plastic and disordered crystals exhibit the full range of frequency coverage sketched in Fig. 9. Molecules with symmetric van der Waals contours, such as $(CH_3)_3CCl$, absorb with essentially the same zero-THz loss profile in the plastic crystalline phase as in the liquid just above the melting point. Any residual difference may then be attributed to the effect of rototranslation in the liquid as opposed to pure libration. Some of the rotational velocity correlation functions of these plastic phases are shown in Figs. 14 to 19 and have been discussed in greater detail by Haffmanns and Larkin[89] and by Davies.[90] In this section we are concerned more with the disordered and amorphous solids giving rise to a zero-THz profile with widely separated loss maxima on the frequency scale (Fig. 9). The rotational freedom remaining in these phases ensures that at THz frequencies a remnant of the liquid Poley-type absorption will remain as an indication of the torsional oscillation of the molecular dipole. This torsional oscillation will not be confined to one potential well over a long period of time, and a gradual movement through larger angles will give rise to an adjunct of the THz loss peaking at kHz frequencies and lower. The complete profile, sometimes covering much more than a dozen decades of frequency, must be amenable to treatment by an equation such as (I.6) represented by approximants such as (I.30), which are sophisticated enough to approximate $C_u(t)$ adequately at short times. On these grounds alone the THz peak and low-frequency peak in the overall loss should form parts of the same continuous function of frequency. In terms of $C_u(t)$ and its second derivative, the former decays exponentially from about 0.5 ps onwards, taking upwards of milliseconds and sometimes much larger, but the latter is oscillatory, being damped to zero in roughly the time that $C_u(t)$ takes to become exponential. Theories of the low-frequency dielectric loss in disordered solids have usually been based on rotational diffusion (or alternatively on inertialess charge carrier hopping) which match the decay characteristics of $C_u(t)$ but leave its second derivative undefined and produce not the required THz resonance but the Debye plateau. The contribution the far infrared can make to the molecular dynamics in these media has therefore been ignored. In this section we attempt to remedy this by showing that even the simplest form (I.30) of

approximant capable of shifting $\bar{\nu}_{max}$ in the THz region may be used to reproduce the overall features of the *complete* zero-THz profile.

The itinerant librator as described in (I.30) and (I.31) is particularly well suited geometrically to describe the loss in the disordered phase of the hexasubstituted benzenes, since these are known to rotate in a plane about their hexad axes (Fig. 49). In pentachloronitrobenzene (PCNB), for example, Aihara, Kitazawa, and Nohara in 1970 detected a loss peaking between 30 Hz and 1 MHz in the temperature range 293 to 372°K with a large energy barrier to rotation.[91] An entropy difference between the stationary and transitional positions was calculated on the basis of plane reorientation between two opposite wells, ignoring the effect of molecular inertia. In the far infrared a peak at 38 cm^{-1} has been identified recently as librational in origin (Fig. 50) by invoking the harmonic approximation for reorientation of six-fold symmetry in the manner of Darmon and Brot,[92] who assume that the angular movement of the molecule occurs in a fixed crystalline potential. The libration frequency $\bar{\nu}_0$ is then defined for

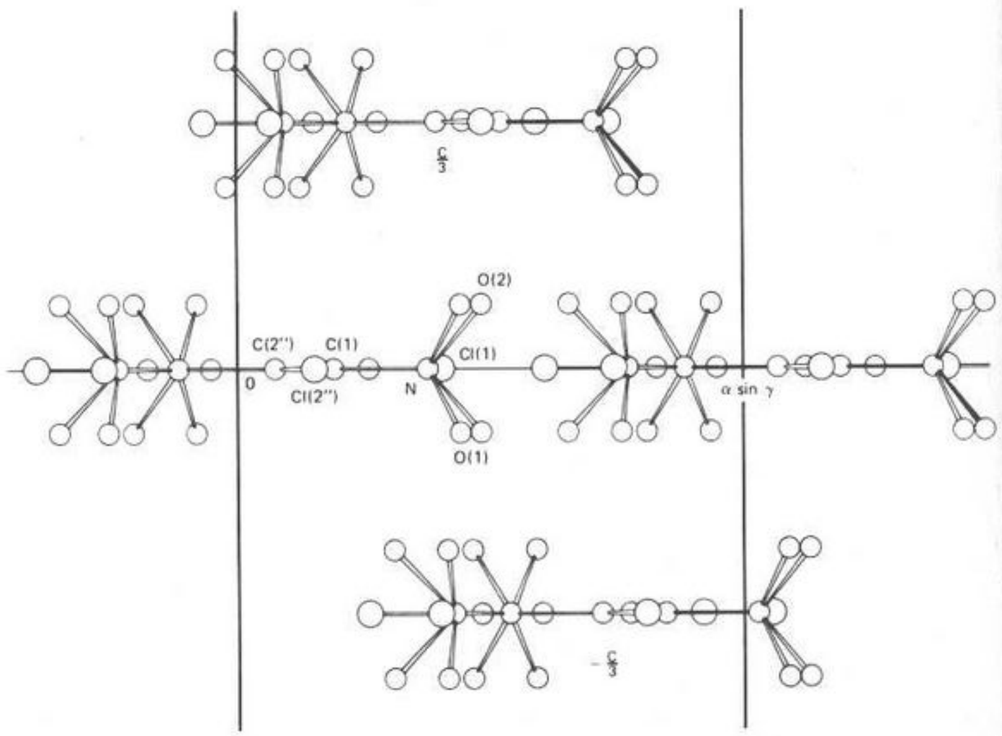

Fig. 49. Projection of the pentachloronitrobenzene crystal structure. [Reproduced by permission from *Acta Crystallogr.*, **30B**, 1546 (1974).]

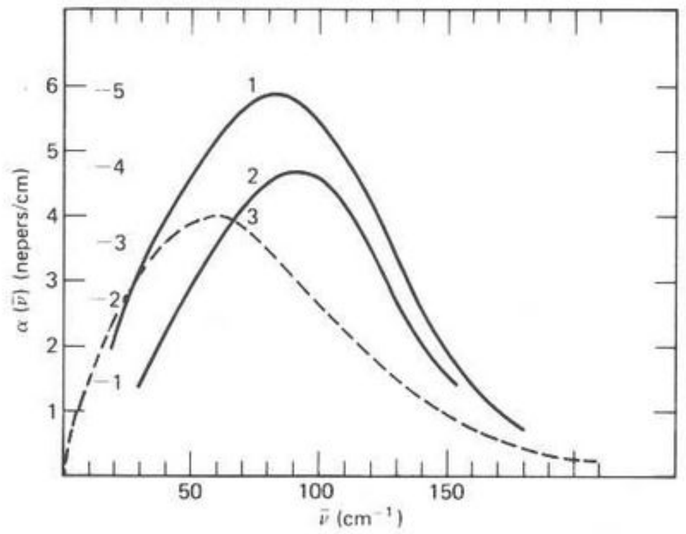

Fig. 50. Far-infrared part of the total loss profile in CH_2Cl_2 solutions. (1) Glass at 118°K (inner scale); (2) glass at 114°K (outer scale); (3) solution (liquid) at 298°K. Ordinate: $\alpha(\bar{\nu})$ (nepers/cm); abscissa: $\bar{\nu}$ (cm^{-1}). [Reproduced by permission from *Chem. Phys. Lett.*, **56**, 529 (1978).]

simple symmetries such as that of benzene by

$$\bar{\nu}_0 = \frac{3}{\pi c}\left(\frac{V}{2I}\right)^{1/2} \tag{II.71}$$

where I is the moment of inertia about the hexad axis. Naturally, (II.71) is an approximation for PCNB, especially since the large NO_2 group will set up potential barriers to rotation of different magnitude, resulting in an observed distribution of dielectric "relaxation times" which become nearly identical only at about 372°K. No account is taken by (II.71) of intermolecular coupling. This results in a distribution of librational frequencies and sets up vibrational waves throughout the lattice. Equation (II.71) has been used[92] to predict the observed Raman or far-infrared peak libration frequencies in plastic crystalline benzene, furane, and some other hexasubstituted benzenes which all lie in the range 30 to 60 cm^{-1}.

The frequency $2\pi\bar{\nu}_0 c$ from (II.71) may be identified with ω_0 of (I.31) in order to reproduce theoretically the required zero-THz profile of PCNB, which ranges experimentally from 30 Hz to 38 cm^{-1}. The factor β_1 of (I.31) is related to the low-frequency loss through τ_D, the inverse of the loss peak frequency. Therefore, the only phenomenological variable to be evaluated empirically is β_2, which has the effect of broadening the 38-cm^{-1}

resonance. No force fitting of the molecular parameters of the itinerant librator model is attempted. The moment of inertia of the annulus I_1 is estimated using the X-ray data of Tanaka, Iwasaki, and Aihara.[93] In the limit $kT/I_2\gamma^2 < 0.1$, the complex polarizability from (I.31) reduces to

$$\alpha_\mu^*(s) = \frac{kT}{I_2}\left[\frac{x(\Omega_0^2-\omega^2)+\omega\beta_1 y - i(\omega\beta_1 x - y(\Omega_0^2-\omega^2))}{x^2+y^2}\right]$$

$$x = \omega^2(\omega^2 - x_3) + x_1(x_4 - x_2\omega^2)$$

$$y = \omega(x_4 + x_1(x_3-\omega^2) - x_2\omega^2) \qquad \text{(II.72)}$$

with

$$x_1 = \frac{kT}{I_1\beta_1}\left[\frac{\beta_1\omega_0^2}{\beta_1\omega_0^2+\beta_2\Omega_0^2}\right]$$

$$x_2 = \beta_1+\beta_2$$

$$x_3 = \omega_0^2+\Omega_0^2+\beta_1\beta_2$$

$$x_4 = \beta_2\Omega_0^2+\beta_1\omega_0^2$$

Values of the various parameters used for PCNB are listed in Table VII.

For $\beta_2 = 0$, the THz resonance at the frequency $(\gamma/2\pi c) = 38\ \text{cm}^{-1}$ is too sharp and Debye loss curves are produced theoretically at the low frequencies, which are too narrow (Fig. 51) in comparison with the broad experimental data. The effect of increasing β_2 is most clearly depicted in terms of the absorption coefficient $\alpha(\omega)$ of Fig. 52, where the THz resonance is depicted theoretically as rising above the intermediate Debye plateau.

TABLE VII
Parameters for PCNB Used in the
Itinerant Librator Model (I.31) ($I_1/I_2 = 10$)

Temperature (°K)	τ_D (sec)	$\frac{kT}{I_2\gamma^2}$	γ/β_1
293	1.1×10^{-4}	0.002	6.4×10^{-6}
313.4	1.3×10^{-5}	0.002	4.9×10^{-5}
333	3.1×10^{-6}	0.002	2.0×10^{-4}
353.7	8.2×10^{-7}	0.0025	6.9×10^{-4}
372.1	2.7×10^{-8}	0.0026	2.0×10^{-3}

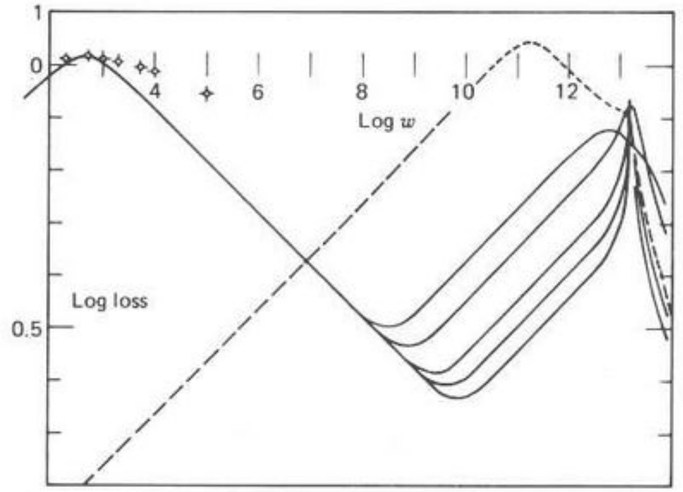

Fig. 51. $\text{Log}_{10}(\epsilon'')$ vs. $\log(\omega)$ representation of the total loss profile in glassy CH_2Cl_2/decalin at 114°K (1.97×10^{21} molecule/cm^3 of CH_2Cl_2). ⊙, Some experimental points indicating that the observed low-frequency loss is broader than the model loss. The various high-frequency curves are for $\beta_2 = 0.1$, 2, 5, 10, and 20 TH_z. This illustrates the broadening effect of this friction coefficient. (----), Loss curve of a solution of CH_2Cl_2 in decalin at 296°K (room temperature). [Reproduced by permission from *Chem. Phys. Lett.*, **56**, 529 (1978).]

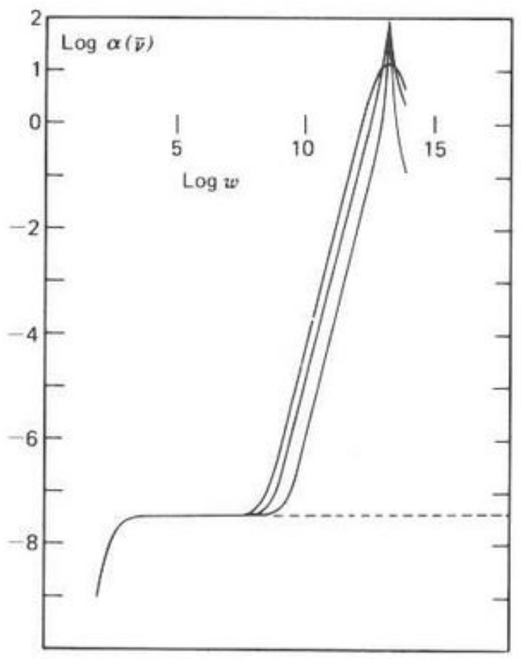

Fig. 52. $\text{Log}\alpha(\omega)$ vs. $\log(\omega)$ representation of the absorption in glassy CH_2Cl_2/decalin. Note the horizontal Debye plateau, which continues as $\omega\to\infty$ for classical theories of Brownian motion. The far-infrared resonance rises steeply above this at 90 cm^{-1} (114°K) in itinerant oscillation. [Reproduced by permission from *Chem. Phys. Lett.*, **56**, 529 (1978).]

Taken overall, then, the approximant of (I.6) represented in (I.31) produces a fairly realistic picture of the overall zero-THz profile in TCTMB which may be extended to the losses observed generally in amorphous and disordered solids, as reviewed recently by Lewis.[36] Here it was emphasized that despite large differences in composition and structure among these solids, it is remarkable that the ac conductivity $[\sigma(\omega) = \omega\epsilon''(\omega)]$ varies according to an apparently simple law, albeit over a restricted range of low frequencies in the zero-THz range. In fact, this law is known to break down at frequencies greater than about 10^{10} Hz, and must do so in the THz range where the Poley resonance still remains on general theoretical grounds.

Examples of these solids are vanadium phosphate glass, doped silica, aluminium oxide, amorphous selenium, organic polymers, and molecular solids such as *trans*-carotene. In dielectric terms the response in these solids is coming from the high-frequency side of a loss peak [i.e., where $\epsilon''(\omega)$ decreases as ω increases], the peak itself and the low-frequency side beyond being inaccessible to conventional experimentation, owing to their very low frequencies. One of the objects of the review was to show that the classical concept of rigid dipole reorientation and that of localized hopping charge carriers can be unified and shown to be capable of describing similar phenomena in a noncrystalline solid. In view of the foregoing arguments, such models, to be entirely realistic, must be able also to produce an equation for the loss that will be realistic in the THz region (the far infrared). This is to say that the molecular libration, taking place as usual at THz frequencies, must be built into the basic equations for elementary polarization induced by donor–acceptor charge transfers. As it stands, the carrier hopping theory produces Debye-type equations for the elementary loss, which is integrated to give the total dielectrical response over all barrier heights in the solid. The broad, very low frequency loss may then be calculated theoretically without recourse to the empirical concept of a spread in Debye times. However, any Debye-type formalism is physically unrealistic when extrapolated to far-infrared frequencies, where the sharp quasiresonant Poley absorption is still to be expected *whenever there is enough molecular freedom of rotation to give rise to a low-frequency loss or ac conductivity*. This is true even though the broad loss peaks at frequencies too low to be measured.

In physical terms the spatial distribution in the solid consists of localized states which are oscillating at high frequencies. At a much lower range of frequencies, charge hopping occurs from one site to another, giving rise to the observed ac conductivity. This may be formulated by considering the

elementary polarization

$$p(t) = V^{-1}\left[\sum_D e(1-f_i)r_i\cos\theta_i - \sum_A ef_i r_i\cos\theta_i\right] \tag{II.73}$$

where e is the electronic charge, f_i the probability that a state i (donor or acceptor) is occupied by an electron, r_i the distance of this state from a chosen origin, the angle between $\mathbf{r}_i$ and $\mathbf{F}(t)$, the probe field (not necessarily the internal field). If the vector $\mathbf{r}_i$ remains fixed in space, Debye-type equations for the elementary loss are obtained after certain simplifying assumptions:

$$\Delta\epsilon''(\omega) = e^2 r_{ij}^2 \frac{\cos^2\theta}{kT} \frac{\omega P_{ij}P_{ji}}{\omega_{ij}\left(\omega^2+\omega_{ij}^2\right)} \tag{II.74}$$

where P_{ij} and P_{ji} are transition rates between sites, and $\omega_{ij} = P_{ij} + P_{ji}$ is the characteristic relaxation frequency for the pair element in question. However, the dipole moment determining the polarization is $e\mathbf{r}_{ij}$, which is affected by a torsional oscillation in $\mathbf{r}_{ij}$ at far infrared frequencies. Thus in (II.73), if $\mathbf{r}_{ij}$ were given a characteristic libration frequency, $\cos\theta_i$ would become time-variant and the necessary high-frequency Poley adjunct would appear. The *overall* time correlation function for the reorientation of $e\mathbf{r}_{ij}$ would then be well behaved. It remains to be seen whether these ideas are mathematically tractable, but certainly librational-type absorptions in the far infrared should be observed for all the amorphous solids mentioned by Lewis as well as in zeolites and clathrates with dipolar guests, where whole molecule rototranslation, as opposed to libration, is the more important consideration. Pardoe and Fleming[94] have recently observed such bands in certain inorganic glasses. It may be mentioned finally that the libration of $e\mathbf{r}_{ij}$ would depend inversely as usual on an effective molecular or intermolecular moment of inertia, thus bringing the charge-carrier hopping model into line with the concept of inertial effects in the far infrared. It should be emphasized that in this type of theory we are not necessarily confined to molecular dipole autocorrelations, since hopping occurs between different librating molecular frameworks. Naturally, $\mathbf{r}_{ij}$ does not coincide with the molecular permanent dipole vector, in general.

F. Zero-THz Absorptions in Glasses and Viscous Liquids

The influence of viscosity in the medium surrounding a particle or molecule undergoing rototranslation in the fluid state is of basic interest. Viscosity is a factor which can be varied conveniently through orders of

magnitude by supercooling solvents such as decalin or o terphenyl. This section purposes to demonstrate the influence of a highly viscous environment on the rotational dynamics of small dipolar molecules (in particular, CH_2Cl_2) in glassy and viscous liquid decalin and other convenient solvents. These manifest themselves in a similar fashion to those described in Section II.E [i.e., over a frequency range extending from audio frequencies (kHz) and below to the far infrared (or THz)]. This is in very marked contrast to the loss in the equivalent room-temperature solution, where it is restricted (as in CH_2Cl_2/decalin, for example) to the microwave (GHz) on the low-frequency side.

In Figs. 50 and 51 we illustrate the low- and high-frequency parts of the experimental loss in a solution containing 1.97×10^{21} molecules/cm^3 of CH_2Cl_2 in glassy decalin at 114°K as represented by the itinerant librator. A temperature difference of 4°K is enough to move the loss peak through almost two decades of frequency, so that the Arrhenius activation enthalpy for the process is high. The far-infrared part of the loss is shown over the temperature range 109 to 113°K in Fig. 50 as the absorption coefficient $\alpha(\omega)$. There is a slight movement to *higher* frequency as the temperature is lowered. There is also a slight drop in intensity. In comparison, the same concentration of CH_2Cl_2 in decalin liquid at 293°K produced a far-infrared peak at 61 cm^{-1}, almost 50 cm^{-1} below that of the glassy solution at 109°K. The low-frequency loss peak, which appears at 3.67 cm^{-1} in the high microwave at 293°K, has of course shifted downward by many decades in the glass.

For $(kT/I_2\gamma^2)<0.1$ (as in this case) (II.72) may be employed to calculate analytically the zero-THz multidecade loss profile. The optimum value of β_2 for best fit to the far-infrared data is 10 THz, while $\beta_1=3.6\times10^{10}$ THz at 109°K. The vast difference between the two friction coefficients reflects the difference between single-molecule libration and collective reorientation of the cage of nearest neighbors—the latter, involving some translation, being much the more energetic and slower process. It is of course only by collective efforts that the encaged dipole ever manages to surmount the potential well in which it is librating at THz frequencies. Such an oversimplified model as (I.31) represents may be expected to reproduce only the gross features in the available experimental data [e.g., a distribution of inverse frequencies (or relaxation times) is seen at low frequencies]. However, the most urgent point here again is that the loss profile is not confined to the kHz frequencies but continues into the THz or far-infrared range where the Poley resonance is still clearly defined.

In the supercooled viscous liquids studied by Johari and others,[95] two absorption peaks (α and β processes) are often observed in molecules containing rigid, asymmetric, aromatic probes such as halogen and methyl-substituted benzenes and naphthalenes. Below the glass transition only the secondary relaxation is still observed. The loss curve we see in glassy CH_2Cl_2/decalin rapidly shifts up to microwave frequencies over a very narrow range of temperature at the glass-to-liquid transition temperature (T_g), in contrast to the larger molecules studied by Johari. With very fine temperature control an α and β spectrum appears in this small temperature range for CH_2Cl_2 also, so that in the viscous liquid the overall loss profile peaks *three times*, in the audio, MHz, and THz frequency regions. It is reasonable to suggest, therefore, that there exists in the viscous CH_2Cl_2/decalin liquid three loss peaks in the zero-THz profile which in general may be designated as primary, secondary, and tertiary processes of the overall dynamical evolution. The tertiary (γ) process is that of libration of the guest dipole showing up at THz frequencies, the other two being well documented by Johari and others and by Williams.[96] The β process represents the influence of nearest-neighbor cage fluctuations on the libration of the γ process, creating a diffusion of the encaged molecule from one energy well to another. It is the remnant of the liquidlike rotational process (more precisely rototranslational of course) first described by Debye in terms of inertialess spherical diffusion. The α process is one of bulk reorientation (inclusive of next nearest neighbors, etc.) and is the slowest. In the glass the cooperative motion becomes infinitely slow, and the α loss peak moves to zero frequency, leaving the β and γ processes to be described by our simplistic itinerant librator (i.e., simplistic in concept, almost intractable analytically).

The far infrared γ peak (i.e., the Poley absorption) is shifted dramatically to higher frequencies in the glassy CH_2Cl_2/decalin solution, (i.e., from 60 cm^{-1} at 298°K to 116 cm^{-1} in the glass). To put this in perspective, the root-mean-square angular velocity for a freely rotating CH_2Cl_2 ensemble is classically 21.2 cm^{-1}, so that the change in $\gamma=2\pi\bar{\nu}_{max}c$ produced by a glassy environment is commensurate with that produced by condensing the infinitely dilute gas into the liquid at ambient temperature. At the same time, the β part of the Zero-THz profile moves from 110 GHz at 298°K to 5 kHz in the glass at 111°K. Very much *smaller* shifts to higher frequency in γ have been observed[125] by compressing under *kilobars* of external pressure liquids such as C_6H_5Cl and CS_2.

In contrast to the behavior of CH_2Cl_2/decalin glass, the enthalpy of activation of the β process of 10% v/v fluorobenzene/decalin is very low (18 kJ/mol). The predominant β process is observed to peak here at 77°K (i.e., 50°K below the glass transition). Assuming that the β process is due to rotation about the sixfold axis in this case, a simple model of harmonic

libration such as that of Darmon and Brot produces a resonant delta function at 60 cm^{-1} using the enthalpy of activation measured at kHz frequencies. The observed γ peak is at 56 cm^{-1}. Across the halogenobenzene series the glassy β process shifts to lower frequencies, and is hardly detectable in bromobenzene. There is a corresponding shift to higher frequencies in the γ part of the overall loss, but not nearly as pronounced as that in CH_2Cl_2/decalin.

Tetrahydrofuran/decalin glass is also interesting and contrasts the CH_2Cl_2/decalin system in that the γ shift is much less and the enthalpy of activation again much smaller.

An oscillatory angular velocity autocorrelation function may be extracted from the best fit of (I.31) to both glassy β and γ parts. In Section III we simulate nitrogen in a high-temperature disordered lattice by computer molecular dynamics and find that this oscillatory behavior is also characteristic of the linear velocity autocorrelation function $C_v(t)$. This increase of the oscillatory character is of course accompanied by the large γ shift. The β shift implies that $C_u(t)$ will decay, almost exponentially, much more slowly in the glass.

III. MACHINE SIMULATIONS OF ROTATIONAL AND TRANSLATIONAL CORRELATION FUNCTIONS

There are available reviews[25,61] and some books[7,28] partially devoted to this topic, usually referenced under "molecular dynamics" and "Monte Carlo methods." Within the scope of this chapter the most incisive use of computer time may be made by pitting these techniques against our preconceptions of the fluid state. Modeling demands a degree of intuition before any equations may be set down on paper. The computer yields enough information about a small ensemble of molecules ($N \doteqdot 10^2$ or 10^3) to sound its depth. The "molecular dynamics" technique is particularly useful in our context since the Liouville (or Newton) equations are solved for a given intermolecular potential, the results being that for each molecule its trajectory is defined over a fraction of a picosecond or longer in terms of the first five derivatives of orientation and position. Therefore, it is possible to draw up a picture of our artificial droplet to a degree of detail which is itself almost as puzzling as a contemplation of the original fluid. Statistics therefore appear in terms of autocorrelation functions and multiparticle correlation functions, the latter being more difficult to compute, since a great deal more averaging is involved.

Some of the models of Table I have already been evaluated using this technique. Rahman,[97] in 1964, using 864 potentials representing argon atoms, demonstrated that the velocity autocorrelation function of the assemblage displayed a negative region out at long times (a few ps). The

Langevin equation (I.6), with $\mathbf{A}=[\mathbf{v}]$, $i\Omega_A$ null, and ϕ_A a delta function, is therefore oversimplified, since $\langle \mathbf{v}(t)\cdot\mathbf{v}(0)\rangle$ is exponentially decaying (but not when rotation is considered). Berne and Harp[25] in this series have simulated numerically the first memory function of CO, with a modified Stockmayer potential. Since then the number of simulations has grown—for example, the J-diffusion testing with rough spheres has already been mentioned. The development with which we are involved here is the extension to atom-atom Lennard-Jones interactions in diatomics of the molecular dynamics technique initiated by Barojas, Levesque, and Quentrec,[42] Cheung and Powles,[98] Streett and Tildesley,[99] and Singer and others.[100] In this section we use the algorithm developed by Streett and Tildesley to add a further dimension to the experimental evaluations of Section II. We simulate also, using disks bound within rough annuli, the analytical results of (I.31) with $\beta_2=0$. Essentially, this allows us to evaluate how well rough annulus/rough annulus interactions reproduce the Wiener statistics. If the match between the analytical results and the simulation is satisfactory in two dimensions, it will be reasonable to extend the simulation to three dimensions, and to simulate joint probability density functions which are intractable analytically. Throughout this section the following dimensionless, or reduced units are employed.

Bond length:	L^*	=	L/σ	(bond length/atom diameter)
Temperature:	T^*	=	kT/ε	
Density:	ρ^*	=	$\rho\sigma_e^3$	(where σ_e is the diameter of a sphere having a volume equal to that of the diatomic)
Pressure:	P^*	=	$P\sigma_e^3/\varepsilon$	

Here ε is defined through the fact that the potential energy of two diatomic molecules interacting via an atom–atom potential is the sum of four interactions between pairs of atoms not on the same molecules. For the Lennard-Jones model the atom–atom interactions take the form

$$U^{LJ}(r)=4\varepsilon\left[\left(\frac{\sigma}{r}\right)^{12}-\left(\frac{\sigma}{r}\right)^{6}\right] \tag{III.1}$$

where r is the distance between atoms on different molecules.

For a purely repulsive (hard) diatomic the equivalent potential is

$$U^{LJR}(r)=4\varepsilon\left[\left(\frac{\sigma}{r}\right)^{12}-\left(\frac{\sigma}{r}\right)^{6}+\frac{1}{4}\right] \qquad (r/\sigma)\le 2^{1/6}$$
$$=0 \qquad (r/\sigma)>2^{1/6} \tag{III.2}$$

A. The Molecular Dynamics Method

We briefly review the method involved, following Streett and Tildesley, who base their algorithm in turn on that developed by Cheung and Powles. The equations of motion are written in vector form:

$$M\ddot{\mathbf{r}}_i = \mathbf{F}_i \tag{III.3}$$

$$ML^2\dot{\boldsymbol{\omega}}_i = 4\mathbf{T}_i \tag{III.4}$$

where $\mathbf{r}_i$ is the center-of-mass coordinate for molecule i, $\boldsymbol{\omega}_i$ its angular velocity, and $\mathbf{F}_i$ and $\mathbf{T}_i$ are the net force and torque exerted on particle i by all other particles. Forces and torques are computed for all molecular pairs having center-to-center separations less than $2.5\sigma + L$, where L is the interatomic separation. This ensures that all atom-atom interactions at distances of 2.5σ or less are counted. At this distance the potential energy of two atoms interacting via the L-J potential (III.1) is of the order of 1% of the well depth. The virial theorem is used (as per Cheung and Powles) to correct the computed pressure and energy for long-range interactions.

Equations (III.3) and (III.4) are integrated numerically by means of a fifth-order predictor-corrector method due to Gear.[101] Since the particles involved are, ideally, linear, all centers of force within a molecule lie on its axis. As a consequence, vectors representing the torque, angular acceleration, and higher derivatives of angular position are always perpendicular to the axial vector **L** of the molecule. This allows the use of (III.4) rather than a second-order equation for angular position. Simulations in this section are carried out with a cube of 256 diatomic molecules arranged initially on an α-nitrogen lattice (fcc). Periodic boundary conditions are used which ensure that when a molecule leaves one side of the cube during the course of the simulation, another replaces it with the coordinates (x,y,z) displaced by the cube side length. After a complicated initial step, the simulation is allowed to run for about 1600 time steps [in units of $(M\sigma^2/\varepsilon)^{1/2}$], each of 0.0016 after rejecting the first few unstable steps. These units each correspond to a real time of the order of 10^{-15} sec. The calculated pressures and configurational internal energies are in excellent agreement with those calculated by Singer and others,[100] who have used a completely different molecular dynamics algorithm based on a different method of solving the equations of motion. The unpublished Monte Carlo calculations of Streett and Tildesley are in excellent agreement with their molecular dynamics data for $L^* = 0.3292\,(N_2)$, as well as with those of Cheung.

1. *Computation of Correlation Functions*

The fifth-order predictor–corrector algorithm used means that the first five derivatives of orientation and position may be stored on magnetic tape for future statistical analysis. For any element **A** of (I.6), its autocorrelation function may be calculated using the running time average

$$C_{\mathbf{A}}(t) = \frac{1}{T}\int_0^T \sum_{j=1}^{256} \mathbf{A}_j(\tau)\cdot\mathbf{A}_j(\tau+t)\,d\tau \tag{III.5}$$

using different initial times. In (III.5) T is the total time over which the simulation runs with j molecules. We notice that in any algorithm which conserves the total linear momentum ($\sum_i M\dot{\mathbf{r}}_i = \mathbf{0}$), the normalized autocorrelation function and cross-correlation of velocity and force will decay identically. This is because

$$\begin{aligned}\mathbf{v}_j(0)\cdot\sum_{k\neq j}\mathbf{v}_k(t) &= \mathbf{v}_j\cdot\left(\sum_{k=1}^{N}\mathbf{v}_k(t) - \mathbf{v}_j(t)\right)\\ &= -\mathbf{v}_j(0)\cdot\mathbf{v}_j(t)\end{aligned} \tag{III.6}$$

Therefore, it is possible to calculate collective correlation functions only when these take forms such as those of the longitudinal and transverse current and spin densities of hydrodynamical theory:

$$C(\mathbf{k},t) = \frac{1}{T}\int_0^T J^*(\mathbf{k},\tau)J(\mathbf{k},t+\tau)\,d\tau \tag{III.7}$$

where the wave vector $\mathbf{k}$ stands for $k_\perp$ or $k_\parallel$, and T is the total simulation time. We have, for current densities,

$$\begin{aligned}\mathbf{J}(\mathbf{k},t) = N^{-1/2}\sum_j \Big[&M\mathbf{v}_j^{(1)}(t)\exp\left(i\mathbf{k}\cdot\mathbf{r}_j^{(1)}(t)\right)\\ &+ M\mathbf{v}_j^{(2)}(t)\exp\left(i\mathbf{k}\cdot\mathbf{r}_j^{(2)}(t)\right)\Big]\end{aligned}$$

where $\mathbf{v}_j^{(1)}(t)$ is the velocity of the first atom of the jth molecule, $\mathbf{v}_j^{(2)}(t)$ that of the second atom. In Section IV we build these up from individual molecular vectors and thus attempt to bridge the gap between molecular and hydrodynamic theories.

We shall illustrate the use of molecular dynamics simulations in evaluating the approximation, (I.31), when the equations are applicable to space-itinerant oscillation of the molecular linear velocity $\mathbf{v}$.

B. Translational Motion— Simulations and Itinerant Oscillation

The itinerant oscillator model for motion in atomic fluids and uncoupled linear motion in molecular fluids was developed by Sears[102] in 1965 following some speculative remarks by Frenkel. Unfortunately, Sears's paper is mathematically a little flawed, as was pointed out by Damle and others.[29]

In this section we shall use the simplest version of this model consistent with the concept involved to calculate $C_v(t)$, the linear velocity autocorrelation function. The analytical $C_v(t)$ is then compared with that simulated using (III.1), (III.3), and (III.4). The self part of the van Hove correlation function $G_s(\mathbf{r},t)$ is evaluated analytically and compared with the experimental neutron scattering results of Dassannacharya and Rao[103] on liquid argon, and the theoretical $C_v(t)$ is also compared with the computer simulation of this function for liquid argon carried out by Rahman.[97] This is a good check on internal and interexperimental consistency, since $G_s(\mathbf{r},t)$ can be expressed in terms of $C_v(t)$ using the techniques of Section I. By evaluating the speed acf (that of $|\mathbf{v}|$) and that of the direction of the velocity, following Berne and Harp,[25] it is shown that a constant-speed approximation is valid in treating translational properties of fluids, confirming their results for CO.

Equation (I.6), for uncoupled, linear motion of the center of mass of an atom or molecule of mass m, reduces to

$$\dot{\mathbf{v}}(t)+\int_0^t K(t-\tau)\mathbf{v}(\tau)\,d\tau=\mathbf{f}(t)/m \tag{III.8}$$

where $\mathbf{f}(t)$ is defined by

$$K(t)=\langle \mathbf{f}(t)\cdot\mathbf{f}(0)\rangle \frac{m}{3kT}$$

Since $\langle \mathbf{f}(t)\cdot\mathbf{v}(0)\rangle=0$, we have the further relations

$$\dot{C}_v(t)=-\int_0^t K(t-\tau)C_v(\tau)\,d\tau \tag{III.9}$$

and the Mori series

$$\frac{\partial}{\partial t}K_{n-1}(t)=-\int_0^t K_n(t-\tau)K_{n-1}(\tau)\,d\tau \tag{III.10}$$

where $n=0,\ldots,N$ are positive integers. In this notation $K_{-1}(t)\equiv C_v(t)$. No intermode coupling or cross-correlations [describable by $G_d(\mathbf{r},t)$, the distinct part of the van Hove function] are accounted for in these equations. Truncating (III.10) with

$$K_1(t)=K_1(0)\exp(-\gamma t)$$

produces a result for $\tilde{C}_v(s)$ formally identical with that for the equations of motion:

$$m\ddot{\mathbf{q}}_1(t)+m\gamma\dot{\mathbf{q}}_1(t)-m_1K_0(0)[\mathbf{q}-\mathbf{q}_1]=m_1\dot{\mathbf{W}}_1(t)$$

$$m\ddot{\mathbf{q}}(t)+mK_0(0)(\mathbf{q}-\mathbf{q}_1)=\mathbf{0} \tag{III.11}$$

$$K_1(0)=(m/m_1)K_0(0)$$

$$K_0(0)=\omega_0^2$$

Here m is the mass of the atom or molecule whose coordinate is $\mathbf{q}$ and which is surrounded by a diffusing "cage" of such particles whose center of mass is at $\mathbf{q}_1$ and whose total mass is m_1. The inner particle m is harmonically bound at a frequency ω_0 to the diffusing cage with a restoring force constant $K_0(0)$. We note that $\mathbf{v}\equiv\dot{\mathbf{q}}$. A frictional force $\gamma\dot{\mathbf{q}}_1$ acts in opposition to the diffusing cage and $\dot{\mathbf{W}}_1(t)$, which is represented by a statistical Wiener process, is the force on the cage caused by "random" collisions. The two versions of $C_v(t)$ [from (III.8) and (III.11)] take the form of (II.39).

The van Hove function $G_s(\mathbf{r},t)$ for self correlations may be evaluated by considering (III.8) in the form

$$\ddot{\mathbf{r}}(t)+\int_0^t K(t-\tau)\dot{\mathbf{r}}(\tau)\,d\tau=\mathbf{f}(t)/m \tag{III.12}$$

and classically from (III.11) by a method to be described shortly. In (III.12) we have $\dot{\mathbf{r}}\equiv\mathbf{v}\equiv\dot{\mathbf{q}}$, the velocity of the tagged inner particle of mass m. $G_s(\mathbf{r},t)$ is the probability of finding this particle at $\mathbf{r}$ at time t given that it could be found at $\mathbf{r}=0$ when $t=0$. Using (I.33) and (I.34), the probability density function

$$p(\mathbf{r}(t),\mathbf{r}(0),\mathbf{v}(0);t)=\left[\frac{3}{2\pi B(t)}\right]^{3/2}\exp\left[-\frac{3|\mathbf{y}(t)|^2}{2B(t)}\right] \tag{III.13}$$

where

$$\mathbf{y}(t)=\mathbf{r}(t)-\mathbf{r}(0)-\Gamma_v(t)\mathbf{v}(0)$$

$$=\frac{1}{m}\int_0^t \Gamma_v(t)\mathbf{f}(t-\tau)\,d\tau$$

is the solution of (III.12). In (III.13)

$$\Gamma_v(t) = \mathfrak{L}_a^{-1}\left[s(s+\tilde{K}(s))\right]^{-1}$$
$$= \int_0^t \frac{\langle \mathbf{v}(t)\cdot\mathbf{v}(0)\rangle}{\langle \mathbf{v}(0)\cdot\mathbf{v}(0)\rangle}\,dt \qquad \text{(III.14)}$$

$$B(t) = \frac{3kT}{m}\left[2\int_0^t \Gamma_v(t)\,dt - \Gamma_v^2(t)\right] \qquad \text{(III.15)}$$

To obtain $G_s(\mathbf{r},t)$ we must average over all initial $\mathbf{v}(0)$ values so that

$$G_s(\mathbf{r},t) = \left[\frac{3}{2\pi B(t)}\right]^{3/2} \exp\left[-\frac{3|\mathbf{r}(t)|^2}{2B(t)}\right] \qquad \text{(III.16)}$$

Equation (III.16) links $G_s(\mathbf{r},t)$ directly to $C_v(t)$. In classical Brownian translational theory, $C_v(t) = \exp(-\beta t)$, so

$$\Gamma_v(t) = (1-\exp(-\beta t))/\beta$$

and

$$B(t) = \frac{3kT}{m\beta^2}(2\beta t + 4e^{-\beta t} - e^{-2\beta t} - 3)$$

in agreement with the calculations of Uhlenbeck and Ornstein.[104] In our case the equivalent expressions are

$$\Gamma_v(t) = x_0\left[1-\exp(-\alpha_1 t)(\cos\beta t + x_1 \sin\beta t) + x_2(1-\exp(-\alpha_2 t))\right]$$

where

$$x_0 = \frac{2\alpha_1 + \Gamma\alpha_2}{(1+\Gamma)(\alpha_1^2+\beta^2)} \qquad x_1 = \frac{\alpha_1^2 - \beta^2 + \Gamma\alpha_1\alpha_2}{\beta(2\alpha_1+\Gamma\alpha_2)} \qquad x_2 = \frac{\Gamma(\alpha_1^2+\beta^2)}{\alpha_2(2\alpha_1+\Gamma\alpha_2)}$$

1. *Probability Density Functions from (III.11)*

Without loss of generality one may consider for purposes of computation the behavior of the ith component ($i = 1,2,3$) of (III.11), which may be written[105] in the matrix form

$$\dot{\mathsf{X}}(t) = \mathsf{A}\mathsf{X}(t) + \mathsf{B}\dot{\mathsf{W}}_i(t) \qquad \text{(III.17)}$$

where

$$\mathsf{A} = \begin{bmatrix} 0 & 0 & 1 & 0 \\ 0 & 0 & 0 & 1 \\ -\omega_0^2 & \omega_0^2 & 0 & 0 \\ \Omega_0^2 & -\Omega_0^2 & 0 & -\beta \end{bmatrix} \qquad \mathsf{B} = \begin{bmatrix} 0 \\ 0 \\ 0 \\ 1 \end{bmatrix} \qquad \mathsf{X} = \begin{bmatrix} X_1 \\ X_2 \\ X_3 \\ X_4 \end{bmatrix} = \begin{bmatrix} R_i \\ r_i \\ \dot{R}_i \\ \dot{r}_i \end{bmatrix}$$

Here

$$\Omega_0^2 = (m_1/m)\omega_0^2 \qquad \mathbf{R} = \mathbf{q}$$

Equation (III.17) may be solved formally to give

$$\mathsf{X}(t) = (\exp \mathsf{A}t)\mathsf{X}_0 + \int_0^t \exp\left[\mathsf{A}(t-\tau)\right]\mathsf{B}\xi(d\tau) \qquad \text{(III.18)}$$

with

$$W_i(t_2) - W_i(t_1) = \xi(t_2 - t_1)$$

The van Hove function may be calculated from (III.17) and (III.18) by virtue of the fact that it is the Gaussian probability density function of $X_1(t)$. Thus

$$G_s(X_1,t) = \left[\frac{3}{2\pi\langle Y_1^2(t)\rangle}\right]^{3/2} \exp\left[-\frac{3Y_1^2(t)}{2\langle Y_1^2(t)\rangle}\right] \qquad \text{(III.19)}$$

It turns out from the formal solution, (III.18), that

$$Y_1(t) = \int_0^t \omega_0^2 \int_0^{t-\tau} g_2(u)\,du\,\xi(d\tau)$$

so that

$$\langle Y_1^2(t)\rangle = \omega_0^4 C^2 \int_0^t \left[\int_0^{t-\tau} g_2(u)\,du\right]^2 d\tau$$

with

$$g_2(t) = \left[(\alpha_1-\alpha_2)^2 - \beta^2\right]^{-1}\left[\frac{(\cos\beta t - (\alpha_2-\alpha_1)\sin\beta t)}{\beta} e^{-\alpha_1 t} - \exp(-\alpha_2 t)\right]$$

The constant C^2 is deduced from the limit at long times of (III.19).

2. *Comparisons with Molecular Dynamics. Simulations of N_2*

The atom-atom computed force, velocity, speed, and direction of velocity autocorrelation functions are shown in Fig. 53 along with the least-mean-squares best fits for the force, ($m\dot{\mathbf{v}}$) acf's calculated from (II.39) with ω_0^2, Ω_0^2, and γ as variables (Table VIII).

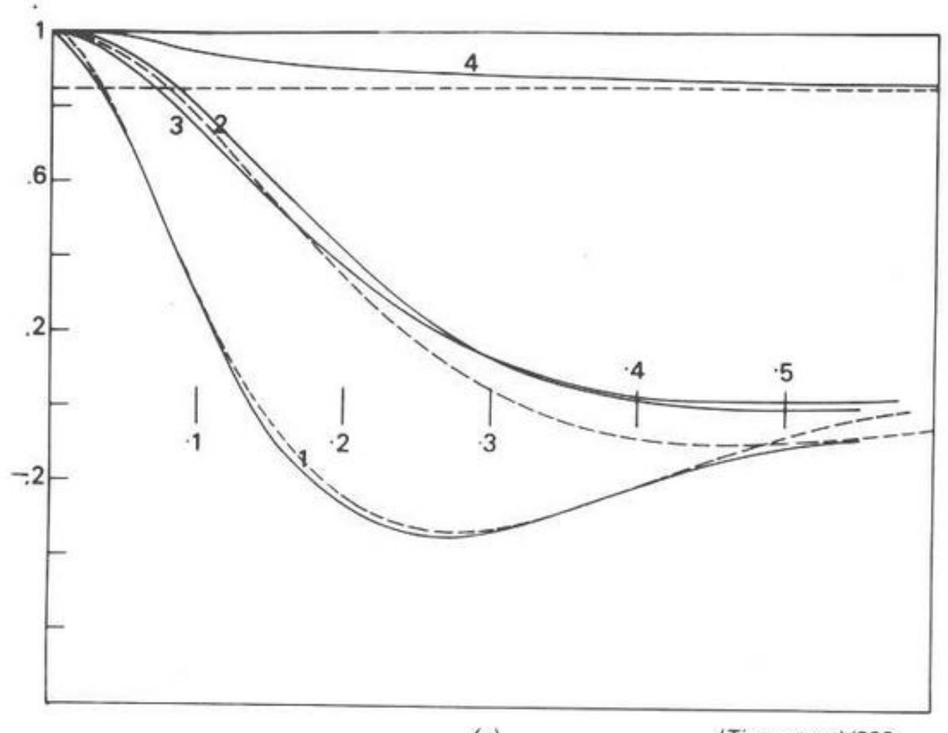

(a) (Time steps)/200

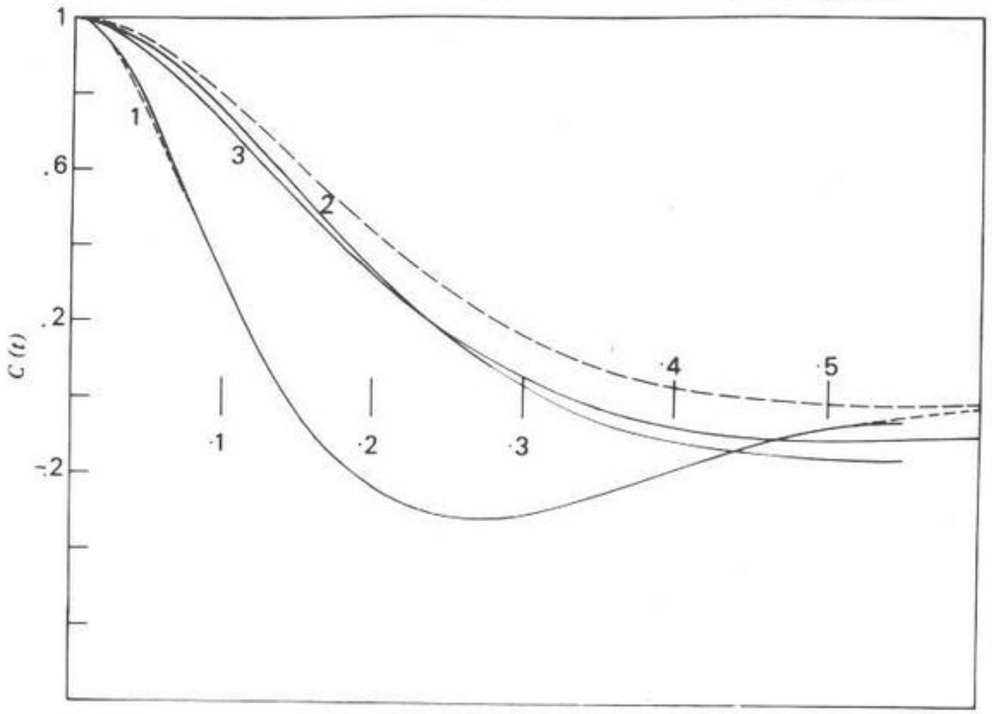

(b)

Fig. 53. (*a*) (—), (1) Atom–atom simulation of the force acf $C_F(t)$ for a reduced interatomic separation, L^* of 0.1. (—), (2) Simulated velocity acf. (—), (3) Simulated direction of velocity acf. (—), (4) Simulated speed acf, the horizontal line is at $8/(3\pi)$. (----), (1) Least-mean-squares best fit of the itinerant oscillator to the simulated $C_F(t)$. (----), (2) $C_o(t)$ (itinerant oscillator), calculated with the ω_o^{2*}, Ω_o^{2*}, and γ^* estimated by fitting $C_F(t)$. (*b*) $L^*=0.3$; (*c*) $L^*=0.5$; (*d*) $L^*=0.7$. Ordinate: $C(t)$; abscissa: (time steps)/200. [Reproduced by permission from *J. Mol. Struct.*, **46**, 395 (1978).]

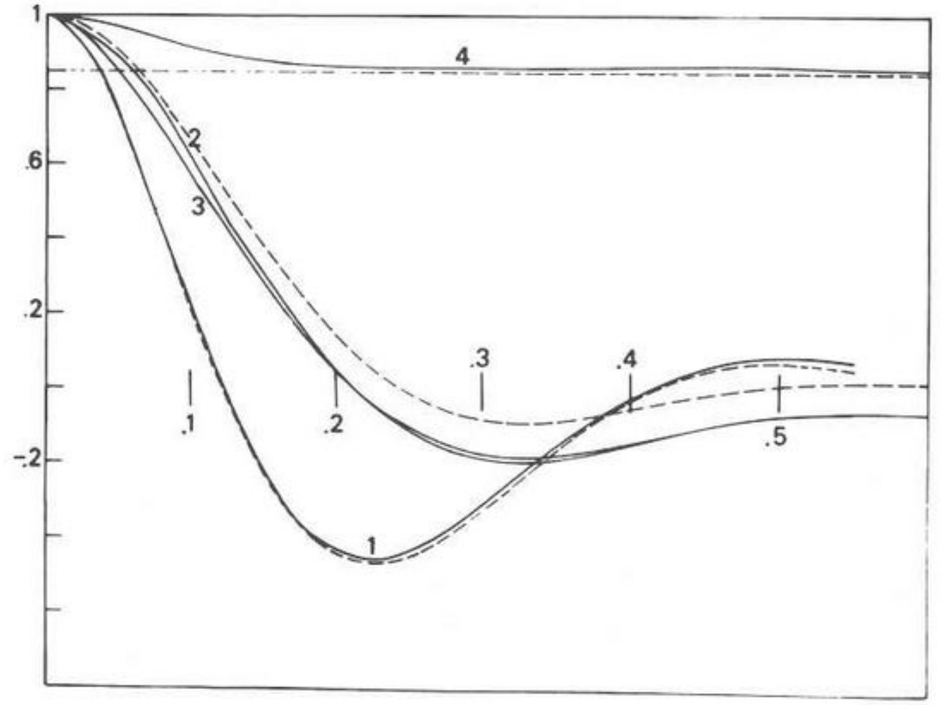

(c) (Time steps)/200

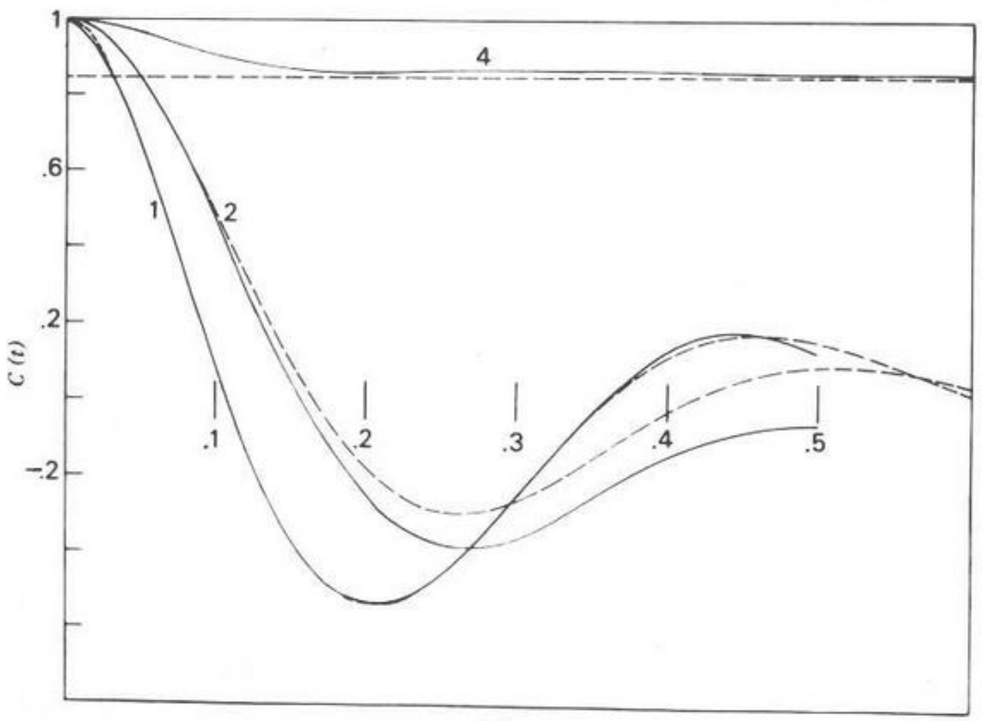

(d)

Fig. 53. Continued

TABLE VIII
Parameters for Least-Mean-Squares Best Fit to Molecular Dynamics Data of $C_F(t)$ ($\rho^* = 0.64$, $T^* = 2.3$)

L^*	ω_0^{2*}	Ω_0^{2*}	γ^*
0.1	56.5	313.9	38.6
0.3	47.8	263.3	29.1
0.5	80.6	213.3	21.4
0.7	127.9	250.6	30.8

ω_0^{2*}, Ω_0^{2*}, and γ^* are in reduced units. Velocity spectra are compared with those simulated by Berne and Harp[25] (on carbon monoxide), and Rahman (on argon) in Fig. 54. From the formal equivalence of $C_v(s), \omega_0^2$ is proportional to the mean-square force, computed as $\langle F^2 \rangle$ using the atom–atom algorithm. This is tested in Fig. 55, where the simulated $\langle F^2 \rangle$ is plotted against ω_0^2 obtained by fitting $C_F(t)$. The overall trend is similar, but ω_0^2 increases the more rapidly as L^* lengthens (i.e., the more anisotropic the intermolecular potential becomes).

Figure 54 shows the least-mean-square best fit to the velocity acf computed for liquid argon in the 864-particle simulation of Rahman. The extended negative tail (or low-frequency peak in the velocity power spectrum) is not reproduced by the itinerant oscillator. The so-called hydrodynamic tail is a decay from the positive side of the $C_v(t)$ axis, and difficult to measure in comparison with the extended negative portion. This is found again in the CO simulation (Fig. 54) and may be discerned (Figs. 53*a* and 53*d*) in the atom–atom $C_v(t)$. In contrast (Fig. 54*d*), the angular velocity acf and power spectrum for CO are fitted more closely overall by the itinerant librator (tractable only in two dimensions). The simulated and analytical mean square forces are plotted in Fig. 55 as a function of L^*.

The parameters obtained from the least-mean-squares best fit to Rahman's $C_v(t)$ are used in Fig. 56 to match the mean-square displacement, defined by

$$\langle \Delta_r^2 \rangle = 2 \int_0^t (t - \tau) \langle \mathbf{v}(\tau) \cdot \mathbf{v}(0) \rangle \, d\tau \qquad \text{(III.20)}$$

simulated by Rahman, and also the $G_s(\mathbf{r}, t)$ derived experimentally by Dasannacharya and Rao,[103] using incoherent, inelastic, thermal neutron scattering.

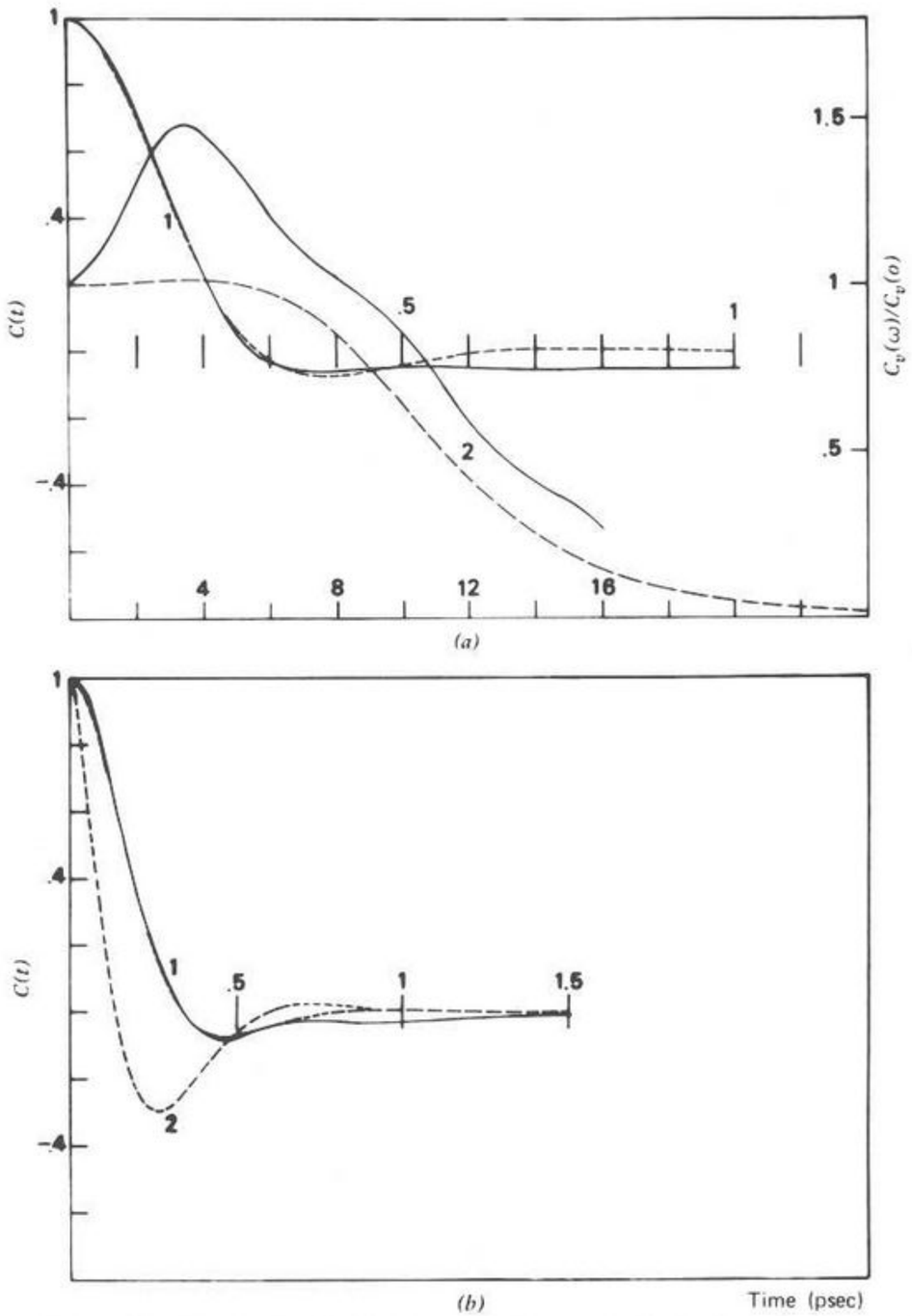

Fig. 54. (*a*) (—), (1) Berne and Harp computed velocity acf for CO. (—), (2) Computed, velocity power spectrum. (----), (1) Itinerant oscillator least-mean-squares best fit to the velocity acf. (---), (2) Corresponding normalized velocity power spectrum. Ordinates: left—$C(t)$; right—$C_v(\omega)/C_v(o)$. Abscissas: top, time (psec); bottom, frequency (THz). (*b*) (—), Rahman $C_v(t)$, simulated for liquid argon by Rahman. (----), (1) Itinerant oscillator, best fit. (---), (2) $C_F(t)$ estimated from the $C_v(t)$ best fit. Ordinate: $C(t)$; abscissa: time (psec). (*c*) (—), Rahman-simulated, normalized, velocity, power spectrum. (---), (1) Velocity power spectrum calculated from the itinerant oscillator best fit to $C_v(t)$ (Fig. 53). (---), (2) Itinerant oscillator normalized force spectrum. Ordinate: intensity; abscissa: frequency (THz). (*d*) (—), (1) Berne and Harp simulated angular velocity acf for liquid CO. (---), (1) Best fit to (1) of the itinerant librator in a plane. (—), (2) Simulated normalized angular velocity power spectrum. (----), (2) Itinerant oscillator normalized power spectrum calculated from fitting the acf. Ordinates: left—$C_\omega(t)$; right—$C_\omega(\omega)/C_\omega(o)$; abscissas: top, time (psec); bottom, ω (THz).

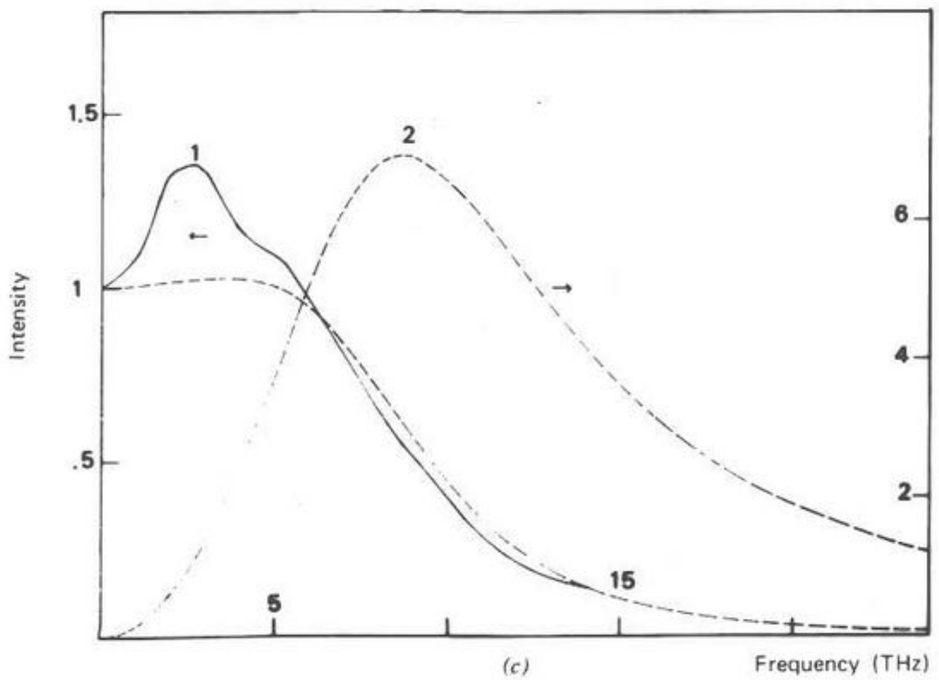

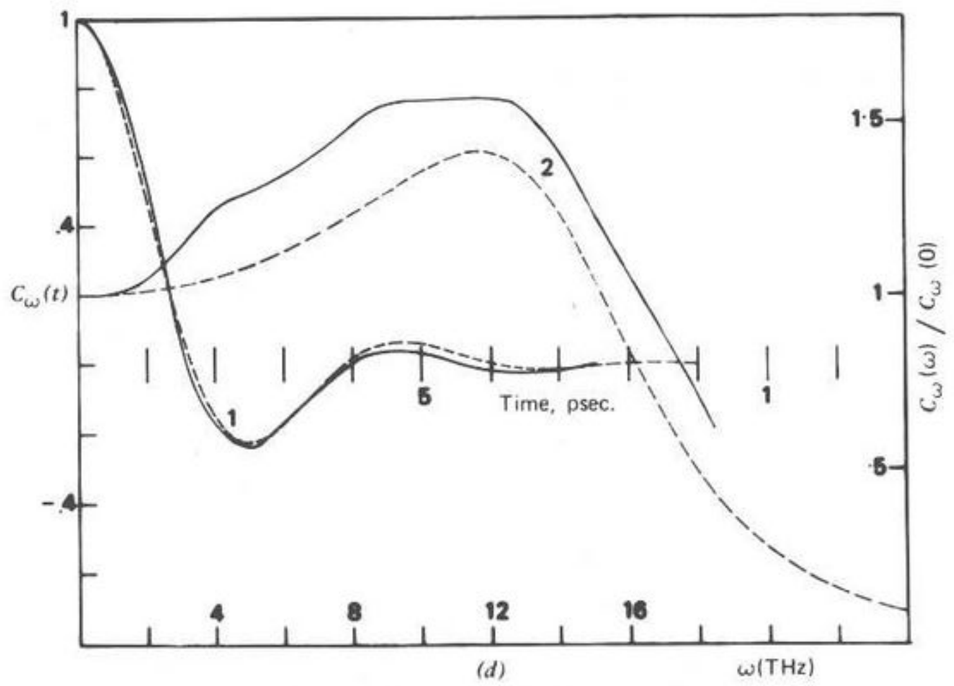

Fig. 54. Continued

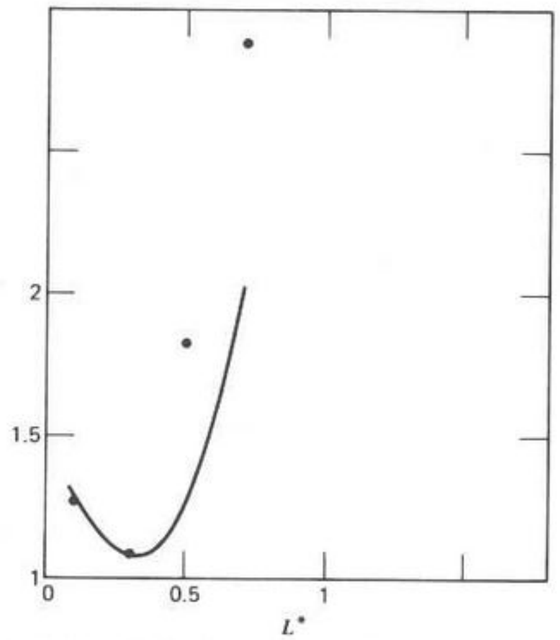

Fig. 55. Plot of (—), $\langle F^2 \rangle$ and (●), ω_0^2 vs. L^* normalized at $L^*=0.3$. [Reproduced by permission from *J. Mol. Struct.*, **46** (1978).]

In Section I it is of interest to know whether the Wiener process is, in fact, a justifiable statistical representation of random force and velocity. We adopt the method of computing acf's of moments of velocity and force to investigate this further. For example, the second moment of velocity (or kinetic energy) acf,

$$C_{2v}(t)=\langle v^2(t)v^2(0)\rangle/\langle v^4(0)\rangle$$

should be related to $C_v(t)$ by

$$C_{2v}(t)=\tfrac{3}{5}\left[1+\tfrac{2}{3}C_v^2(t)\right] \qquad \text{(III.21)}$$

where the probability density function of velocities is Gaussian. Similarly,

$$C_{4v}(t)=\left(225+600C_v^2(t)+120C_v^4(t)\right)/945 \qquad \text{(III.22)}$$

and so on, as evaluated by Berne and Harp. The functions $C_{2v}(t)$ and $C_{4v}(t)$ are calculated analytically using the atom-atom $C_F(t)$ to optimize ω_0^2, and Ω_0^2, and γ. They can also be simulated independently using the atom-atom algorithm, and the two sets of functions are compared in Fig. 57.

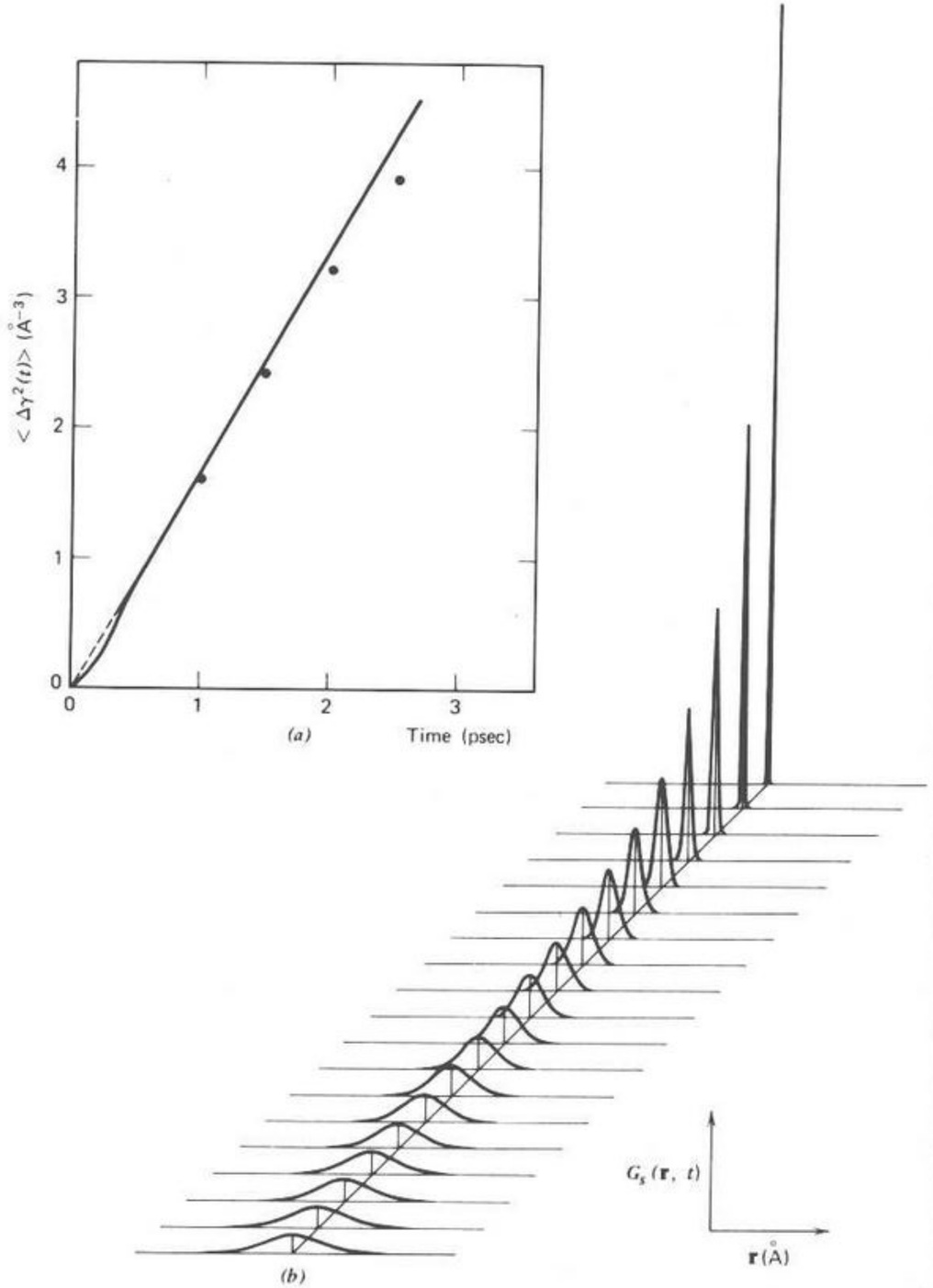

Fig. 56. (*a*) Plot of mean-square displacement. (—) $\langle \Delta r^2(t) \rangle$ calculated from the itinerant oscillator fitting to Rahman's $C_v(t)$. ●, Mean-square displacements computed independently by Rahman. Ordinate: $\langle \Delta r^2(t) \rangle$ (Å); abscissa: time (psec). (*b*) Plot of $G_s(r,t)$ calculated for the itinerant oscillator from fitting the Rahman $C_v(t)$ function. Ordinate: $G_s(r,t)$ ($\mathring{A}^{-3}$); abscissa: r (Å). [Reproduced by permission from *J. Mol. Struct.*, **46** (1978).]

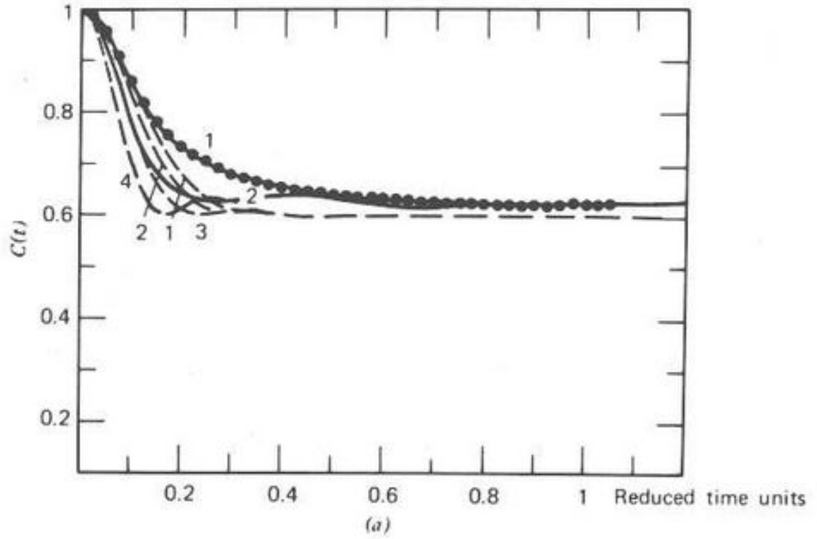

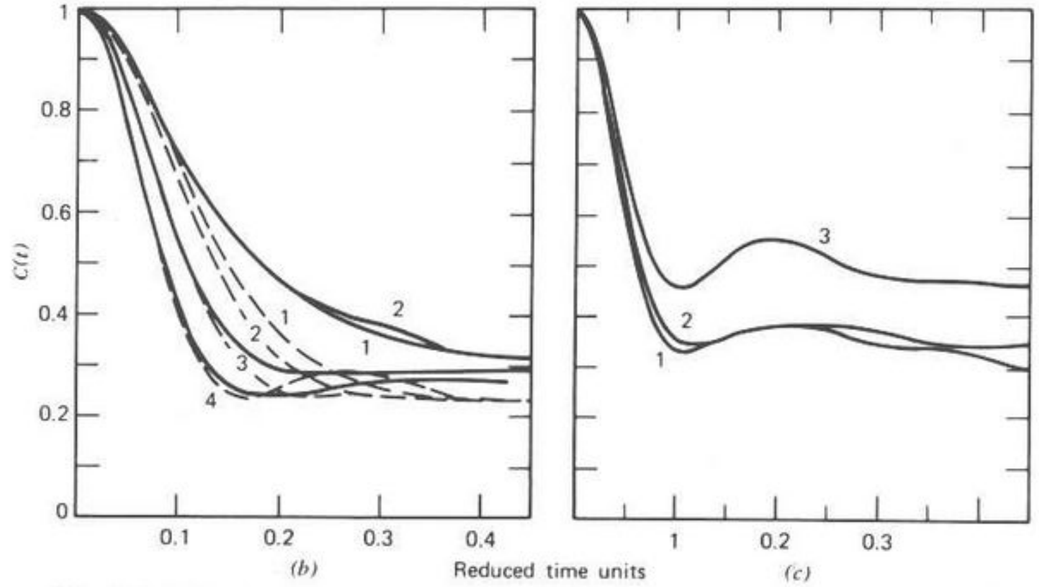

Fig. 57. (*a*) Kinetic-energy acf's. (—), (1) $L^* = 0.1$ Atom–atom simulation: (—) (2) $L^* = 0.5$; (OOO), (1) $L^* = 0.3$. Itinerant oscillator, calculated from fitting $C_F(t)$: (----), (1) $L^* = 0.1$; (2) $L^* = 0.3$; (3) $L^* = 0.5$; (4) $L^* = 0.7$. The horizontal line represents the Gaussian limit. Ordinate: $C(t)$; abscissa: reduced time units. (*b*) As for (*a*), $C_{4v}(t)$. (*c*) $\langle F^2(t)F^2(0) \rangle / \langle F^4(0) \rangle$, atom–atom potential. (1) $L^* = 0.1$; (2) $L^* = 0.3$; (3) $L^* = 0.5$. Ordinate: $C(t)$; abscissa: time steps. [Reproduced by permission from *J. Mol. Struct.*, **46**, (1978).]

In the classical theory of uncoupled translational Brownian motion, $C_v(t)$ decays exponentially,[104] and is therefore incapable of reproducing any negative parts of the computed velocity acf's. Further, in the classical case the mean-square force is not defined, since $\exp(-\gamma|t|)$ is not differentiable at the origin. Not only is $\langle F^2 \rangle$ well defined (through ω_0^2) in itinerant oscillation, but also $C_F(t)$ can be followed, by optimizing ω_0^2, Ω_0^2, and β as L^*, the interatomic distance is increased (Fig. 53). As L^* increases, both $C_F(t)$ and $C_v(t)$ become markedly oscillatory, such being the case also for the acf of the direction of velocity, while in contrast the speed acf (that of $|\mathbf{v}|$) consistently and quickly decays to its theoretical long-time value of $8/(3\pi)$. The similarity between $C_v(t)$ and the acf of velocity direction favors theories with a constant-speed approximation, as was pointed out by Berne and Harp, who first suggested this type of simulation.

Knowing $C_F(t)$ analytically means that $C_v(t)$, $\langle \Delta r^2(t) \rangle$, and $G_s(\mathbf{r},t)$ may be calculated and compared with those independently computed or measured experimentally. In Fig. 53 this is done for $C_v(t)$, and it can be seen that there is a consistent small difference between the simulated $C_v(t)$ and that calculated from the optimized $C_F(t)$, although the main features are similar. At $L^*=0.3$ and $L^*=0.5$ there are indications of negative long-time tails in the simulated $C_v(t)$. This tail is well defined for CO and argon, and causes low-frequency peaks in the velocity power spectra which are not reproduced by itinerant oscillation as treated analytically in this paper. Damle and others[29] have obtained agreement with Rahman's velocity spectrum with a six-parameter model of itinerant oscillation with two friction coefficients, two fluctuating forces **A** and **B**, and thus two memory functions corresponding to $\langle \mathbf{A}(t)\cdot\mathbf{A}(0) \rangle$ and $\langle \mathbf{B}(t)\cdot\mathbf{B}(0) \rangle$, respectively, the latter being assumed exponential or Gaussian. In either case two parameters were needed for their definition. Equations (III.11) compose a zeroth-order approximant of the Damle et al. equations, but with fewer parameters. Both treatments neglect the cross-correlation in the total velocity correlation function as distinct from the autocorrelation function. This is tantamount to a neglect of intermolecular dynamical coherence, embodied in $G_d(\mathbf{r},t)$ the distinct van Hove correlation function, which is the probability of finding *another* particle at **r** given one at the origin initially.

Light- and neutron-scattering experiments are interpretable generally in terms of the sum

$$G_s(\mathbf{r},t)+G_d(\mathbf{r},t)=\frac{1}{n}\langle n(\mathbf{r},t)n(\mathbf{0},0)\rangle$$

where the time-dependent particle density $n(\mathbf{r},t)$ is given by

$$n(\mathbf{r},t)=\sum \delta(\mathbf{r}-\mathbf{r}_i(t))$$

and it is never straightforward to separate $G_s(\mathbf{r},t)$, usually estimated on a molecular basis, from $G_d(\mathbf{r},t)$ estimable on a hydrodynamic basis. However, this has been attempted experimentally for liquid argon at 84.5°K and therefrom found to be Gaussian within the uncertainty. The Rahman simulations of $C_v(t)$ is carried out at 94.4°K, but it is instructive to compare $G_s(\mathbf{r},t)$ calculated from the itinerant oscillator fitting to $C_v(t)$ at 94.4°K with the $G_s(\mathbf{r},t)$ estimated at 10°K lower. The results are illustrated in Fig. 56. The mean-square displacement is reproduced well, but this is in any case rather insensitive to environmental effects on molecular motion compared with van Hove's functions. The overall features of the experimental $G_s(\mathbf{r},t)$ are reproduced [e.g., the itinerant oscillator decays to zero at about the same **r** values for given t, but the experimental $G_s(\mathbf{r},t)$ is always much the larger in magnitude]. The greatest difference is at $t=0.1$ psec, where the experimental $G_s(\mathbf{r},t)$ is 27 Å^{-3} at $\mathbf{r}=0$ and the itinerant oscillator about 6.5 Å^{-3}.

Rahman[97] has demonstrated that the simulated $G_s(\mathbf{r},t)$ in argon displays an initial non-Gaussian behavior lasting until 10 psec, and in the atom–atom simulation of Fig. 57 it seems that up to 200 or more time steps (ca. 1 psec) the Gaussian limit in $C_{2v}(t)$, 0.6, is not reached. This is confirmed in Fig. 57*b*, where the simulated $C_{4v}(t)$ does not reach its equivalent limit of 0.2381. In Fig. 57*c* the acf $\langle F^2(t)F^2(0) \rangle / \langle F^4(0) \rangle$ is displayed for $L^*=0.1$, 0.3 and 0.5, and it is clear that no common, single-valued (or

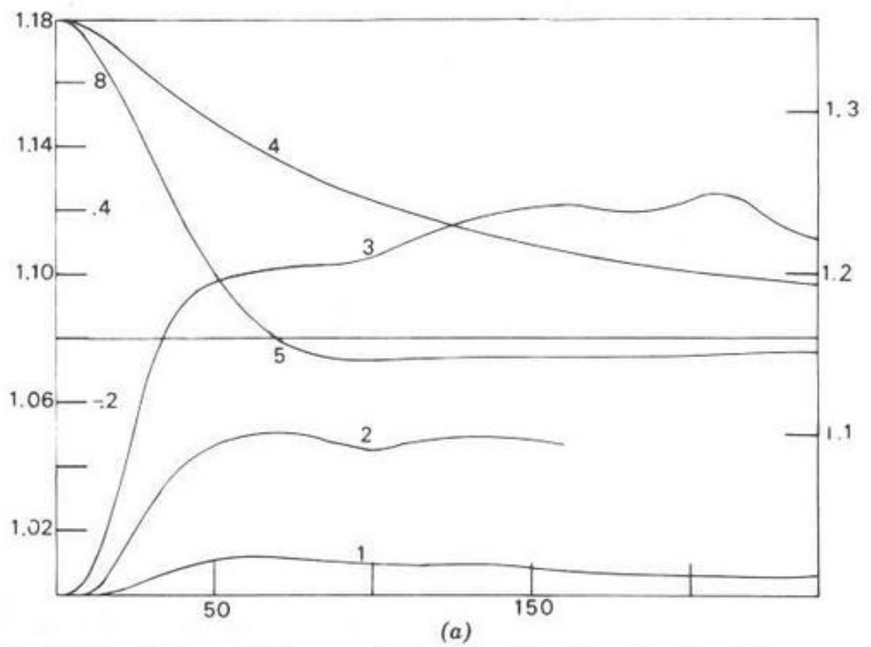

(*a*)

Fig. 58. Rotation–translation speed-correlation functions for $T^*=2.32$, $p^*=0.643$. (1) $\frac{\langle|v(0)||\omega(t)|\rangle}{\langle|v(0)||\omega(0)|\rangle}$; (2) $\frac{\langle v^2(0)\cdot\omega^2(t)\rangle}{\langle v^2(0)\cdot\omega^2(0)\rangle}$; (3) $\frac{\langle v^4(0)\cdot\omega^4(t)\rangle}{\langle v^4(0)\cdot\omega^4(0)\rangle}$; (4) $\frac{\langle v(0)\cdot v(t)\rangle}{\langle v(0)\cdot v(0)\rangle}$; (5) $\frac{\langle \omega(0)\cdot\omega(t)\rangle}{\langle \omega(0)\cdot\omega(0)\rangle}$. (*a*) $L^*=0.200$; (*b*) $L^*=0.2392$ (N_2); (*c*) $L^*=0.500$. In (*a*) to (*c*), all curves are computed averaging over 1500 times steps.

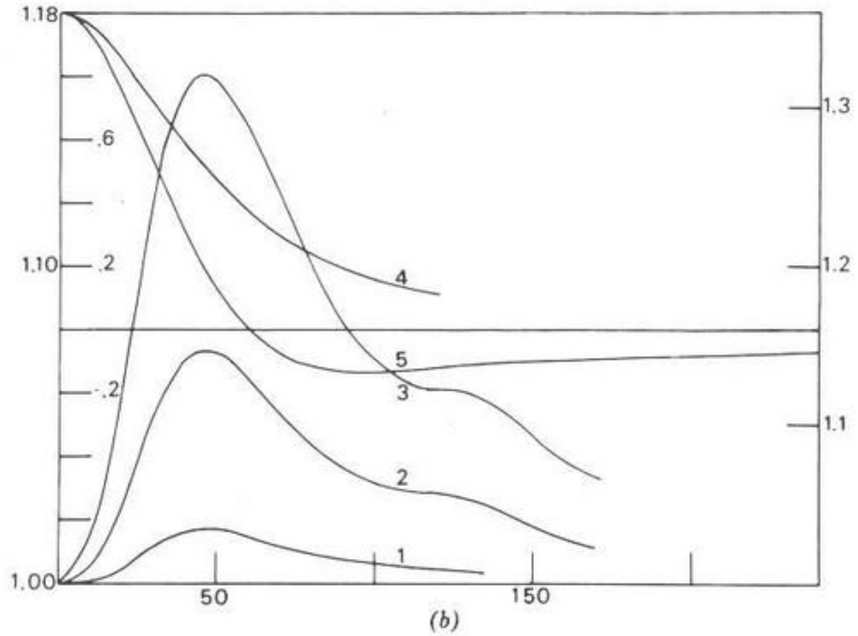

(b)

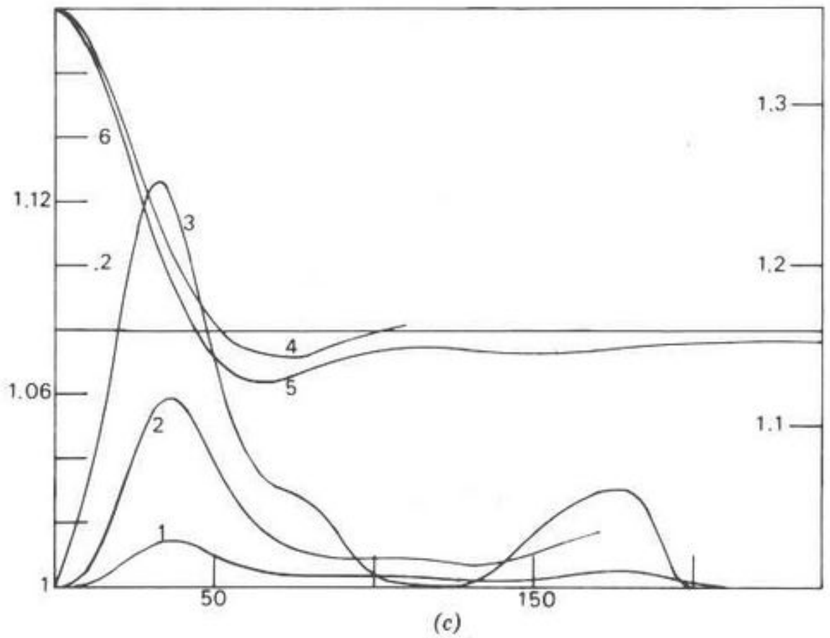

(c)

Gaussian) long-time limit is arrived at among these three potentials. Thus generally it seems that $\mathbf{v}, \mathbf{f}$ (the projected force), and $G_s(\mathbf{r}, t)$ are non-Gaussian variates, as well as being non-Markovian, even in atomic fluids. The analytical treatment of such behavior is, of course, more difficult and compounded by rotation/translation coupling (Fig. 58) and short time effects (Fig. 59).

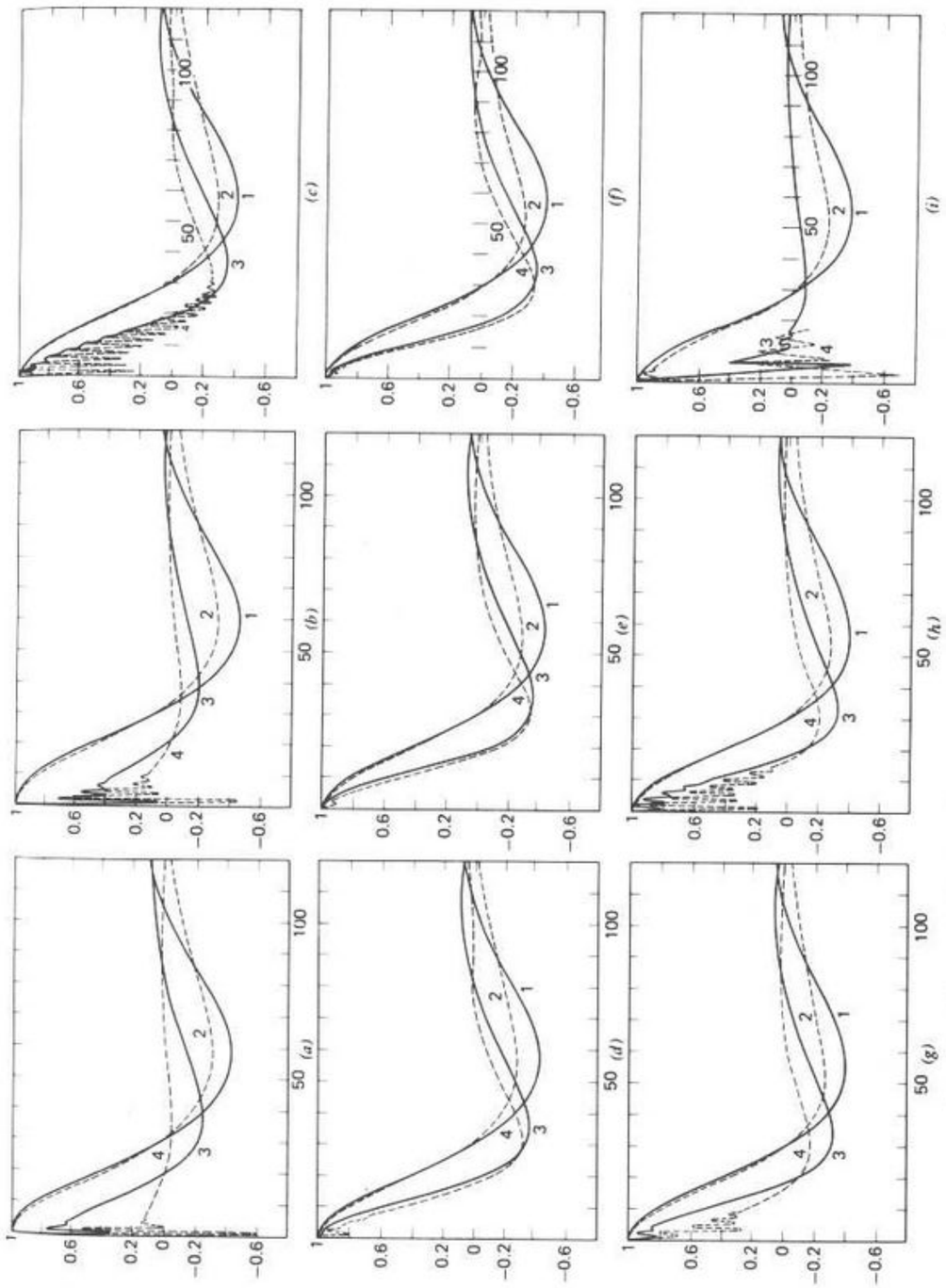

Fig. 59. Autocorrelation functions $C_1(t)$ to $C_4(t)$ for constant $p^* = 0.696$, varying T^* at $d^* = 0.3292$ (N_2). The acf's above are labeled: (1) $C_1(t)$; (2) $C_2(t)$; (3) $C_3(t)$; (4) $C_4(t)$. (*a*) $T^* = 1.50$; (*b*) $T^* = 1.55$; (*c*) $T^* = 1.60$; (*d*) $T^* = 1.65$; (*e*) $T^* = 1.70$; (*f*) $T^* = 1.75$; (*g*) $T^* = 1.80$; (*h*) $T^* = 1.85$; (*i*) $T^* = 2.00$. [Reproduced by permission from *Mol. Phys.*, **33**, 1805 (1977).]

3. *Translations in Glassy, or Amorphous, Nitrogen*

By using a reduced density $\rho^* = 0.80$ and a reduced temperature $T^* = 2.00$, nitrogen may be simulated in a metastable solid state induced by kilobars of external pressure at a temperature beyond the normal melting point. In this case $G_s(\mathbf{r},t)$ is markedly non-Gaussian, as expressed by non-zero values of $a_n(t)$, defined by

$$a_n(t) = \frac{\langle [\mathbf{r}(t) - \mathbf{r}(0)]^{2n} \rangle}{\alpha_n \langle [\mathbf{r}(t) - \mathbf{r}(0)]^2 \rangle^n} - 1 \qquad \text{(III.23)}$$

where $\alpha_n = (2n+1), \ldots, 5.3.1/3^n$. The link with the van Hove function is

$$\langle [\mathbf{r}(t) - \mathbf{r}(0)]^{2n} \rangle = \int r_1^{2n} G_s(\mathbf{r}_1, t)\, d\mathbf{r}_1$$

$$\equiv \frac{1}{N} \sum_{i=1}^{N} [\mathbf{r}_i(t) - \mathbf{r}_i(0)]^{2n}$$

where $\mathbf{r}_1 = \mathbf{r}(t) - \mathbf{r}(0)$. Berne and Harp, in their simulation of CO with a modified Stockmayer potential, found $a_n(t)$ to be moderately sensitive to variations in N, the number of molecules used. $a_n(t)$ become less significant as N is changed from 256 to 500 or thereabouts. Accordingly, it is expected that our simulation would overstress these deviations [of $a_n(t)$ from zero] to an unspecified extent. Further, it is difficult to estimate the effect of our periodic boundary conditions on these functions. Berne[106] has discussed their effect on long tails in the autocorrelation of angular velocity. The complicated dependence of $a_n(t)$ $(n = 2,3,4)$ upon time (from an arbitrary $t = 0$) (Fig. 60) is not correlated with statistical noise in the ratio of rotational to translational kinetic energy, as illustrated in Fig. 60. It would be difficult to follow these analytically with the techniques available at present except perhaps in the case of computer argon and other atomic fluids where the curves $a_n(t)$ are simpler in overall form.

The mean-square displacement of argon atoms as simulated by Rahman[97] is reproduced satisfactorily by a process of itinerant oscillation (Fig. 56), but Fig. 61 shows clearly that the rate of diffusion in the glass is far too high analytically. This analytical rate is again calculated by a least-mean-squares best fit to the force correlation function. Only at times close to the start are the simulated and analytical functions similar; thereafter the former flatten out and increase only slowly with a tendency to oscillate as in a clathrate solid. It seems therefore that an improved rototranslational itinerant oscillation model should be capable of taking this high-density behavior in the glass in its stride. The rotational constraints are clearly discernible in Fig. 62, where elongation of interatomic distance is

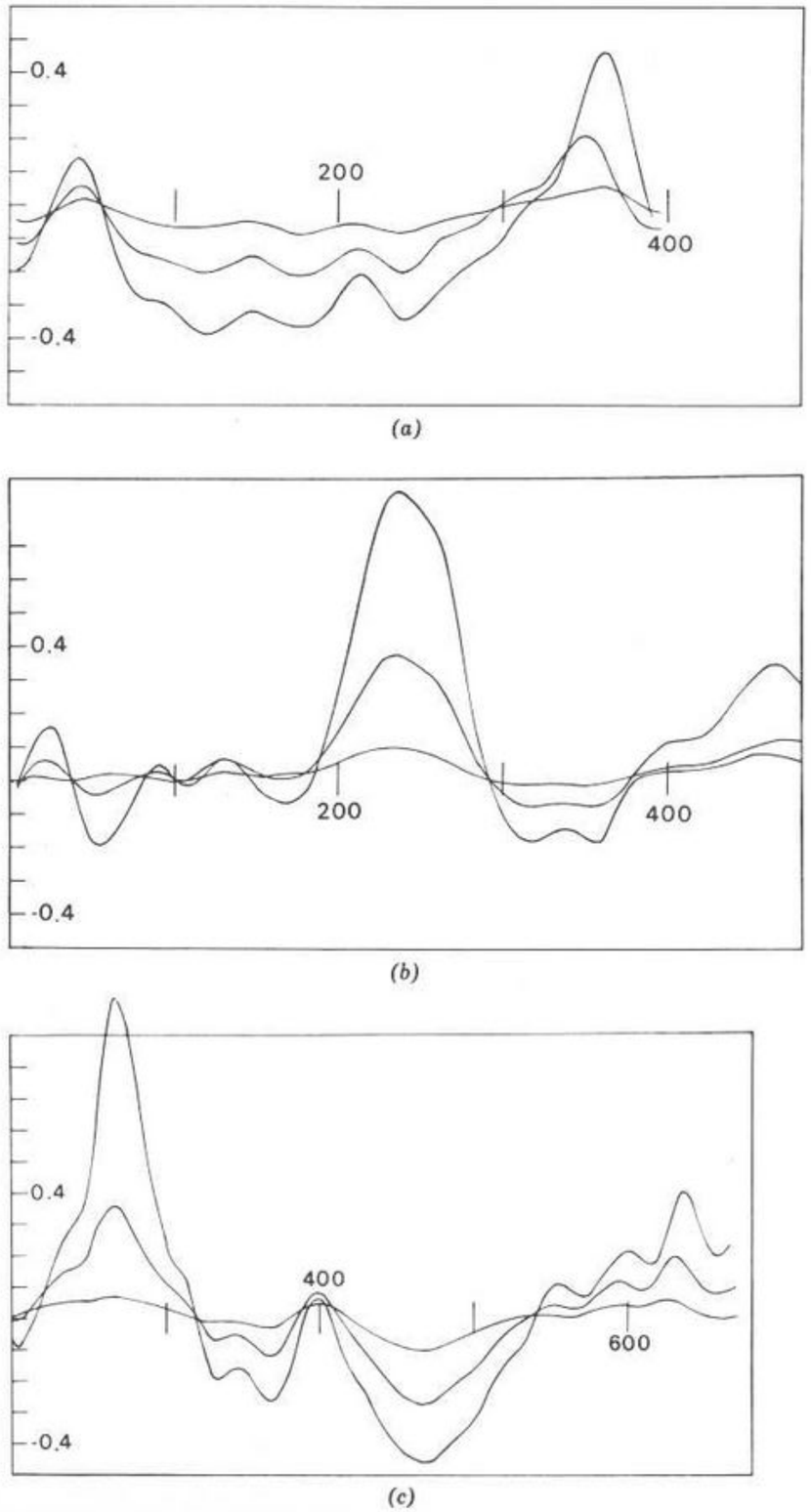

Fig. 60. (*a*) Plot of $a_n(t)$ (see text) for $n = 2,3,4$; $L^* = 0.200$. (*b*) As in (*a*) $L^* = 0.3292$. (*c*) As in (*a*) $L^* = 0.400$ (200 to 600 time steps). (*d*) As in (*a*) $L^* = 0.400$ (after rejecting 800 steps). (*e*) Ratio of kinetic to rotational energy. (—), After 800 steps; (---), 200 to 600 steps. Abscissas: (*a*) to (*e*), time steps (see text).

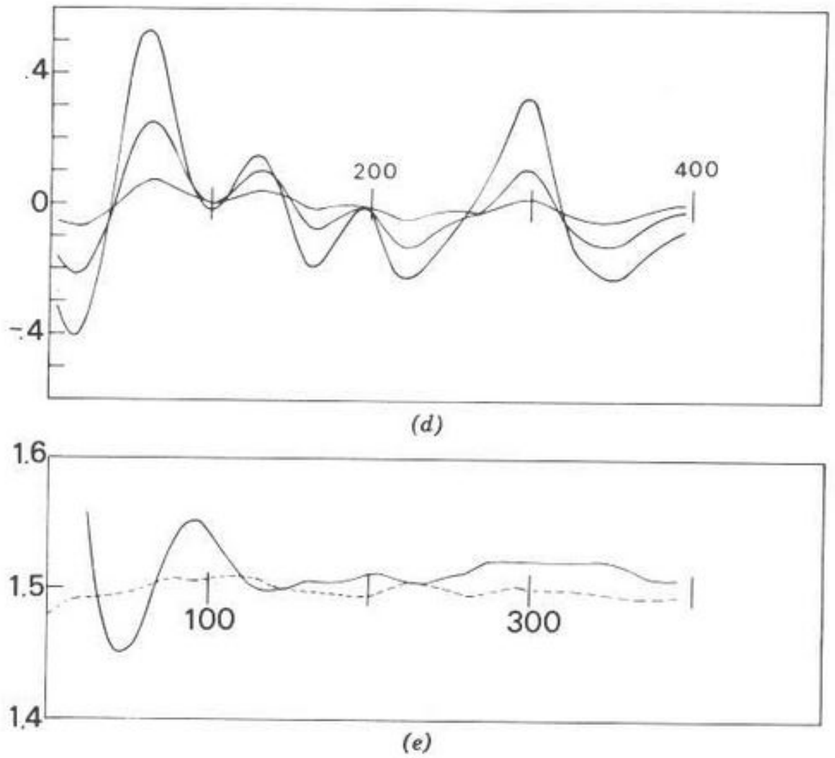

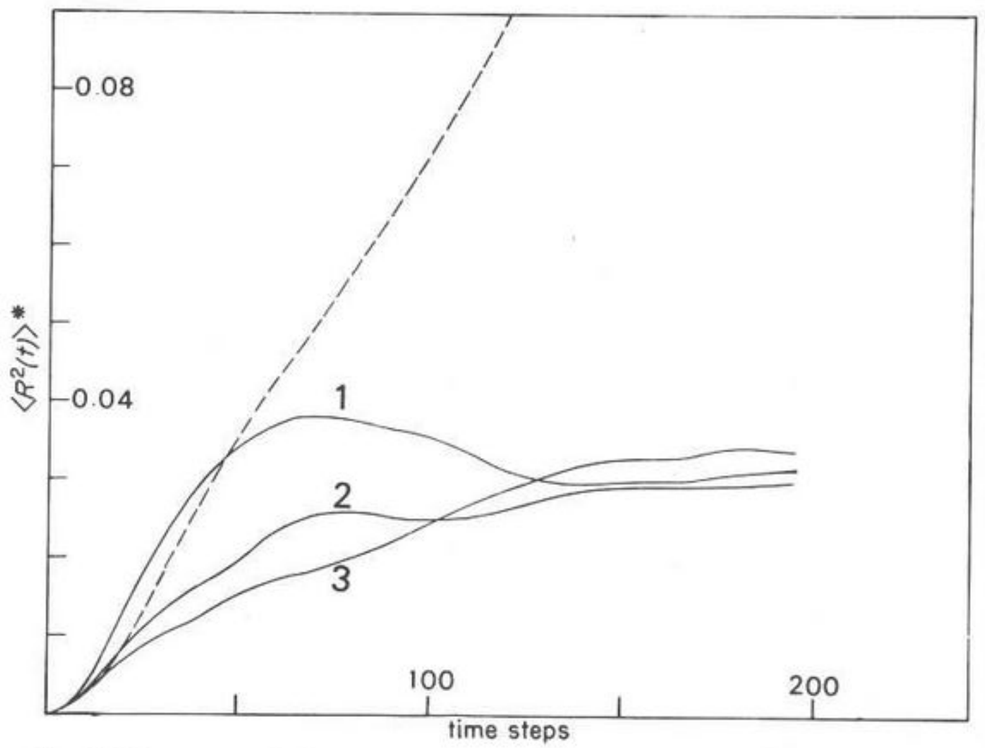

Fig. 61. Mean-square displacements. (—), (1) $L^* = 0.20$; (—), (2) $L^* = 0.3292$; (—), (3) $L^* = 0.40$. (—), (3) i.o. mean-square displacement calculated from the optimized $C_F(t)$. Ordinate: $\langle R^2(t)\rangle^*$; abscissa: time steps.

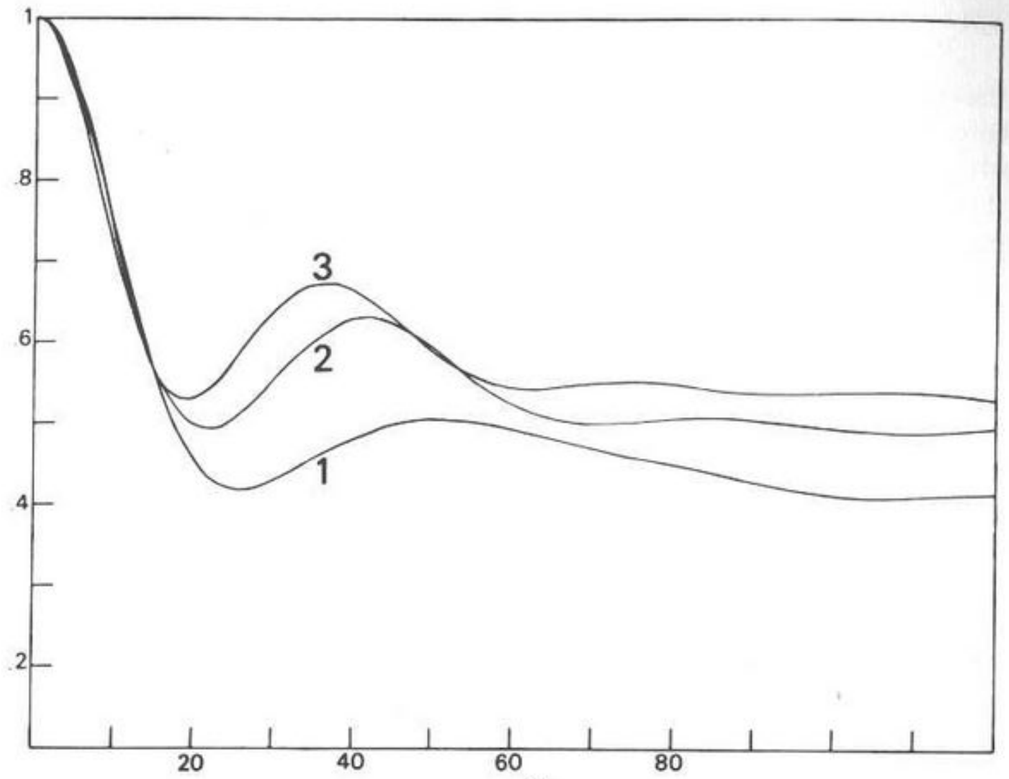

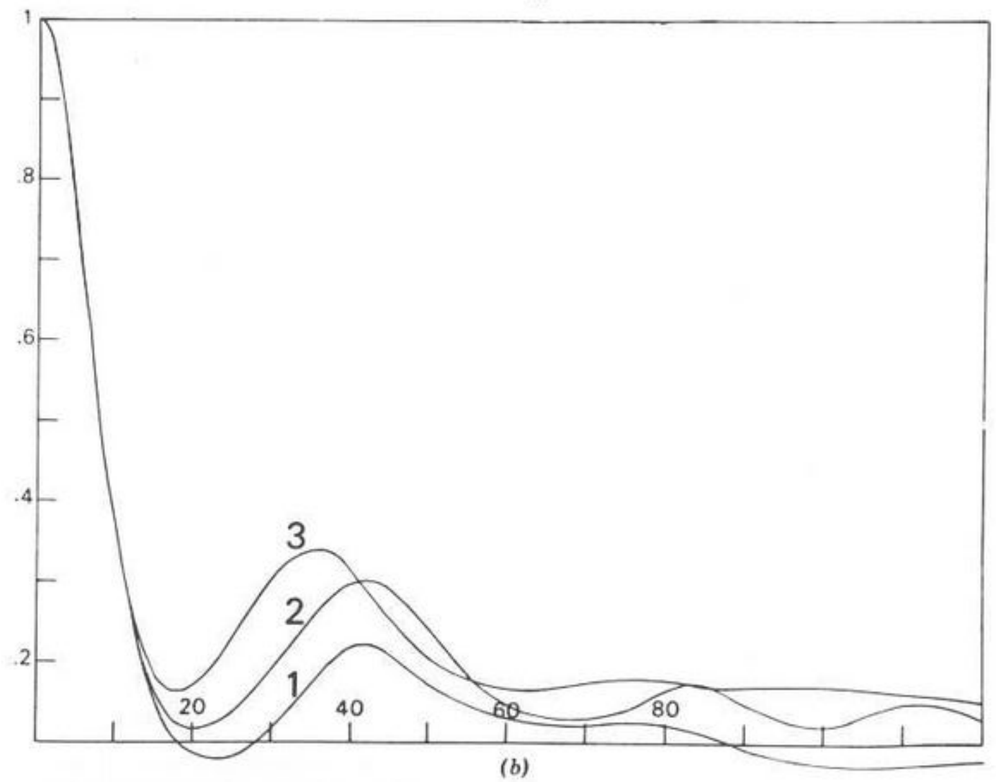

Fig. 62. (*a*) $\langle F^2(t)F^2(0)\rangle / \langle F^4(0)\rangle$; (*b*) $\langle F^4(t)F^4(0)\rangle / \langle F^8(0)\rangle$: (1) $L^* = 0.200$; (2) $L^* = 0.3292$; (3) $L^* = 0.400$. Abscissas: time steps.

the only variable. Figure 62*b* brings out the coupling through the fourth force moment acf, a function which for free translation falls at the time origin immediately to its long-time limit. The falloff is collision-free and thus the same for all elongations up to 10 time steps or so, but thereafter molecular interaction occurs and the three curves behave differently, even though ρ^* and T^* are identical for each. In fact, throughout Fig. 62 the constant long-time limits expected of Gaussian statistics are reached with difficulty (if at all) for both the second- and fourth-moment acf's of velocity and force. There is little doubt, however, that this is due in part to statistical noise in the averaging [e.g., the simulated $C_{4v}(t)$ function for $L^*=0.3292$ falls below the theoretical limit of 0.2381]. In other instances, however, these moment acf's behave similarly to those computed by Berne and Harp for CO, in that a limiting constant is reached at long times. Finally, it is clear that acf's of molecular speed must be conserved fairly well in any system [decaying, as they do, to only $8/(3\pi)$ of their initial value], but even here there are discernible effects of elongation on the translational motion, the decay being oscillatory and faster the longer the molecule. The influence of center-of-mass translation upon the rotational velocity in nitrogen and symmetrical diatomics may be simulated (so far only in the liquid) using the functions

$$\langle |\mathbf{v}(0)||\boldsymbol{\omega}(t)| \rangle \qquad \text{and} \qquad \langle \mathbf{v}^{2n}(0)\boldsymbol{\omega}^{2n}(t) \rangle$$

$n=1,2$, which are products of scalar quantities (speeds) which have no directive properties. These are illustrated in Fig. 58 for $L^*=0.2$, 0.3292 (N_2), and 0.50. Despite the statistical noise at $L^*=0.50$ (due to the similarity in the decays of $\langle \mathbf{v}(t)\cdot\mathbf{v}(0)\rangle/\langle \mathbf{v}(0)\cdot\mathbf{v}(0)\rangle$ and $\langle \boldsymbol{\omega}(t)\cdot\boldsymbol{\omega}(0)\rangle/\langle \boldsymbol{\omega}(0)\cdot\boldsymbol{\omega}(0)\rangle$ at longer times), it can be seen that the interaction is very sensitive to molecular elongation. $\langle \mathbf{v}(0)\cdot\boldsymbol{\omega}(t)\rangle$ and $\langle \mathbf{v}^{2n+1}(0)\cdot\boldsymbol{\omega}^{2n+1}(t)\rangle$ are zero for molecular symmetries such as those of N_2, but not necessarily so for lower symmetries (e.g., C_{2v}, the angular triatomic). As L^* shortens, the interaction functions are longer-lived and more featureless than those in the more pronounced dumbbell represented by N_2, where oscillatory features become more discernible. At $L^*=0.5$ there is a sharp surge of interaction at periodic intervals and the interaction functions are pronouncedly oscillatory.

We are in the course of investigating these simulation results with the stochastic Liouville equation in the Mori form by using the column vector $\begin{bmatrix} \mathbf{v} \\ \boldsymbol{\omega} \end{bmatrix}$ to evaluate the interaction-speed correlation functions using a truncated continued fraction. By forcing a fit between the theoretical and simulated autocorrelation functions of $\mathbf{v}$ and $\boldsymbol{\omega}$, we hope to reproduce, at least in outline, the interaction functions simulated here. Simulations will

then be extended to triatomic molecules of C_{2v} symmetry and the cycle repeated. In this way we hope to discern stochastic features in how the center-of-mass molecular translation affects $\langle \boldsymbol{\omega}(0)\cdot\boldsymbol{\omega}(t)\rangle$ and therefore the spectral functions

$$P_n\langle \mathbf{u}(t)\cdot\mathbf{u}(0)\rangle$$

in the case $\langle \mathbf{v}(0)\cdot\boldsymbol{\omega}(t)\rangle \neq 0$. This will enable us to check whether these latter are directly or indirectly sensitive to molecular translation, and if so, in what way. Are they, in the purist sense, rotational or strictly rototranslational? For which symmetries is it then valid to use a purely rotational stochastic Liouville equation? We hope to answer these fundamental questions aided by computer simulation.

C. Simulations of High-Derivative Autocorrelation Functions

In this section we investigate the time decay of correlation functions of high derivatives of position and orientation. This is necessary because the equilibrium (zero-time) values of successive memory functions $K_n(t)$ are defined in terms of

$$C^{(n)}(0)=\langle A^{(n)}(0)A^{(n)}(0)\rangle$$

where (n) denotes the nth derivative of A. Thus, if the $C^{(n)}(t)$ are intricate functions of time, then by implication so are the $K_n(t)$ $(n=0,\ldots,N)$. Specifically, we aim to see whether the exponential approximation $K_1(t)$ is worthwhile. The decay with time of each member of the set $[K_0(t), K_1(t), \ldots,]$ is determined by that of the successive $C^{(n)}(t)$. It is difficult and time-consuming to calculate the memory functions $K_n(t)$ directly because of their definition only in terms of projection operators, but such is not the case for $C^{(n)}(t)$, since the predictor–corrector algorithms used in molecular dynamics to solve the initial equations depend for their usefulness upon the calculation and storage of up to the first five derivatives of a dynamical variable A, typically the center-of-mass velocity $\mathbf{v}$ or the total angular velocity $\boldsymbol{\omega}$. The autocorrelation functions

$$C_1(t)=\langle \dot{\mathbf{v}}(t)\cdot\dot{\mathbf{v}}(0)\rangle,$$
$$C_2(t)=\langle \ddot{\mathbf{v}}(t)\cdot\ddot{\mathbf{v}}(0)\rangle,$$
$$C_3(t)=\langle \dot{\boldsymbol{\omega}}(t)\cdot\dot{\boldsymbol{\omega}}(0)\rangle,$$
$$C_4(t)=\langle \ddot{\boldsymbol{\omega}}(t)\cdot\ddot{\boldsymbol{\omega}}(0)\rangle$$

are simulated using the atom-atom algorithm, over a range of temperature

(T^*) at constant number density (ρ^*), and vice versa. In the first calculation an interatomic distance (L^*) of 0.3292 was used, corresponding to N_2. In the second we used the best available Lennard-Jones parameters for nitrogen with an interatomic distance of 0.4, so that we do not deal in this case with a "real" molecule. The statistical stability of the computed acf's is judged as usual by using different numbers of time steps (ca. 5×10^{-15} sec) for the ensemble averaging.[107] No difference could be perceived between runs of 200 and 400 steps. All the results shown here were obtained with the latter. A few runs of up to 1600 steps were carried out initially to look for any drift in quantities such as the mean-square torque and force as well as thermodynamic data. The first 100 or 50 steps of each run are unstable and are rejected in forming averages of any kind, and no acf is plotted beyond about 0.5 psec. Real time was divided into batches of up to 1200 decimal seconds each of CDC 7600 (U.M.R.C.C.) time.

It is clear from Fig. 59 that $C_2(t)$ and $C_4(t)$ are intricate functions of time, being oscillatory sometimes, sometimes very rapidly decaying, but more often with a decay on the same time scale as C_1 and C_3. Therefore, were we to take the set $[\boldsymbol{\omega},\dot{\boldsymbol{\omega}},\ddot{\boldsymbol{\omega}}]$ or $[\mathbf{v},\dot{\mathbf{v}},\ddot{\mathbf{v}}]$ in a three-variable formalism, the autocorrelation functions of each would decay usually on much the same time scale and the "fast variable" hypothesis would be inapplicable.

The complicated analytical form of members of the set $[K_0(0),\ldots,K_n(0)]$ for n greater than 2 may be clearly demonstrated as below for the orientation, dipole unit vector $\mathbf{u}$ by evaluating the Maclaurin expansion and coefficients of $\langle\mathbf{u}(t)\cdot\mathbf{u}(0)\rangle$. Here we carry this out for the coefficients up to that of t^8 in a symmetric-top or linear model. The terms to be evaluated are

$$M_0\equiv 1 \text{ (the coefficients of } t^0)$$
$$M_2=\langle\mathbf{u}^2(0)\rangle \qquad M_4=\langle\ddot{\mathbf{u}}^2(0)\rangle$$
$$M_6=\langle\dddot{\mathbf{u}}^2(0)\rangle \qquad M_8=\langle\ddddot{\mathbf{u}}^2(0)\rangle$$

The method employed is an extension of that of Desplanques,[39] which aims at an expansion of each coefficient in terms of $\boldsymbol{\omega}_\perp$, the component of the angular velocity perpendicular to the C_{3v} axis. This is useful since its time derivative is a torque component, itself a derivative of a potential with respect to orientation.

Gordon has evaluated M_2 and M_4 for a linear molecule, and Desplanques has extended this to the symmetric-top symmetry. We have

$$M_2=\langle\dot{\mathbf{u}}(0)\cdot\dot{\mathbf{u}}(0)\rangle=2kT/I_B \tag{III.24}$$

$$M_4=\langle\ddot{\mathbf{u}}(0)\cdot\ddot{\mathbf{u}}(0)\rangle = 2\left(2\frac{kT}{I_B}\right)^2\left(1+\frac{I_A}{4I_B}\right)+\frac{\langle O(V)^2\rangle}{I_B^2} \tag{III.25}$$

where I_B and I_A are the usual moments of inertia of the asymmetric top and $\langle O(V)^2\rangle$ denotes the mean-square torques, V being the mean intermolecular potential. This is in the direction perpendicular to the C_{3v} axis. Thus $K_1(0)$ for $\mathbf{u}$ is proportional to $\langle O(V)^2\rangle$. The expansion of m_6 and m_8 may be accomplished by repeated differentiation of the relation

$$\ddot{\boldsymbol{\omega}}=\dot{\mathbf{u}}\times\ddot{\mathbf{u}}+\mathbf{u}\times\dddot{\mathbf{u}} \tag{III.26}$$

so that

$$M_6=\langle\dddot{\mathbf{u}}(0)\cdot\dddot{\mathbf{u}}(0)\rangle = \langle\omega_\perp^6\rangle+\langle\omega_\perp^2(\dot\omega_\perp)^2\rangle+\langle(\ddot\omega_\perp)^2\rangle + \tfrac{5}{2}\left\langle\left[\frac{d}{dt}(\omega_\perp^2)\right]^2\right\rangle-\left\langle\omega_\perp^2\frac{d^2}{dt^2}(\omega_\perp^2)\right\rangle \tag{III.27}$$

The coefficient of t^6 is related to the mean-square torque derivative term (the third) and also *four others* of the same dimension. m_6 is related to $K_2(0)$ and therefore throughout its domain of existence ($t>0$) must reflect the time decay of all the vector terms in the right-hand side of (III.27), and is consequently an intricate function of time.

Differentiating (III.26), we have

$$\boldsymbol{\omega}_\perp=2\dot{\mathbf{u}}\times\dddot{\mathbf{u}}+\mathbf{u}\times\ddddot{\mathbf{u}} \tag{III.28}$$

giving

$$\langle\ddddot{\mathbf{u}}(0)\cdot\ddddot{\mathbf{u}}(0)\rangle=\langle\ddot\omega_\perp^2\rangle-2\langle\omega_\perp^8\rangle-4\langle\omega_\perp^2(\ddot\omega)^2\rangle + 2\langle\dot\omega_\perp^4\rangle+10\left\langle\omega_\perp^2\left(\frac{d}{dt}(\omega_\perp^2)\right)^2\right\rangle-9\left\langle\omega_\perp^4\frac{d^2}{dt^2}(\omega_\perp^2)\right\rangle - 5\left\langle(\dot\omega_\perp)^2\frac{d^2}{dt^2}(\omega_\perp^2)\right\rangle-\frac{5}{4}\left\langle\left(\frac{d^2}{dt^2}(\omega_\perp^2)\right)^2\right\rangle + 3\left\langle\frac{d}{dt}(\omega_\perp^2)\left[\frac{d^3}{dt^3}(\omega_\perp^2)-\frac{3}{2}\frac{d}{dt}(\dot\omega_\perp)^2-\frac{3}{2}(\omega_\perp^4)\right]\right\rangle$$

The coefficient m_8 is related to $K_3(0)$.

The overall time dependence of functions such as these is supplied in great detail by a molecular dynamics calculation and one of the more obvious results (Fig. 59) is that both $C_2(t)$ and $C_4(t)$ seem to be sensitive to small changes in T^* or ρ^*, whereas $C_1(t)$ and $C_3(t)$ are not. C_2 and C_4, being probes into the extreme short-time dynamical properties of the molecular ensemble, are revealing details about changes in the linear and angular

acceleration, those changes which must be taking place during the course of an interaction or "collision." The fact that all the acf's exhibit negative regions is not surprising in view of the fact that the velocity and angular velocity acf's themselves oscillate out to fairly long times (see previous sections) at higher values of ρ^*. It is not surprising either that C_2 and C_4 oscillate so rapidly in comparison with C_1 and C_3, the same relationship has been observed spectroscopically, of course, for $\langle \mathbf{u}(t)\cdot\mathbf{u}(0)\rangle$ and $\langle \dot{\mathbf{u}}(t)\cdot\dot{\mathbf{u}}(0)\rangle$. It is merely another expression of the increased sensitivity of derivative auto correlation functions to short-time, or high-frequency phenomena.

An interesting fact of the molecular motion is revealed when C_2 and C_4 are plotted together as in Figs. 59, since the types of decay at each different T^* and ρ^* resemble each other so closely. When one function is rapidly oscillatory, then so is the other, and the same is true when both are long-lived. This seems to be indicative of a great deal of those translation-rotation effects, typified in the extreme case by the propeller action. It is known that in the Markov limit such coupling is rigorously zero for symmetry inclusive of $C_{\infty v}$ and $D_{\infty h}$. Needless to say, the Markov limit is unrealistic (delta memories) but under inversion $\mathbf{v}\rightarrow-\mathbf{v}$ and $\omega\rightarrow\omega$, whereas the Liouville operator remains unchanged. This implies that

$$C_{v\omega}(0) = -C_{v\omega}(0) = 0$$

but $C_{v\omega}^{(2n)}(t)\equiv\langle v^{2n}(0)\omega^{2n}(t)\rangle$ is finite (Figs. 58). It needs to be emphasized that a similar decay rate for the velocity and angular velocity autocorrelation functions is not itself indicative of coupling, since in the absence of any intermolecular interaction, both normalized autocorrelation functions would remain indefinitely at unity.

To close this section we emphasize that the intricate nature of these functions does not imply that the memory function expansion of Mori is unusable, but the protagonists of two and three formalisms should note in particular the longevity of the autocorrelation functions of some of the higher derivatives. Also, we are of course always considering an artificial droplet of liquid.

D. General Dynamic Properties of Computer Nitrogen: Collective Correlation Functions

In this section we use the Tildesley–Streett algorithm to study the behavior of five autocorrelation functions: linear and angular velocity, orientation, torque, and force under the following conditions: (1) increasing number density (ρ^*) at constant temperature (T^*) and interatomic distance (L^*), (2) increasing L^* at constant T^* and ρ^*, and (3) increasing T^* at constant ρ^* and L^*. The following indications appear: (1) The mean-square torque and mean-square force can exhibit maxima or minima as a function of ρ^* or L^*, but over a restricted range seem linear in T^* at constant ρ^* and L^*. (2) Autocorrelation functions of high derivative of the interatomic vector $\mathbf{u}$ or the angular velocity ω decay generally on the same time scale as the vectors themselves and become more complicated, as described in the previous section. (3) The effect of elongation at constant ρ^* on dynamical properties such as the above is much more pronounced than is that of ρ^* at constant L^*, indicating that hard-core anisotropy is the important factor in the determination of, for example, nematic behavior. By increasing L^* we effectively change from a pseudospherical molecular shape to a dumbbell, and so measure the effect of increasing geometrical anisotropy on spectral properties.

The results are illustrated in Figs. 63 to 66 in terms of several different autocorrelation functions and as plots of mean-square torque and mean-square force against reduced number density ρ^* at a constant temperature, and vice versa. The features of these functions can be used to criticize the models in Table I. It is clear that purely rotational diffusion is inadequate to explain the simulations, even in its inertia-corrected form, where the angular momentum autocorrelation function is a single exponential, and where the torque autocorrelation function is not defined. The M and J diffusion models for the motion of the interatomic vector $\mathbf{L}^*$ may be derived quite easily using projectors whereby the autocorrelation functions of $\mathbf{L}^*$ and $\dot{\mathbf{L}}^*$ are slowly decaying compared with that of $\ddot{\mathbf{L}}^*$. Since the autocorrelation function $\langle \ddot{\mathbf{L}}^*(0)\cdot\ddot{\mathbf{L}}^*(t)\rangle$ has the units of angular acceleration, it is related to the torque autocorrelation function, which in Fig. 59 decays on the same time scale as $\langle \mathbf{L}^*(0)\cdot\mathbf{L}^*(t)\rangle$. It seems that $\langle \omega(t)\cdot\omega(0)\rangle$ sometimes decays on a much longer scale, but more often it does not. Even the autocorrelation function $\langle \ddot{\omega}(t)\cdot\ddot{\omega}(0)\rangle$ (previous section) sometimes takes longer to decay than $\langle \mathbf{L}^*(t)\cdot\mathbf{L}^*(0)\rangle$, and apparently is a much more complicated function of time than the latter. The Mori continued-fraction representation depends partly for its usefulness on the hope that autocorrelation functions of derivatives of $\mathbf{L}^*$ might have simpler time dependencies than that of $\mathbf{L}^*$ itself. It seems that successive kernels in Mori's series are more complicated than envisaged (on the results of Section III.C), but Singer et al.'s[100] simulation of memory functions shows that these are much less so than are high derivative acf's such as $\langle \ddot{\omega}(t)\cdot\ddot{\omega}(0)\rangle$. Also, of course, the memory function series is a useful way of generating the whole time dependence of an autocorrelation function knowing only the *short-time* behavior of, say, its second memory function. We discuss hereafter some specific systems.

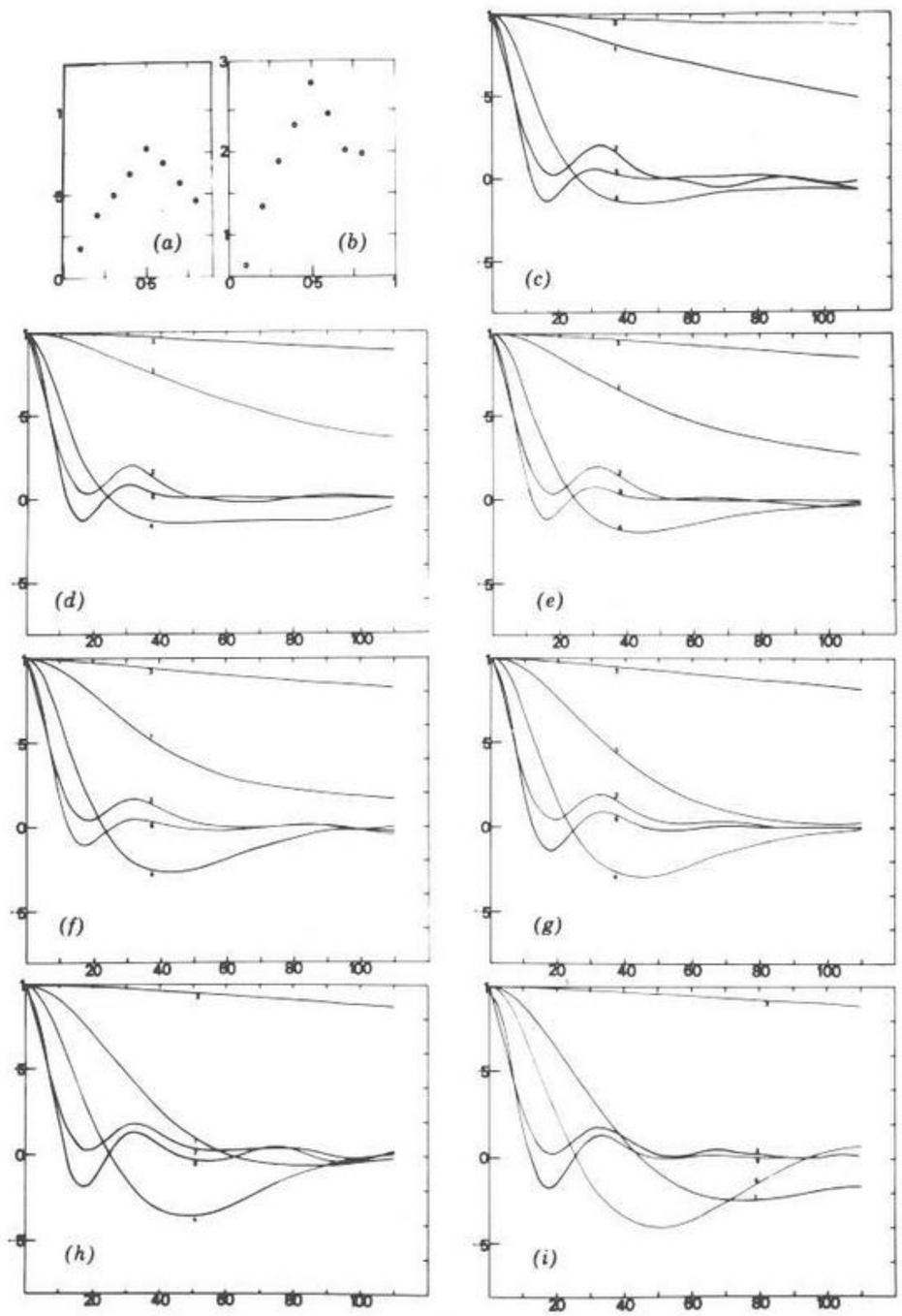

Fig. 63. Left to right, top to bottom ($T^*=3.6$, $L^*=0.1$): (*a*) Plot of $10^3\langle Tq^2\rangle$ vs. ρ^*. (*b*) Plot of $\langle F^2\rangle$ vs. ρ^*. (*c*) Autocorrelation functions for $\rho^*=0.2$: (1) velocity; (2) orientation; (3) angular velocity; (4) force; (5) torque. (*d*) As in (*c*), $\rho^*=0.3$. (*e*) As in (*c*), $\rho^*=0.4$. (*f*) As in (*c*), $\rho^*=0.5$. (*g*) As in (*c*), $\rho^*=0.6$. (*h*) As in (*c*), $\rho^*=0.7$. (*i*) As in (*c*), $\rho^*=0.8$. Ordinates: (*a*) $10^3\langle Tq^2\rangle$, (*b*) $\langle F^2\rangle$; abscissas: (*a*) ρ^*, (*b*) ρ^*, (*c*) to (*i*) time steps. [Reproduced by permission from *Adv. Mol. Rel. Int. Proc.*, **11**, 295 (1977).]

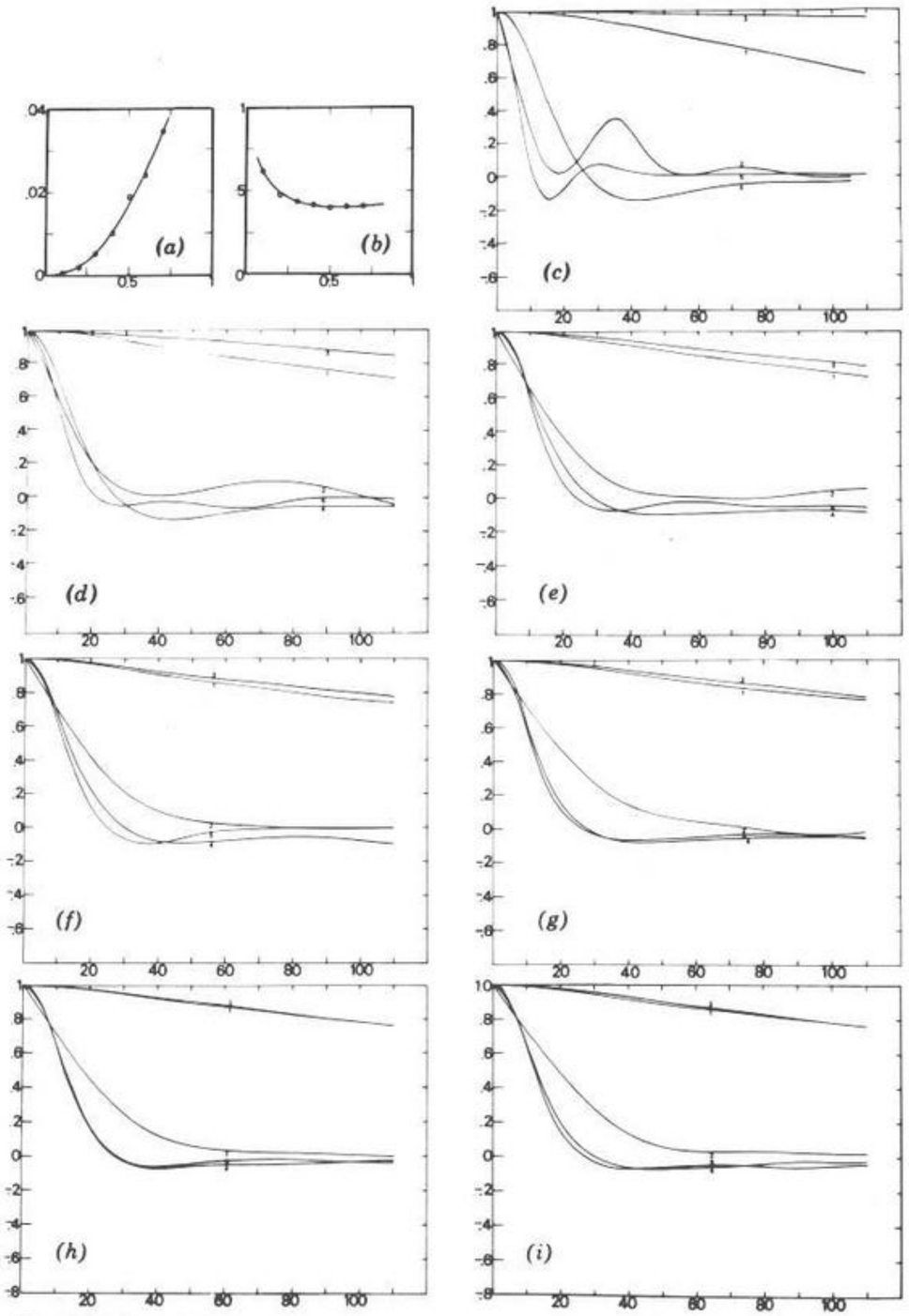

Fig. 64. Left to right, top to bottom ($\rho^*=0.1$; $T^*=3.6$): (*a*) $\langle Tq^2\rangle$ vs. L^*. (*b*) $\langle F^2\rangle$ vs. L^*. (*c*) autocorrelation functions: (1) velocity; (2) orientation; (3) angular velocity; (4) force; (5) torque, $d^*=0.1$. (*d*) as in (*c*), $d^*=0.2$. (*e*) as in (*c*), $d^*=0.3$. (*f*) as in (*c*), $d^*=0.4$. (*g*) as in (*c*) $d^*=0.5$. (*h*) as in (*c*), $d^*=0.6$. (*i*) as in (*c*), $d^*=0.7$. Ordinates: (*a*) $\langle Tq^2\rangle$, (*b*) $\langle F^2\rangle$; abscissas: (*a*) L^*, (*b*) L^*, (*c*) to (*i*) time steps. [Reproduced by permission from *Adv. Mol. Rel. Int. Proc.*, **11**, 295 (1977).]

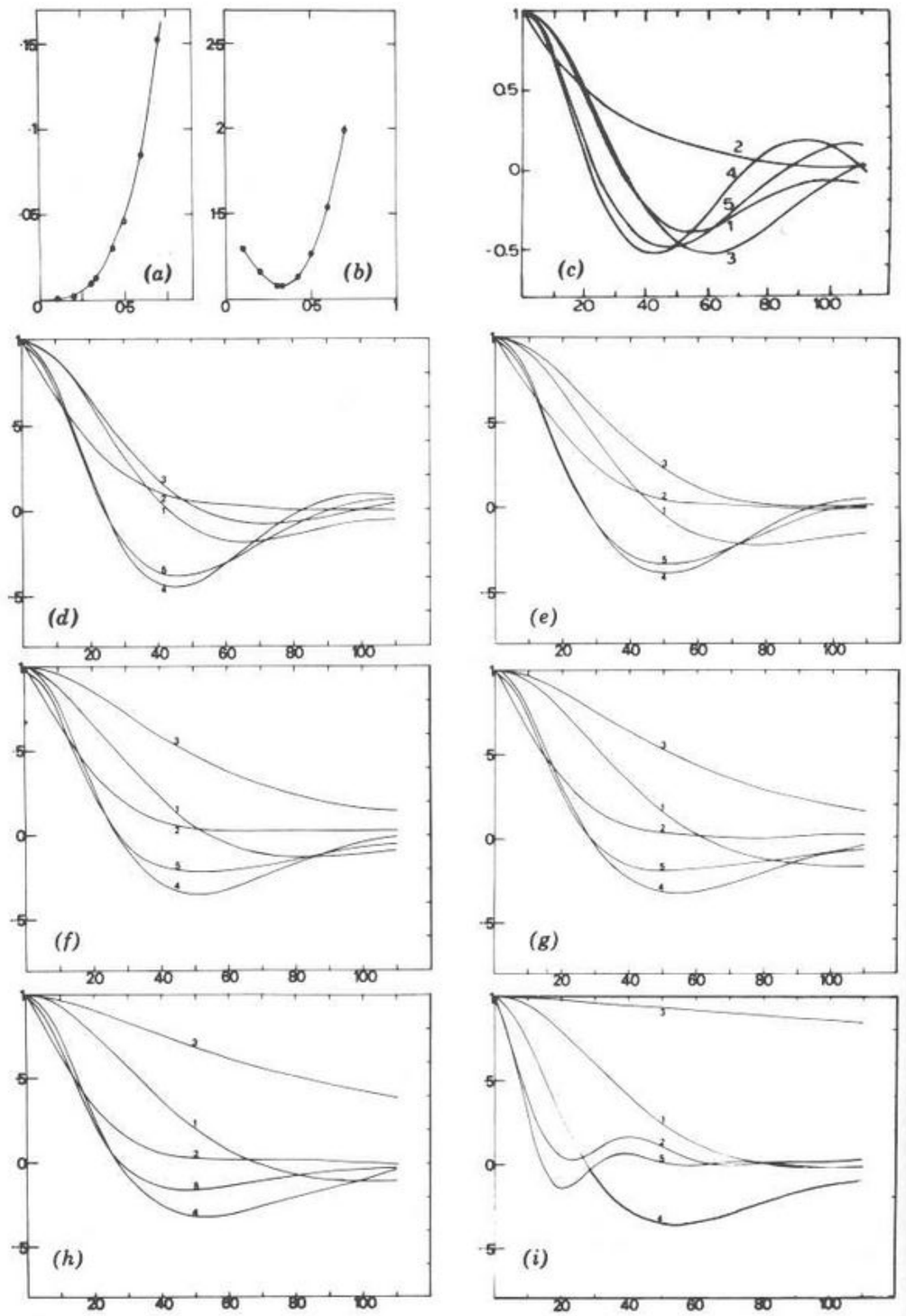

Fig. 65. Left to right, top to bottom ($\rho^* = 0.643$, $T^* = 2.3$): (*a*) $\langle Tq^2 \rangle$ vs. L^*. (*b*) $\langle F^2 \rangle$ vs. L^*. (*c*) autocorrelation functions: (1) velocity; (2) orientation; (3) angular velocity; (4) force; (5) torque; $L^* = 0.7$. (*d*) as in (*c*) $L^* = 0.5$. (*e*) as in (*c*), $L^* = 0.425$. (*f*) as in (*c*), $L^* = 0.3292$. (*g*) as in (*c*), $L^* = 0.3$. (*h*) as in (*c*), $L^* = 0.2$. (*i*) as in (*c*) $L^* = 0.1$. Ordinates: (*a*) $\langle Tq^2 \rangle$, (*b*) $\langle F^2 \rangle$; abscissas: (*a*) L^*; (*b*) L^*, (*c*) to (*i*) time steps. [Reproduced by permission from *Adv. Mol. Rel. Int. Proc.*, **11**, 295 (1977).]

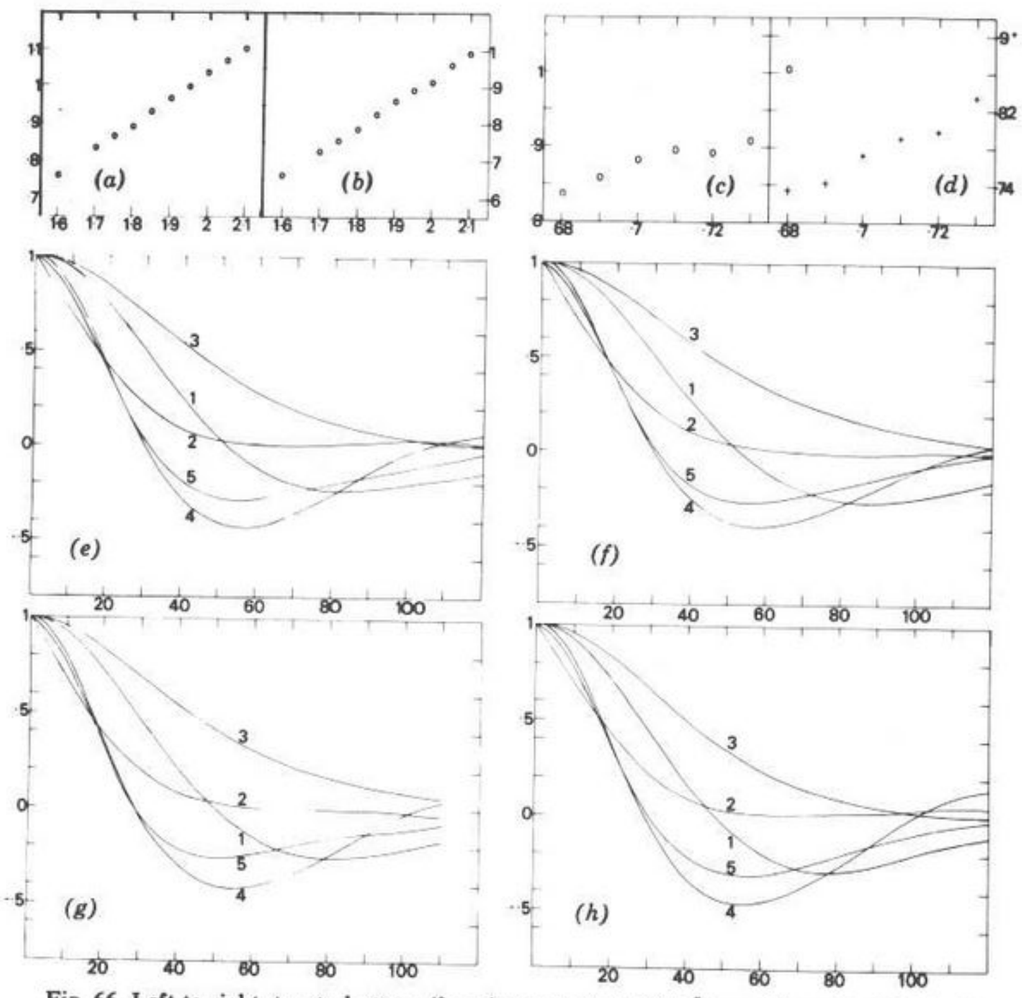

Fig. 66. Left to right, top to bottom (for nitrogen): (*a*) $10\langle Tq^2 \rangle$ vs. T^* at $\rho^* = 0.6964$, $d^* = 0.3292$. (*b*) $\langle F^2 \rangle$ vs. T^* at $\rho^* = 0.6964$, $d^* = 0.3292$. (*c*) $10\langle Tq^2 \rangle$ vs. ρ^* at $T^* = 1.75$, $d^* = 0.3292$. (*d*) $\langle F^2 \rangle$ vs. ρ^* at $T^* = 1.75$, $d^* = 0.3292$. (*e*) Autocorrelation functions: (1) velocity; (2) orientation; (3) angular velocity; (4) force; (5) torque; $T^* = 1.75$, $\rho^* = 0.6964$. (*f*) As for (*e*), $T^* = 1.75$; $\rho^* = 0.68$. (*g*) As for (*e*), $T^* = 1.9$; $\rho^* = 0.6964$. (*h*) As for (*e*), $T^* = 1.75$; $\rho^* = 0.74$. Ordinates: (*a*) $10\langle Tq^2 \rangle$, (*b*) $\langle F^2 \rangle$, (*c*) $10\langle Tq^2 \rangle$, (*d*) $\langle F^2 \rangle$. Abscissas: (*a*) T^*, (*b*) T^*, (*c*) ρ^*, (*d*) ρ^*, (*e*) to (*h*) time steps. [Reproduced by permission from *Adv. Mol. Rel. Int. Proc.*, **11**, 295 (1977).]

$T^* = 3.6$, $L^* = 0.1$, $\rho^* = 0.2$ to 0.8 (Fig. 63). This set of data is intended to simulate the effect of increasing reduced number density on a roughly spherical molecule at constant reduced temperature. Throughout, the orientational autocorrelation function is inertia-dominated, decaying rapidly and exhibiting a secondary maximum similar to that observed by Kneubühl and Keller[38] for the exceptionally free rotations of HF and HCl in SF_6 solvents. The torque acf tends to oscillate at the higher ρ^*. It is significant that both the mean-square torque and mean-square force go through a minimum at $\rho^* = 0.5$, whereas theories of hard collisions and

harmonic well oscillations predict a monatomic increase with number density. Recent work on the far-infrared induced absorption of compressed gaseous ethylene has suggested that the mean-square torque exhibits a turning point with increasing pressure, and similar work of CCl_4 and CS_2 liquids has revealed that the mean-square torque may increase or decrease with temperature at constant ρ^*.

The force and linear velocity acf's have maximum variation through this pressure range. At $\rho^* = 0.2$ the latter decays very slowly and the former has an extended negative tail. At $\rho^* = 0.7$ the force acf oscillates with a long period, and the velocity acf in turn develops the well-known negative tail. The slowly decaying acf's at the high ρ^* are those of angular and linear velocity, although their short-time behavior becomes progressively different. These, together with the fact that there is now an apparent shift in the minimum of the orientational acf, shows up the considerable freedom of angular movement and gradual constraint upon translational movement as ρ^* increases. The changes in the autocorrelation functions throughout their range are indicative of the nature of the collision rather than any "structuring" in the fluid.

$T^* = 3.6$, $\rho^* = 0.1$, $L^* = 0.2$ to 0.7 (Fig. 64). The torque increases by an order of magnitude with elongation, and the angular velocity acf simultaneously decays more quickly. The most interesting aspect of this progression is that the velocity and angular velocity acf's get progressively closer together and at $d^* = 0.7$ decay at virtually the same rate as do those of force and torque. It is apparent from a comparison of this progression with the first that elongation has a larger impact than number density in this respect at constant reduced temperature. Here we have the first vague indications of factors important in the formation of a nematic phase—the molecular log-jam leading to birefringence. The only one of the five acf's to decay more quickly with increasing elongation is that of angular velocity, and this occurs even though the molecular moment of inertia is increasing with L^*, which in the absence of intermolecular effects would alone cause the torque, angular velocity, and orientation to decay more slowly on the scale of absolute time (in psec). The mass of the molecule is, of course, unaffected by elongation.

$\rho^* = 0.643$, $T^* = 2.3$, $L^* = 0.1$ to 0.7 (Fig. 65). At this density there is a pronounced change from gaslike to liquidlike behavior as the elongation L^* increases at constant T^*. For example, the angular velocity acf decays slowly at $L^* = 0.1$, but is oscillatory at $L^* = 0.7$, where so are all the others except the orientational. Hard-core anisotropy must be an important factor in the determination of "structure" in liquids and, in this limit, in the appearance of nematic properties, where the orientational acf has been observed to be a slowly decaying exponential, and where the memory function, which is $\langle \dot{\mathbf{L}}^*(0) \cdot \dot{\mathbf{L}}^*(t) \rangle$ at $t = 0$, oscillates very rapidly. In an Einstein solid the velocity acf is a pure cosine, but the nematic phase is characterized by rotational (albeit restricted) and translational freedom, and the forms of the five acf's may well be an extreme version of ours at $d^* = 0.7$ for the Lennard-Jones dumbbell.

The linear velocity acf at $\rho^* = 0.643$ decays initially much more quickly for the longer molecules, the torque and orientational acf's more slowly, but at $L^* = 0.1$, the decay time of the orientational acf's at $\rho^* = 0.643$ and $\rho^* = 0.1$ are virtually identical, although the linear velocity acf decays much faster at the higher number density. On the other hand, for $L^* = 0.7$, the velocity acf at the *lower* number density is slower to decay. For the longest molecule the decay time of the orientation is much longer at the higher number density.

The effect of elongation at constant reduced number density is much more pronounced than the effect of ρ^* at constant elongation, and the built-in hard-core repulsive part of our double Lennard-Jones potential seems dominant in promoting oscillations in some of our acf's.

$T^* = 1.75$, $L^* = 0.3292$, $\rho^* = 0.68$ to 0.74 (Fig. 66). In this range the five acf's change very little, but the mean-square torque and force trend upward in value with increasing ρ^*, although there is an inflexion, or maybe a slight maximum, at $\rho^* = 0.715$. The elongation corresponds to that of N_2, so our results are for a real molecule at constant reduced temperature. It is interesting to note that the mean-square torque for ethylene, calculated from far-infrared pressure-induced absorption, shows a minimum as pressure decreases at constant temperature. Ethylene is isoelectronic with nitrogen.

It is clear from the varied forms of autocorrelation function displayed here that further experiments (such as scattering of laser radiation, depolarization of fluorescence, infrared, and Raman wings) will be more fruitful when carried out simultaneously on one selected fluid, so that several different aspects of the motion of $\mathbf{L}^*$ can be discerned. It is clear that a study of $\langle \mathbf{L}^*(t) \cdot \mathbf{L}^*(0) \rangle$ done by one experimental technique in isolation disposes of a lot of information by statistical averaging; and in fact experiments on Debye relaxation at frequencies below those of the far infrared look at the long-time tail of this autocorrelation function, which is almost always exponential. Such experiments, although carried out with great experimental skill and effort, thus yield the minimum information about the trochilics of a typical molecular fluid, even when this happens to be dipolar. Now we are fortunate in having available large computers which, with admittedly rough-and-ready intermolecular potentials, can be used to yield useful, complementary, incisive data.

1. *Collective Motions—Hydrodynamics and the Mori Equation*

One of the clearest illustrations of the use of (I.6) in the field of hydrodynamics is that by Lallemand. A further incisive discussion on the topic is that of Kruus.[28] In this section we simulate functions such as the current and spin density from the molecular level, and attempt to fathom the gap between molecular and hydrodynamic theories of the fluid condition. This relation will continue to be intractable without the aid of computer simulation techniques, whereby information on individual molecules may be averaged to produce the correlation functions employed in the hydrodynamic equations of mass, momentum, and energy conservation leading to the linearized Navier-Stokes equation and to the Brillouin peaks of scattered light.

In this section we present some preliminary results on the simulation of current and spin density correlation functions for N_2 in the liquid and glassy states starting from the atom–atom potential and Newton's equations for individual molecular motions. The results are discussed very generally in terms of generalized hydrodynamic theory as first propounded by

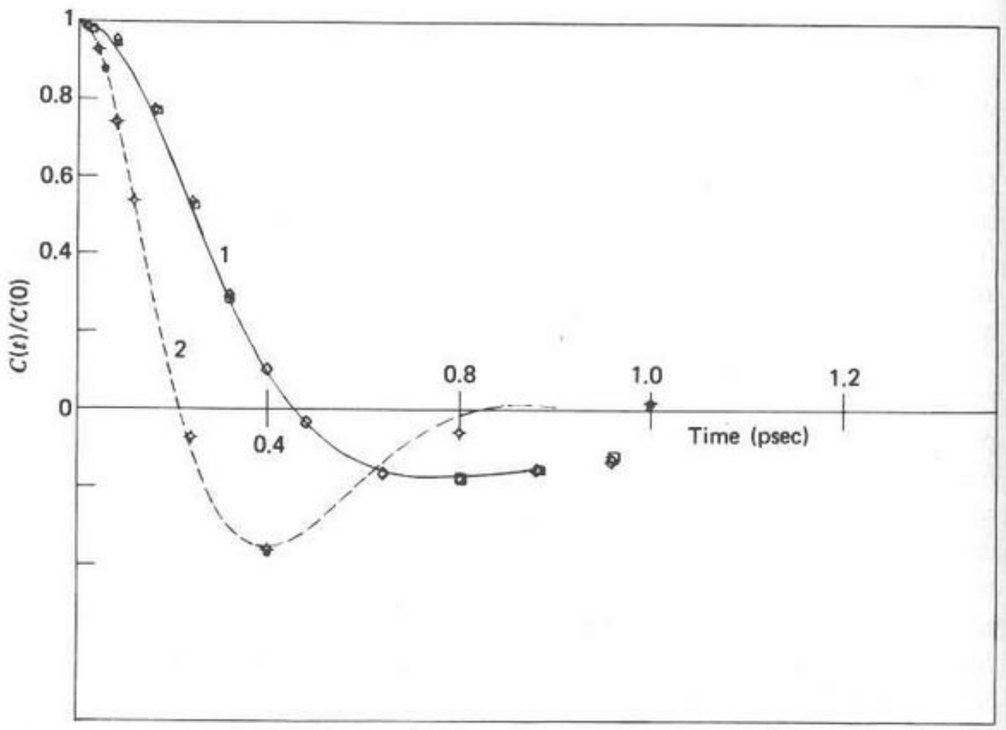

Fig. 67. (1) Autocorrelation function of velocity for N_2 in the liquid state at a reduced number density (p^*) of 0.643, reduced temperature (T^*) of 2.32. □, Cross-correlation of velocity, 1000 time steps; ◇, cross-correlation of velocity, 1600 time steps. (2) Autocorrelation function of force for N_2 in the same liquid state. ⊹, Cross-correlation function 1600 time steps; ⊙, cross-correlation function 1000 time steps. Ordinate: $C(t)/C(0)$; abscissa: time (psec). [Reproduced by permission from *Chem. Phys. Lett.*, (1978).]

Zwanzig et al. for computer argon. This is the hydrodynamic equation formally equivalent to (I.6). Both the longitudinal and transverse current-density correlation functions are expected to be purely exponential decays on the basis of classical hydrodynamic theory, and so is the transverse spin-density correlation function. The spin-density correlation functions (longitudinal and transverse) are evaluated similarly. To check on the reliability of the statistics in the simulation of these collective correlation functions, the cross-correlation functions of velocity and force were evaluated using 1600 time steps and checked against the equivalent autocorrelation functions. Figure 67 shows that the decay of each is satisfactorily similar. All the hydrodynamic functions were thereafter evaluated using 1600 time steps of ca. 5×10^{-15} sec after rejecting the first 200.

In Fig. 68 are illustrated some longitudinal current density correlation functions $C_{\|}(\mathbf{k},t)$ for large and intermediate values of momentum transfer (wave vector) $\mathbf{k}$. In the N_2 fluid, $C_{\|}(\mathbf{k},t)$ is oscillatory with pronounced negative regions as $\mathbf{k}$ increases. Even with $|\mathbf{k}|=0.1$ (in reduced units of $1/\sigma$, where σ is the Lennard-Jones parameter for N_2), the correlation function is far from exponential, as is the assumption of classical Navier–Stokes equations. Our calculations of the transverse current correlation

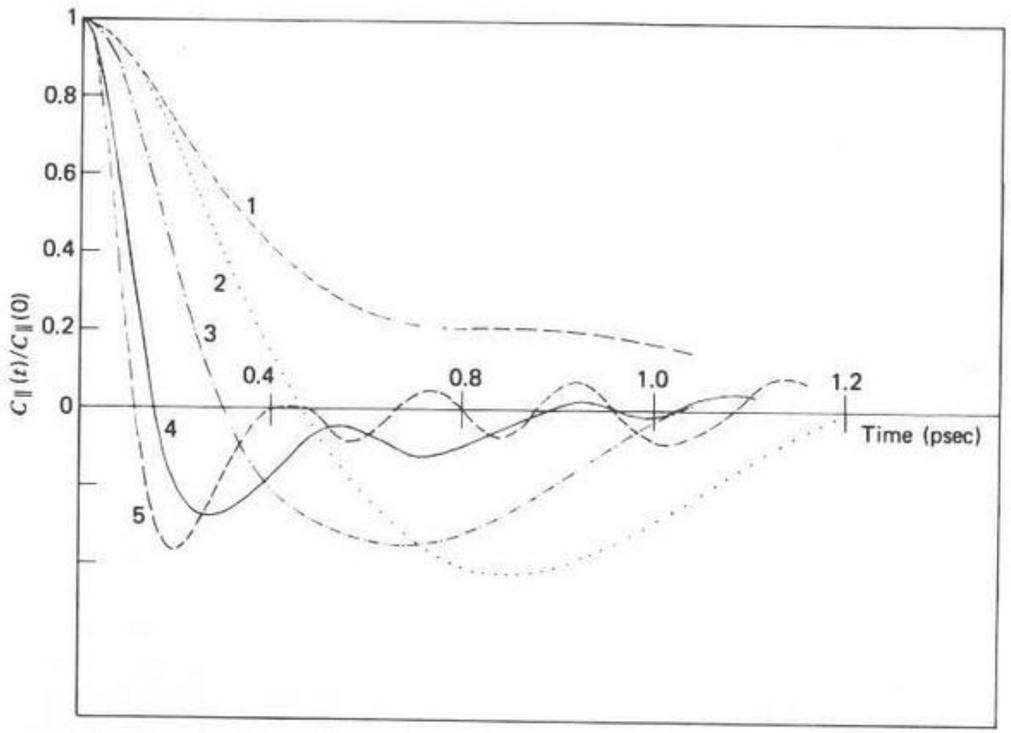

Fig. 68. Longitudinal current density correlation functions for different values of momentum transfer $\mathbf{k}$ (in reduced units of σ). (1) $|\mathbf{k}|^2=0.3$; (2) 3; (3) 15; (4) 45; (5) 60. Ordinate: $C_{\|}(t)/C_{\|}(0)$; abscissa: time (psec). [Reproduced by permission from *Chem. Phys. Lett.*, (1978).]

function indicate the same results. It is clear that a generalized hydrodynamic formalism is needed to account for the correlation functions simulated in this paper. The form suggested by Ailawadi et al. is

$$\frac{\partial}{\partial t} C_{\parallel}(\mathbf{k},t) = -\int_0^t K_l(\mathbf{k},t-t') C_{\parallel}(\mathbf{k},t')\, dt' \tag{III.29}$$

where the memory function $K_l(\mathbf{k},t)$ may be expressed as the sum

$$K_l(\mathbf{k},t) = k^2\left[\frac{kT}{m} S(\mathbf{k}) + \phi_{\parallel}(\mathbf{k},t)\right] \tag{III.30}$$

Here $S(\mathbf{k})$ is the equilibrium structure factor determined by a $\mathbf{k}$-dependent compressibility, and $\phi_{\parallel}(t)$ is an after effect, or memory function, describing the delayed response of the longitudinal part of the stress tensor to a change in the rate of shear. We propose here, very tentatively, to develop (III.29) into a Mori continued fraction and in order to maintain compatibility between macroscopic and microscopic levels the series of equations in the Mori expansion of (III.29) may be truncated at the three-variable level already widely used in molecular theories of itinerant oscillations cited in this section.

$$\frac{\tilde{C}_{\parallel}(\mathbf{k},s)}{\tilde{C}_{\parallel}(\mathbf{k},0)} = \left[s + \frac{K_l^{(0)}(\mathbf{k},0)}{s + \dfrac{K_l^{(1)}(\mathbf{k},0)}{s+\gamma(\mathbf{k})}} \right] \tag{III.31}$$

Here $K_l^{(0)}(\mathbf{k},0)$ and $K_l^{(1)}(\mathbf{k},0)$ are the first and second memory functions of $\tilde{C}_{\parallel}(\mathbf{k},s)$ at $t=0$. $\gamma(\mathbf{k})$ is defined by

$$K_l^{(1)}(\mathbf{k},t) = K_l^{(1)}(\mathbf{k},0)\exp[-\gamma(\mathbf{k})t] \tag{III.32}$$

Naturally, (III.31) is empirical in the sense that three parameters are unknown: $K_l^{(0)}(\mathbf{k},0)$, $K_l^{(1)}(\mathbf{k},0)$, and $\gamma(\mathbf{k})$ and have to be fixed by least-mean-squares iteration to the simulated $C_{\parallel}(\mathbf{k},t)$. However, some physical significance and dependence on $|\mathbf{k}|$ may be extracted as illustrated in the article by Ailawadi et al.[108]

The transverse current density correlation function and the spin density correlation functions oscillate about the time axes in the same way as the foregoing representative curves, being drawn in Figs. 68 and 69. The transverse spin density correlation function may not be derived in any other way than by computer simulation, since neutron scattering is insensitive in this context. It is obvious that the coupling between transverse spin and

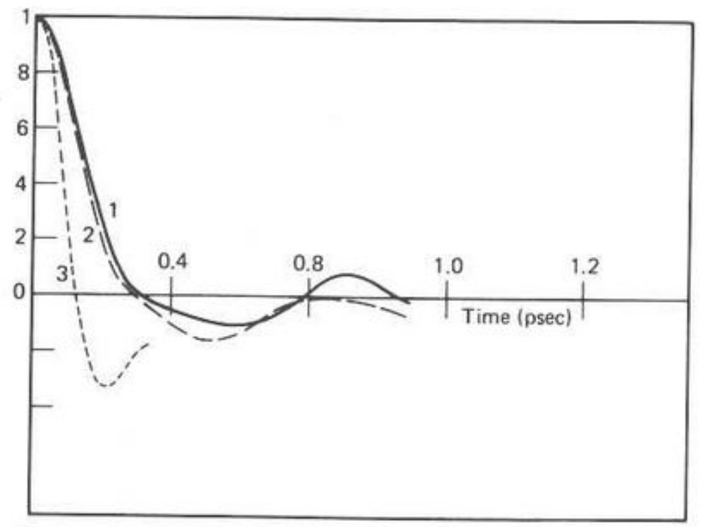

Fig. 69. (1) Longitudinal spin-density correlation function N_2, $p^*=0.643$; $T^*=2.32$; $|\mathbf{k}|^2=45$. (2) Transverse spin-density correlation function, N_2, $p^*=0.643$; $T^*=2.32$; $|\mathbf{k}|^2=30$. (3) Longitudinal current density correlation function, N_2; $|\mathbf{k}|^2=60$. N_2 in the glassy state at $p^*=0.800$, $T^*=2.30$. Abscissa: time (psec). [Reproduced by permission from *Chem. Phys. Lett.*, (1978).]

current density will be complicated in fluids of more pronounced shape anisotropy than N_2, and the limit of analytical tractability will be reached very quickly in dealing with this rotation–translation problem. This leaves only computer simulation as a practical means of investigation given a suitable intermolecular potential and improved numerical method. It would be particularly useful, therefore, in further work to solve numerically the equations of motion for a given *molecular* model, such as the itinerant oscilator, and then to determine directly whether the current and spin density correlation functions are describable by the same type of Mori approximant as are their molecular counterparts. This type of simulation would then be effectively a method of evaluating hydrodynamic functions from a specific model, of, say, a Brownian plus resonance type. In the next section we take the first step toward this goal by numerically solving (I.31) with the molecular dynamics techniques developed by Bellemans and Hermans, Kestemont, van Loon, and Finsy.[109]

E. Molecular Dynamics Simulation of the Planar Itinerant Librator

In this section we use the molecular dynamics method to simulate the system of ring/annulus itinerant libration developed by Coffey et al., (I.31), for angular planar reorientation of the asymmetric-top dipole vector. The main aim is the limited one of ascertaining to what precision the

numerical solution of the equations of motion used in the numerical simulation reproduces the *stochastic* differential equations of the analytical approach. Therefrom, the simulation may be extended to fields beyond analytical tractability. The assumptions inherent in a model of molecular motion may be satisfied exactly by (for example) rough-sphere simulations, and therefrom analytical and simulated autocorrelation functions may be compared. In this way, O'Dell and Berne[108] have demonstrated clearly the limits of applicability of the J-diffusion model for spherical tops. Similarly, the itinerant librator model of molecular motion may be simulated by a two-dimensional molecular dynamics system consisting of rough rings within which are disks, bound harmonically. Exchange of linear and angular momentum occurs when two rings collide. This may be compared with the system devised analytically where the annulus of moment of inertia I_1 is subjected to Brownian motion with friction coefficient ζ. It turns out that the analytical results varying ζ may be simulated very precisely, so that the latter may be used to extend the formalism to three dimensions, or to include, for example, the effects of rotation–translation coupling.

1. *Computational Details*[109]

We use an assembly of 120 particles (i.e., disks/annuli) of total mass m and diameter D. The motion of the annulus is perturbed by collisions, between which the center of each particle moves along a straight line at constant velocity and total angular momentum. The rotational motion of the annulus and disk is governed by

$$I_1\ddot{\theta}_1(t) = -\gamma[\theta_1(t)-\theta_2(t)] \tag{III.33}$$

$$I_2\ddot{\theta}_2(t) = \gamma[\theta_1(t)-\theta_2(t)] \tag{III.34}$$

Here I_1 and I_2 are the moments of inertia of the annulus and the disk; θ_1 and θ_2 specify the position of a point on the rim of the annulus and the position of the dipole on the disk. γ is the restoring torque constant between ring and disk. The dipole on the inner disk is supposed vanishingly small so that dipole-dipole coupling is neglected. When a collision occurs, an energy transfer takes place between rotational and translational degrees of freedom, depending on the dimensionless quantity

$$\tau = \frac{4I_1}{mD^2} \tag{III.35}$$

We seek to establish how closely τ may be used to simulate the frictional torque $\zeta\dot{\theta}_1(t)$ and $\lambda(t)$, the random couple of the Brownian motion assumed analytically. In the molecular dynamics the change of linear and angular

velocities at a collision between particles A and B are given by the following set of equations:

$$\mathbf{v}'_A = \mathbf{v}_A + \frac{\tau}{1+\tau}\left[\mathbf{v} + \frac{1}{\tau}\mathbf{k}(\mathbf{k}\cdot\mathbf{v})\right] \tag{III.36}$$

$$\mathbf{v}'_B = \mathbf{v}_B - \frac{\tau}{1+\tau}\left[\mathbf{v} + \frac{1}{\tau}\mathbf{k}(\mathbf{k}\cdot\mathbf{v})\right] \tag{III.37}$$

$$\omega'_A = \omega_A - \frac{2}{(1+\tau)D}\mathbf{k}\times\mathbf{v} \tag{III.38}$$

$$\omega'_B = \omega_B - \frac{2}{(1+\tau)D}\mathbf{k}\times\mathbf{v} \tag{III.39}$$

Here $\mathbf{v}_A$ and $\mathbf{v}_B$ are the translational velocities and ω_A and ω_B are the angular velocities of the annulus, that of the inner disk being unaffected by the collision. The primed variables correspond to the situation just after the collision. $\mathbf{k}$ is the unit vector directed from the center of the B particle to that of A at the time of collision. $\mathbf{v}$ is the relative velocity of the points in contact:

$$\mathbf{v} = \mathbf{v}_B - \mathbf{v}_A - \tfrac{1}{2}D\mathbf{k}\times(\omega_A+\omega_B) \tag{III.40}$$

Initially, the 120 particles are arranged in 12 rows of 10 at the nodes of a triangular lattice whose dimensions are chosen to obtain the desired density d expressed as the number of particles per unit surface. Periodic boundary conditions are used, and initially the translational and angular velocities and the orientation of the two parts of each particle are randomly distributed. Reduced units of $I_1/kT=1$, $D=1$, $\alpha=\gamma/kT$, and $R=I_1/I_2$ are used. After the system has reached equilibrium it is followed for up to 1024 time intervals of $t=0.05(kT/I_1)^{-1/2}$. The two components of the unit vector parallel to the dipole, the two components of the derivative of this vector, the angular velocity of the disk, and the torque on it are recorded for each particle for subsequent calculation of correlation functions.

In Fig. 70 some autocorrelation functions for this system are illustrated. The analytical curves for least-mean-squares best fit behave similarly and are inseparable by eye for various values of ζ. This justifies the use of simulation in two dimensions, and therefore future computation in three dimensions for itinerant libration or itinerant libration–oscillation may be contemplated. These simulations will be of great utility in, for example, the evaluation of the approximation to (I.6) of (I.31). It would be useful to define the difference between these equations in the itinerant librator–oscillator system, and future work will concentrate on this. It will also be possible

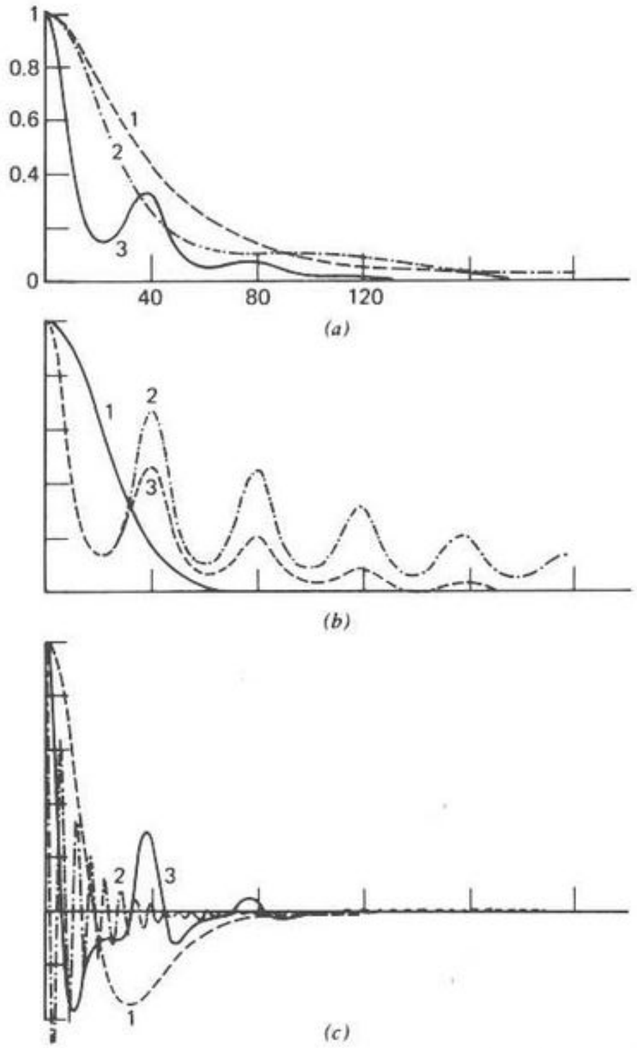

Fig. 70. Autocorrelation functions of orientation of the disk dipole vector $\boldsymbol{u}$. (*a*) (1) Reduced density $(d^*)=0.6$; $\alpha=10^3$; $R=10$, $\tau=0.50$; (2) $d^*=0.8$; $\alpha=1.0$; $R=1$, $\tau=0.50$; (3) $d^*=0.6$; $\alpha=1.0$; $R=10$, $\tau=0.50$. (*b*) (1) $d^*=0.6$; $\alpha=0.1$; $R=1$, $\tau=0.50$; (2) $d^*=1.0$; $\alpha=1.0$; $R=10$, $\tau=0.50$; (3) $d^*=0.8$; $\alpha=1.0$; $R=10$, $\tau=0.50$. (*c*), (*d*) Autocorrelation function $\langle \dot{\boldsymbol{u}}(t)\cdot\dot{\boldsymbol{u}}(\mathrm{o})\rangle$. (*c*) (1) Reduced density $(d^*)=0.6$; $\alpha=1.00$; $R=1.00$; $\tau=0.50$; (2) $d^*=0.6$; $\alpha=10^3$; $R=10.00$; $\tau=0.50$; (3) $d^*=0.6$, $\alpha=1.00$; $R=10.00$; $\tau=0.50$. (*d*) (1) Reduced density $(d^*)=0.6$; $\alpha=0.10$; $R=1.00$; $\tau=0.50$; (2) $d^*=1.0$; $\alpha=1.00$; $R=10.00$; $\tau=0.50$; (3) $d^*=0.6$; $\alpha=10.00$; $R=1.00$; $\tau=0.50$. (*e*), (*f*) Autocorrelation function of the disk angular velocity $\langle \boldsymbol{\omega}(t)\cdot\boldsymbol{\omega}(\mathrm{o})\rangle$. (*e*) (1) Reduced density $(d^*)=0.6$; $\alpha=1.00$; $R=1.00$; $\tau=0.50$; (2) $d^*=0.6$; $\alpha=10^3$; $R=10.00$; $\tau=0.50$; (3) $d^*=0.6$; $\alpha=1.0$; $R=10.00$; $\tau=0.50$; (*f*) (1) Reduced density $(d^*)=0.6$; $\alpha=0.10$; $R=1.00$; $\tau=0.50$; (2) $d^*=0.6$; $\alpha=10.00$; $R=1.00$; $\tau=0.50$; (3) $d^*=0.8$; $\alpha=1.00$; $R=1.00$; $\tau=0.50$. (*g*), (*h*) Autocorrelation function of the disk torque $\langle \dot{\boldsymbol{\omega}}(t)\cdot\dot{\boldsymbol{\omega}}(\mathrm{o})\rangle$. (*g*) (1) Reduced density $(d^*)=0.6$; $\alpha=0.10$; $R=1.00$; $\tau=0.5$; (2) $d^*=0.6$; $\alpha=10^3$; $R=10.00$; $\tau=0.5$; (3) $d^*=0.6$; $\alpha=1.0$; $R=10.00$; $\tau=0.5$. (*h*) (1) $d^*=0.8$; $\alpha=1.0$; $R=1.00$; $\tau=0.5$; (2) $d^*=0.6$; $\alpha=1.0$; $R=1.00$; $\tau=0.5$; (3) $d^*=0.6$; $\alpha=10.00$; $R=1.00$; $\tau=0.5$. Abscissas: time steps. [Reproduced by permission from *Chem. Phys. Lett.*, **58**, 521 (1978).]

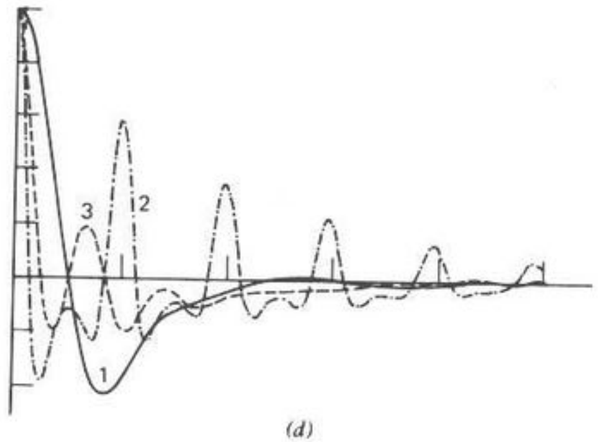

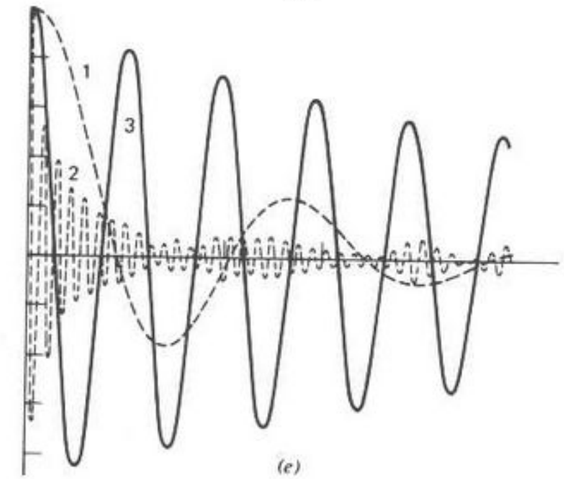

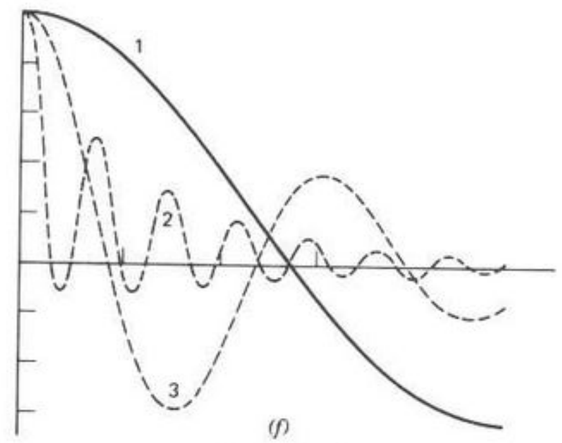

Fig. 70. Continued

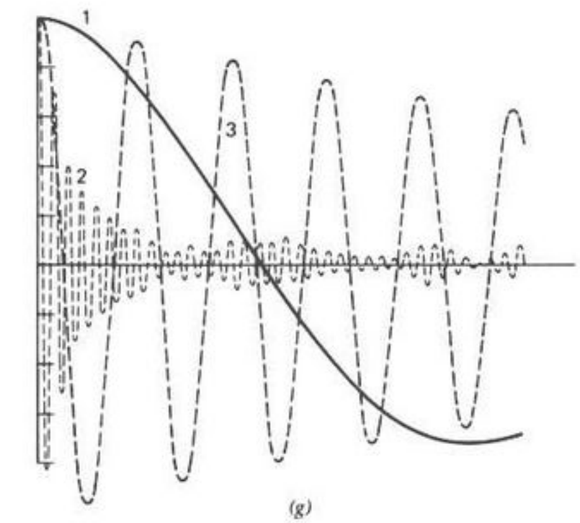

(g)

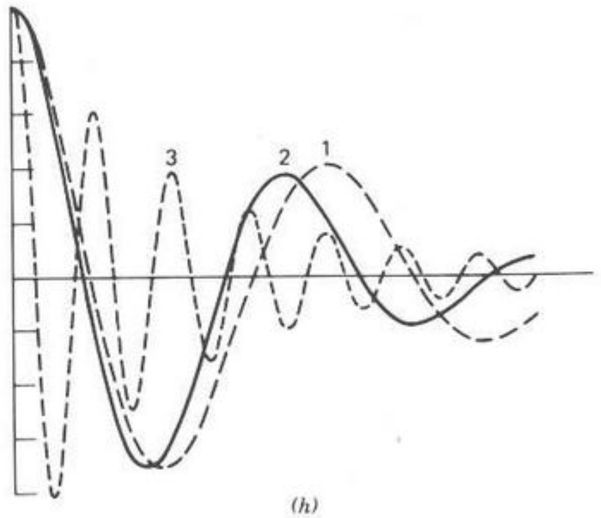

(h)

Fig. 70. Continued

numerically to simulate probability density functions which are analytically almost intractable by classical methods, although less so with those of Section I.

IV. INDUCED ZERO-THZ ABSORPTIONS AND ROTATION/TRANSLATION OF MOLECULES

We have mentioned in Section I that nondipolar liquids and compressed gases absorb in the zero-THz frequency region due to a fluctuating (time-dependent) dipole induced by the other molecules in the ensemble. Here

we consider how the phenomenon may be measured in terms of the molecular rototranslations and intermolecular potential energies. Although only broad bands are observable, whose breadth corresponds roughly to the lifetime of the induced dipole, a quantum theory using a multipole expansion of the electrodynamic field has often been used as an approximate representation, using radial averaging of the Lennard-Jones potential. We review this briefly and adopt also a classical description in terms of the Mori expansion which is empirical in approach, but affords a very close fit to the available data and is useful for their intercomparison.

Early evidence of an absorption at high microwave frequencies in highly purified nondipolar liquids was presented by Whiffen.[110] The first indication that the absorptions are of a rototranslational rather than purely translational origin came via Savoie and Fournier,[111] who obtained the far-infrared spectra of CH_4 and CD_4 as the liquid and plastic crystal down to 12°K. The liquid exhibits a broad maximum at about 200 cm^{-1} for CH_4 and 150 cm^{-1} for CD_4, which the authors interpreted as $I^{1/2}$ (rotational) rather than $m^{1/2}$ (translational) dependence. Davies, Chamberlain, and Davies[112] made the first attempt to interpret these bands in terms of the torsional oscillation of a molecule within the cage formed by its neighbors. They carried out refractive-index measurements on nondipolar liquids, and discovered that these indices had shallow minima in the far-infrared region. Evidence of a substantial intermolecular mean-square torque which hinders the molecular rotational-type motions in liquid CO_2 as compared with the compressed gas put forward by Birnbaum and Rosenberg[113] and by Baise.[114] The absorption of the liquid at 273°K has an integrated intensity an order of magnitude less than that in the gas phase, where rotational type $J \rightarrow J+2$ (quadrupole-induced) band shapes predominate. Significant intermolecular forces shift the peak by about 25 cm^{-1} to higher frequencies in the liquid. The authors argue then that the large quadrupole moment of CO_2, which has a dominant effect on the gas-phase absorption, is apparently much reduced in value in the liquid. This is the result of the "local order" and the symmetry arising, for example, in three-body collisions, the effective induced dipole being smaller. Carrying this argument to the static limit, collision-induced absorption would disappear if each molecule occupied a site of inversion symmetry. Such behavior was verified by Evans[115] in the more strongly quadrupolar cyanogen, and by Baise[114] in the weakly dipolar nitrous oxide.

Thus the evidence is in favor of a torsional cum rotational diffusion type of motion as the principal source of the far-infrared absorptions in these nondipolar liquids, closely analogous to that in their dipolar counterparts, so that (I.6) may be used to predict the spectral function $\tilde{C}(s)$. In this case the relevant element of **A** is the net induced dipole moment at the instant t.

The simplest theories may be constructed classically with this one element alone. First, however, we summarize the quantum theory as developed in symmetric tops by Frost.[116]

A. Multipole-Induced Absorption in Symmetric-Top Molecules

Nondipolar molecules absorb in the zero-THz region because intermolecular electrostatic fields distort the overall symmetry of a given molecule's electron cloud, producing upon "collision" a small dipole moment that changes in magnitude and direction rapidly with time. Thus compressed gaseous mixtures of rare gas atoms absorb, whereas the components when separated and moderately pressurized do not. A pair of colliding helium atoms, for example, will not possess a resultant electronic cloud of dipolar asymmetry, whereas a helium–neon pair will modulate the electromagnetic field over a broad band of far-infrared frequencies commensurate with the most probable frequencies at which interatomic collisions occur. Atomic-induced absorption is of a purely translational origin, a mechanism that persists in molecular fluids such as hydrogen and nitrogen as the absorption $\Delta J=0$, where J is the rotational quantum number. A dipole moment set up between a pair of colliding molecules will in addition absorb by rotational means since even without relative translation of molecular centers, the effect on each other of their rotatory electrostatic fields will not cancel. A practical means of dealing with these intermolecular absorption mechanisms is to treat them separately. The rotational absorption is dealt with by expanding the field in terms of multipole tensors, which all vanish only in the case of spherical symmetry such as that of atoms.

Pseudospherical molecules such as SF_6 retain the higher multipoles (those above and including the hexadecapole for O_h symmetry), and thus display a weak, rotational-induced band at moderately higher number densities. The first nonvanishing multipole in a homogeneous diatomic such as N_2 is the quadrupole, which produces a dipole on molecule A which is modulated by the rotational motion of the inducing molecule B. The symmetry of the quadrupole moment is such that it rotates twice as fast as the molecule itself and thus produces quantum absorptions with the selection rule $\Delta J=2$, in contrast with the $\Delta J=1$ rule for the rotation of a permanent dipole. Similarly, the first nonzero multipole moment for T_d symmetry—the octopole—produces $\Delta J=3$, and the hexadecapole $\Delta J=4$. The formal quantum-mechanical equation for multipole-induced dipole absorption has been developed by Colpa and Ketelaar[117] for linear molecules, and extended as follows by Frost.[116]

The absorption is attributed to the mutually induced dipole moment $\mu(R)$ on orientations of the molecules is expressed by expanding $\mu(R)$ in terms of quantities $D^{\lambda_1}_{\mu_1\nu_1}(\phi_1,\theta_1,\chi_1)D^{\lambda_2}_{\mu_2\nu_2}(\phi_2,\theta_2,\chi_2)$, where a $D^{\lambda}_{\mu\nu}$ is a matrix element of an irreducible representation of the rotation group. This permits evaluation of matrix elements of $\mu(R)$ between eigenstates of a molecular pair. The expansion coefficients are then evaluated in terms of the polarizabilities and multipole moments (of any order) of the molecules. The theory performs summations over "uninteresting" magnetic quantum numbers and produces expressions for the intensity of pressure-induced in terms of Clebsch–Gordan coefficients. The center-of-mass motion of each molecule is treated classically, with each molecule at rest, so translational absorption is ignored. The pressure-induced intensity of an absorption band is calculated in terms of quantities:

$$\sum_{m_i m_f} |\langle im_i|\mu(R)|fm_f\rangle|^2 \tag{IV.1}$$

where $|im_i\rangle, |fm_f\rangle$ denote rotation–vibration energy eigenstates for the pair, with m_i, m_f as degenerate magnetic quantum numbers. The dipole moment $\mu(R)$ which occurs in (IV.1) is a sum of two parts:

$$\mu(R)=\mu(1;R)+\mu(2;R) \tag{IV.2}$$

where $\mu(1;R)$ is the moment induced in molecule 1 by the electric field of molecule 2, and vice versa. The electric field at 1 due to 2 depends on the orientation ϕ_2; θ_2, χ_2 and the vibration coordinate s_2 of 2, while the polarizability of 1 depends on its orientation ϕ_1, θ_1, χ_1 and vibration coordinate s_1. Therefore, $\mu(1;R)$ depends on the orientation and vibration coordinates of both molecules. The same applies to $\mu(2;R)$, so

$$\mu(R)=\mu(R;\phi_1,\theta_1,\chi_1,s_1;\phi_2,\theta_2,\chi_2,s_2)$$

Although the molecules are interacting, it is assumed that an eigenstate of the pair is simply a product of eigenstates of the isolated molecules. This result is exact only if the intermolecular potential is independent of the Euler angles θ, ϕ, χ, and therefore the theory is restricted to the range where R is determined primarily by the central part $U(R)$ of the interaction potential. Frost now takes the intensity (I) of the absorption band as defined by Colpa and Ketelaar for a gas consisting of two types of molecule, species A of number density n_A and species B.

$$I=I_{AA}+I_{BB}+I_{AB} \tag{IV.3}$$

where

$$I_{AB}=\frac{8\pi^3\nu}{3hc}\frac{(2-\delta_{AB})}{2}n_A n_B \sum_{\substack{i,f\\ E_f-E_i\simeq h\nu}}\left(\frac{F_i^{AB}}{d_i^{AB}}-\frac{F_f^{AB}}{d_f^{AB}}\right)$$

$$\times\int 4\pi R^2\exp(-U_{AB}(R)/kT)\sum_{m_i m_f}\left|\langle im_i|\mu^{AB}(R)|fm_f\rangle\right|^2 dR$$

The summations over the quantum numbers i,f are restricted to those transitions $i\to f$ for which the absorbed frequency $h^{-1}(E_f-E_i)$ lies in the absorption band of approximate frequency ν. The quantities d_i, d_f are the degeneracies of the quantum numbers i, f $[d_i=(2J_1+1)(2J_2+1)]$. The quantities F_i, F_f are the fractional populations of pair states with quantum numbers i, f, respectively: for example,

$$F_i=\frac{d_i\exp(-E_i/kT)}{\sum_j d_j\exp(-E_j/kT)}$$

We emphasize that $\mu(R)$ is the *induced* dipole moment of a pair of molecules and does not include the permanent dipole moment $\mathbf{p}^{(1)}+\mathbf{p}^{(2)}$ of the pair. The latter is independent of R and leads to a divergence of (IV.3), which gives absorption which may be attributed, *with the neglect of pressure broadening effects*, to transitions of isolated molecules. Later we shall show how pressure broadening may be accounted for classically using approximants of (I.6). Evaluation of the dipole moment matrix elements yields; for pure rotational transitions

$$\sum_{m_i m_f}\left|\langle im_i|\mu(R)|fm_f\rangle\right|^2$$

$$=\sum_{\lambda_1\lambda_2}\sum_{\mu_1\mu_2}\sum_m|F_m(R,\lambda_1,\mu_1,K_1'-K_1;\lambda_2,\mu_2,K_2'-K_2)|$$

$$\times\frac{2J_1+1}{2\lambda_1+1}C(J_1,\lambda_1,J_1';K_1,K_1'-K_1,K_1')^2$$

$$\times\frac{2J_2+1}{2\lambda_2+1}C(J_2,\lambda_2,J_2';K_2,K_2'-K_2,K_2')^2 \qquad \text{(IV.4)}$$

in terms of Clebsch–Gordan coefficients C. Here the dipole moment $\mu(R)$ is regarded with rectangular Cartesian components $\mu_j(R)(j=1,2,3)$ relative to the space fixed frame. These are Hermitian operators. Each of μ_1 in

(II.5) then ranges from $-\lambda_1$ to $+\lambda_1$. J and K are defined by the rotational part of the molecular eigenstate of a rigid symmetric top:

$$|JKM\rangle=\psi_{JKM}(\phi,\theta,\chi)=\left(\frac{2J+1}{8\pi^2}\right)^{1/2}D^J_{-M,-K}(\phi,\theta,\chi)$$

where the D values are the irreducible representations of the rotation group as defined by Rose. The expansion coefficient F_m depends on molecular parameters such as the polarizability and is in practice negligible for all but a few values of λ_1 and λ_2. To evaluate F_m we want the Cartesian components in the space fixed frame of the induced dipole moment $\mu(R)$ in the form

$$\mu_j(R)=\sum_k\alpha_{jk}^{(1)}(s_1,\phi_1,\theta_1,\chi_1)E_k^{(2)}(R;s_2,\phi_2,\theta_2,\chi_2)$$

$$+\sum_k\alpha_{jk}^{(2)}(s_2,\phi_2,\theta_2,\chi_2)E_k^{(1)}(R;s_1,\phi_1,\theta_1,\chi_1) \qquad \text{(IV.5)}$$

where, for example, the $\alpha_{jk}^{(1)}$ are the components of the polarizability tensor $\alpha^{(1)}$ of molecule 1, while the $E_k^{(2)}$ are the components of the electric field at molecule 1 due to molecule 2. The polarizability tensor is then cast into a spherical form relative to the space fixed frame. Let $\bar{x}_1$, $\bar{x}_2$, $\bar{x}_3$ denote the body fixed principal axes of inertia of a symmetric-top molecule, chosen so that the x_3 axis is the symmetry axis. Then there are also the principal axes of polarizability of the molecule; that is, if it is subjected to an external electric field, with Cartesian coordinates $\bar{E}_j$ relative to the $\bar{x}$-frame, the components of the induced moment are

$$\bar{\mu}_j=\sum_k\bar{\alpha}_{jk}(s)\bar{E}_k \qquad \bar{\alpha}=\begin{pmatrix}\alpha_\perp & 0 & 0\\ 0 & \alpha_\perp & 0\\ 0 & 0 & \alpha_\parallel\end{pmatrix} \qquad \text{(IV.6)}$$

The spherical component version of (IV.6) is then

$$\bar{\mu}_m=\sum_m\bar{A}_{m'm}(s)\bar{E}_m \qquad A=\begin{pmatrix}\alpha_\perp & 0 & 0\\ 0 & \alpha_\parallel & 0\\ 0 & 0 & \alpha_\perp\end{pmatrix} \qquad \text{(IV.7)}$$

The space fixed x-frame is then rotated into the $\bar{x}$-frame along with the components of the field and polarizability. It turns out that as far as polarizability is concerned, symmetric tops behave like linear molecules since, for both sorts, (IV.6) has two equal components.

The electric field is now expanded in terms of multipole moments. The electrostatic potential caused by a molecule at a point R, with polar coordinates R, Θ, Φ in the x-frame is then given by

$$V(R)=\sum_{\lambda=0}^{\infty}\sum_{\mu=-\lambda}^{\lambda}\left(\frac{4\pi}{2\lambda+1}\right)^{1/2}\frac{Q_\mu^\lambda Y_{\lambda\mu}^*}{R^{\lambda+1}}(\Theta,\Phi) \tag{IV.8}$$

Here the μth component of the λth multipole moment of the molecule in the x-frame is

$$Q_\mu^\lambda=\left(\frac{4\pi}{2\lambda+1}\right)^{1/2}\int\int\int \xi^\lambda Y_{\lambda\mu}(\alpha\beta)_p(s,\xi\alpha\beta)\xi^2 d\xi\sin\alpha\, d\alpha\, d\beta$$

where p is the charge density of the molecule at a point ξ with polar coordinates ξ, α, β in the x-frame. We then have for the required fields:

$$E_m(R^\pm)=\sum_\lambda E_m^\lambda(R^\pm)$$

with

$$E_m^\lambda(R^\pm)=(-1)^{m+1}(\pm 1)^{\lambda+1}\left(\sqrt{(\lambda+1)(2\lambda+3)}\ /R^{\lambda+2}\right)$$
$$\times C(\lambda+1,1,\lambda;0,-m,-m)\sum_\nu D^\lambda_{-m,\nu}(\phi\theta\chi)\overline{Q}_\nu^{\lambda *}$$

Here R^+ denotes the case $\Theta=0$ while R^- denotes $\Theta=\pi$. The multipole moment components of $\overline{Q}_\mu^\lambda$ of a symmetric top are severely limited by the fact that the x_3-axis is an n-fold axis of rotational symmetry, with $n\geq 3$. Therefore:

1. For $\lambda=1$, only $\overline{Q}_0^1$ is nonzero. Since $Q_\mu^{\lambda *}=(-1)^\mu Q^\lambda$, this quantity is real and is the usual dipole moment of the molecule.
2. For $\lambda=2$, only $\overline{Q}_0^2$ is nonzero. This real quantity is the usual quadrupole moment defined by $Q_0^2=q=q_{33}$, where

$$q_{ij}=\tfrac{1}{2}\int\int\int\rho\left(s,\bar\xi_1\bar\xi_2\bar\xi_3\right)\left[3\bar\xi_i\bar\xi_j-\bar\xi^2\delta_{ij}\right]d\bar\xi_1 d\bar\xi_2 d\bar\xi_3$$

   is the Cartesian quadrupole moment tensor in the principal frame.
3. For $\lambda=3$, only $\overline{Q}_0^3$ and $\overline{Q}_{\pm 3}^3$ are nonzero if $n=3$, while only $\overline{Q}_0^3$ is nonzero for $n>3$.
4. For $\lambda>3$ (hexadecapole moment and higher), the number of nonzero components $\overline{Q}_\mu^\lambda$ depends in an obvious way on n. For a linear molecule $n=\infty$, and each multipole moment has only one nonzero component $\overline{Q}_0^\lambda$.

The expansion coefficient F_m of (IV.4) may now be evaluated in terms of polarizability and multipole moments. The dipole moment induced in molecule 1 is then

$$\mu_m(1;R)=\alpha_0^{(1)}\sum_{\lambda_2}(-1)^{\lambda_2+1}\sqrt{(\lambda_2+1)(2\lambda_2+3)}\ R^{-(\lambda_2+2)}$$
$$\times\sum_{\mu_2\nu_2}(-1)^{1-\mu_2}\delta_{-\mu_2,m}\overline{Q}_{\nu_2}^{(2)\lambda_2^*}C(\lambda_2+1,1,\lambda_2;0,\mu_2,\mu_2)D^0_{0,0}(1)D^{\lambda_2}_{\mu_2\nu_2}(2)$$
$$+(-1)^m\sqrt{\frac{2}{3}}\ \delta^{(1)}\sum_{\lambda_2}(-1)^{\lambda_2+1}\sqrt{(\lambda_2+1)(2\lambda_2+3)}\ R^{-(\lambda_2+2)}$$
$$\times\sum_{\mu_1}\sum_{\mu_2\nu_2}(-1)^{1-\mu_2}\overline{Q}_{\nu_2}^{(2)\lambda_2^*}C(1,1,2;-m,-\mu_2,\mu_1)$$
$$\times C(\lambda_2+1,1,\lambda_2;0,\mu_2,\mu_2)D^2_{\mu,0}(1)D^{\lambda_2}_{\mu_2\nu_2}(2) \tag{IV.9}$$

A similar expression for $\mu_m(2;R)$ is obtained from (IV.9) by first omitting the factor $(-1)^{\lambda_2+1}$ and then interchanging all superscripts and subscripts 1 and 2. The sum of these yields an expansion of $\mu_m(R)$ in terms of the orientation functions $D^{\lambda_1}_{\mu_1\nu_1}(1)D^{\lambda_2}_{\nu_2\mu_2}(2)$. The expansion coefficients contain the polarizabilities α_0, anisotropies δ, and the multiple moments $\overline{Q}_\mu^\lambda$ of the molecules, quantities which are functions of the vibration coordinates s. Consequently, from each coefficient in this expansion of $\mu_m(R)$, we obtain the corresponding F_m by setting all vibration coordinates to their equilibrium values, (i.e., by using the equilibrium polarizabilities and multipole moments). It follows from (IV.9) and the corresponding equation for $\mu_m(2;R)$ that an $F_m(R;\lambda,\mu_1\nu_1;\lambda_2\mu_2\nu_2)$ is nonzero only if one of λ_1 or λ_2 is 0 or 2. F_m ($\lambda_1=0,\lambda_2=0$) is zero, since we presume that each molecule has no net charge (i.e., $\overline{Q}_0^0=0$). An F_m ($\lambda_1=0$ or $2,\lambda_2\neq 2$) is obtained entirely from the expansion of $\mu_m(1;R)$ (i.e., such an F_m depends only on the dipole moment induced in molecule 1 by molecule 2). An F_m ($\lambda_1\neq 2,\lambda_2=0$ or 2) is obtained entirely from the expansion of $\mu_m(2;R)$. The coefficient F_m ($\lambda_1=2,\lambda_2=2$) is the only one which must be calculated from the sum. The quantities

$$\sum_{m\mu_1\mu_2}|F_m(R,\lambda_1\mu_1\nu_1,\lambda_2\mu_2\nu_2)|^2$$

of (IV.4) may now be evaluated since they reduce to sums of Clebsch–Gordan coefficients. They are tabulated in Table IX.

TABLE IX
Summation of F_m in (IV.4)

λ_1	λ_2	$\Sigma\|F_m^2\|$
0	1	$\delta_{0\nu_1}\delta_{0\nu_2}6(\alpha_0^{\{1\}}\rho^{(2)})^2R^{-6}$
0	2	$\delta_{0\nu_1}\delta_{0\nu_2}15(\alpha_0^{\{1\}}q^{(2)})^2R^{-8}$
0	Any λ_2	$\delta_{0\nu_1}(\lambda_2+1)(2\lambda_2+1)(\alpha_0^{\{1\}}\|\bar{Q}_{\nu_2}^{(2)\lambda_2}\|)^2R^{-2(\lambda_2+2)}$
2	1	$\delta_{0\nu_1}\delta_{0\nu_2}(20/3)(\delta^{(1)}\rho^{(2)})^2R^{-6}$
2	Any $\lambda_2\neq 0,2$	$\delta_{0\nu_1}(10/9)(\lambda_2+1)(2\lambda_2+1)(\delta^{(1)}\|\bar{Q}_{\nu_2}^{(2)\lambda_2}\|)^2R^{-2(\lambda_2+2)}$
2	2	$\delta_{0\nu_1}\delta_{0\nu_2}(10/3)[5(\delta^{(1)}q^{(2)})^2+5(\delta^{(2)}q^{(1)})^2-6\delta^{(1)}\delta^{(2)}]R^{-8}$

Selection rules in (IV.3) arise from two sources:

1. General limitations on Clebsch–Gordan coefficients.
2. The nature of symmetric-top molecules is such that $\Sigma|F_m^2|$ is nonzero only for restricted values of ν_1 and ν_2. A term in (IV.4) is zero unless:

$$\Delta J_1 = J_1' - J_1 = 0, \pm 1, \ldots, \pm\lambda_1$$
$$\Delta K_1 = K_1' - K_1 = 0, \pm n_1, \ldots, \pm m_1 n_1 \qquad (m_1 n_1 \leq \lambda_1)$$
$$\Delta J_2 = J_2' - J_2 = 0, \pm 1, \ldots, \pm\lambda_2$$
$$\Delta K_2 = K_2' - K_2 = 0, \pm n_2, \ldots, \pm m_2 n_2 \qquad (m_2 n_2 \leq \lambda_2)$$

Here m_1 or m_2 is a positive integer or zero, while n_1 or n_2 denotes the rotational symmetry class of molecule 2, respectively. Since one of λ_1 or λ_2 in (IV.4) must be 0 or 2, the allowed transitions are any ΔJ_1, ΔJ_2 provided that one of $|\Delta J_1|, |\Delta J_2| \leq 2$; $\Delta K_1 = \pm m_1 n_1$, $\Delta K_2 = \pm m_2 n_2$ provided that one of $m_1, m_2 = 0$; $m_1 = 0$ if $|\Delta J_2| > 2$, $m_2 = 0$ if $|\Delta J_1| > 2$. An allowed transition will contribute to (IV.4) only through terms with λ_1, λ_2 such that $\lambda_1 \geq \max[|\Delta J_1|, |\Delta K_2|]$, $\lambda_2 \geq \max[|\Delta J_2|, |\Delta K_2|]$. For example, if the dipole and quadrupole moments are the only important ones, the summation in (IV.4) is over $\lambda_1 \leq 2$; $\lambda_2 \leq 2$, and the selection rules reduce to $\Delta J_1 = 0, \pm 1, \pm 2$; $\Delta K_1 = 0$; $\Delta J_2 = 0, \pm 1, \pm 2$; $\Delta K_2 = 0$. If the octopole moments are also important, and if both molecules have threefold rotational symmetry, the summation in (IV.4) is over $\lambda_1 \leq 3$, $\lambda_2 \leq 3$, and the selection rules are

$\pm\Delta J_1 = 0, 1, 2$	0, 1, 2	3	0, 1, 2
$\pm\Delta J_2 = 0, 1, 2$	0, 1, 2	0, 1, 2	3
$\pm\Delta K_1 = 0$	3	0, 3	0
$\pm\Delta K_2 = 0, 3$	0	0	0, 3

where any combination may be chosen within a given block. For a given allowed transition in a pair of true symmetric tops, there will in general be contributions to (IV.4) from all (λ_1, λ_2) terms with λ_1 and λ_2 bounded below and above by the selection rules, by whatever are taken as the important multiple moments and by the demand that one of λ_1 or λ_2 is 0 or 2. For example, if the transition is $\Delta J_1 = 1$, $\Delta J_2 = 1$, $\Delta K_1 = \Delta K_2 = 0$, then in general all the terms with $(\lambda_1, \lambda_2) = (1,2), (2,1), (2,2), (2,3), (3,2)\ldots$ will contribute to (IV.4). Finally, only those terms contribute in (IV.4) for which $\lambda_1 + \Delta J_1$ is even.

For a pair of linear molecules the selection rules become any ΔJ_1, ΔJ_2 provided one of ΔJ_1 or ΔJ_2 is 0 or ± 2. An allowed transition will contribute only through (λ_1, λ_2) terms for which

$$\lambda_1 \geq |\Delta J_1| \qquad \lambda_1 + \Delta J_1 \text{ is even}$$
$$\lambda_2 \geq |\Delta J_2| \qquad \lambda_2 + \Delta J_2 \text{ is even}$$

B. Linear Molecules—The Intermolecular Potential in O_2 Gas[118]

In this section we illustrate the intricate general theory by demonstrating how the rotational absorptions of the O_2-induced dipole may be explained in terms of a modified potential consisting of a quadrupole and hexadecapole moment. The theory is applied to the case of compressed O_2 gas, whose absorption, observed by Bosomworth and Gush[119] in the region 20 to 400 cm^{-1}, could not be explained satisfactorily on the basis of quadrupole-induced dipole absorption alone. Values of $|Q|$ and $|\Phi|$, the quadrupole and hexadecapole moments, are obtained from the best fit to the experimental intensity and band shape. A justification for the use of the very short range (R^{-12}-dependent) hexadecapole field is based on the evaluation of the approximate range of the induced dipole moment. Equation (IV.4) is conveniently presented in terms of the dipole, quadrupole, octopole, and hexadecapole terms. We include the anisotropy terms (δ), but these are small.

Dipole / Induced Dipole Absorption

$$A^{\mu}_{J\to J+1} = \frac{4\pi^3\mu^2N^2}{3hcZ}\int_0^\infty 4\pi R^{-4}\exp(-U_{AA}(R)/kT)dR$$
$$\times(1-\exp(-hc\bar{\nu}_1(J)/kT))\exp(-E_J hc/kT)\bar{\nu}_1(J)$$
$$\times\left(4\alpha_0^2(J+1)+\frac{8}{3}\delta^2\frac{(J+1)^2(J+2)}{(2J+3)}\right) \qquad \text{(IV.10)}$$

where

$$\bar{\nu}_1(J)=2B(J+1) \qquad \text{and} \qquad E_J=BJ(J+1)$$

Quadrupole / Induced Dipole Intensity

$$
\begin{aligned}
{}_IA^{Q}_{J\to J+2}=&\frac{4\pi^3Q^2N^2}{3hcZ}\int_0^\infty 4\pi R^{-6}\exp(-U_{AA}(R)/kT)dR\\
&\times(1-\exp(-hc\bar{\nu}_2(J)/kT))\exp(-E_Jhc/kT)\bar{\nu}_2(J)\\
&\times\left[9\alpha_0^2\frac{(J+1)(J+2)}{(2J+3)}+\frac{18}{5}\delta^2\left(\frac{(J+1)(J+2)}{(2J+3)}\right)^2\right] \qquad \text{(IV.11)}
\end{aligned}
$$

where $\bar{\nu}_2(J)=2B(2J+3)$.

Octopole / Induced Dipole Intensity

$$
\begin{aligned}
{}_IA^{\Omega}_{J\to J+3}=&\frac{4\pi^3\Omega^2N^2}{3hcZ}\int_0^\infty 4\pi R^{-8}\exp(-U_{AA}(R)/kT)dR\\
&\times(1-\exp(-hc\bar{\nu}_3(J)/kT))\exp(-E_Jhc/kT)\bar{\nu}_3(J)\\
&\times\left[40\alpha_0^2\frac{(J+1)(J+2)(J+3)}{(2J+3)(2J+5)}+\frac{80}{3}\delta^2\left(\frac{(J+1)(J+2)}{(2J+3)}\right)^2\frac{(J+3)}{(2J+5)}\right]
\end{aligned}
\qquad \text{(IV.12)}
$$

where $\bar{\nu}_3(J)=6B(J+2)$.

Hexadecapole / Induced Dipole Intensity

$$
\begin{aligned}
{}_IA^{\Phi}_{J\to J+4}=&\frac{4\pi^3\Phi^2N^2}{3hcZ}\int_0^\infty 4\pi R^{-10}\exp(-U_{AA}(R)/kT)dR\\
&\times(1-\exp(-hc\bar{\nu}_4(J)/kT))\exp(-E_Jhc/kT)\bar{\nu}_4(J)\\
&\times\left[\frac{175(J+1)(J+2)(J+3)(J+4)}{2(2J+3)(2J+5)(2J+7)}\alpha_0^2\right.\\
&\left.+\frac{875}{12}\delta^2\left(\frac{(J+1)(J+2)}{(2J+3)}\right)^2\frac{(J+3)(J+4)}{(2J+5)(2J+7)}\right] \qquad \text{(IV.13)}
\end{aligned}
$$

where $\bar{\nu}_4=4B(2J+5)$.

By comparison with oxygen, the induced zero-THz absorption in N_2 is much narrower and is fairly well simulated by the frequencies and relative intensities of the unbroadened $\Delta J=2$ rotational transitions calculated[119] with an equation similar to (IV.11). The *induced* absorption in N_2 has also been simulated by computer molecular dynamics by Jacucci, Buontempo, and Cunsolo.[120] Bosomworth and Gush[119] attributed the high-frequency part of the oxygen spectrum to a short-range overlap contribution to the dipole moment, but made no quantitative analysis of the phenomenon. However, with (IV.10) to (IV.13) it is possible to simulate the oxygen band with two contributions to the bimolecular collision-induced dipole moment, assumed to arise from the quadrupole and hexadecapole moments of the field of the second oxygen molecule, and vice versa. Oxygen has no dipole or octopole moment by symmetry. The hexadecapole field, being R^{-12}-dependent, is important only at very short separations R. Justification for its employment comes from a simple analysis given by Bosomworth and Gush involving a rough measurement of p, the range of the induced dipole moment, which may be obtained from the width of the spectrum. Classically, the spectrum is proportional to the Fourier transform of the correlation function of the dipole moment; the width function of the induced dipole is roughly equal to the duration of the collision. Thus

$$\tau=\frac{1}{2\pi\bar{\nu}_{1/2}c} \qquad \text{(IV.14)}$$

where $\bar{\nu}_{1/2}$ is the width of the spectrum at half peak height. For oxygen at 300°K, $\bar{\nu}_{1/2}=160\ \text{cm}^{-1}$; thus $t=0.1$ psec. Then p can be estimated by multiplying the duration of collision (τ) by the average rate of change of the intermolecular distance ($\dot{R}_{av}$). Now $\frac{1}{2}m\dot{R}_{av}^2=\frac{1}{2}kT$, where m is the reduced mass of the colliding molecules. Thus $p=R_{av}\tau=0.055$ nm at 300°K. The Lennard-Jones diameter (σ) of an O_2–O_2 pair is 0.792 nm; thus the induced dipole moment is practically zero until the colliding O_2 molecules enter the repulsion part of the intermolecular potential, and rises rapidly as the van der Waals contours interpenetrate. In other words, the high-frequency wing arises from the absorption of the dipole moment induced in the temporary O_2–O_2 pairs.

Values of $|Q|$ and $|\Phi|$ can be estimated (Fig. 71) by resolving the O_2 profile into a quadrupole-induced and hexadecapole-induced dipole absorption band. These are based on line spectra calculated from the even J values in (IV.11) and (IV.13) since oxygen has no odd J due to nuclear spin statistics. Of course, the considerable broadening of each line expected in practice might lead to a different overall profile than that suggested by the

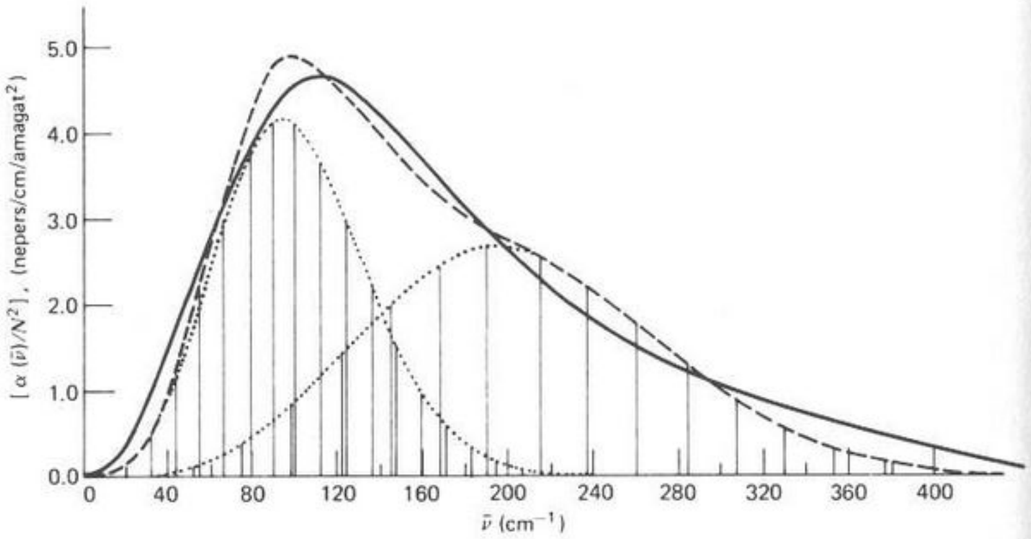

Fig. 71. (—), Experimental (Bosomworth and Gush) absorption of compressed oxygen. (· · · ·), Profiles of the $J \rightarrow J+2$ (quadrupole-induced) and $J \rightarrow J+4$ (hexadecapole-induced) dipole transitions. (---), Overall theoretical profile. Ordinate: $[\alpha(\bar{\nu})/N^2]$ (nepers/cm/amagat^2); abscissa: $\bar{\nu}$ (cm^{-1}). [Reproduced by permission from *Mol. Phys.*, **29**, 1345 (1975).]

line spectrum even if this ever exists in practice; nevertheless, a forced agreement can be obtained[118] with simple profile joining. Using $\epsilon/k = 118°\text{K}$, $\sigma = 0.346$ nm, $B = 1.45$ cm^{-1}, $\alpha_0 = 1.6\times10^{-24}$ cm^3, $\delta = 1.14\times10^{-24}$ cm^3 gives

$$\sum_{2nJ} {}_{l}A^{Q}_{J\rightarrow J+2} = 3.61\times10^{-5}N^2Q^2 \quad \text{nepers/cm}^2\text{/amagat}^2$$

$$\sum_{2nJ} {}_{l}A^{\Phi}_{J\rightarrow J+4} = 4.51\times10^{-5}N^2\Phi^2 \quad \text{nepers/cm}^2\text{/amagat}^2$$

$$\left(\int_0^\infty \frac{\alpha(\bar{\nu})}{N^2}\,d\bar{\nu}\right) = 8.65\times10^{-5} \quad \text{nepers/cm}^2\text{/amagat}^2$$

Summing (IV.11) and (IV.13) over 2 nJ, we find, for empirical (forced) agreement,

$$|Q| = 1.0\times10^{-40}\ \text{cm}^2 \qquad |\Phi| = 3.7\times10^{-60}\ \text{cm}^4$$

The value of $|Q|$ compares well with that of -1.34×10^{-40} cm^2 found by induced birefringence, and $|\Phi|$ is the "expected" order of magnitude.

The hexadecapole moment is one facet of transient O_4 formation which may be interpreted perhaps in other ways which are theoretically less convenient. A complete treatment of the O_2 absorption would have to include in addition such complicated factors as:

1. The overlap dipole contribution.
2. Translational and rotational contributions of the interference between the quadrupolar and overlap induction, and of the hexadecapole and overlap induction.
3. The pure translational ($\Delta J_1 = \Delta J_2 = 0$) contribution observable clearly in the H_2-induced absorption.[119]
4. Classical broadening[121] of the quantum stick spectra.

In the next section we use the J-diffusion model to investigate the effect factor 4 for cyanogen and its zero-THz absorption.

C. Quadrupole Induced Absorption in $(CN)_2$: Classical Broadening

In order to develop this theory we need to extract the Fourier transforms of (IV.10) to (IV.13) as follows. These equations may be manipulated into a continuous form, conveniently with time as a variable. The usual expression for a rotational absorption band shape, in terms of transitions between quantum states, is

$$I(\omega) = \frac{3\hbar c\sigma(\omega)}{4\pi^2\omega[1-\exp(-\hbar\omega/kT)]} \tag{IV.15}$$

where σ is the absorption cross-section per molecule. The Fourier transform

$$F(t) = \int_{-\infty}^{\infty} \omega^2 I(\omega)\exp(i\omega t)\,d\omega \tag{IV.16}$$

is recommended by Gordon and used here to weight the intensity toward the higher frequencies ($10 \lesssim \bar{\nu} \lesssim 450$ cm^{-1}), where accurate data are available. Here $\sigma(\omega) = \alpha(\omega)/N$, where α is the power absorption coefficient and N the number density in molecules/cm^3. The theoretical functions of time are obtained by substituting into (IV.16) using the continuous expression for the contours passing through the points of $I(\bar{\nu})$ obtained by eliminating J. For a linear molecule in the absence of broadening, one has then the

theoretical contour

$$I_{\text{th}}(\bar{\nu}) \propto \left(\frac{\bar{\nu}}{2B} - \frac{2B}{\bar{\nu}}\right) Q^2 \exp\left[-\frac{hcB}{4kT}\left(\frac{\bar{\nu}}{2B} - 3\right)\left(\frac{\bar{\nu}}{2B} - 1\right)\right] A_8$$
$$\times \left[12\alpha_0^2 + \frac{24}{5}\left(\frac{\bar{\nu}}{2B} - \frac{2B}{\bar{\nu}}\right)\delta^2\right] + \frac{(\bar{\nu}+4B)(\bar{\nu}+12B)}{\bar{\nu}(\bar{\nu}+8B)}\Phi^2$$
$$\times \exp\left[-\frac{hcB}{4kT}\left(\frac{\bar{\nu}}{4B} - 5\right)\left(\frac{\bar{\nu}}{4B} - 3\right)\right] A_{12}\left[\frac{175}{96}\alpha_0^2\left(\frac{(\bar{\nu}-12B)(\bar{\nu}-4B)}{B(\bar{\nu}-8B)}\right)\right.$$
$$\left. + \frac{875}{36}\delta^2\left(\frac{\bar{\nu}}{2B} - \frac{2B}{\bar{\nu}}\right)^2\right] \qquad \text{(IV.17)}$$

where

$$A_n = \frac{\pi^3 N^2}{hcZ}\int_0^\infty 4\pi^2 R^{-n} \exp(-U_{AA}(R)/kT) R^2 dR \qquad \text{(IV.18)}$$

In the time domain, therefore,

$$C_{\text{th}}(t) = \int_0^\infty I_{\text{th}}(\bar{\nu})\bar{\nu}^2 \exp(2\pi i\bar{\nu}ct)\, d\bar{\nu} \Big/ \int_0^\infty I_{\text{th}}(\bar{\nu})\bar{\nu}^2\, d\bar{\nu}$$

The direct Fourier transform of the experimental data can be made in the same way, giving

$$C_{\text{exp}}(t) = \int_0^\infty \frac{\bar{\nu}\alpha(\bar{\nu})\exp(2\pi i\bar{\nu}ct)\, d\bar{\nu}}{(1-\exp(-hc\bar{\nu}/kT))} \Big/ C_{\text{exp}}(0) \qquad \text{(IV.19)}$$

The functions $C_{\text{th}}(t)$ and $C_{\text{exp}}(t)$ are compared for various values of $|Q|$ and $|\Phi|$ in Figs. 72 to 74 in the compressed gaseous states of oxygen, carbon dioxide, and cyanogen. Fourier transforms are carried out directly, by Simpson's rule, and via the fast Fourier transform algorithm of Cooley and Tukey, implemented in *Algol* by Singleton and developed by Baise.[122] The time functions seem to be extraordinarily sensitive to small changes in $|Q|$ and $|\Phi|$ used. This is illustrated in Fig. 72 for oxygen where the previous section's frequency-domain curve fittings, using values of $|Q| = 0.30 \times 10^{-26}$ esu, yields a $C_{\text{th}}(t)$ function which is quite severely underdamped compared with $C_{\text{exp}}(t)$. However, with slight changes, $|Q| = 0.36 \times 10^{-26}$ esu, and $|\Phi| = 0.4 \times 10^{-42}$ esu a much better fit is obtained, $C_{\text{th}}(t)$ now showing very short time "oscillations," although they are slightly displaced along the time axis from those of $C_{\text{exp}}(t)$. Analysis in the time domain, then, is quite pronouncedly more sensitive than that in the frequency domain.

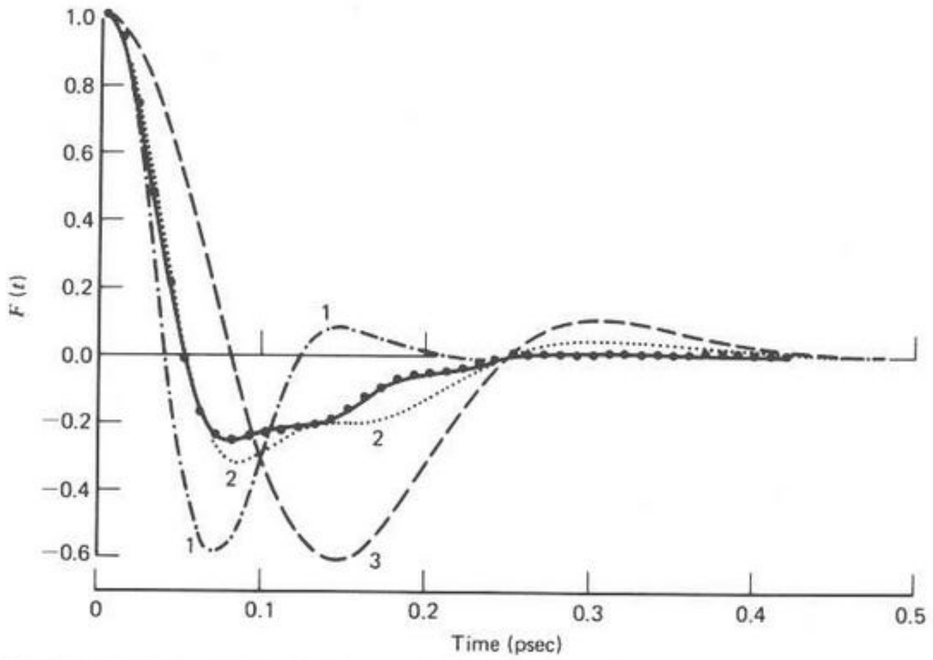

Fig. 72. Fourier transforms for O_2 gas at 300°K, 35 to 75 amagat. (●–●–●), Exp(t) as derived from two different algorithms. (----), (1) $C_{\text{th}}(t)$ calculated with $|Q| = 0.30 \times 10^{-26}$ esu, $|\Phi| = 1.1 \times 10^{-42}$ esu; (2) $F_{\text{th}}(t)$ with $|Q| = 0.36 \times 10^{-26}$ esu, $|\Phi| = 0.4 \times 10^{-42}$ esu; (3) $F_{\text{th}}(t)$ with $|Q| = 0.38 \times 10^{-26}$ esu, $|\Phi| = 0$. [Reproduced by permission from *J. Chem. Soc. Faraday Trans. 2*, **71**, 1257 (1975).]

However, for cyanogen, no satisfactory fit can be obtained. The extraction of a continuous-time-domain function $C_{\text{th}}(t)$ by transforming the sum of the profiles of the $\delta(\bar{\nu})$ functions may be affected by neglect of the classical broadening of each line observed in practice (i.e., the experimental absorption is a broad band and not an assembly of lines). A broadening mechanism based on the Gordon J-diffusion will be considered presently, but a few remarks on the cyanogen spectrum are needed first. The only satisfactory feature of Fig. 74 is that of the $|Q|$ and $|\Phi|$ used confirm an intuitive expectation of certainly a large molecular quadrupole moment, and possibly a large hexadecapole moment as well. The $C_{\text{th}}(t)$ curves are not underdamped compared with the $C_{\text{exp}}(t)$ curves, which suggests that triple collisions are not important at 33.5 bars. Attempts to modify the Frost theory[116] with angle-dependent intermolecular potentials such as $U_{AA}(R) + U_{QQ}$ will have no effect on the normalized line shape because U_{QQ} is independent of the rotational state of a molecule provided that the rotational wave functions are assumed to be unperturbed. While the ab-

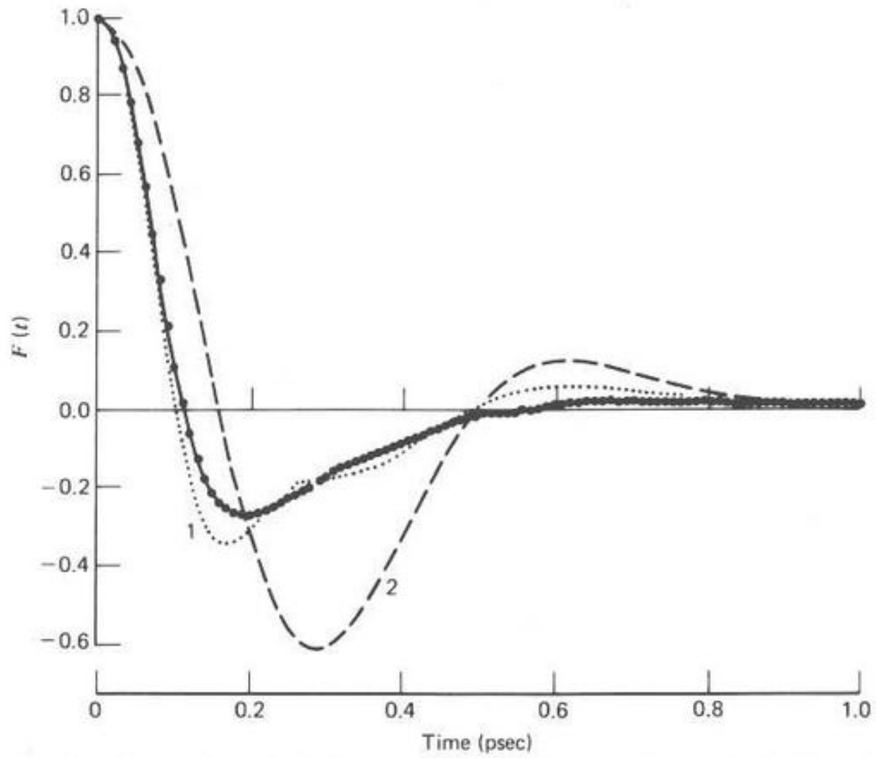

Fig. 73. Fourier transforms for CO_2 gas at 273°K, 85 amagat. (●–●–●) $C_{expt}(t)$ as derived from two separate algorithms. (----), (1) $C_{th}(t)$ with $|Q|=5.0\times10^{-26}$ esu, $|\Phi|=6.1\times10^{-42}$ esu. (2) $C_{th}(t)$ with $|Q|=5.2\times10^{-26}$ esu, $|\Phi|=0$. [Reproduced by permission from *J. Chem. Soc. Faraday Trans. 2*, **71**, 1257 (1975).]

solute values of $|Q|$ and $|\Phi|$ are very sensitive to the Lennard-Jones parameters ϵ/k and σ, the relative values of A_n will not be changed much. Therefore, ϵ/k and σ have little effect on the normalized line shape represented by $C_{th}(t)$. Quantum mechanically, therefore, a theory of pressure-induced absorption is needed which either disposes with point multipole expansions of the electrostatic field, or retains this approximation and then proceeds (albeit discordantly) to take into account the effect of molecular anisotropy on the eigenstate of a pair of molecules.

To broaden the set of $J\rightarrow J+2$ absorptions in compressed cyanogen, oxygen, or carbon dioxide, we assume that the broadened contour $C_b(t)$ has the general property of being an even function in time, and is also a solution of the integrodifferential equation

$$\dot{C}_b(t)=-\int_0^t K_b(t-\tau)C_b(\tau)\,d\tau \qquad \text{(IV.20)}$$

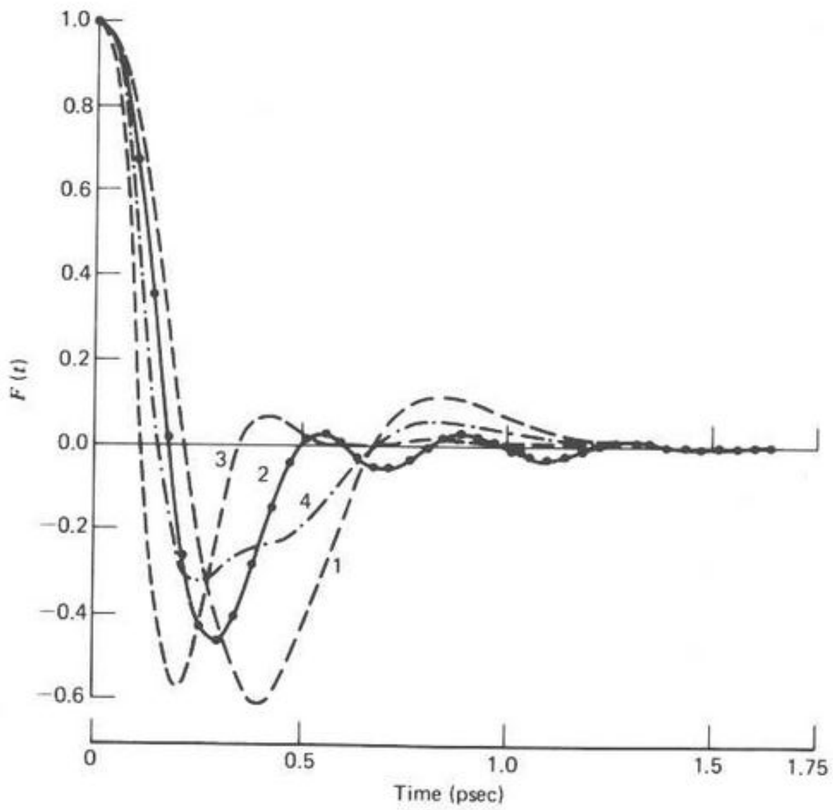

Fig. 74. Fourier transforms for $(CN)_2$ gas at 383°K, 33.5 bars. (●–●–●), $C_{exp}(t)$ as derived from two separate algorithms. (1) $C_{th}(t)$ with $|Q|=15.5\times10^{-26}$ esu, $|\Phi|=0$; (2) $C_{th}(t)$ with $|Q|=12.0\times10^{-26}$ esu, $|\Phi|=44\times10^{-42}$ esu; (3) $C_{th}(t)$ with $|Q|=9\times10^{-26}$ esu, $|\Phi|=56\times10^{-42}$ esu; (4) $C_{th}(t)$ with $|Q|=14.5\times10^{-26}$ esu, $|\Phi|=24\times10^{-42}$ esu. [Reproduced by permission from *J. Chem. Soc. Faraday Trans. 2*, **71**, 1257 (1975).]

where the memory kernel may be expanded in a set of coupled integrodifferential equations analogous to the Mori expansion.

$$\frac{\partial}{\partial t}K_{n-1}^{(b)}(t)=-\int_0^t K_n^{(b)}(\tau)K_{n-1}^{(b)}(t-\tau)\,d\tau \qquad \text{(IV.21)}$$

To effect broadening we now forge a link analogous to that leading to J-diffusion in the case of permanent dipolar absorption:

$$K_0^{(b)}(t)=K_s(t)\exp(-|t|/\tau) \qquad \text{(IV.22)}$$

where $K_s(t)$ is associated through an equation identical with (IV.20), with

$C_\delta(t)$ the correlation function of the set of unbroadened $J\rightarrow J+2$ transitions. For bimolecular, quadrupole-induced dipolar absorption in linear, nondipolar molecules, neglecting the hexadecapole term, we have

$$C_\delta(t)=\frac{\int_0^\infty f_0(\Omega)\cos\Omega t d\Omega}{\int_0^\infty f_0(\Omega)d\Omega} \tag{IV.23}$$

for each $J\rightarrow J+2$ transition, where

$$f_0(\Omega)=\left(\frac{\Omega}{4\pi Bc}-\frac{4\pi Bc}{\Omega}\right)\exp\left[-\frac{hcB}{4kT}\left(\frac{\Omega}{4\pi Bc}-3\right)\left(\frac{\Omega}{4\pi Bc}-1\right)\right] \tag{IV.24}$$

For nondipolar symmetric tops, up to the quadrupole term a similar, more complicated expression may be derived. $C_b(t)$ and $C_\delta(t)$ may now be linked by equations identical with (II.41) the broadened set of $J\rightarrow J+2$ lines is extracted from

$$\begin{aligned} C_b(\omega)&=\mathrm{Re}[\,C_b(i\omega)\,] \\ &=\mathrm{Re}\left[\frac{C_\delta(i\omega+\tau^{-1})}{1-\tau^{-1}C_\delta(i\omega+\tau^{-1})}\right] \end{aligned} \tag{IV.25}$$

where

$$C_\delta(i\omega+\tau^{-1})=\Gamma+i\Lambda$$

with

$$\Gamma(\omega)=\int_0^\infty f_0(\Omega)\left[\frac{\tau^{-1}(\Omega^2+\omega^2+\tau^{-2})}{(\Omega^2-\omega^2+\tau^{-2})^2+4\omega^2\tau^{-2}}\right]d\Omega\Big/\int_0^\infty f_0(\Omega)d\Omega$$

$$\Lambda(\omega)=\int_0^\infty f_0(\Omega)\left[\frac{\omega(\Omega^2-\omega^2-\tau^{-2})}{(\Omega^2-\omega^2+\tau^{-2})^2+4\omega^2\tau^{-2}}\right]d\Omega\Big/\int_0^\infty f_0(\Omega)d\Omega$$

The absorption coefficient $\alpha(\omega)$ is then given by

$$\alpha(\omega)=\frac{(\epsilon_0-\epsilon_\infty)\omega^2}{n(\omega)c}C_b(\omega) \tag{IV.26}$$

where $n(\omega)$ is the frequency-dependent refractive index, and c the velocity of light. For quadrupole-induced dipole absorption in pair collisions,

$$(\epsilon_0-\epsilon_\infty)=\frac{16\pi^2}{kT}N^2\bar{\alpha}_p Q\int_0^\infty R^{-6}\exp\left[-\frac{U_{AA}(R)}{kT}\right]dR$$

with $\bar{\alpha}_p$ as the mean molecular polarizability and Q the quadrupole moment.

Figure 75 shows how (IV.26) produces an absorption which simulates the broadening and eventually fuses the $J\rightarrow J+2$ lines in cyanogen ($B=0.1570\ \mathrm{cm}^{-1}$). A broad continuum is reached at $\tau=10$ psec, which, according to kinetic theory, corresponds to a mean free path of about 38 Å. Therefore, a continuum is reached well before triple collisions become sta tistically significant. Equation (IV.26) is matched with nitrogen data[121] in Figs. 76 and 77 (gas and liquid). An effective quadrupole moment of $|Q|=5\times10^{-40}\ \mathrm{cm}^2$ was extracted from this curve-fitting procedure for the total dispersion $(\epsilon_0-\epsilon_\infty)$. Despite the neglect of many factors, such as translational and electronic overlap absorption, this estimate of $|Q|$ compares

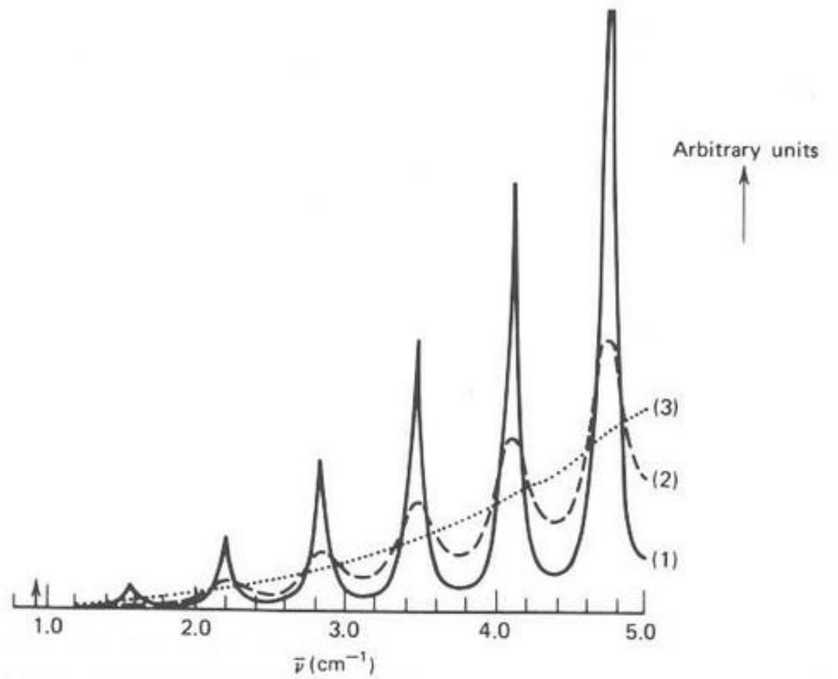

Fig. 75. First few $J\rightarrow J+2$ transitions for cyanogen broadened by (IV.26) at 350°K. (Rotational constant $B=0.1571\ \mathrm{cm}^{-1}$.) (1) $\tau=100$ psec, (2) $\tau=35$ psec, (3) $\tau=10$ psec. Abscissa: $\bar{\nu}$ (cm^{-1}). [Reproduced by permission from *Spectrochim. Acta*, **32A**, 1253 (1976).]

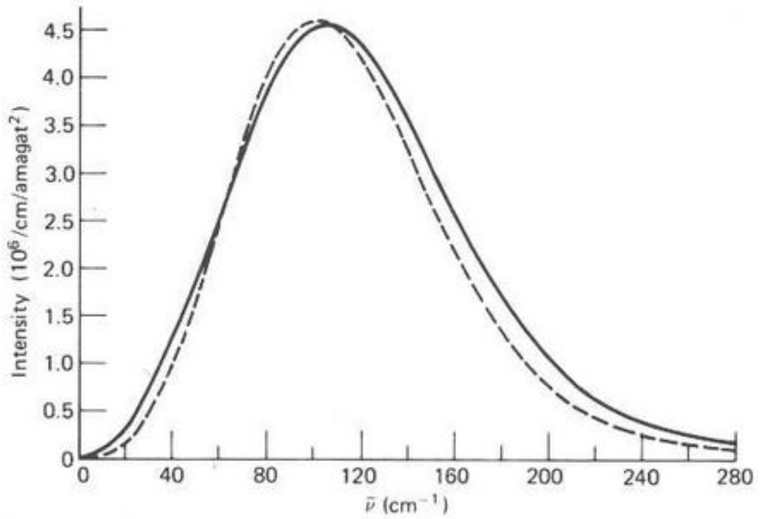

Fig. 76. (—), Experimental absorption of compressed nitrogen at 300°K. (----), Equation (IV.26) with $\tau = 0.4$ psec. $|Q| = 5 \times 10^{-40}$ cm^2. Ordinate: intensity (10^6 cm^{-1}/amagat^2); Abscissa: $\bar{\nu}$ (cm^{-1}). [Reproduced by permission from *Spectrochim. Acta*, **32A**, 1253 (1976).]

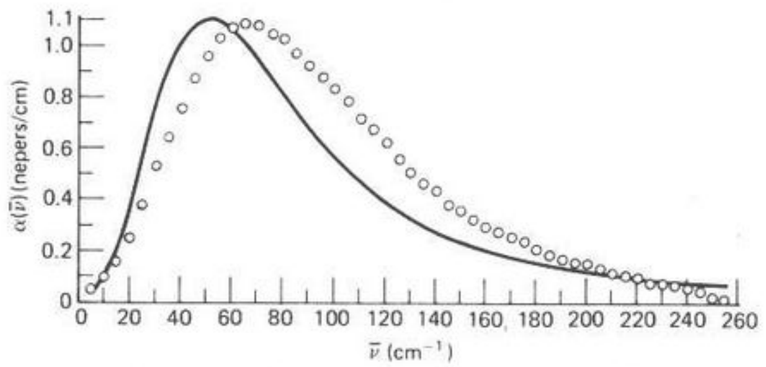

Fig. 77. O, Absorption of liquid nitrogen at 76.4°K. (—), Equation (IV.26) with $\tau = 0.1$ psec, $|Q| = 3 \times 10^{-40}$ cm^2. Ordinate: α (neper cm^{-1}); abscissa: $\bar{\nu}$ (cm^{-1}). [Reproduced by permission from *Spectrochim. Acta*, **32A**, 1253 (1976).]

favorably with Kielich's collection[123] of $|Q| = 4.5 - 6.9 \times 10^{-40}$ cm^2. Equation (IV.26) is less successful for $N_2(1)$ at 76.4°K (Fig. 77). The calculated curve is for $\tau = 0.1$ psec and normalized to the α_{max} of the observed band. The $|Q|$ estimated from this is 3×10^{-40} cm^2, significantly less than that deduced from the gas.

This apparent decrease in $|Q|$ on going from compressed gas to liquid is characteristic of a model of bimolecular-induced absorption. An explanation is the reduced effectiveness of multimolecular collisions in generating induced dipoles, as discussed earlier. In liquid CO_2, for example,[113] that

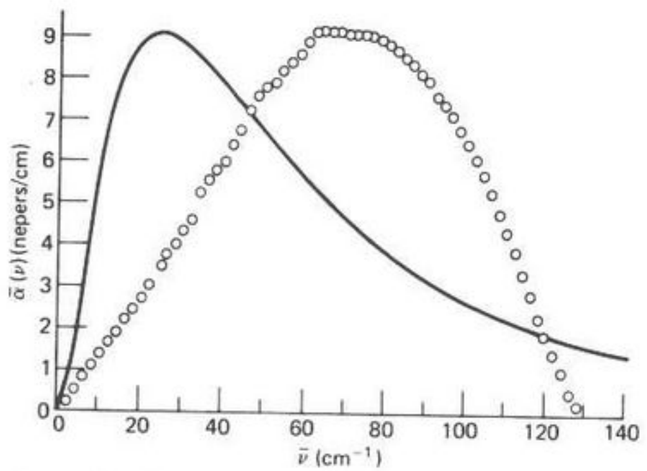

Fig. 78. Absorption of liquid cyanogen at 301°K. (—), Equation (IV.26) with $\tau = 0.1$ psec. $|Q| = 9.7 \times 10^{-26}$ esu. Ordinate: $\alpha(\bar{\nu})$ (nepers/cm); abscissa: $\bar{\nu}$ (cm^{-1}). [Reproduced by permission from *Spectrochim. Acta*, **32A**, 1253 (1976).]

part of the induced dipole moment due to quadrupolar induction is effectively canceled in the liquid, leaving essentially the contribution from shorter-range interactions.

Equation (IV.26) is not successful at all for cyanogen liquid[115] at 301°K, where analogously to the case of permanent dipole absorption, there is a large discrepancy between the observed and calculated $\bar{\nu}_{max}$ (Fig. 78). This shift in the observed $\bar{\nu}_{max}$ can be interpreted reasonably in terms of the increased amount of shorter-range interactions in the liquid phase where the torques in the rod-like molecules $(CN)_2$ will be greater than those N_2. This is saying merely that collision-interrupted free rotation is not the case in the liquid phase of the great majority of both nondipolar and dipolar liquids. The present J-diffusion type of model cannot move the position of $\bar{\nu}_{max}$ because the reorientation of the molecular angular momentum is assumed to take place during an infinitely short time, and it is thus impossible to get any information about, or take account of, the intermolecular mean-square torque.

However, a different continued-fraction representation might yield the correct absorption contour, by involving implicitly averages such as $K_0(0)$ and $K_1(0)$ which are both torque-dependent. An expression for $C_{th}(t)$ might then in principle be attainable which takes account of the contour in terms of the mean-square torque and its derivative. This method has been employed for compressed ethylene gas,[124] where the quantum theory fails even at low pressures. This empirical approach has been used successfully in nondipolar liquids, as described in the next section.

D. Absorptions in Nondipolar Liquids—Use of the Continued Fraction

Any absorption band in the infrared, whatever its molecular dynamical origin, is a probability distribution of frequencies, $C(\omega)$, and is related to a correlation function $C(t)$ by the fundamental statistical theorem, which is classically

$$C(t)=\int_0^\infty \cos\omega t\, dC(\omega) \tag{IV.27}$$

The quantum theory of induced absorptions in an N-body interaction is obviously hugely complicated, but in the classical limit (IV.27) holds quite generally if we define the correlation function $C(t)$ as follows:

$$C(t)=\sum_{i,j}\langle \boldsymbol{\mu}_j(t)\cdot\boldsymbol{\mu}_i(0)\rangle \tag{IV.28}$$

where $\boldsymbol{\mu}_i$ is the induced dipole on molecule i at time t. $C(t)$ is an orientation/interaction correlation function dependent simultaneously at time t on the orientation of a molecule with respect to all the others. We now expand $C(t)$ in a continued fraction formally identical to that of Mori, and truncate with

$$\tilde{K}_1(s)=K_1(0)/(s+\gamma) \tag{IV.29}$$

Using an equation such as (IV.26) then allows us to fit directly the frequency-domain data[5] iterating on $K_0(0)$, $K_1(0)$, and γ (Table X).

TABLE X
Parameters $K_1(0)$, $K_0(0)$, and γ for Nondipolar Liquids[a]

Liquid	Temp. (°K)	$10^{40}I_B$ (g·cm²)	$\gamma(I_B/2kT)^{1/2}$	$K_0(I_B/2kT)$	$K_1(I_B/2kT)$	$(\epsilon_0-\epsilon_\infty)$
Nitrogen	76.4	12.2	10.6	5.9	37.8	0.005
Carbon dioxide	273	71.2	11.5	8.6	51.9	0.007
CCL_4	296	484	14.2	10.9	80.6	0.002
CH_4 (rot. phase I)	76	5.34	10.6	14.7	47.9	0.009
Cyanogen	301	155	10.9	14.9	66.5	0.050
Methane	98	5.34	14.5	16.8	75.7	0.007
Benzene	296	198	12.8	20.8	100.6	0.023
CS_2	296	259	20.3	26.2	170.2	0.026
Cyclohexane	296	178	21.1	28.4	194.3	0.040
Trans-Decalin	296	1020	22.7	70.7	335.3	0.003
1,4-Dioxan	296	160	7.8	10.4	46.5	0.06

[a]Reproduced by permission from *J. Chem. Soc. Faraday Trans.* 2, **72**, 1194 (1976).

The three-variable fit is very close in the far infrared (Figs. 3 and 79) and there also is a tendency for $K_0(0)$ and $K_1(0)$ to increase as the geometrical anisotropy of each molecule. The absolute magnitude of the absorption can be related via $(\epsilon_0-\epsilon_\infty)$ to an "effective induced dipole" or higher multipole given some simplifying assumption about the molecular dynamical and electrostatic origin of these very broad bands. The increase in $K_0(0)$ and $K_1(0)$ is illustrated in Table X in units which take account of inertial factors. The satisfactory fits to experimental data over almost three decades of frequency show that the analytical dependence of α upon $\bar{\nu}$ is that of (IV.26) in this frequency range, but the physical interpretation of $K_0(0)$, $K_1(0)$, and γ remains obscure, apart from the obvious interaction dependence. The curves for $C(t)$ then can be calculated and are illustrated in Fig. 80, where are illustrated also some predictions of the "cell" model of Litovitz and co-workers and (where applicable) the model of multipole-induced absorption in a two-molecule collision. The latter is usually inadequate in describing the more complex interactions of the condensed phase.

We note finally that in deriving (IV.26) we are assuming that the molecular ensemble obeys classical equations of motion ($\hbar\to 0$). This is consistent with our basic assumption that Mori formalism is applicable to the classical correlation fraction defined in (IV.27). This assumption rests on the broad and related generalizations which lie at the root of our present understanding of transport properties (i.e., *linear* response and fluctuation–dissipation). Classically, the latter can be derived for a canonical ensemble using the Liouville equation:

$$\frac{dB}{dt}=\sum_i\left(\frac{\partial H}{\partial p_i}\frac{\partial B}{\partial q_i}-\frac{\partial H}{\partial q_i}\frac{\partial B}{\partial p_i}\right)$$

describing the motion of B which depends on time t by the intermediacy of coordinates q_i and their conjugate momenta p_i. Using quantized mechanics the Poisson brackets are replaced by the commutator $\hbar^{-1}[H,B]$, and the relation between a classical correlation function $\langle\boldsymbol{\mu}_i(0)\cdot\boldsymbol{\mu}_j(t)\rangle$ and the quantized analog $\langle[\boldsymbol{\mu}_i(0)\cdot\boldsymbol{\mu}_j(t)]\rangle$ is

$$\int e^{i\omega t}\langle[\boldsymbol{\mu}_i(0)\cdot\boldsymbol{\mu}_j(t)]\rangle\, d\omega=(1-e^{-\hbar\omega/kT})\int e^{i\omega t}\langle\boldsymbol{\mu}_i(0)\cdot\boldsymbol{\mu}_j(t)\rangle\, d\omega$$

The quantum-mechanical correlation function is real and contains odd powers of t in its Maclaurin expansion. The classical correlation function contains only even powers of t, in accord with the Onsager principle of time reversibility. Mori has shown that the equation of motion of an arbitrary dynamical variable of an arbitrary system can be transformed rigorously to a linear generalized Langevin equation form; and Kubo

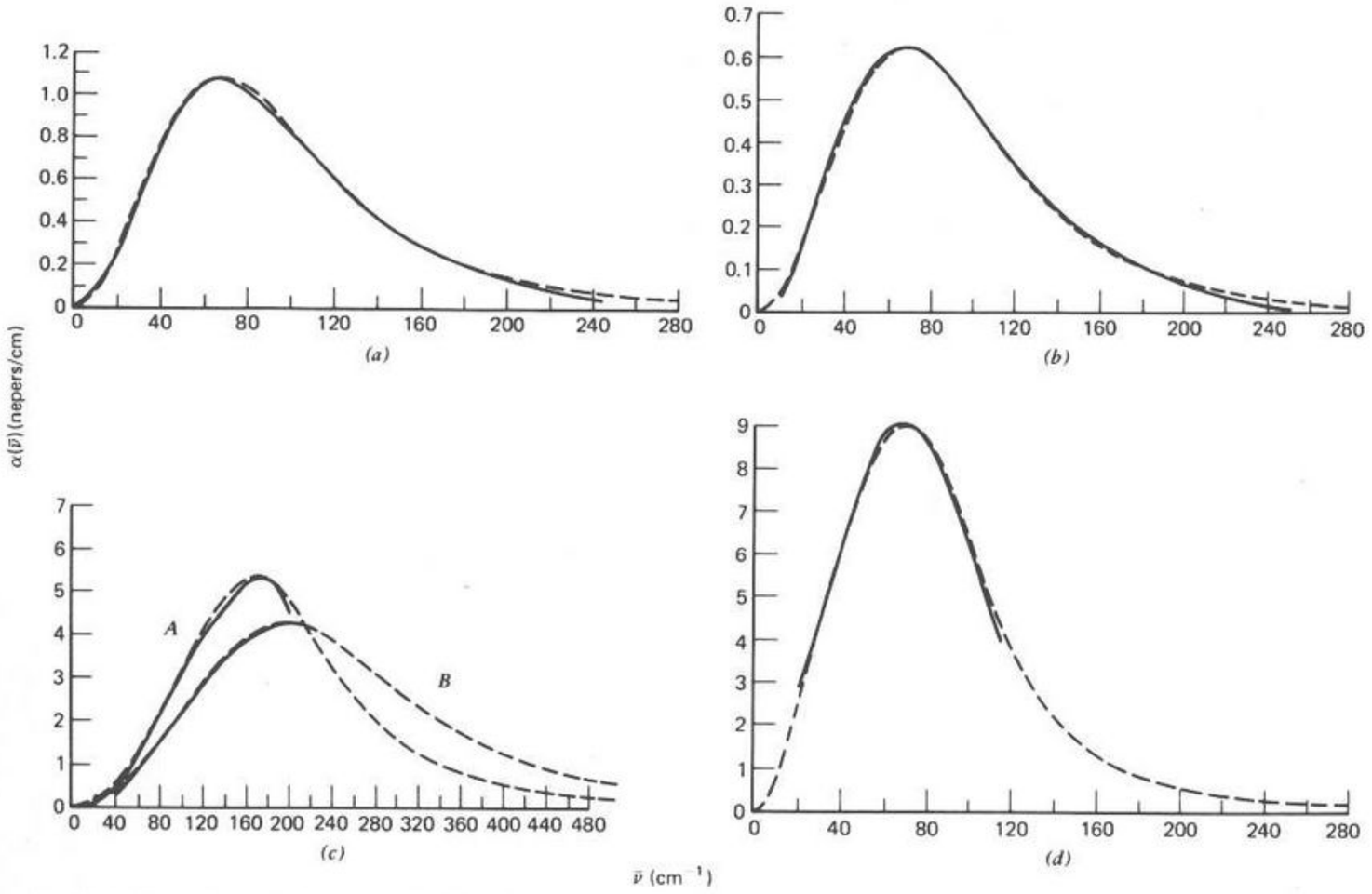

Fig. 79. (*a*) Experimental absorption for liquid nitrogen at 76.4°K. (----), Mori three-variable fit (Table X). (*b*) Liquid carbon dioxide at 273°K. (*c*) (*A*) Methane (rotator phase) at 76°K; (*B*) methane (liquid) at 98°K. (*d*) Liquid cyanogen at 301°K. [Reproduced by permission from *J. Chem. Soc. Faraday Trans. 2*, **72**, 1195 (1976).]

Fig. 80. Fourier transforms of $\alpha(\bar{\nu})$ for some nondipolar liquids. (1) Benzene; (2) carbon disulfide; (3) carbon tetrachloride; (4) cyclohexane; (5) *p*-difluorobenzene; (6) bicyclohexyl; (7) *trans*-decalin; (8) 1,4-dioxan; (9) trans-1,2-dichloroethylene. (—), Experimental; (—·—·—), free rotor; (---), Litovitz "cell" model; (···), function derived from three-variable theory. [Reproduced by permission from *J. Chem. Soc. Faraday Trans. 2*, **72**, 1195 (1976).]

shows that a subsystem of an ensemble when perturbed will relax to thermal equilibrium via the same generalized Langevin equation. Neither the arbitrary subsystem nor the variable need be quantized. That an ensemble of molecules as small as nitrogen or methane can be treated with classical equations of motion is the basis of the technique of computer molecular dynamics, including the simulations of Section III.

E. Effect of Kilobar Pressures on Liquids—Plastic Nondipolar Crystals

In this section we are concerned with the approach to the solid state in nondipolar fluids by application of external hydrostatic pressure and by freezing. Carbon disulfide can be solidified at room temperature by the application of 12 to 13 kbars of external pressure. The only far-infrared study available of the dependence of the induced absorption upon pressure is still that of Bradley, Gebbie, Gilby, Kechin, and King[125] in 1965, using prototype apparatus and pressures of up to 11.6 kbars. They found that the absorption peak shifts by about 35 cm^{-1} to higher frequency through the pressure-induced phase change at 293°K. We show here that this is equivalent to a large increase in both $K_0(0)$ and $K_1(0)$ [i.e., an increase in the mean-square torque (in the slope of the intermolecular potential dependence on orientation)]. Such pressure data are technically very difficult to come by, and we have taken the other approach (temperature) in liquid CCl_4 (298 to 343°K). The change in $K_0(0)$ and $K_1(0)$ with temperature is less pronounced, but real. The results are summarized in Table XI and Figs. 81 and 82. They were obtained[126] by fitting (IV.26) to the experimental data on the three-variable basis of Section (IV.D). At 11.6 kbars in $CS_2(l)$ it is clear from the zero-THz band that there is a greater probability that the motion of the induced dipole moment is associated with the central frequency (ω_0) of $\sim$100 cm^{-1} (0.33 psec). This process is reflected in the behavior of the correlation function associated with these bands (Fig. 81b). The less-damped behavior at 11.6 kbars is an indication that the orientational correlation is greater.

The angular forces resulting from mechanical anisotropy seem to be enhanced at the greater pressure, an effect that can be seen reflected in the very large increase in the torque-dependent parameters $K_0(0)$ and $K_1(0)$ (Table XI). The equivalent correlation function of depolarized Rayleigh scattering has recently been observed with applied pressure by Dill, Livovitz, and Bucaro,[127] van Konynenburg and Steele,[128] and Perrot, Devaure, and Lascombe.[129] The effect of temperature is not as pronounced on $K_0(0)$ and $K_1(0)$ as that of pressure, but for $CS_2(l)$ both increase with T. This dependence of mean-square torque upon temperature is predicted both by harmonic well dynamics and hard-core collisions. Therefore, no discernible

TABLE XI
Parameters for $CS_2(l)$ and $CCl_4(l)$[a]

Liquid	Temp. (°K)	P (bars)	$10^{40}I$ (g·cm²)	$xK_0(0)$	$xK_1(0)$	$x^{1/2}\gamma$	$(\epsilon_0-\epsilon_\infty)$
CS_2	296	1	258.6	26.2	170.2	20.3	0.026
	293	11,600	"	79.9	247.6	32.7	0.018
	232	1	"	21.9	114.3	12.0	0.034
	315	1	"	29.9	212.0	27.0	0.020
CCl_4	296	1	242	10.9	80.6	14.2	0.019
	313	1	"	10.2	65.1	12.2	0.017
	328	1	"	9.1	51.2	10.1	0.016
	343	1	"	10.3	77.7	14.6	0.016

[a]Reproduced by permission from *J. Chem. Soc. Faraday Trans.* 2, **72**, 1206 (1976).

$$x = \frac{I}{2kT}$$

"loosening up" of internal structure can be observed in $CS_2(l)$ over the range 232 to 315°K, the intermolecular torque being determined by the thermal energy available to each molecule (kT).

The situation is different in the spherical top CCl_4 (Fig. 82) over the range 296 to 343°K, the latter being a few degrees below the boiling point at 1 bar. Both $K_0(0)$ and $K_1(0)$ *decrease* as T increases, although the values at 343°K are slightly anomalous (Table XI). Therefore, there must be a considerable increase in free volume, and thereby translational freedom, as the boiling point is approached in order to overcome the purely thermal increase ($\propto kT$) in the mean-square torque. An important indication is that the mean-square torque is always much smaller for CCl_4 than for CS_2, implying that molecular geometry plays an important part in rotational freedom of motion. This is particularly so in the plastic crystalline phase of CBr_4 dealt with below.

It is relevant to note that the nuclear magnetic resonance spin-rotation relaxation time T_1 of liquids is observed to decrease as temperature is raised, following an Arrhenius law. T_1 is inversely proportional to τ_J, the angular momentum correlation time, which thus increases with temperature. τ_J is a measure of the mean time during which a molecule seems to retain its angular momentum, and in spherical-top molecules in the liquid state it is known that spin-rotation interaction is the dominant relaxational mechanism, τ_J becoming long even at temperatures well below the critical point. In contrast, for asymmetric tops and sticklike molecules, spin-rotation interaction becomes appreciable only at high temperatures, the ratio

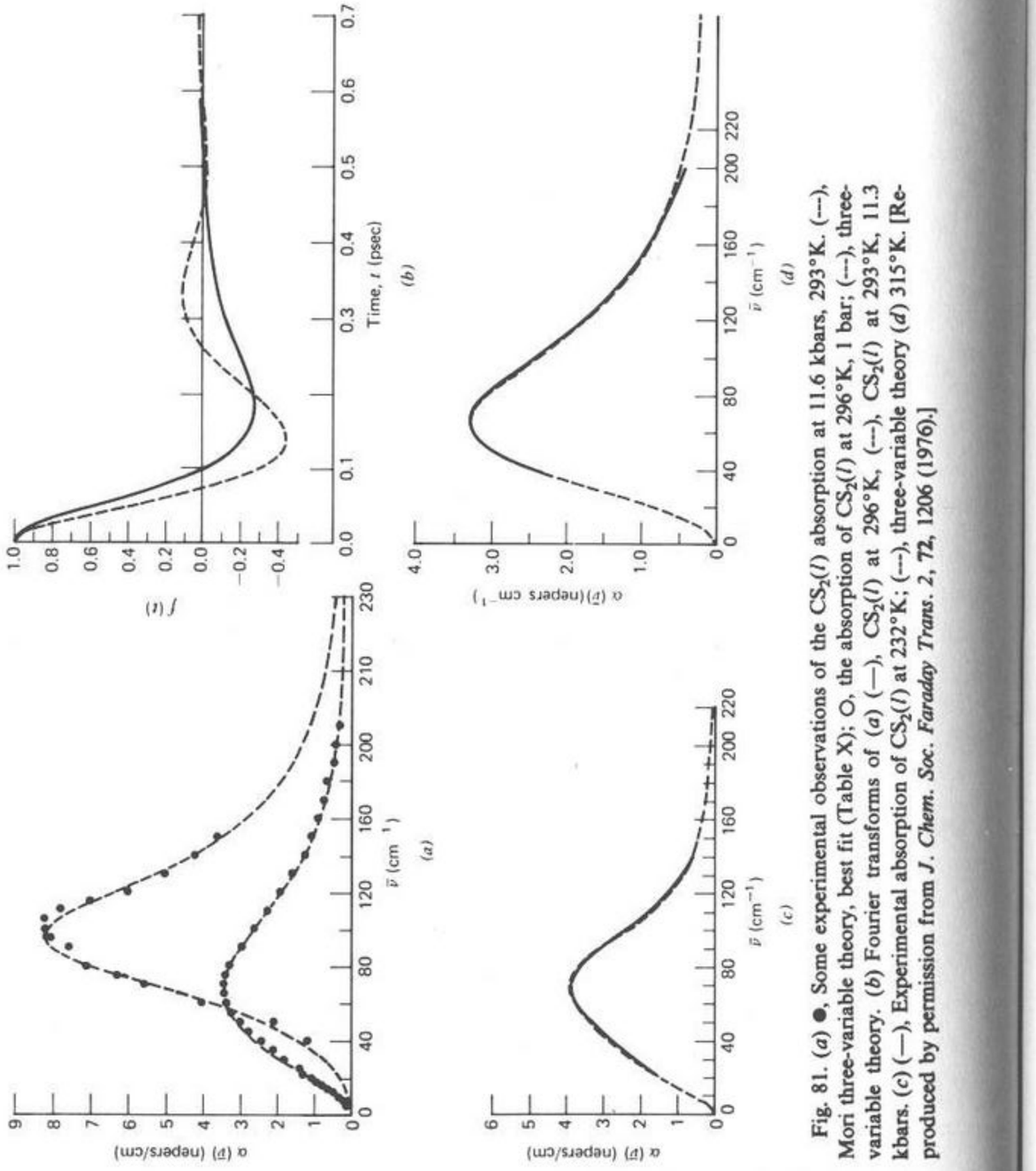

Fig. 81. (*a*) ●, Some experimental observations of the $CS_2(l)$ absorption at 11.6 kbars, 293°K. (---), Mori three-variable theory, best fit (Table X); ○, the absorption of $CS_2(l)$ at 296°K, 1 bar; (---), three-variable theory. (*b*) Fourier transforms of (*a*) (—), $CS_2(l)$ at 293°K, 11.3 kbars. (*c*) (—), Experimental absorption of $CS_2(l)$ at 232°K; (---), three-variable theory (*d*) 315°K. [Reproduced by permission from *J. Chem. Soc. Faraday Trans. 2*, **72**, 1206 (1976).]

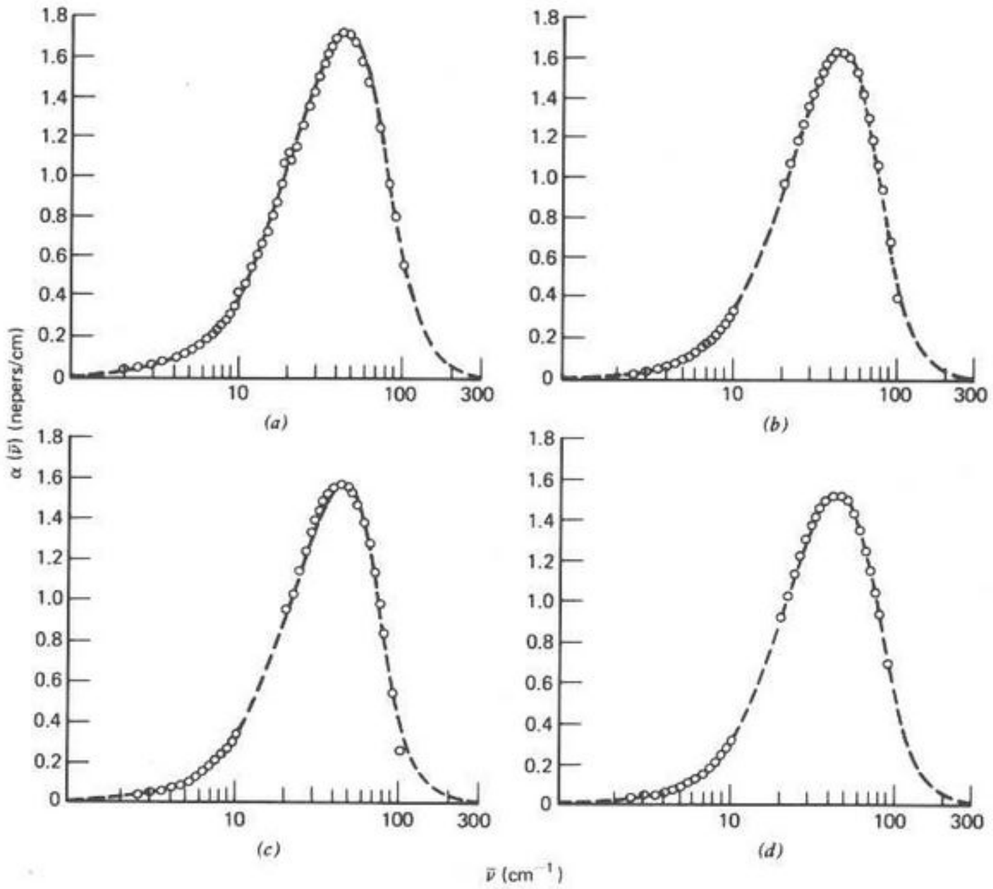

Fig. 82. Far infrared absorptions of $CCl_4(l)$. ○, Experimental: (---), Mori three-variable theory. (*a*) 296°K; (*b*) 313°K; (*c*) 328°K; (*d*) 343°K. [Reproduced by permission from *J. Chem. Soc. Faraday Trans. 2*, **72**, 1206 (1976).]

between dielectric and NMR relaxation times being close to the Hubbard ratio of 3 (rotational diffusion). In sticklike molecules, the motions about different symmetry axes is often observed to be highly anisotropic (e.g., in liquid propane near the critical point) the rotation about the C_{3v} axis is eight times faster than that about the perpendicular,[130] the contribution of spin-rotation relaxation being about equal to that of the spin-spin magnetic dipolar correlation time, and not dominant, as in spherical tops.

The apparent dispersion $(\epsilon_0 - \epsilon_\infty)$ is lower at 11.6 kbars than at 1 bar on $CS_2(l)$ and also decreases with temperature for both liquids. There remains a considerable amount of theoretical work to do, probably with the aid of computer simulations, before the observables can be interpreted in terms of molecular constants.

1. *Rotational Correlations in Plastic CBr_4 Crystals*

In this final section we comment upon the zero-THz induced far-infrared absorptions in plastic crystalline and liquid CBr_4 in order to study the change in rotational dynamics brought about by the increased translational constraint and packing symmetry of the solid. It turns out[131] that the barrier to rotational motion is slightly *increased* on going from the solid to the liquid a few degrees above the melting point. The integrated intensity per molecule is slightly greater in the liquid, which suggests that the spatial disposition of the electrostatic part of the intermolecular potentials is important in determining the magnitude of the molecular-induced dipole moment. The dipole cross-correlation function corresponding to these bands is compared with that of octopole-induced dipole absorption of a two molecule collision of spherical tops, and with the autocorrelation function for a Maxwellian ensemble of freely rotating molecules of this symmetry. It is found that the mean torque greater initially in the condensed phases; thereafter rotational motion is correlated.

In the plastic crystalline phase of CBr_4, in comparison with the room-temperature monoclinic form, each molecule is left with a characteristically

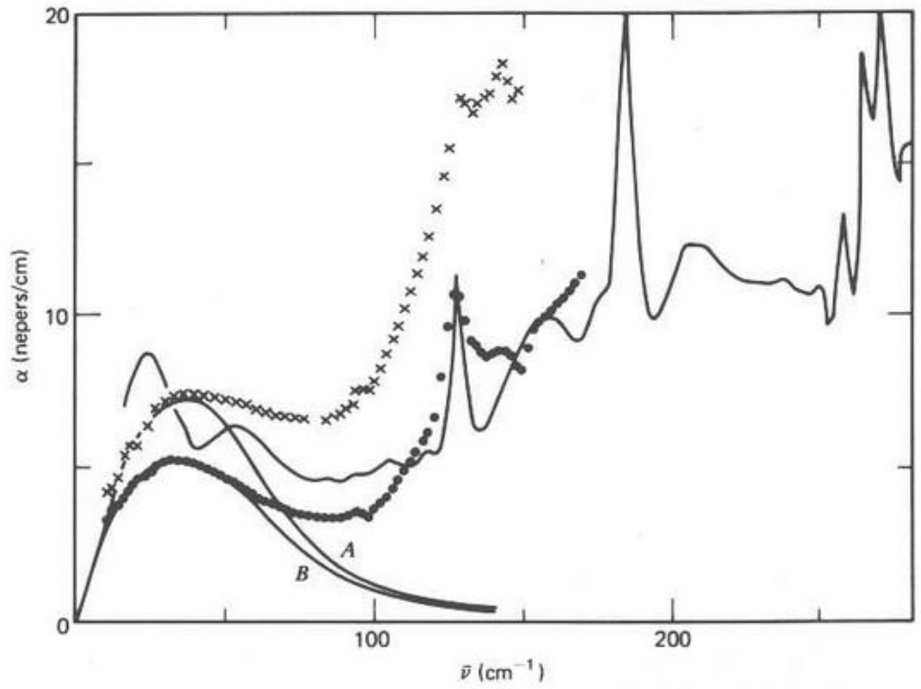

Fig. 83. Absorption of the $Th^6(Pa^3)$ monoclinic phase at 298°K. ●, Absorption of the plastic (simple cubic) single crystal at 358°K; •, absorption of the liquid at 376°K; (—), (*A*), (*B*) Mori three-variable theory. [Reproduced by permission from *J. Chem. Soc. Faraday Trans. 2*, **72**, 2147 (1976).]

generous amount of rotational freedom, but translational freedom is limited, although not entirely absent. In contrast, both types of dynamics are available and strongly coupled in the liquid. The broad bands centered near 32 cm^{-1} (Fig. 83) in both liquid and rotator phase are interpreted as intermolecular in origin, since they do not correspond to any known difference modes or overtones or fundamental, and occur at frequencies where such bands are prevalent for nondipolar molecules. In the $Th^6(Pa^3)$ monoclinic phase at 298°K this band is replaced by a doublet, both components of which are considerably broader than the fundamentals at 125 cm^{-1} and 270 cm^{-1}. In the plastic crystalline phase at 376°K, the fundamental at 124 cm^{-1} is broadened compared with the monoclinic phase, and considerably so in the liquid.

If a CBr_4 molecule whose center of mass is at the point $\mathbf{R}(\mathbf{r},\theta,\phi,\chi)$ is assumed to develop a temporary dipole moment under the influence of the electrostatic fields of its neighbors, then the vector sum of these fields at **R** at any instant will be determined by the relative positions of all other molecules in the ensemble at that time, and consequently will be a measure of the disorder or ordering in the lattice of molecules near enough for their fields to be sufficiently influential. In order then to estimate absolutely the degree of rotational freedom retained in these condensed phases, it is profitable to compare the correlation function derived experimentally (Fig. 84)

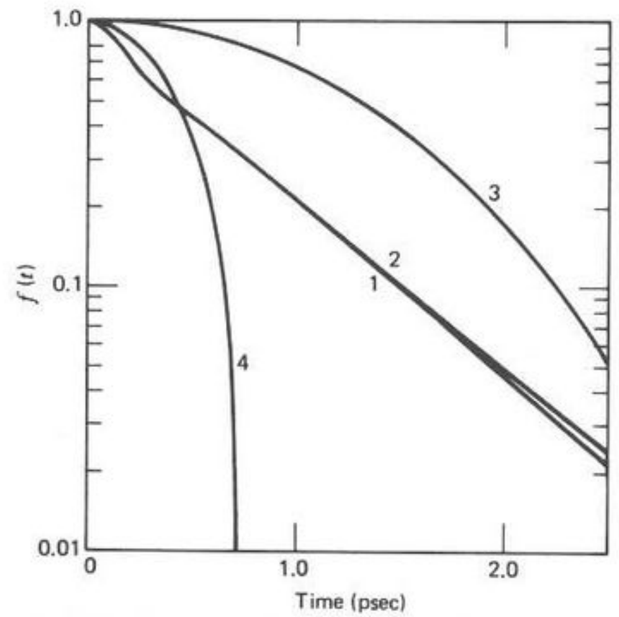

Fig. 84. Correlation functions for CBr_4 from induced far-infrared bands. (1) $C(t)$ (liquid); (2) plastic crystal; (3) $C_{FR}(t)$; (4) $C_{\Omega}(t)$. [Reproduced by permission from *J. Chem. Soc. Faraday Trans. 2*, **72**, 2147 (1976).]

with those estimated using models of rotational motion in the gas phase. The correlation function for the free rotation of a Maxwellian distribution of spherical tops is given by the classical expression

$$C_{FR}(t)=\frac{2}{3}\left(1-t^2\frac{kT}{I}\right)\exp\left(-t^2\frac{kT}{2I}\right)+\frac{1}{3}$$

This is illustrated in Fig. 84 for CBr_4 at 376°K and decays much more slowly than the functions $C(t)$ of the condensed phase. Thus the effect of intermolecular forces is clearly seen in the time domain. The bimolecular octopole-induced band produces in the classical limit a correlation function $C_\Omega(t)$ as follows, and is compared with $C_{FR}(t)$ and $C(t)$ in Fig. 84.

The total integrated intensity of an octopole-induced dipole absorption band spherical tops is given by Ozier and Fox[132] as

$$A=\sum_{J\neq J} A(J,J')$$

where

$$A(J,J')=\frac{(8\pi)^4N^2\Omega^2\alpha_0^2}{280hcZ}\int_0^\infty R^{-8}\exp(-U(R)/kT)dR$$
$$\times\bar{\nu}(J,J')(2J+1)(2J'+1)\left[\exp(-aJ(J+1))-\exp(-aJ'(J'+1))\right]$$

with

$$a=Bhc/kT \qquad \bar{\nu}(J,J')=B\left[J'(J'+1)-J(J+1)\right]$$

and where $\Delta J=J'-J=0$, 1, 2, 3 are allowed. Here N is the molecular number density, α_0 the polarizability, B the rotational constant (cm^{-1}), and Z rotational partition function.

$$Z=\sum_J(2J+1)^2\exp(-aJ(J+1))$$

Thus the overall band is the sum of the individual transition intensities $A(J,J+1)$, $A(J,J+2)$, and $A(J,J+3)$. The correlation function is thus given by

$$C_\Omega(t)=\sum_{i=1,3}^{3}\int_0^\infty\frac{A(J,J+i)\cos(2\pi\bar{\nu}ct)d\bar{\nu}}{{}^{(i)}\bar{\nu}\left[1-\exp(-h^{(i)}\bar{\nu}c/kT)\right]}$$

with

$${}^{(1)}\bar{\nu}=2B(J+1) \qquad {}^{(2)}\bar{\nu}=2B(2J+3) \qquad {}^{(3)}\bar{\nu}=6B(J+2)$$

It may be shown that

$$A(J,J+1)\propto{}^{(1)}\bar{\nu}(2J+1)(2J+3)\exp\left[-aJ(J+1)\right]\left[1-\exp(-hc^{(1)}\bar{\nu}/kT)\right]$$
$$A(J,J+2)\propto{}^{(2)}\bar{\nu}(2J+1)(2J+5)\exp\left[-aJ(J+1)\right]\left[1-\exp(-hc^{(2)}\bar{\nu}/kT)\right]$$
$$A(J,J+3)\propto{}^{(3)}\bar{\nu}(2J+1)(2J+7)\exp\left[-aJ(J+1)\right]\left[1-\exp(-hc^{(3)}\bar{\nu}/kT)\right]$$

the proportionality constant being in each case the J-independent part of (I.7). We have, finally, in the classical sense

$$C_\Omega(t)\propto\int_0^\infty\left[\left(\frac{\bar{\nu}}{B}-1\right)\left(\frac{\bar{\nu}}{B}+1\right)\exp\left[-a\left(\frac{\bar{\nu}}{2B}-1\right)\frac{\bar{\nu}}{2B}\right]\right.$$
$$+\left(\frac{\bar{\nu}}{2B}-2\right)\left(\frac{\bar{\nu}}{2B}+2\right)\exp\left[-a\left(\frac{\bar{\nu}}{4B}-\frac{3}{2}\right)\left(\frac{\bar{\nu}}{4B}-\frac{1}{2}\right)\right]$$
$$\left.+\left(\frac{\bar{\nu}}{3B}\quad\left(\frac{\bar{\nu}}{3B}+3\right)\exp\left[-a\left(\frac{\bar{\nu}}{6B}-2\right)\left(\frac{\bar{\nu}}{6B}-1\right)\right]\right]\cos 2\pi\bar{\nu}ct\,d\bar{\nu}$$

This function ($C_\Omega(t)/C_\Omega(0)$) displayed in Fig. 84 looks very little like the correlation functions of the condensed phase bands, which fall off initially faster and thereafter exponentially and more slowly. This octopolar function becomes negative after 0.7 psec, exhibits a minimum at 1.2 psec, and is damped to zero after 5.0 psec. The fact that $C_\Omega(t)/C_\Omega(0)$ falls off faster than $C_{FR}(t)$ means that a_2 is affected in some way by molecular interaction in the classical expansion

$$C(t)=1-a_2\frac{t_2}{2!}+\cdots$$

From Fig. 83 it is clear that CBr_4 molecules in both the liquid and plastic crystalline experience a torque almost immediately after the arbitrary $t=0$. This is greater in magnitude than that in a bimolecular encounter of octopole fields, since $C(t)$ falls off faster initially than $C_\Omega(t)/C_\Omega(0)$. Rotation motions are then correlated in the condensed phases, and after ~0.7 psec both $C(t)$ become exponential and decay relatively slowly compared with $C_\Omega(t)/C_\Omega(0)$. O'Dell and Berne[108] have discovered recently that rotational motion is freer in the *solid* just below the melting point in rough-hard-sphere ensembles. This seems to be the case here since $C(t)$ for the liquid

falls off initially a little faster. The greater initial torque in the condensed phases can be explained superficially in terms of the greater packing density since the intermolecular potential would be much greater on average with van der Waals radii overlapping (repulsive domain) for a greater percentage of the time. However, this is, as always, too simple a view, since the packing density in the plastic solid is the greater while the mean torque is smaller. This can only mean that symmetry of packing and the resultant restriction on molecular diffusion is an important factor in determining the ease of rotational movement in the plastic phase.

ACKNOWLEDGMENT

S.R.C. is thanked for an equipment grant and a fellowship grant (to G.J.E.). M.W.E. thanks the Ramsay Memorial Trust for the 1976–1978 Fellowship. Mrs. Vincent of the Applied Mathematics Department and Mrs. Evans of the Chemistry Department are thanked for their usual high standard of typing.

Finally, M.W.E. wishes to thank publishing, technical and computer staffs for their help and advice.

REFERENCES

1. K. D. Muller and W. G. Rothschild, *Far-Infrared Spectroscopy*, Wiley-Interscience, New York, 1971. This book contains a list of all 1512 papers on the far-infrared up to 1970.
2. G. W. Chantry, *Submillimetre Spectroscopy*, Academic, London, 1971.
3. A. Gerschel, *Mol. Phys.*, **32,** 679, (1976).
4. N. E. Hill, A. H. Price, W. E. Vaughan, and M. Davies, *Dielectric Properties and Molecular Behaviour*, Van Nostrand-Reinhold, London, 1969.
5. G. J. Davies and M. Evans, *J. Chem. Soc. Faraday Trans.* 2, **72,** 1194 (1976).
6. D. R. Bosomworth and H. P. Gush, *Can. J. Phys.*, **37,** 362 (1959); **43,** 751 (1965).
7. J. -P. Hansen and I. R. McDonald, *Theory of Simple Liquids*, Academic, London, 1976.
8. B. K. P. Scaife, *Complex Permittivity*, English University Press, London, 1971, p. 35.
9. R. Zwanzig, *J. Chem. Phys.*, **38,** 2766 (1963).
10. J. Orban and A. Bellemans, *J. Chem. Phys.*, **49,** 363 (1968); J. Orban, J. van Craen, and A. Bellemans, *J. Chem. Phys.*, **49,** 1778 (1968).
11. R. H. Cole, *Mol. Phys.*, **27,** 1 (1974).
12. J. M. Deutch, *Faraday Symp. Chem. Soc.*, **11,** 1977.
13. W. T. Coffey, *Mol. Phys.*, in press.
14. J. H. van Vleck and V. Weisskopff, *Rev. Mod. Phys.*, **17,** 227 (1945).
15. R. Lobo, J. E. Robinson, and S. Rodriguez, *J. Chem. Phys.*, **59,** 5992 (1973).
16. D. Frenkel, G. H. Wegdam, and J. van der Elsken, *J. Chem. Phys.*, **57,** 2691 (1972).
17. D. Kivelson and P. Madden, *Mol. Phys.*, **30,** 1749 (1975).
18. H. Mori, *Prog. Theor. Phys.*, **33,** 423 (1965).
19. P. Langevin, *J. Phys.*, **4,** 678 (1905).
20. A. R. Davies and M. W. Evans, *Mol. Phys.*, **35,** 857 (1978).
21. A. Morita, *J. Phys. D.*, in press.
22. J. T. Lewis, J. McConnell, and B. K. P. Scaife, *Proc. R. Irish Acad. A*, **76,** 43 (1976); G. W. Ford, J. T. Lewis, and J. McConnell, *Proc. R. Irish Acad. A*, **76,** 117 (1976).

23. A. D. Fokker, *Ann. Phys.*, **43,** 812 (1914); M. Planck, *Sitzungsber. Preuss. Akad.*, 324 (1917).
24. S. A. Adelman, *J. Chem. Phys.*, **64,** 124 (1976); S. A. Adelman and B. J. Garrison, *Mol. Phys.*, **33,** 1671 (1977).
25. B. J. Berne and G. D. Harp, *Adv. Chem. Phys.*, **17,** 63 (1970).
26. B. J. Berne and R. Pecora, *Dynamic Light Scattering with Applications to Chemistry, Biology and Physics*, Wiley, New York, 1976.
27. D. A. McQuarrie, *Statistical Mechanics*, Harper & Row, 1975.
28. P. Kruus, *Liquids and Solutions, Structure and Dynamics*, Dekker, New York, 1977.
29. J. H. Calderwood and W. T. Coffey, *Proc. R. Soc. Ser. A*, **356,** 269 (1977); P. S. Damle, A. Sjölander, and K. S. Singwi, *Phys. Rev.*, **165,** 277 (1968).
30. W. T. Coffey, G. J. Evans, M. W. Evans, and G. H. Wegdam, *J. Chem. Soc. Faraday Trans. 2*, **74,** 310 (1978).
31. L. van Hove, *Phys. Rev.*, **95,** 249 (1954).
32. B. J. Berne and J. A. Montgomery, *Mol. Phys.*, **32,** 363 (1976).
33. D. Chandler, *J. Chem. Phys.*, **60,** 3508 (1974).
34. R. G. Gordon, *Adv. Magn. Reson.*, **3,** 1 (1968); R. E. D. McClung, *J. Chem. Phys.*, **57,** 5478 (1972).
35. K. V. Mardia, *Statistics of Directional Data*, Academic, New York, 1972.
36. T. J. Lewis, in M. Davies, Ed., *Dielectric and Related Molecular Processes*, Vol. 3, The Chemical Society, London, 1977, p. 186.
37. P. Debye, *Polar Molecules*, Dover, New York, 1954.
38. B. Keller and F. Kneubühl, *Helv. Phys. Acta*, **45,** 1127 (1972).
39. P. Desplanques, "Absorption dipolaire et dynamique moleculaire en phase liquide," thesis, University of Lille, 1974.
40. F. Bliot and E. Constant, *Chem. Phys. Lett.*, **29,** 618 (1974).
41. G. J. Evans, G. H. Wegdam, and M. W. Evans, *Chem. Phys. Lett.*, **42,** 331 (1976).
42. J. Barojas, D. Levesque, and B. Quentrec, *Phys. Rev. A*, **7,** 1092 (1973).
43. M. W. Evans, in Ref. 36, p. 1.
44. M. Drawid and J. W. Halley, *Magnetism and Magnetic Materials—1976*, Publ. 34, American Institute of Physics, New York, 1976, p. 211.
45. K. Lindenberg and R. I. Cukier, *J. Chem. Phys.*, **62,** 3271 (1975).
46. D. Kivelson and T. Keyes, *J. Chem. Phys.*, **57,** 4599 (1972); D. Kivelson, *Mol. Phys.*, **28,** 321 (1974).
47. M. Guillot and S. Bratos, *Mol. Phys.*, in press (1979).
48. P. G. Wolynes and J. M. Deutch, *J. Chem. Phys.*, **67,** 733 (1977).
49. P. G. de Gennes, *The Physics of Liquid Crystals*, Oxford University Press, New York, 1974, Chap. 3.
50. Eighty papers will be published in the Proceedings of the 3rd International Conference on Submillimetre Waves, Infrared Physics, held at Guildford in 1978.
51. G. Williams, *Chem. Soc. Rev.*, **7,** 89 (1978).
52. C. Brot, in Ref. 36, Vol. 2., p. 1.
53. W. A. Steele, *Adv. Chem. Phys.*, **34,** (1976).
54. G. J. Evans, C. J. Reid, and M. W. Evans, *J. Chem. Soc. Faraday Trans. 2*, **74,** 343 (1978).
55. P. van Konynenburg and W. A. Steele, *J. Chem. Phys.*, **62,** 2301, (1975).
56. J. P. Poley, *J. Appl. Sci.*, **4B,** 337 (1955).
57. J. Chamberlain, *Infrared Phys.*, **11,** 22, (1971).
58. D. H. Martin and E. Puplett, *Infrared Phys.*, **10,** 105 (1970).
59. G. J. Evans, thesis, University of Wales, 1977.

60. J. W. Flemming, *Infrared Phys.*, **10,** 57 (1970).
61. W. B. Streett and K. E. Gubbins, *Annu. Rev. Phys. Chem.*, **28,** 373 (1977).
62. J. S. Rowlinson and M. Evans, *Annu. Rep. Chem. Soc.*, **72A,** 5 (1975). This contains references to six separate and different derivations of this theorem.
63. D. E. Sullivan and J. M. Deutch, *J. Chem. Phys.*, **62,** 2130 (1975).
64. J. L. Greffe, J. Goulon, J. Brondeau, and J. L. Rivail, in J. Lascombe, Ed., *Molecular Motion in Liquids*, Dordrecht, 1974, p. 151.
65. R. Kubo, *Lectures in Theoretical Physics*, Wiley-Interscience, New York, 1959.
66. M. W. Evans, *Adv. Mol. Rel. Int. Proc.*, **10,** 203 (1977).
67. G. J. Davies, G. J. Evans, and M. W. Evans, *J. Chem. Soc. Faraday Trans. 2*, **72,** 1904 (1976).
68. M. W. Evans, *J. Chem. Soc. Faraday Trans. A*, **72,** 2138 (1976).
69. G. W. F. Pardoe and H. A. Gebbie, Symposium on Submillimetre Waves, Polytechnic Inst., Brooklyn, 1970, p. 643.
70. J. Hasted, in Ref. 36, Vol. 1.
71. J. A. Janik, in Ref. 36, p. 45.
72. D. Frenkel and G. H. Wegdam, *J. Chem. Phys.*, **61,** 4671 (1974).
73. D. Frenkel, *Faraday Symp. Chem. Soc.*, 11, (1976).
74. M. W. Evans, *Mol. Phys.*, **34,** 963 (1977).
75. P. N. Brier and A. Perry, *Adv. Mol. Int. Rel. Proc.*, in press (1978).
76. J. Goulon, D. Canet, M. Evans, and G. J. Davies, *Mol. Phys.*, **30,** 973 (1975).
77. G. Williams and M. Cook, *J. Chem. Soc. Faraday Trans. 2*, **67,** 990 (1971).
78. T. E. Faber and G. R. Luckhurst, *Annu. Rep. Chem. Soc., Lond.*, **75A,** 31 (1975).
79. B. J. Bulkin and W. B. Lok, *J. Phys. Chem.*, **77,** 326 (1973).
80. M. W. Evans, M. Davies, and I. Larkin, *J. Chem. Soc. Faraday Trans. 2*, **69,** 1011 (1973).
81. N. E. Hill, *Proc. Phys. Soc.*, **82,** 723 (1963).
82. G. A. P. Wyllie, *J. Phys. C.*, **4,** 564 (1971).
83. G. J. Evans and M. W. Evans, *J. Chem. Soc. Faraday Trans.* 2, **72,** 1169 (1976).
84. E. Sciesinska, J. Sciesinski, J. Twardowski, and J. D. Janik, *Inst. Nucl. Phys.*, 847/PS (1973).
85. G. J. Evans and M. W. Evans, *J. Chem. Soc. Chem. Commun.*, 267 (1978).
86. G. J. Evans and M. Evans, *J. Chem. Soc. Faraday Trans 2*, **73,** 203 (1977).
87. M. Schwartz and L. H. Wang, private communication to B. J. Bulkin, Ref. 79.
88. M. S. Beevers, J. Crossley, D. C. Garrington, and G. Williams, *J. Chem. Soc. Faraday Trans. 2*, **72,** 1482 (1976).
89. R. Haffmanns and I. W. Larkin, *J. Chem. Soc., Faraday Trans.* 2, **68,** 1729 (1972).
90. M. Davies, *Annu. Rep. Chem. Soc.*, **67A,** 65 (1970).
91. A. Aihara, C. Kitazawa, and A. Nohara, *Bull. Chem. Soc. Jap.*, **43,** 3750 (1970).
92. I. Darmon and C. Brot, *Mol. Cryst.* **2,** 301 (1967).
93. I. Tanaka, F. Iwasaki, and A. Aihara, *Acta Crystallogr.*, **30B,** 1546 (1974).
94. G. W. F. Pardoe and J. Flemming, to be published.
95. G. P. Johari and C. P. Smyth, *J. Chem. Phys.*, **56,** 4411 (1972); G. P. Johari and M. Goldstein, *J. Chem. Phys.*, **53,** 2372 (1970); G. P. Johari, *J. Chem. Phys.*, **58,** 1766 (1973).
96. G. Williams, in Ref. 36, Vol. 2.
97. A. Rahman, *Phys. Rev. A*, **136,** 405 (1964).
98. P. S. Y. Cheung and J. G. Powles, *Mol. Phys.*, **30,** 921 (1975).
99. W. B. Streett and D. J. Tildesley, *Proc. R. Soc. Lond.*, **348A,** 485 (1976); **355A,** 239 (1977).

100. J. W. E. Lewis and K. Singer, *J. Chem. Soc. Faraday Trans. 2*, **71,** 301 (1975); K. Singer, A. Taylor, and J. V. L. Singer, *Mol. Phys.*, **33,** 1757 (1977).
101. C. W. Gear, *Numerical Initial Value Problems in Ordering Differential Equations*, Prentice-Hall, Englewood Cliffs, N. J., 1971, pp. 148–150.
102. V. F. Sears, *Proc. Phys. Soc.*, **86,** 953 (1965).
103. B. A. Dasannacharya and K. R. Rao, *Phys. Rev. A*, **137,** 417 (1965).
104. G. E. Uhlenbeck and L. S. Ornstein, *Phys. Rev.*, **36,** 823 (1930).
105. W. T. Coffey and M. W. Evans, *Mol. Phys.*, **35,** 975 (1978).
106. B. J. Berne, *Faraday Symp. Chem. Soc.*, **11,** (1977).
107. G. H. Wegdam, G. J. Evans, and M. Evans, *Mol. Phys.*, **33,** 1805 (1977).
108. J. O'Dell and B. J. Berne, *J. Chem. Phys.*, **63,** 2376 (1975).
109. F. Hermans, E. Kestemont, R. van Loon, and R. Finsy, Proceeding of the 3rd International Conference on Submillimetre Waves, Guildford, 1978, Infrared Physics, to be published.
110. D. H. Whiffen, *Trans. Faraday Soc.*, **46,** 124 (1950).
111. R. Savoie and R. P. Fournier, *Chem. Phys. Lett.*, **7,** 1 (1970).
112. G. J. Davies, J. Chamberlain, and M. Davies, *J. Chem. Soc. Faraday Trans. 2*, **69,** 1223 (1973); G. J. Davies and J. Chamberlain, *J. Chem. Soc. Faraday Trans. 2*, **68,** 1739 (1973).
113. W. Ho, G. Birnbaum and A. Rosenberg, *J. Chem. Phys.*, **55,** 1028 (1971).
114. A. I. Baise, *J. Chem. Soc. Faraday Trans. 2*, **68,** 1904 (1972).
115. M. Evans, *J. Chem. Soc. Faraday Trans. 2*, **69,** 763 (1973).
116. B. S. Frost, *J. Chem. Soc. Faraday Trans. 2*, **69,** 1142 (1973).
117. J. P. Colpa and J. A. A. Ketelaar, *Mol. Phys.*, **1,** 343 (1958).
118. M. Evans, *Mol. Phys.*, **29,** 1345 (1975).
119. D. R. Bosomworth and H. P. Gush, *Can. J. Phys.*, **43,** 751 (1965).
120. G. Jacucci, U. Buontempo, and S. Cunsolo, *J. Chem. Phys.* **59,** 3750 (1973).
121. M. Evans, *Spectrochim. Acta*, **32A,** 1253 (1976).
122. A. I. Baise, *J. Chem. Phys.*, **60,** 2936 (1974).
123. S. Kielich, in Ref. 36, Vol. 1, pp. 192–387.
124. G. J. Evans and M. W. Evans, *Adv. Mol. Rel. Int. Proc.*, **9,** 1 (1976).
125. C. C. Bradley, H. A. Gebbie, A. C. Gilby, V. V. Kechin, and J. H. King, *Nature*, **211,** 839 (1966).
126. M. W. Evans and G. J. Davies, *J. Chem. Soc. Faraday Trans. 2*, **72,** 1206 (1976).
127. J. F. Dill, T. A. Litovitz, and J. A. Bucaro, *J. Chem. Phys.*, **62,** 3839 (1975).
128. P. van Konynenburg and W. A. Steele, *J. Chem. Phys.*, **62,** 2301 (1975).
129. M. Perrot, J. Devaure, and J. Lascombe, *Mol. Phys.*, **30,** 97 (1975).
130. J. Jonas and T. M. Di Gennaro, *J. Chem. Phys.*, **50,** 2392 (1969).
131. G. J. Davies, G. J. Evans, and M. W. Evans, *J. Chem. Soc. Faraday Trans. 2*, **72,** 2147 (1976).
132. I. Ozier and K. Fox, *J. Chem. Phys.*, **52,** 1416 (1970).